ZIRCALOY-4 AND INCOLOY 800H/HT ALLOYS FOR THE CURRENT AND FUTURE NUCLEAR FUEL CLADDINGS

A Thesis Submitted to the College of

Graduate Studies and Research

In Partial Fulfillment of the Requirements

For the Degree of Doctor of Philosophy

In the Department of Mechanical Engineering

University of Saskatchewan

By
Hamed Akhiani

PERMISSION TO USE

In presenting this thesis in partial fulfillment of the requirements for a postgraduate degree from the University of Saskatchewan, I agree that the Libraries of this University may make it freely available for inspection. I further agree that permission for copying of this thesis in any manner, in whole or in part, for scholarly purposes may be granted by the professor who supervised my thesis work or, in their absence, by the Head of the Department or the Dean of the College in which my thesis work was done. It is understood that any copying or publication or use of this thesis or parts thereof for financial gain shall not be allowed without my written permission. It is also understood that due recognition shall be given to me and to the University of Saskatchewan in any scholarly use which may be made of any material in my thesis.

Requests for permission to copy or to make other use of material in this thesis in whole or part should be addressed to:

Head of the Department of Mechanical Engineering
57 Campus Dr.
University of Saskatchewan
Saskatoon, Saskatchewan (S7N 5A9)

ABSTRACT

Fuel cladding is one of the most critical components of nuclear reactors; so it is important to improve our understanding of various properties and behaviors of the cladding under different conditions approximating the nuclear reactor environment. Moreover, the efficiency of energy production, in addition to safety concerns, has resulted in progressive improvement of nuclear reactors design from Generation I to Generation IV. To complement this progressive trend, materials used for fuel cladding need to be improved or new materials should be developed. In this thesis, I address problems in the improvement of present fuel cladding and also investigate fuel cladding materials to be used in future Generation IV nuclear reactors.

In the case of current Zircaloy-4 fuel claddings, a detailed evaluation of the surface roughness effects on their performance and properties of Zircaloy-4 fuel claddings was studied. A smoother surface on Zircaloy-4 cladding tubes is demanded by the customers; however no systematic study is available addressing the effect of surface roughness on the claddings' performance. Thus the effects of surface roughness on texture, oxidation, hydriding behaviors and mechanical properties of Zircaloy-4 cladding tubes were investigated using various methods. It was found that surface roughness has some effects on the oxidation of Zircaloy-4. Increasing the surface roughness would increase the weight gain, however, this effect was more pronounced at the initial oxidation stages.

Synchrotron techniques were used to characterize the electronic structure of zirconium alloys in their oxidized and hydrided states. With this approach, complex interactions between hydrogen and oxygen in the zirconium matrix could be investigated, which could not be resolved using conventional methods.

As a candidate for future fuel cladding material, Incoloy 800H/HT, which is expected to be considered in super-critical water-cooled Gen IV reactors, was studied in order to optimize microstructure, texture and grain boundary characteristics. A specific Thermo-Mechanical Processing (TMP) was employed to manipulate the texture, microstructure and grain boundary character distribution. The deformation and annealing textures of thermo-mechanically processed samples were investigated by means of X-ray diffraction and orientation imaging microscopy. It was found that different rolling paths lead to different textures.

The origin of different textures in differently (unidirectional and cross) rolled Incoloy 800H/HT at high deformation strains were investigated. In addition, the recrystallization kinetic of differently rolled samples was studied. It was found that the oriented nucleation plays an important role in determining the recrystallization texture. Unidirectional rolled samples exhibited a faster recrystallization kinetic compared with cross rolled ones, due to the presence of γ-fibre.

The effect of the aforementioned microstructural parameters (grain size, texture and GBCD) on the oxidation resistance of Incoloy 800H/HT in super-critical water was investigated. It was found that the oxidation resistance of Incoloy 800H/HT can be improved by TMP. The optimum TMP process for enhancing the oxidation resistance was proposed. Microstructural parameters that can improve the oxidation resistance of Incoloy 800H/HT were identified. These findings will contribute to the effective selection of fuel cladding material for application in Gen IV SCW reactors.

AKNOWLEDGMENT

I would like to express my sincere gratitude to my supervisor, Professor Jerzy Szpunar for his continuous advice, support and encouragement throughout this research.

I also appreciate the Department of Mechanical Engineering faculty and staff members, particularly the graduate chair Professor Reza Fotouhi. I greatly acknowledge the advisory committee members: Professor Akira Hirose, Professor Akindele Odeshi, Professor Daniel Chen and Professor Scott Noble for their valuable comments.

My special thanks to Mr. Sami Penttila (VTT Finland), Ms. Golsa Kafili, Mr. Majid Nezakat and my colleagues in the Advance Materials and Renewable Energy (AMRE) research team.

Finally I acknowledge Cameco Corporation, Natural Sciences and Engineering Research Council of Canada (NSERC), Cameco CRD-NSERC, and the Canada Research Chair programs for financial support. I also express my gratitude to Cameco Corporation and VTT Technical Research Centre of Finland for their technical assistance.

Last, by no means least, I owe my love to my family. It would have been much harder to finish a PhD without their support.

DEDICATION

This thesis is dedicated to my beloved parents, my first teachers, who taught me the true meaning of life and unconditional love.

TABLE OF CONTENTS

LIST OF TABLES

LIST OF FIGURES

ACRONYMS

BWR	Boiling Water Reactor
CANDU	CANada Deuterium Uranium
EDS	Energy Dispersive Spectroscopy
EBSD	Electron Backscattered Diffraction
Gen	Generation (of nuclear reactors)
GBCD	Grain Boundary Character Distribution
GBE	Grain Boundary Engineering
HAGB	High Angle Grain Boundary
LAGB	Low Angle Grain Boundary
PWR	Pressurized Water Reactors
PHWR	Pressurized Heavy Water Reactor
RBMK	High Power Channel-type Reactor (Russian)
SCW	Super-Critical Water
SEM	Scanning Electron Microscope
TMP	Thermo-Mechanical Processing
XPS	X-ray Photoelectron Spectroscopy
XRD	X-ray Diffraction

CHAPTER 1

Introduction

1.1. Overview of Chapter 1

In this chapter we briefly discuss the importance of fuel-cladding materials in the nuclear industry. With reference to Gen I, II, III and IV nuclear reactors, we elucidate the issues and knowledge gaps in understanding the structure and properties of current and future fuel cladding materials, which clarifies the objectives of the project.
A literature review for each part of this study is presented in the introduction section of each chapter. Therefore to avoid repetition, this chapter does not include a detailed literature review.

1.2. Nuclear energy: Safety issues and materials challenges

A direct result of a constantly increasing global population has been a demand for new sources of energy. Consequently, nuclear energy has been considered as an important source of energy that will play a significant role in the future energy demands. 15% of the world's electricity is produced by nuclear reactors in power plants and that contribution is ranked fourth among the other sources for electricity production (coal, gas, and oil respectively) [1]. As of April 2014, over 430 nuclear power plant units were in operation in 31 countries, and over 70 were under construction in 16 countries [2]. Considering upcoming new reactors worldwide, the role of nuclear power will be manifested significantly.

Production efficiency, in addition to the greater overall safety of nuclear energy, has led to the progressive development of nuclear reactors from Generation I to Generation IV [1]. Analysis of this growth suggests that nuclear power is developing toward a reliable and affordable source of energy for future generations.

However, the occurrence of nuclear disasters (e.g. Three Mile Island, Chernobyl and Fukushima) raised concerns for the safety perspective of these reactors. Human errors are often to blame in engineering failure cases, and this was the case in the aforementioned nuclear accidents. These errors can only be alleviated by detailed and comprehensive training. Despite this factor, safety can be ensured by the proper performance of the structural materials used inside the nuclear reactor. Accordingly, safe operation of current reactors relies on continual maintenance and efficient troubleshooting.

It is expected that some of Gen IV reactors will be fully implemented and operational by the year 2020 [1]. However, there are still decisions to be made as to what materials should be selected for fuel claddings in some of the new Gen IV reactors. Hence, finding the high performance fuel cladding materials for these new reactors is a principal concern.

1.3. Fuel cladding materials; current and future

Fuel cladding, since it carries the radioactive fuel, is one of the most important components of the nuclear reactor core. The selection of fuel cladding materials is often influenced by the choice of other core components (fuel, moderator, and coolant). However, certain properties for fuel claddings such as neutron transparency, mechanical strength, toughness, creep and oxidation resistance at operating temperatures, must be considered as priorities and should be optimized for particular design of the reactor [3]. Considering these peroperties, zirconium alloys have been used widely as fuel cladding materials in most of the generation II and III nuclear reactors (e.g. BWR, PWR and CANDU). Nevertheless, despite extensive research, there are still few unsolved issues particularly with their oxidation and hydriding. As the reactors of these generations are still in service and with many more are planned to be completed in the near future, research on zirconium based fuel cladding is still necessary.

In addition to the current generation of nuclear reactors, Gen IV reactors have been introduced to achieve better production efficiency and greater safety, although this is often linked to a more severe service condition for materials used in the reactor's core. The Gen IV six selected reactor systems are described in the Generation IV International Forum (GIF) road map [1,4]. The design specifications for these reactor systems are summarized in Table 1.1.

Table 1.1. The six selected reactor designs for Gen IV [1,5,6].

Reactor type	Coolant	Temperature (°C)	Pressure (MPa)	Fuel	Size(s) (MWe)
Gas-cooled Fast Reactor (GFR)	helium	850	7	U-238 +	1200
Lead-cooled Fast Reactor (LFR)	lead or Pb-Bi	480-800	0.1	U-238 +	20-180 300-1200 600-1000
Molten Salt Reactor (MSR)	fluoride salts	700-800	0.1	UF in salt	1000
Sodium-cooled Fast Reactor (SFR)	sodium	550	0.1	U-238 & MOX	30-150 300-1500 1000-2000
Supercritical Water-cooled Reactor (SCWR)	water	510-625	25	UO_2	300-700 1000-1500
Very High Temperature Reactor (VHTR)	helium	900-1000	7	UO_2 prism or pebbles	250-300

+ = with some U-235 or Pu-239

Among these systems, Canada is mostly involved in the Supercritical Water-cooled Reactor (SCWR) concept. One of the main challenges for implementing the SCWR is materials selection for the core of the reactor [7]. The SCW environment is uniquely corrosive and there is no comprehensive database on the behavior of engineering materials within it. In addition, higher fuel burn up in SCWR results in higher fuel cladding temperatures. Therefore zirconium alloys, which are the primary cladding materials for the current nuclear reactors, are no longer appropriate for this purpose in the aforementioned Gen IV reactors [1,3,7–9].

As previously mentioned, fuel cladding materials must be neutron transparent to minimize the neutron losses, since neutrons are necessary to sustain the nuclear chain reaction. Table 1.2 illustrates the neutron absorption cross section for some of the materials used in the reactor core.

Beryllium and cadmium have the lowest and the highest absorption, respectively. Although beryllium was considered for fuel cladding in the 1950s, due to its toxicity, brittleness, and cost, it was not an appropriate choice [3]. Cadmium, because of high neutron absorption is used in control rods to cease the chain reaction because it can efficiently absorb the neutrons. Among the other materials, zirconium has the lowest neutron absorption. Nevertheless, for the aforementioned reasons (e.g. higher service temperature) it would not be a strong candidate for fuel cladding in SCWR reactors. Moreover, there is a clear trade-off between the service temperature and neutron transparency for the fuel cladding materials. For higher service temperatures, the application of nickel and iron-based super-alloys, due to their superior high temperature properties, would be good choices. However, as illustrated in Table 1.2, their neutron transparencies are about 14 and 24 times lower than zirconium, respectively. This, coupled with swelling and embrittlement, associated with formation of helium bubbles make the application of Ni-based alloys problematic and less favorable as fuel cladding materials. Nevertheless, comparing the cladding materials solely based on neutron transparency, iron-based alloys remain a better choice.

Table 1.2. Neutron absorption cross section for selected elements used inside nuclear reactors [3,10]

Atomic number	**Element**	**Neutron absorption cross section σa/barns**
4	Be	0.0092
40	Zr	0.184
26	Fe	2.56
28	Ni	4.49
92	U	7.57
48	Cd	2450

Among iron-based super-alloys, Incoloy 800H receives more attention due to its properties. A brief description of its history and specifications will clarify the reasons for choosing this alloy. Incoloy 800H is an austenitic Fe-Ni super-alloy, which has been used in fossil fuel plants for decades. The material has high temperature strength and resistance to oxidation and other types of high temperature corrosion. This alloy is mainly strengthened by solid solution with the constituent alloying elements. Since the 1950s, when introduced to the market, it has been used to make petrochemical furnace tubes and electrical heating elements [11,12].

Incoloy 800H has been also studied for nuclear applications in various countries. In the 1970s, it was first introduced in High Temperature Gas Cooled Reactor (HTGR) research in the United States, Japan and Germany. In fact, the experience gained in using this alloy for HTGR during three decades makes it an attractive candidate for the upcoming Gen IV reactors. However, for use as a structural material in SCWR environments, some modifications must be considered [12,13].

Furthermore, for construction of any pressure vessel, such as nuclear reactor core containment, the construction materials should meet the American Society of Mechanical Engineers, Boiler and Pressure Vessel (ASME BPV) code criteria. Incoloy 800H has already been approved by the ASME BPV code for construction of some specific components inside the nuclear reactor core. The list of the approved parts with their allowable service temperatures can be found in the references [12,14].

Moreover, the original GIF road map lists some of the promising candidates for use as structural materials in all Gen IV reactor types, which are summarized in Table 1.3 [1]. As shown, Incoloy 800H is listed for use as both cladding and structural components for the SCWR. It is noteworthy that in the most recent roadmap update (2014) from GIF [4], the candidate materials have been reduced to austenitic steels with more than 20% chromium. Incoloy 800H/HT, with its high chromium content as shown in Table 1.4, still remains in the new materials list. The chromium content in this alloy will form the protective oxide layer, while nickel will stabilize the oxide layer [11]. Although Ni-based alloys were involved in the first selection of GIF [1], they gradually received less attention because of their associated swelling and embrittlment [4].

Table 1.3. The proposed candidate materials for Gen IV reactor designs[1] [1]

				Structural Materials	
System	**Spectrum, T_{outlet}**	**Fuel**	**Cladding**	**In-core**	**Out-of-core**
GFR	Fast, 850°C	MC/SiC	Ceramic	Refractory metals and alloys, Ceramics, ODSVessel: F-M	Primary Circuit: Ni-based superalloys 32Ni-25Cr-20 Fe-12.5W-0.05C Ni-23Cr-18W-0.2 CF-M w/ thermal barriersTurbine: Ni-based alloys or ODS
LFR	Fast, 550°C and Fast, 800°C	MN	High-Si F-M, Ceramics, or refractory alloys		High-Si austenitics, ceramics, or refractory alloys
MSR	Thermal, 700–800°C	Salt	Not Applicable	Ceramics, refractory metals, High-Mo Ni-base alloys (e.g., INOR-8), Graphite, Hastelloy N	High-Mo Ni-base alloys (e.g., INOR-8)
SFR (Metal)	Fast, 520°C	U-Pu-Zr	F-M (HT9 or ODS)	F-M ducts 316SS grid plate	Ferritics, austenitics
SFR (MOX)	Fast, 550°C	MOX	ODS	F-M ducts 316SS grid plate	Ferritics, austenitics
SCWR-Thermal	Thermal, 550°C	UO_2	F-M(12Cr, 9Cr, etc.) (Fe-35Ni-25Cr-0.3Ti) Incoloy 800, ODS Inconel 690, 625, & 718	Same as cladding options	F-M
SCWR -Fast	Fast, 550°C	MOX, Dispersion	F-M (12Cr, 9Cr, etc.) (Fe-35Ni-25Cr-0.3Ti) Incoloy 800, ODS Inconel 690 & 625	Same as cladding options	F-M
VHTR	Thermal, 1000°C	TRISO UOC in Graphite Compacts; ZrC coating	ZrC coating and surrounding graphite	Graphites PyC, SiC, ZrC Vessel: F-M	Primary Circuit: Ni-based superalloys 32Ni-25Cr-20Fe-12.5 W-0.05CNi-23Cr-18 W-0.2CF-M w/ thermal barriers Turbine: Ni-based alloys or ODS

Abbreviations:
F-M: Ferritic-martensitic stainless steels (typically 9 to 12 wt% Cr)
ODS: Oxide dispersion-strengthened steels (typically ferritic-martensitic)
MN: (U,Pu)
MC: (U,Pu)C
MOX: $(U,Pu)O_2$

Incoloy 800H is also under consideration for the VHTR in the United States [12]. For this type of reactor, Incoloy 800H can be used for construction of the steam generator and intermediate heat

[1] Reprinted by permission from GIF website (https://www.gen-4.org). Use of information provided on the GIF website and in documents that can be downloaded from the GIF website is allowed provided the source of the information (i.e. GIF website https://www.gen-4.org/).

exchanger components, such as shut-down cooling system tubes, steam generator tubing, core barrel, bellows and helium circulator [12].

Table 1.4. Chemical composition (wt%) of Incoloy 800H/HT.

Fe	Ni	Cr	Mn	Al	Ti	Mo	Cu	Si	Co	P	C	S
45.41	30.19	20.5	0.98	0.55	0.54	0.42	0.4	0.32	0.3	0.22	0.07	0.0001

Accordingly, Incoloy 800H appears to be a good choice for Gen IV nuclear reactors based on its high strength and oxidation resistance in high temperature environments. In fact, based on these properties, it was selected by GIF in 2002. The previous high temperature service experiences in fossil fuel plants have accumulated an important database for the various types of behaviors (e.g. oxidation, mechanical, etc.) of this material. However, due to different service conditions in various nuclear reactors (e.g. SCW), some microstructural modifications need to be engineered for this alloy.

1.4. Objectives of the Project

Having highlighted the importance of fuel cladding in the current and future nuclear reactors, my project address some problems in the materials which is used and considered for the present and future fuel cladding by:

- Analyzing and characterizing some properties of the current zirconium fuel cladding;
- Evaluating a new alloy for potential use in fuel cladding operations in the Generation IV nuclear reactor.

The objectives of the project were defined as a result of discussion with Cameco Corporation, one of the world's largest uranium fuel providers. Initially, they raised technical problems related to manufacturing the zirconium fuel cladding tubes. Nuclear reactor companies as their customers requested additional polishing on Zircaloy-4 cladding tubes; however, no systematic study is available addressing the effect of surface roughness on the claddings' performance. Thus, we dedicated the first phase of the research to evaluate the role of surface roughness on the performance and properties of the fuel claddings. Using various methods, we investigated texture, oxidation, hydriding and mechanical behaviors and we paid specific attention to the structure of oxide that is considered as a barrier against oxidation and hydrogen ingress.

Consequently, we developed a novel experimental method based on synchrotron techniques to characterize the zirconium alloys in their oxidized and hydrided states. By this method, one can investigate the complex interactions between hydrogen and oxygen within the zirconium matrix.

Despite the excellent neutron transparency of zirconium alloys, their mechanical properties at the proposed design temperature for Gen IV SCWR (e.g. 600 °C) would disqualify them for service in this reactor. Therefore, the second phase of the project is focused on evaluating a candidate material for Gen IV SCWR reactor. Based on the collected data, available literature, and discussion with many scholars including AECL staff, Incoloy 800H was selected for our study.

To withstand more severe service conditions, certain properties such as grain boundary diffusion and corrosion must be improved. Several studies reveal that many of these properties depend on grain boundary character Distribution (GBCD) [15–17]. Researchers have made many attempts to improve the physical and mechanical properties of various alloys by modifying the GBCD, using Grain Boundary Engineering (GBE) [18]. Therefore we planned to use Thermo-Mechanical Processing (TMP) to manipulate the grain boundary character distribution in the Incoloy 800H/HT, for enhancing the oxidation resistance of this alloy in SCW at high temperatures.

Accordingly, the research objectives are categorized in two general sections:

1.1. Evaluation the effect of surface roughness on the properties of the current fuel cladding, including the structure of oxide film, oxidation rate and allotropies, hydride formation and mechanical properties;

1.2. Development of novel experimental methods, based on synchrotron radiation, for characterizing zirconium alloys in the oxidized and hydrided states;

2.1. Offer a candidate material (Incoloy 800H/HT) for the future fuel cladding in SCWR and propose a thermo-mechanical method to engineer the grain boundary character distribution and texture.

2.2. Evaluation of possible application of Incoloy 800H/HT for fuel cladding in Supercritical Water-cooled Reactor (SCWR).

These objectives are covered in the manuscript-based chapters 2, 3, 4, 5, and 6:

In Chapter 2 the results of investigations of surface roughness on various fuel-cladding properties are presented. This manuscript addresses the first objective (1.1) of the thesis and it is published in the *Applied Surface Science*.

In Chapter 3, we address the objective 1.2 in the manuscript style chapter. The synchrotron techniques that were used for characterizing the oxidation and hydriding behavior of zirconium alloys are analyzed. This manuscript is published in the *Journal of Alloys and Compounds*.

Chapters 4, 5 and 6 cover the various goals of objective 2.1. In Chapter 4 we describe the proposed TMP and explain the deformation and annealing textures of Incoloy 800H/HT following the TMP. This chapter includes the manuscript, which is published in the *Materials Science & Engineering A.*

Discussion of the nucleation and growth mechanism in the proposed TMP regime is described in Chapter 5. This chapter encloses the manuscript covers part of the 2.1 objective of the thesis and is published in the *Materials Science & Engineering A.*

In Chapter 6, we describe the GBCD evolution and discuss the feasibility of GBE by the proposed TMP. This chapter includes the manuscript that is also published in the *Materials Science & Engineering A.*

In Chapter 7, the results on oxidation behavior of Incoloy 800H/HT in supercritical water and the roles of microstructure, texture and GBCD in Incoloy 800H/HT oxidation is discussed. This manuscript covers the last objective (2.2) of the thesis and is submitted to the *Journal of Supercritical Fluids* for publication.

Finally, we stated the conclusion and suggestions for future work on this project in Chapter 8.

CHAPTER 2

EFFECT OF SURFACE ROUGHNESS ON THE TEXTURE AND OXIDATION BEHAVIOR OF ZIRCALOY-4 CLADDING TUBE

2.1. Overview of Chapter 2

This chapter is focused on the first objective of the thesis which is about elaborating the role of surface roughness on the texture and oxidation behavior of Zircaloy-4 cladding tube.

This chapter is presented as manuscript # 1 (Effect of surface roughness on the texture and oxidation behavior of Zircaloy-4 cladding tube). My contributions to the manuscript are: a) preparation and processing of the samples b) SEM, EDS and EBSD analyses c) Reviewing the relevant literature and writing the manuscript.

The manuscript was published in Journal of Applied Surface Science:

- H. Akhiani and J. Szpunar, "Effect of surface roughness on the texture and oxidation behavior of Zircaloy-4 cladding tube", Applied Surface Science, 285 (2013) 832–839.

The copyright permission to use the manuscript in the thesis was obtained and provided in the Appendix section. The references for this chapter along with references from other chapters are provided at the end of the thesis.

The manuscript presented here is different from that of published in two parts:

- The mechanical properties methods for tensile and burst tests are described in the experimental

procedure. They are added to clarify the mechanical testing procedure.

- The mechanical properties results are incorporated to the last section of the manuscript.

Hamed Akhiani and Jerzy Szpunar

Department of Mechanical Engineering, University of Saskatchewan, Saskatoon, Canada

2.2. Abstract

Conventional pressure water reactors like CANDU use Zircaloy-4 as a fuel cladding tube. Surface roughness that arises from the manufacturing process, pilgering, may alter these tubes' properties in various ways. This paper presents a comparative study of cladding tubes with different surface conditions in order to investigate their effect on the Zircaloy-4 substrate and oxide textures as well as the oxidation kinetic. The experimental results reveal that surface roughness affects the oxidation rate and weight gain of the cladding tubes. Although surface polishing slightly changes the substrate texture, it induces no significant change in the oxide texture. Moreover, oxidation time does not significantly change the preferred orientation of the zirconium oxide.

Keywords: Zircaloy-4, pilgering, surface roughness, oxidation kinetic, zirconium oxide texture

2.3. Introduction

Fuel cladding tube is one of the most critical parts in a nuclear reactor`s core. To avoid any possible accidents, it should be manufactured in a very strict clearance and have high structural integrity. Conventional pressure water reactors like CANDU use Zircaloy-4 as a cladding tube. These tubes are manufactured by a cold extrusion-like process called pilgering. In this process reciprocal movement of grooved dies with a static mandrel forms the tube. Thus, the wall thickness and the inner diameter reduce progressively. Abe and Furugen described and evaluated the workability in pilgering process by performing systematic pilgering tests and establishing plastic deformation state during the process [19]. Furugen and Hayashi carried out a comprehensive study on pilgering process and determined stress strain and roll separating forces during pilgering using the theory of plasticity [20]. Montmitonnet et. Al carried out a rigorous 3D elastic-plastic simulation of cold pilgering of Zircaloy tubes [21]. They emphasized that the

pilgering process is a cold deformation process where a complex stress system is applied to the tube. In such a process surface conditions (e.g. roughness) would be affected during consecutive multi-pass processing routes. Since the final tube has a relatively rough surface, further polishing is required in order to get a bright and smooth surface. This polishing treatment can change the substrate texture thus affecting the formation of an oxide layer, particularly in the initial oxide formation stage. On the other hand, increasing/decreasing surface area by rough/fine polishing will directly change the oxidation kinetic, which can subsequently affect the hydrogen ingress and hydrides precipitation. As zirconium hydrides are brittle phases that adversely affect the mechanical properties, polishing treatments may have considerable effects on the service performance of the Zircaloy-4 cladding tubes.

To date, there is no in-depth study of surface polishing effects on the properties of the cladding tubes. The literature shows that researchers mostly agree about the general effects of surface roughness such as its influence on oxidation kinetic, its affinity to react with contaminants, coolant flow and fluid turbulence on the studied surface. Huntz et al. studied the effect of surface roughness on Ni oxidation [22]. They showed that the surface roughness can affects the oxidation, particularly at initial stages. The effects of thermohydraulics are not in the scope of this paper, but have been studied elsewhere; Guillen and Yoder studied the thermal hydraulic effect of fuel plate surface roughness with analytical approaches which followed by simulation [23]. They claimed that if the fuel surface roughness exceeds 1.5 μm, the coolant flow rate drops. This will increase the fuel temperature dramatically. They emphasized that the order of magnitude of surface roughness is very decisive in fuel temperature, coolant flow rate and temperature. Krogstadt and Antonia stated that surface profile significantly affects the flow turbulence [24]. Despite these thermohydraulic reports, there are few studies that address the effects of surface roughness on metals oxidation. Uran et al. studied the influence of surface roughness on the oxide thickness and residual stress on Fe-Cr-Al alloys [25]. They found that surface roughness can alter the sequence of oxidation of the alloying elements. In another study, Evans reported that by increasing surface roughness, weight gain increased [26]. However, zirconium is a different case. Oxidation of zirconium and its alloys will form a protective surface layer of zirconium oxide. It is well known that zirconium oxide, known as zirconia, has three different allotropes: monoclinic, cubic and tetragonal. Monoclinic and tetragonal allotropes are stable below and above 1000 ˚C respectively. Therefore, in the air and in-reactor oxidation

regimes, monoclinic and tetragonal oxides are more pronounced. The amount of tetragonal phase has a significant effect on the oxidation behavior; however there are controversial data in the literature on this effect. While some studies report a higher oxidation rate and lower protectiveness for the oxide with higher amounts of tetragonal phase, other researchers report that lower amounts of tetragonal phase will result in a more protective oxide layer. Lin et al. analyzed the zirconium oxide formed on Zircaloy-4 and Zr-2.5Nb during heavy water oxidation [27]. They showed that higher tetragonal percentage leads to better oxidation resistance. Yilmazbayhan et al. studied the corrosion behavior of zirconium alloys formed in pure water [28]. They found that the samples with higher tetragonal fraction had higher corrosion rate. Qin et al. stated that many complicated factors like tetragonal percentage, compressive stress near the interface, internal stress induced by tetragonal to monoclinic transformation can affect the oxidation resistant [29]. However, researchers agree that the tetragonal phase has an effect on the protectiveness of the oxide layer. Since the zirconia layer works as a protective barrier against hydrogen ingress and further oxidation, the structure of zirconium oxide is important. Despite many research papers about the zirconium oxide structure, many questions still remain open.

There is no detailed study of the effects of surface condition on oxidation resistance and oxides allotropies of zirconium alloys. Surface conditioning could be used to modify an industrial processing route if it could improve the oxidation resistance of fuel cladding. It could also be applied at the final stage of manufacturing without changing tube-forming processes. Because the focus of this research is on the oxidation kinetic and oxide structure (texture and allotropies), air oxidation tests were conducted in order to limit the hydrogen ingress and hydride formation effects and also to characterize the air oxidation kinetic.

2.4. Experimental procedure

We used Zircaloy-4 cladding tubes with the composition of 1.45%wt Sn, 0.24%wt Fe, 0.13%wt Cr, 0.1%wt O, and balance Zr. In order to explore the effects of surface roughness, we first characterized various surface conditions and then oxidized the material. Table 2.1 illustrates the conditions of the samples, which include both, tube that was unpolished and polished tube with its final surface finished after the pilgering.

Table 2.1. Surface condition of Zircaloy-4 tube

Samples name	Surface condition
G	Ground by 60 grit SiC paper
U	Unpolished
P	Polished

The other sample (G) was polished in our laboratory using 60 grit SiC abrasive paper. Surface properties such as R_a, R_q, R_{Sk}, and R_{Ku} were measured using a Mitutoyo SJ-400 profilometer. After surface treatments, five sets of samples were oxidized at 700˚C in the air for 1, 3, 5, 8, 16, 22 and 35 hours, to investigate the texture evolution in the oxide layer versus time. Besides, textures of Zircaloy-4 substrates with different roughness have been studied. For textural studies, we employed a Bruker D8 X-ray diffractometer with Eulerian cradle using Cu-Kα with 0.5 mm collimator. We used incomplete pole figures to calculate Orientation Distribution Function (ODF) as well as the texture component, by means of ResMat® software. We identified monoclinic zirconium oxide, tetragonal zirconium oxide and zirconium using JCPD 037-1484, 01-080-0784 and 005-0665 respectively. For presentation of textural data the axial, radial and tangential directions of the tube aligns with RD, ND and TD (crystal reference frame) of the pole figure.

In order to study the oxidation kinetic, we performed Thermo Gravimetric Analysis (TGA) for ground (60 grit), polished and unpolished tube surfaces at 500, 700 and 1100˚C. We used a TA Instruments Q600 at 10°C/min temperature ramping rate to analyze the samples, which were purged with air at a flow rate of 500 mL/min., cleaned with acetone for 3 minutes in an ultrasonic bath, dried and placed in alumina pans. The reference was an empty alumina pan.

We used reactor-like conditions (e.g. 10 MPa and 400˚C) for the autoclave tests for different surface roughness following the TGA and textural studies. For comparison with the autoclave test, and for clarification of the surface roughness effects in different media, we conducted an air oxidation test at the same temperature.

To investigate the effect of oxide layer and hydrides on the mechanical properties of the Zircaloy-4 cladding tubes, two sets of samples were prepared from as received, polished, and unpolished Zircaloy-4 tubes. First set was pre-oxidized at 400 °C for 24 hours in air. Second set was not oxidized. The samples were then subjected to hydriding tests. Hydriding experiments were carried out in a quartz tube furnace at 400 °C for two hours. A noncombustible mixture of

Ar-2.5% H_2 was purged in to the tube at approximately 1.0 L/min as a hydrogen source. The samples were furnace cooled in the same atmosphere. After cooling down, the sample were cut from cross section, cold mounted and etched using 50 mL nitric acid (70%) and 2 drops of HF (48%).

The etched cross sections of hydrided samples were studied by optical microscope. The amount of hydrogen in the hydrided samples was measured by an inert-gas-fusion process with LECO hydrogen determinator. Tensile tests have been conducted using conventional Instron testing machine at 667 N preload and 1.27 mm/min strain rate. Burst tests were carried out using a hydraulic press which pumps the water in to the tube. The hydrostatic pressure inside the tube increases till the tube fails. Upon measuring the failure pressure and minimum wall thickness hoop stress was calculated. The circumference of the cross section of the tube before the test and after the failure was used to calculate the elongation.

$$P = \frac{L}{A} \qquad (1)$$

Where A: cross sectional area of test rig cylinder, P = failure pressure, and L = Load.

$$\text{Ultimate Hoop Stress} = \frac{P.D}{2\,t_{min}} \qquad (2)$$

Where, D and t_{min} are mean inside diameter and minimum measured wall thickness, respectively. The sample lengths for tensile and burst test were 20.3 and 17.8 cm, respectively. The samples preparation conditions for the mechanical tests are summarized in table 2.2.

Table 2.2. Preparation conditions for the mechanical test samples

Sample code	Description
PX	Polished; Pre-oxidized @ 400 ˚C + hydrides
PH	Polished; Hydrided w/o oxidation
P	Polished; w/o hydrides and oxide layer
U	Unpolished; w/o hydrides and oxide layer
UH	Unpolished; Hydrided w/o oxidation
UX	Unpolished; Pre-oxidized @ 400 ˚C + hydrides

2.5. Results and discussion

2.5.1. Surface profile and roughness

Table 2.3 illustrates the measurement of various surface roughness parameters. All the reported numbers are the average of five measurements on different regions of the samples. R_a and R_q are the arithmetic average and root mean square of surface asperities and valleys, respectively. R_{sk} (Skewness) shows the number of asperities and valleys regarding the base surface profile, while R_{ku} (Kurtosis) shows the sharpness of these asperities and valleys. R_{sk} is negative if the surface has more valleys than asperities based on surface profile mean line and vice versa. R_{ku} below 3 is for dull and flat surface morphology while higher than 3 is for sharp and pointed asperities and valleys. Comprehensive surface parameters and formulas can be found in the reference [30].

Table 2.3. Surface roughness parameters of Zircaloy-4 tubes

surface condition	**measured surface roughness**			
	R_a ±0.02 (μm)	R_q ±0.04 (μm)	R_{Sk} ±0.01	R_{Ku} ±0.05
Ground (G)	2.79	3.314	0.15	4.61
Unpolished (U)	0.384	0.539	-1.87	7.27
Polished (P)	0.206	0.267	-0.51	2.65

As can be seen in table 2.3, R_a, the most common parameter which characterizes the roughness, is higher in the ground sample as expected. Unpolished and polished samples are smoother than the ground sample. R_q has the same trend as R_a, since they both calculated from the height of asperities and valleys on the surface. Interestingly, the trend for the next two parameters, R_{sk} and R_{ku} is not the same; the ground sample has slightly positive R_{sk} (0.15) while polished and unpolished samples have negative values.

These data show that the ground sample has more asperities than valleys on its surface while valleys are dominant in polished and unpolished samples. On the other hand, R_{ku}, for polished samples is below 3, which shows blunt tips on the surface, but above 3 for the G sample and particularly for the U sample, which has very sharp asperities and valleys in comparison with the others. Fig.2.1 shows SEM images of these surfaces, which support the roughness measurements. Fig. 2.1.a shows the unpolished sample surface. The grooves on the surface are due to the pilgering manufacturing process.

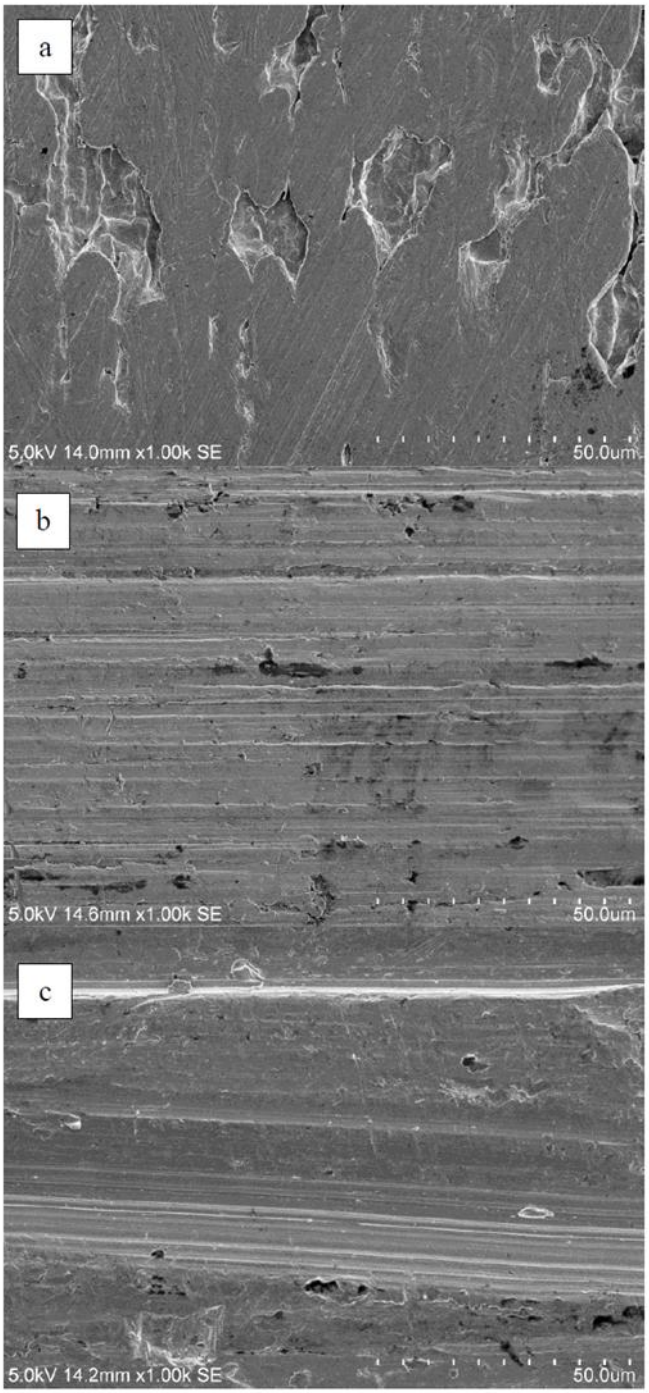

Fig. 2.1. SEM image of a) unpolished, b) polished c) ground surface of Zircaloy-4 tube

On the other hand, polished tube has a smoother surface (Fig. 2.1.b). It seems that polishing filled and flattened the grooves. The ground sample has a similar morphology to the polished one

due to an equivalent polishing method, although the difference between the valleys' depth and asperities' height is significantly larger. Indeed, the R_a and R_q of these surfaces illustrate this difference.

2.5.2. Thermo Gravimetric Analysis (TGA)

We conducted the TGA tests for polished (P), unpolished (U) and ground surfaces (G) at 700 °C isothermally for 4 hours. Fig. 2.2 illustrates the weight gain for these samples as a function of time.

Because oxidation is a thermally activated phenomenon, the oxidation mechanism is highly dependent on the oxidation temperature and is therefore expected to have the same oxidation kinetic at each constant temperature. As Fig. 2.2 illustrates, the oxidation kinetics have approximately the same trend for the tested surfaces. The ground (G) sample exhibits almost the highest oxidation weight gain while polished (P) and unpolished (UP) samples have slightly lower oxidation rates. The final weight gain for the G, U, and P were 4, 3.2, and 3 % respectively. The TGA/DSC tests also were done at 500 and 1100˚C. The oxidation kinetic changed at each temperature, but the trend of changes of oxidation rates with surface roughness remained the same. As stated by Baek et al. [31], the oxidation kinetic does change with the temperature regarding the phase transformation of Zircaloy-4, especially for temperatures beyond 800˚C.

In addition, we performed Differential Scanning Calolimetry (DSC) simultaneously with TGA. Fig. 2.3 shows the DSC overlay for the same set of samples. As shown, the trends of heat flow for the samples are almost the same with minor differences: the initial drop in heat flow curve corresponds to the heat absorption of the sample. It seems that due to a larger surface area in the G sample, the heat absorption stage was longer. Following this stage, small bumps illustrate minor increases that might correspond to initial surface absorption or the first stage of oxidation. The abrupt second drop can be ascribed to the oxide formation activation energy. It appears that this heat release depends on the surface roughness/area of the samples. Over the following 65 min., the steady oxidation process generated heat and the DSC curves appear to converge. We performed the TGA/DSC tests 5 times to ensure correct data and reproducible results. Standard deviation for TGA/ DSC was about ±0.05 at 700˚C. From these observations of TGA and DSC,

we conclude that when the sample reaches the critical point a bumpy increase occurs that might be related to oxygen adsorption to the surface. The larger surface area in the rough sample provided more area for the oxidation process. Thus we expected higher weight gain in the rough (G) sample.

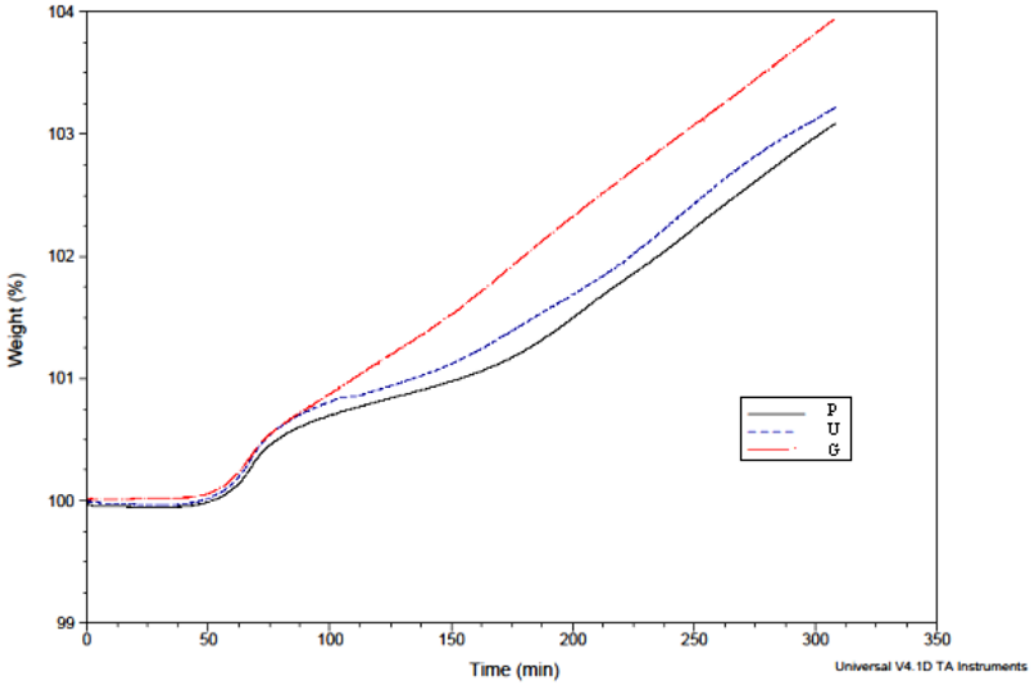

Fig. 2.2.Thermogram overlay of G, U and P samples run at a ramp rate of 10 °C per minute to 700 °C and held at maximum temperature for 4 hours.

A general surface oxidation (gas/metal) process has five distinct steps [32]:

$$O_{2\,(g)} \rightarrow O_{2\,(ad)} \rightarrow 2O_{\,(ad)} + 2e = 2O^{-}_{\,(chem)} \rightarrow 2O^{2-}_{\,(lattice)} + 4h^{\cdot} \rightarrow \text{Anion/Cation diffusion} \qquad (1)$$

Adsorptions, dissociation of oxygen molecule to atomic oxygen, and chemisorption of oxygen anion on the surface, are the key steps in the gas/metal reaction. After these steps, anion or cation diffusion will start, which leads to oxide formation and growth at the gas/metal or metal/oxide interface, respectively. In the case of zirconium oxide, which is an n-type oxide with anion deficiency, the inward diffusion of oxygen anion forms the zirconium oxide layer in the metal/oxide interface [32].

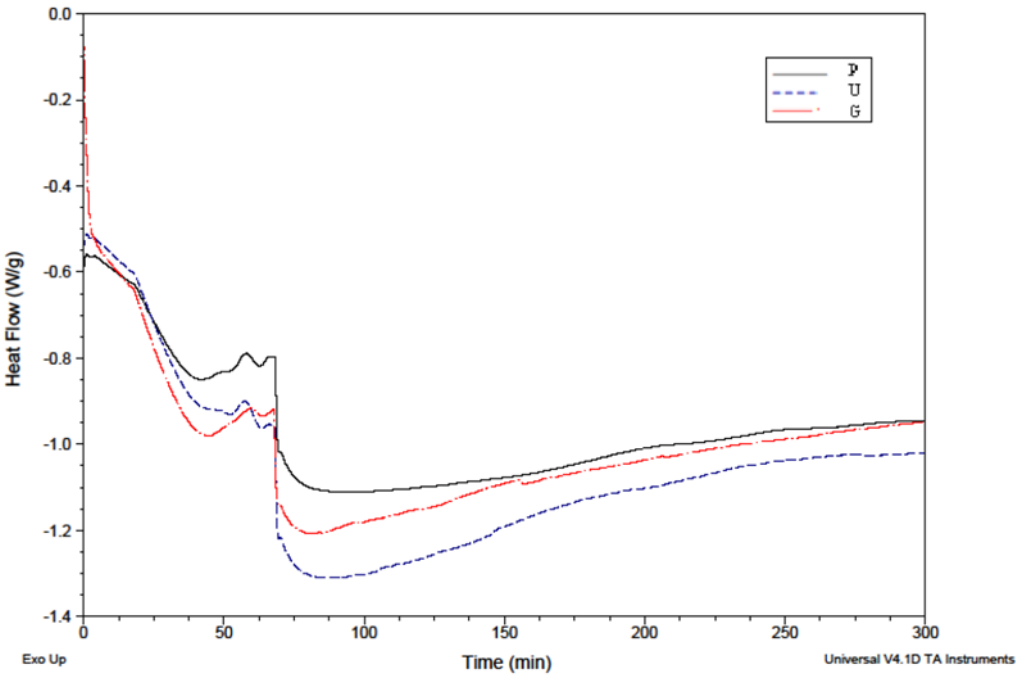

Fig. 2.3. Differential scanning calorimetric overlay for G, U and P samples at 700 °C/4 hours.

Moreover it is the surface roughness that mostly affects the initial layers of oxidation. As oxide grows thicker, the anion diffusion through the oxide thickness would become the rate-controlling step. As illustrated in Fig. 2.2, in this situation according to the equation given below, the oxidation rate is linear:

$$\Delta w/w = Kt + C \qquad (2)$$

Where; Δw: weight gain, w: initial sample weight, K: oxidation rate constant, t: time and C: y-interception constant. C can be a function of initial temperature, pressure and also surface conditions [32,33]. Considering the weight gain trends, Fig. 2.2 depicts that within the initial 50 min of oxidation, the weight was almost constant. After this time a rapid increase in weight gain occurred that corresponds to the initial surface absorption and oxidation. After 75 min, the slope of the curve (K) tends to be lower. After 160 min, the weight gain curves become parallel, showing the same slope. As calculated in the linear regions of the weight gain curves, the slope (K) is equal to 0.014 ±0.001 min^{-1}. However C constant, which is equal to Δw/w-Kt is different for different specimens. We used dimensionless parameters for deriving the correlation between oxidation C constant and surface roughness. For this purpose we defined C and roughness (ε)

respectively as $\Delta w/w\text{-}Kt$ and R_a/t_t, where t_t is the thickness of the tested samples. In this way we plotted C variations versus roughness in Fig. 2.4 and applied linear and power regressions to fit the experimental data. Fig. 4 shows that regarding the coefficient of determination (R^2) value, the power regression fits better to the measured data. On the other hand, we expected that by increasing surface roughness, there might be a maximum limit for C. In other words, surface roughness could not increase the weight gain beyond the specific roughness. Similarly, Huntz et al. reported that surface roughness can increase the oxidation rate only at the initial stages of oxidation [22]. Thus it appears that the power fitting follows the physical process of oxidation. As mentioned earlier, a higher area with a rough surface exposed to oxidation, explains the higher oxidation weight gain. The transition point where all surfaces with different roughness behave the same in terms of oxidation rate could be related to a critical oxide thickness. It appeared that after approximately 3 hours, the rate of oxidation would be identical. At this point, depending on the surface roughness of the samples, oxide thickness was around 10 to 20 μm. Interestingly, this thickness is in the order of tens of magnitude of the original surface roughness (R_a). Indeed, after this critical thickness, the surface roughness had no role in the oxidation rate, although it affected the overall weight gain of the samples.

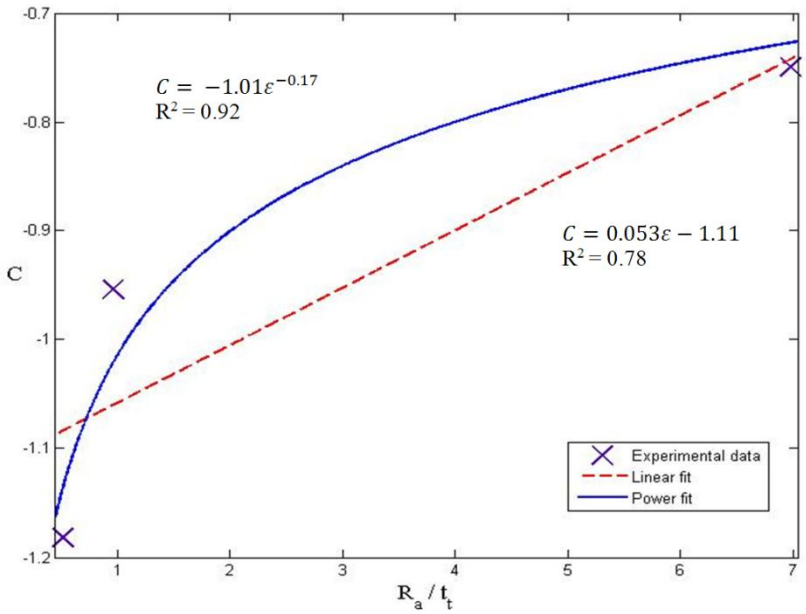

Fig. 2.4. Experimental and fitted data for C (=$\Delta w/w\text{-}Kt$) as a function of dimensionless surface roughness.

2.5.3. Autoclave Tests

In order to compare the effect of surface conditions on the oxidation behavior of the Zircaloy-4 cladding tube in different media, we performed autoclave (steam) and air oxidation tests at 400˚C for 72 hours. The autoclave test, to some extent, approximated in-reactor service conditions with 10 MPa. Fig. 2.5 shows the compared weight gains for these tests. As expected, G sample has the highest weight gain while P sample has the lowest one. These results are in accordance with TGA results that were shown before.

As depicted earlier in table 2.1, U sample has the greatest absolute value for skewness (deep valleys) and kurtosis (sharp valleys), which tend to increase the oxidation weight gain. On the other hand, G sample has the highest R_a which maximizes the surface area that is exposed to oxidation. The slight difference in the G and U weight gain reveals that all these parameters play a possible role in increasing the oxidation rate. However, in the air oxidation tests the weight gain differences, particularly in P sample, are more pronounced. This fact is likely related to the pressure and nature of oxidation media more than surface condition.

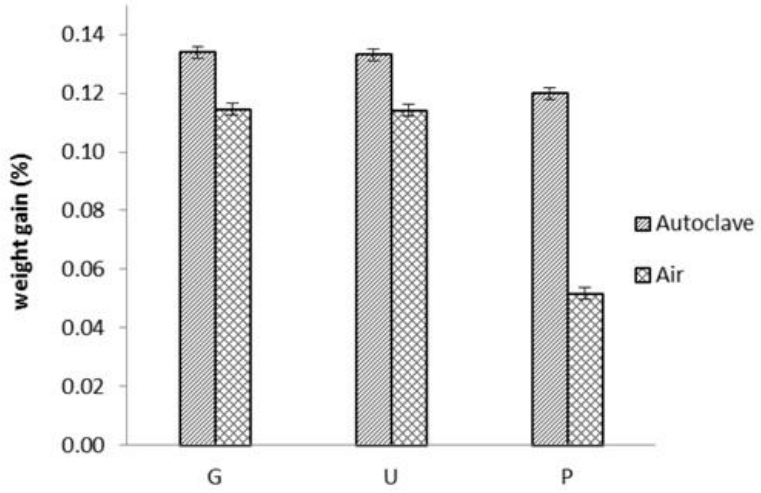

Fig. 2.5. Weight gains for different surface roughness sample after autoclave and air oxidation tests.

2.5.4. Oxidation

2.5.4.1. Texture

As shown in previous sections, after a certain time the weight gain and oxidation rate for the samples with different surface roughness changed in a similar way. In other words, the effect of surface roughness is significant mostly for short oxidation times. Such conclusion can also be derived from the results presented in Fig. 2.4.

In this section we discuss the effect of surface roughness on oxide texture. We conducted oxidation tests on sets of Zircaloy-4 tube samples at 700˚C for 1, 3, 5, 8, 16, 22 and 35 hours in the air in order to characterize the effect of surface roughness on oxidation texture.

We examined the effect of polishing on the texture of the Zircaloy-4 substrate prior to oxide texture measurements. Fig. 2.6 shows (0002) pole figures of ground, polished and unpolished tubes. The unpolished sample has typical basal plane pole figure for HCP metal with c/a<1.63 (c/a_{Zr} =1.59). The comprehensive texture illustration of Zirconium alloys has been done by Tenckhoff (2005). The maximas show $(01\bar{1}4)<10\bar{1}0>$ orientation, which means that the basal plane is shifted along TD by 20˚. After the polishing, the splitting of the {0001} pole was reduced. Also upon further grinding, only one {0001} maxima could be seen. In addition, the low intensity of $(01\bar{1}0)<0001>$ orientation, which existed in unpolished and polished samples, was deleted completely in the ground sample. We point out that due to the low x-ray penetrating depth, these textural data solely depict the surface texture, not the bulk texture of the tube. In order to study the oxide texture, we compared $(\bar{1}11)$, (111), (200) and (110) pole figures of monoclinic zirconia obtained after 1, 3, 5, 8, 16, 22 and 35 hours' oxidation at 700˚C in the air. We found no significant differences in pole figures' intensity and preferred orientations upon increasing the oxidation time. As an example, Fig. 2.7 shows the polished sample that was oxidized for 8 hours. Under the test conditions, all the oxide pole figures look the same. The (110) pole figure clearly shows that the (110) planes of monoclinic zirconia are aligned on the sample surface. The maxima points on $(\bar{1}11)$ and (111) pole figures are also related to $(110)[\bar{1}10]$ orientation. In addition, the ODF and recalculated pole figures show the weak texture of $(01\bar{2})$ fiber, $(1\bar{2}0)[211]$, and $(10\bar{3})[\bar{3}01]$. As mentioned, these are the pole figures` forms of monoclinic zirconia that formed under testing conditions. It is notable that pole figures for the autoclave oxidation are almost identical to the air oxidation ones.

We calculated the tetragonal pole figure and ODF using (101) tetragonal ZrO_2 peak at $2\theta=30^{\circ}$. Fig. 2.8 shows the tetragonal and pole figures. From ODF and other recalculated pole figures, we found that (010)[100] was the preferred orientation of tetragonal zirconia that formed on Zircaloy-4 tubes.

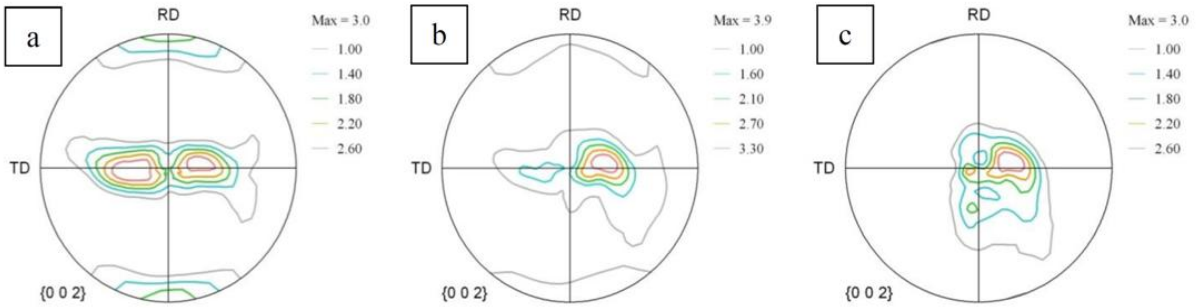

Fig. 2.6. (0002) pole figure of Zircaloy-4 cladding tubes in different surface roughness: a) unpolished, b) polished, c) ground.

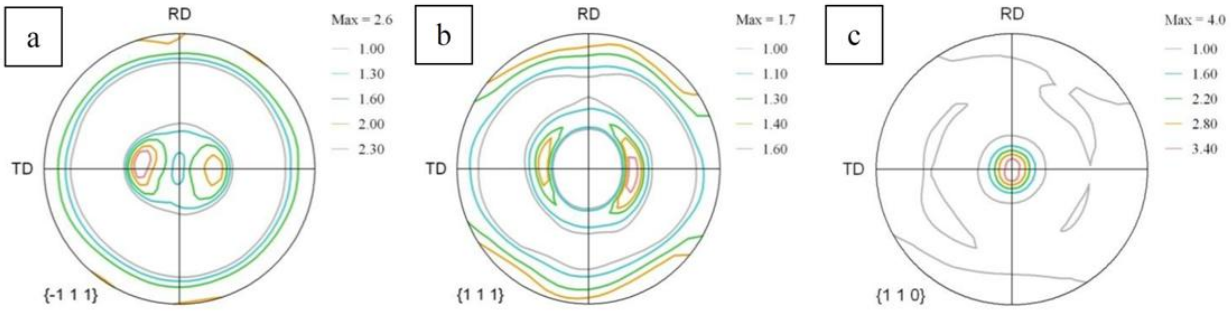

Fig. 2.7. Pole figures of Monoclinic Zirconia formed on Zircaloy-4 cladding tubes

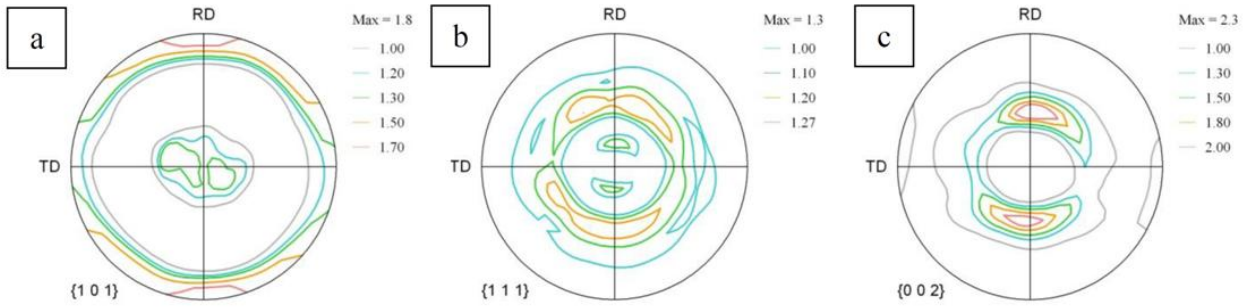

Fig. 2.8. Pole figures of tetragonal Zirconia formed on Zircaloy-4 cladding tubes.

To provide a better description of the orientation of the zirconium, monoclinic and tetragonal zirconia grains, we measured inverse pole figures (IPF). Fig. 2.9 shows the typical, normal-direction IPFs of substrate and its oxide allotropies. Fig. 2.9.a shows that the [0001] direction of hexagonal zirconium is aligned with the normal direction of the tube, which corresponds to the basal pole figure in Fig. 2.6. In the case of tetragonal zirconia, [100] direction is aligned with the sample`s reference ND. Fig. 2.9.c shows the IPF of monoclinic zirconia. The two maxima regions at each quarter are related to [110].

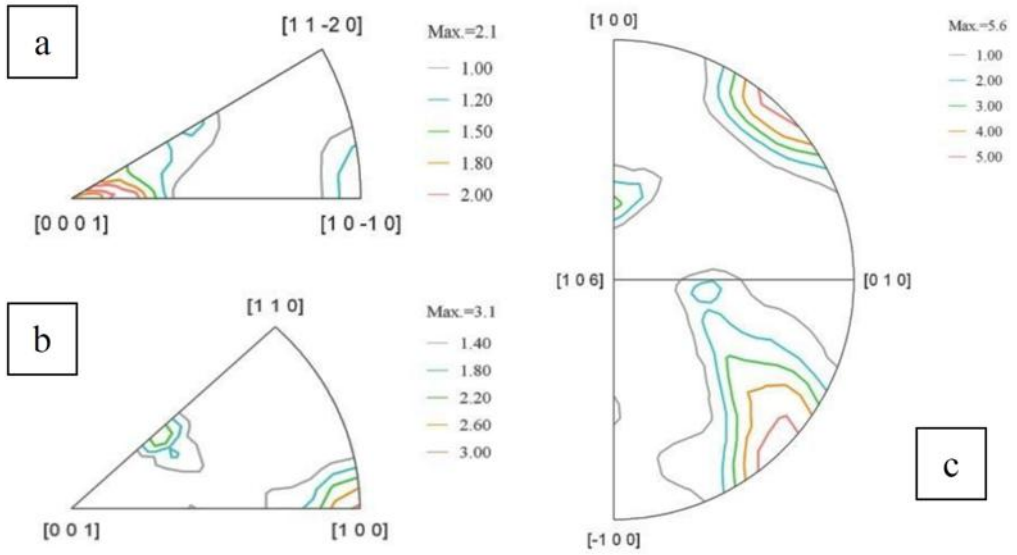

Fig. 2.9. Inverse pole figures of a) Zircaloy-4 tube, b) tetragonal and c) monoclinic zirconia formed on Zircaloy-4 cladding tubes.

The results presented above enabled us to determine the orientation relationships between the oxide allotropes and zirconium substrate. While the near basal planes fibers are the dominant texture of the zirconium substrate, monoclinic and tetragonal zirconium oxide have $(110)<\bar{1}10>$ and $(010)<100>$ orientations, respectively. Thus it can be concluded that (110) planes of monoclinic zirconia are aligned with (0002) planes of Zr_{α}. Similarly, the orientation relation for the tetragonal zirconia would be $(0002)_{Zr\alpha} \parallel (010)_{t\text{-}ZrO2}$. As mentioned, increasing oxidation time and oxide layer thickness produced no significant change in pole figures and ODFs of the oxide phases. The results show that the orientations of oxide grains did not change appreciably during the oxide growth, a fact that Favergeon et al. [35] and Petigny [36] have observed independently in their studies on the oxidation of Zircaloy. We assumed that Electron Backscatter Diffraction (EBSD) through the oxide section could reveal the minor changes and therefore made many attempts to perform the EBSD on the oxide layer cross section. However we were unable to obtain a clear sharp pattern due to the very fine grain size and high strain in the oxide microstructure. Iltis et al. reported the same difficulty for indexing the Kikuchi patterns in EBSD of zirconium oxide [37].

Fig. 2.10 illustrates the trend of oxide thickness growth with oxidation time. The slope showed dramatic growth of oxide after 8 hours, possibly indicating the initiation of breakaway oxidation. This may happen due to the micro-cracking in the oxide layer. The origination of these micro-cracks is embedded in the nature of zirconium oxidation. The Pilling-Bedworth ratio (PBR) for Zr/ZrO_2 is 1.56, which means that the volume of zirconium oxide is 1.56 times greater than the zirconium metal. Greater oxide volume will generate compressive stress in the oxide layer while it has a tensile stress on the zirconium substrate. This stress increases with the oxide growth and along with it; another stress arising from zirconia allotropic transformation can initiate the micro-cracking through the oxide thickness. In other words, transformation of the tetragonal to monoclinic phase can assist the Pilling-Bedworth induced stress to initiate the micro-cracks. Qin et al. and Cox [29,38] reviewed the parameters that can affect this transformation and its followed cracks. Initiation of micro-cracks will result in a dramatic increase in oxidation rate, which is known as breakaway oxidation. From this point the protectiveness of the zirconia layer will be diminished.

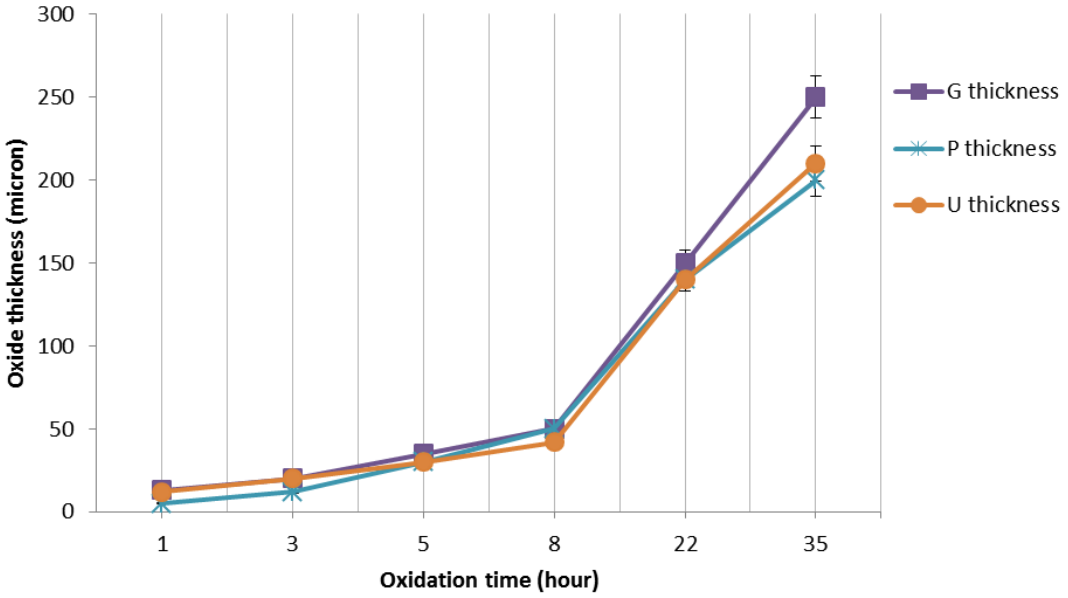

Fig. 2.10. Zircaloy-4 oxide thickness as a function of oxidation time.

Indeed, this phenomenon occurred for all samples with different surface roughness. However, the fact that G sample has the higher weight gain while the P sample has the lowest is in agreement with the TGA data in section 3.2 and Fig 2.2.

2.5.4.2. Allotropes

As mentioned before, zirconium oxide has three allotropes. In most of the oxidation regimes for Zircaloy-4, including the current oxidation condition, monoclinic and tetragonal zirconia can be characterized. It is well known that the amount of tetragonal phase has a significant effect on the protectiveness of the oxide layer against hydrogen ingress. In this section, we calculated the percentage of tetragonal phase for various oxidation times for different roughness. Various researchers have used a special formula to find the percentage of tetragonal zirconia in the zirconium oxide layer [39–41]. The total integrated intensities I(hkl) of the $(\bar{1}11)_m$, $(111)_m$ monoclinic and $(111)_t$ tetragonal phase were used to find the tetragonal percentage with the formula given below:

$$X_t = \frac{V_t}{V_m + V_t} = \frac{I(111)_t}{C[I(11\bar{1}) + I(111)_m] + I(111)_t} \quad (3)$$

For Cu K_α, the C coefficient is l.381[27]. I(hkl) is the calculated area under the (hkl) peak. Fig. 2.11 illustrates these peaks in an x-ray diffractogram of P sample after 5 hours' oxidation. Fig. 2.12 shows the percentage of tetragonal phase for different surface roughness at various oxidation times. These results indicate that by increasing the oxidation time (which corresponds to higher oxide thickness), the percentage of tetragonal phase decreased. This result is in agreement with Lin et al.[27] and Maroto et al. [42] on their characterization studies of zirconium alloys. As the oxide grows, the tetragonal phase will start transforming to monoclinic phase. The tetragonal phase is not stable at ambient temperature and pressure, but it might be stabilized under certain conditions. Some researchers have mentioned small crystallite size and high compressive stress as the stabilizing reasons [27,29,41]. As oxide grows, the mean crystallite size will increase. Also because of the high PBR of Zirconium (1.56), the high compressive stress will be induced into the growing oxide layer. At the same time, the transformation of tetragonal to monoclinic phase takes place and shear stress from the twining deformation can initiate the micro-cracks. Initiation of oxide cracking as a result of the compressive stress and tetragonal to monoclinic transformation, will relax the residual stresses.

Due to these facts, we expect that the percentage of tetragonal phase will be reduced as the oxide thickens.

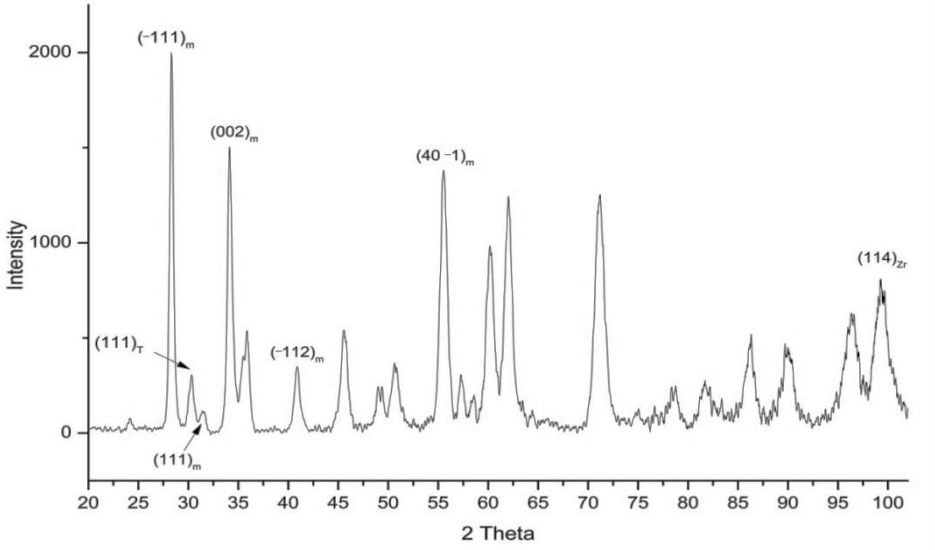

Fig. 2.11. X ray diffractogeram of polished sample after 5 hours oxidation.

The polished sample had the highest initial percentage of tetragonal phase, while the unpolished sample had the lowest percentage. The decreasing trend in tetragonal phase amount versus oxidation time for G, U and P samples was almost constant; however at each oxidation time, P and U samples had respectively the highest and the lowest amounts. Comparing the weight gains in Fig. 2.5, we conclude that higher tetragonal content resulted in less weight gain in P and U samples. Maroto et al. [42] and Lin et al. [27] found the same trend in their studies on zirconium alloys. The decreasing trend of tetragonal phase content of the ground sample was observed and placed between the polished and unpolished samples, although it was rather similar to the unpolished samples. As shown in Fig. 2.5 and Fig. 2.12, there were slight differences between U and G samples, which correlate with the observed differences between the roughness parameters of the samples.

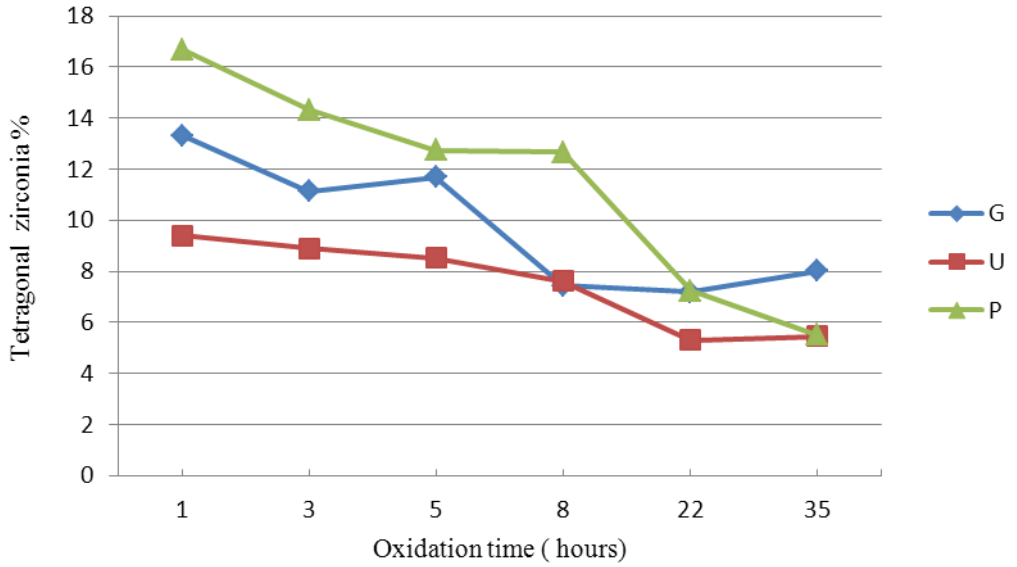

Fig. 2.12. Tetragonal percentage of oxide layer at various oxidation times in the air.

2.5.5. Mechanical Properties

Hydrides morphology and distribution in UX, UH, PX and PH (described in table 2.2) are illustrated in Fig. 2.13. The most significant difference is the amount and morphology of hydrides in pre-oxidized and non-oxidized samples. It seems that the oxide layer alleviate the hydrogen ingress and thus less hydrides with smaller sizes formed in the pre-oxidized samples than non-oxidized ones. LECO Hydrogen determinator shows that the amount of hydrogen in the pre-oxidized samples is twice of that in the non-oxidized ones (table 2.4). Moreover, the unpolished tube has about 10% less hydrogen content than polished tube in both pre-oxidized and non-oxidized conditions. These results are in agreement with the hydrides quantification results by the image processing technique. It seems that due to the surface condition after pilgering in the unpolished samples, the hydrogen absorption and hydride formation process in these samples are completely different from that in the polished ones.

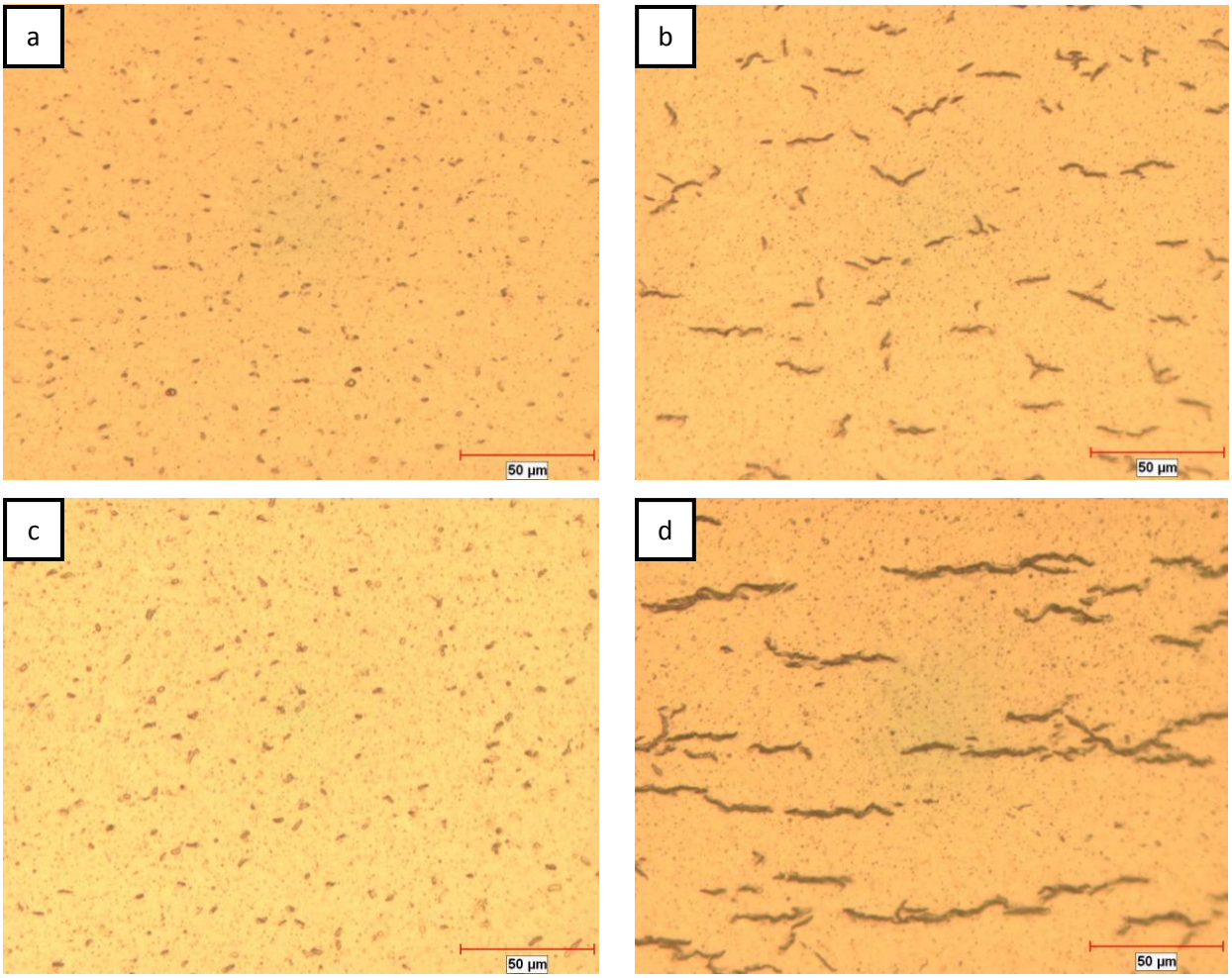

Fig. 2.13. Optical microscope image of etched cross section of a) UX, b) UH, c) PX, and d) PH samples.

To investigate the effects of hydrides on the Zircaloy-4 mechanical properties, Ultimate Tensile Strength (UTS), 0.2% yield stress, and toughness were measured upon tensile tests, and hoop stress was calculated from the burst test. Fig. 2.14 depicted the stress-strain curves for the tested samples. As can be seen, the deformation behavior/mechanism of all the samples looks similar. The results of tensile test and burst test are illustrated in table 2.4. It can be seen due to hydrides presence, UTS, yield and elongation of the samples has been altered. The as-received polished tubes have slightly higher elongation than unpolished tubes, while UTS and yield stress are almost the same. This might be related to the differences in the surface morphology of the tubes. As can be seen in Fig. 2.1, the valleys on the surface of unpolished tube can act as stress raisers and may lead to earlier fracture of unpolished tube.

Comparing UX and PX samples, UX has higher UTS and lower elongation than PX. This could be due to the different oxidation and hydride formation behavior of the unpolished tube. Same

trend can be seen for UH and PH samples. It is worth mentioning that the amount of strain till UTS point is almost the same for all samples. The fracture elongation difference is resulted from non-uniform plastic deformation after UTS. The increase of UTS in unpolished tubes by introduction of oxide and hydrides might be due to the oxidation and hydriding process. As described in experimental section, hydriding and oxidizing procedure have been done at 400˚C, so this might slightly change the Zircaloy-4 microstructure and properties itself. The other point is that non-radial (circumferential) hydrides can act as second phase and increase the UTS and yield. This might be the case for the higher UTS in UH and PH in compare with UX and PX samples. Nevertheless, hydriding reduced the elongation in all of the samples.

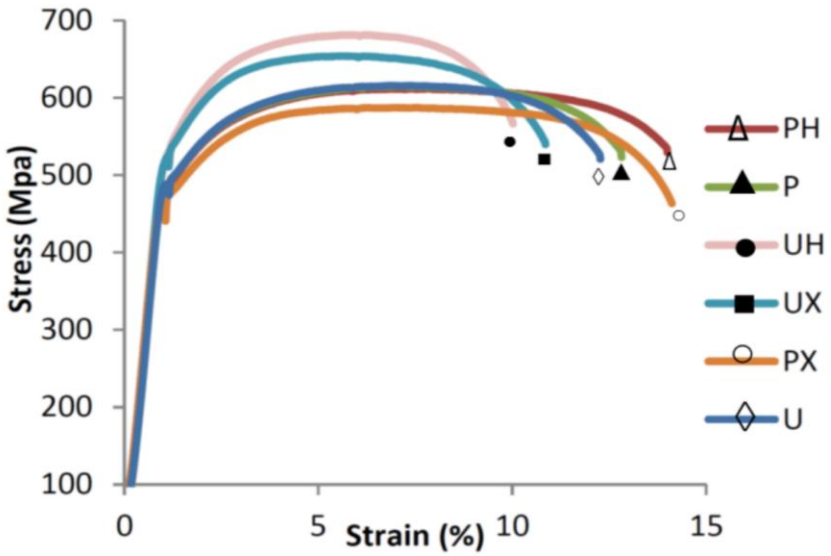

Fig. 2.14. Stress-strain curve for polished and unpolished samples with the conditions stated in Table 1.

In addition to the tensile test, the role of hydrides in altering the mechanical properties can also be traced in the hoop stress. As illustrated in Table 2.4, there are slight differences in the hoop stresses of the samples. PX and UX have exhibited higher hoop stress than, respectively PH and UH. In addition, U samples have higher hoop stress as well as UTS and yield stress. Finally as can be anticipated, P and U samples do not show considerable differences in the tested mechanical properties since the hydrogen content in these samples are almost identical.

Table 2.4. Tensile and burst test results

Sample code	UTS (MPa) ±5	Yield Stress (MPa) ±5	Hoop stress (KPa) ±4	Hydrogen (ppm) ±0.5
PX	569.53	449.55	837.66	17.1
PH	612.28	473.68	828.69	35.8
P	615.72	488.85	860.43	8.0
U	611.59	484.72	859.23	7.5
UH	655.02	504.71	856.98	31.2
UX	643.99	512.99	910.11	15.5

It appears that the hoop stress is correlated to hydrogen content. The higher the hydrogen content, the lower the hoop stress. As hydrides are more brittle than zirconium matrix, it is anticipated that higher amount of hydride lowers the hoop stress. Since higher hydrogen concentration is correlated with platelet hydrides, no conclusion could be derived on the role of hydrides morphology. Indeed, hydride morphology and it's orientation are very important and decisive in the mechanical properties of zirconium base alloys [43].

2.6. Conclusion

We studied surface roughness effects on the oxidation of Zircaloy-4 cladding tubes in air and steam at specific temperatures. We observed slight differences regarding oxidation kinetics and weight gain. In almost all oxidation tests, the ground (roughest) sample had the highest weight gain. The surface roughness effect was more pronounced for the initial weight gain and oxidation rate, while it became less important for longer oxidation times. This means that, at the early stages of the oxidation, the higher the Zircaloy-4 surface roughness, the higher the oxidation rate.

Autoclave oxidation weight gain tests show the same trend as the air oxidation tests for different surface roughness. Analysis of the oxide texture shows that by increasing the oxidation time, the pole figures' intensity increased. The preferred orientation of monoclinic zirconia oxide slightly changed with the oxidation time. Although there were considerable changes in zirconium substrate texture, we detected no major difference in the oxide texture. The most significant difference detected during the oxide growth stage, was the decreasing percentage of tetragonal phase content in the oxide layer.

It was demonstrated that surface oxide layer acted as a barrier against hydrogen ingress. Polishing alter the hydrogen pick-up and hydrides amount and morphology. Interpreting the tensile test data is complicated due to rather complex role of high temperature pre-oxidation and hydriding processes. The deleterious effect of hydrides presence was clearly demonstrated by the results of the burst test.

Considering the results, we conclude that surface roughness does have some effects on the oxidation of Zircaloy-4, in aspects that are studied here. Increasing the surface roughness would increase the weight gain due to the surface area effect and/or the amount of tetragonal phase. Since we observed no significant difference in weight gain after a period of time, we presume that the surface area effect is more pronounced at the initial oxidation stages. It is important to note that these results are not necessarily indicative of fuel performance inside a reactor and some complementary studies such as irradiation effects are needed to determine which surface treatment would be ideal for fuel cladding performance in a real nuclear reactor environment.

CHAPTER 3

THE ELECTRONIC STRUCTURE OF ZIRCONIUM IN HYDRIDED AND OXIDIZED STATES

3.1. Overview of Chapter 3

In the previous chapter, the effect of surface roughness on the oxidation and texture of Zircaloy-4 tubes was explained. This chapter aims to study the surface roughness effect in the oxidation and hydriding of Zircaloy-4 tubes in further details using the synchrotron techniques. In addition, a qualitative analysis of Zr electronic structure at its oxide, hydride and alloyed states was performed to clarify the interactions of hydrogen and oxygen with the zirconium substrate.

This chapter is presented as manuscript # 2 (The electronic structure of zirconium in hydrided and oxidized states). My contributions to the manuscript are: a) preparation and processing of the samples b) SEM, EBSD, XRD and XPS analyses c) Reviewing the relevant literature and writing the manuscript. The calculations were performed on Compute Canada WestGrid HPC consortium by two of the co-authors (Adrian Hunt and Alexander Moewes). Dr. Xiaoyu Cui is the CLS beamline Scientist who helped us in acquiring and analyzing the synchrotron data. The manuscript is published in the Journal of Alloys and Compounds:

- H. Akhiani, A.Hunt, X. Cui, A. Moewes, J. Szpunar, "The electronic structure of zirconium in hydrided and oxidized states", Journal of Alloys and Compounds, 622, (2015), 463-470.

The copyright permission to use the manuscript in the thesis was obtained and provided in the Appendix section. The references for this chapter along with references from other chapters are provided at the end of the thesis.

The electronic structure of zirconium in hydrided and oxidized states

Hamed Akhiani[1], Adrian Hunt[2], Xiaoyu Cui[3], Alexander Moewes[2], and Jerzy Szpunar[1]

[1] Department of Mechanical Engineering, University of Saskatchewan, Saskatoon, Canada
[2] Department of Physics and Engineering Physics, University of Saskatchewan, Saskatoon, Canada
[3] Canadian Light Source, Saskatoon, Canada

3.2. Abstract

Valence band energy shifts for pure zirconium and a model zirconium alloy (Zircaloy-4) in oxidized and hydrided states have been investigated with X-ray photoelectron spectroscopy (XPS) and X-ray Absorption Near-Edge structure (XANES) technique. With XANES, we show that O/H interactions in oxidized Zr can be detected in the near-edge region of O K. Using density functional theory (DFT) simulations, we have determined where H atoms bond in the monoclinic ZrO_2 lattice. The preferred stoichiometry is ZrO_2:H, but the O-H bond is weak; increasing H causes the H atoms to form H_2 molecules rather than O-H bonds. These interactions cause energy shifts in the Zr 3d XPS spectra. The results illustrate the complex processes of hydrogen and oxygen interactions at the Zr surface.

Keywords: Zirconium, Zirconium oxide, Zirconium hydride, XPS, XANES

3.3. Introduction

Zirconium and its alloys are among the materials that are widely used in nuclear reactors as structural materials. The main advantage of these alloys is their exceptional combination of neutron transparency, oxidation behavior and mechanical properties at the service temperatures. Pure Zr and Zr alloys can form a spontaneous oxide layer on their surface. This layer protects against further oxidation and is similar to that formed on the surface of aluminum and titanium based alloys [32]. Inhibiting further oxidation and hydriding of Zr-alloys used in nuclear reactors is a crucial design consideration, because these chemical reactions cause the brittleness and the interior mechanical stresses within the fuel rods to increase, which may lead to premature failure and rupture of the fuel cladding. Understanding the structural changes that Zr alloys undergo is therefore critical from the standpoint of nuclear reactor safety.

The protectiveness of this oxide layer depends on its morphology and crystal structure [44,45]. Zirconium oxide, known as zirconia, has three common allotropes; monoclinic, cubic and tetragonal. Monoclinic and tetragonal allotropes are stable below and above 1000 ˚C, respectively. After lengthy oxidation at temperatures above 1900 ˚C, cubic, trigonal and pseudo-hexagonal structural modifications have been reported [25]. Therefore, monoclinic and tetragonal oxides are the phases of zirconia that will most likely form within in a nuclear reactor during service.

Zirconia is used for many applications besides nuclear fuel claddings, such as thermal barrier coatings, refractory materials, biomaterials manufacturing, and jewelry. Due to the wide application range of zirconia and its allotropes, characterizing the various types of zirconia is of a great importance and interest to these other industries, as well as the nuclear power industry.

There are many literatures on ZrO_2 formation, micro structure, texture, and allotropes. Most of these studies are based on X-ray diffraction and Raman spectroscopy. In this study, synchrotron radiation at the Canadian Light Source (CLS) has been used to study the Zr oxide and hydride structure. X-ray photoemission spectroscopy (XPS) and X-ray absorption near-edge structure (XANES) techniques are used to follow the changes in electronic structure of Zr before and after oxidation and hydriding of pure Zr and a model Zr alloy (Zircaloy-4).

3.4. Materials and methods

To study the effects of oxidation and hydriding on pure Zr and Zircaloy-4, commercially pure Zr 702 (99.8%, All-chemie LTD) and Zircaloy-4, with the composition of 1.45%wt Sn, 0.24%wt Fe, 0.13%wt Cr, 0.1%wt O, and balanced Zr, were used in this study. Four samples of pure Zr, not including the control, are listed in Table 3.1. Pre-oxidizing of the samples was performed in a tube furnace at 400˚C for 24 hours. In addition, one Zircaloy-4 sample has been oxidized for one hour to illustrate the effect of a thin oxide layer in the XPS spectra. Similarly, hydriding was done in the same furnace at 400˚C under Ar - 2.5% H_2 atmosphere for 3 hours. The samples were then furnace cooled, cut into approximately 5 mm x 5 mm pieces and ultrasonically cleaned with methanol for 5 minutes prior to the experiments. In order to reveal the hydrides on the surface and characterize them by Electron Backscattered Diffraction (EBSD), one of the hydrided samples was etched by an acidic solution consisting of HF: HNO_3: H_2O= 1:10:10.

Table 3.1. Pure zirconium samples preparation condition

Sample name	Description	Treatment procedure
Zr	Pure Zr	
Zr.hyd	Pure Zr + Hydrided	Hydriding at 400 °C in Ar- 2.5% H_2 for 3 hours
Zr.hyd.e	Pure Zr + Hydrided + etched	Hydriding at 400 °C in Ar- 2.5% H_2 for 3 hours + surface etching by an acidic solution
Zr.ox	Pure Zr + Preoxidized	Pre-oxidizing at 400 °C in air for 24 hours
Zr.hyd.ox	Pure Zr + Preoxidized + Hydrided	Pre-oxidizing at 400 °C in air for 24 hours + Hydriding at 400 °C in Ar- 2.5% H_2 for 3 hours

Four samples of Zircaloy-4, not including the controls, were also prepared. Table 3.2 shows the Zircaloy-4 sample conditions. For Zircaloy-4 samples, two different surface roughness as well as pre-oxidized and hydrided states were studied. The two surface roughness were 1) as received sample (P) with R_a= 0.2 μm and 2) G sample with R_a= 2.79 μm which was ground in our laboratory using 60 grit SiC abrasive paper. Our previous work (Chapter 2) [46,47] showed that increasing the surface roughness will increase the weight gain of Zircaloy-4 samples, however the oxidation rate is almost the same. Thus we seek to understand if the surface roughness can induce any changes to Zr electronic states on the surface that experienced both oxidizing and hydriding regimes.

To characterize the electronic structure of all of the samples, X-ray photoemission spectra (XPS) were measured at the PGM beamline at the Canadian Light Source (CLS). The PGM beamline utilizes a Variable Line Spacing Plane Grating Monochromator (VLS PGM). This beamline is optimized for flux in the energy range between 5 and 250 eV. All spectra were performed with the Scienta SES100 analyzer with a total energy resolution of 40 meV under 10^{-10} Torr vacuum.

In addition to the XPS measurements, Zr $M_{4,5}$ XANES spectra were also measured at the PGM beamline; with a resolving power E/ΔE greater than 10,000, the energy resolution of the spectrometer on the PGM beamline at the Zr $M_{4,5}$ edge is 20 meV. Oxygen K spectra were recorded at the RIXS endstation of the REIXS beamline [48]. The resolution on the O K edge is 50 meV. Spectra were collected using the total fluorescence yield (TFY) and total electron yield (TEY) detection schemes.

Table 3.2. Zircaloy-4 samples preparation condition

Sample code		Surface roughness Ra ±0.02 (μm)	Treatment procedure
Zrly		0.20	
G	G2	2.79	Pre-oxidized (400 °C/ 24 hours/ air) + Hydrided (400 °C/ 3 hours/ Ar- 2.5% H_2)
	G4		Hydrided (400 °C/ 3 hours/ Ar- 2.5% H_2)
P	P2	0.20	Pre-oxidized (400 °C/ air/24 hours) + Hydrided (400 °C/ 3 hours/ Ar- 2.5% H_2)
	P4		Hydrided (400 °C/ 3 hours/ Ar- 2.5% H_2)

Simulations of the XANES spectra were accomplished using WIEN2k, which is a DFT-based code that utilizes a full-potential muffin-tin approach when it calculates the electronic structure. The 'muffin tins' are spherical regions of space that surround each atom, and contain the core electrons as well as some of the valence states. The state of the core electrons is explicitly solved using an atomic Hamiltonian, which gives WIEN2k its status as a full-potential code. However, the Kohn-Sham equations are solved to find valence and conduction band states using a linearized augmented plane wave (LAPW) basis set. The Kohn-Sham equations are solved in reciprocal space on a grid within the irreducible part of the Brillouin zone. Higher symmetry cells thus require few k-points.

The final state of an atom after an X-ray absorption event has a hole in the core level. This core hole perturbs the local states sufficiently that the system can no longer be considered in the ground state, and the excited state must be explicitly modeled for accuracy. To model the core hole effect, we constructed a 2x2x2 super cell, then placed a core hole at one of the non-equivalent sites in that cell. We also added a background charge to conserve the charge within the super cell. This typically reduced the symmetry dramatically. A calculation was then allowed to proceed as normal, albeit with a core hole and background charge. This process was repeated for all non-equivalent sites, and the results of each simulation were added together with appropriate weighting to account for multiplicity of each site.

In order to validate the presence of hydride phase, some XRD measurements along with EBSD imaging of structure were performed. Monoclinic ZrO_2, tetragonal ZrO_2, ZrH_x (where $1 < x < 2$) and zirconium were identified, respectively using JCPD 037-1484, 01-080-0784, 034-0649 and 005-0665. XRD studies were done with a Bruker D8 X-ray diffractometer using Cu-Kα with

0.5 mm collimator and 3 mm oscillation on the plane of sample. EBSD imaging was done with Oxford hardware and HKL software installed on Hitachi SU-6600 FE-SEM.

3.5. Results

3.5.1. XPS analysis

Zr 3d photoemission spectra were obtained for all pure Zr and Zircaloy-4 samples. Fig. 3.1 shows the Zr 3d XPS spectra of pure Zr samples with different conditions that were stated in table 1. The control sample (pure Zr: black curve in Fig. 3.1) shows a doublet at 182.5 and 184.9 eV. These energies coincide well with the references [49–51]. Pure Zr which has been pre-oxidized (green curve in Fig. 3.1) shows a 1 eV shift toward higher binding energy, which is corresponding to the formation of Zr bonds with oxygen. Pure Zr sample with hydrides (blue curve in Fig. 3.1), shows almost no shift compared to pure Zr. The penetration depth of electrons in this kinetic energy range is around few Å. It could be that most of the ZrH_x does not exist near the surface. After etching the surface of the hydrided sample (orange curve in Fig. 3.1), a slight shift toward higher binding energy can be observed in this sample. Interestingly, the sample which has been pre-oxidized and then hydrided shows a significant shift (~4 eV). The detailed discussion will be shown later in section 3.6.

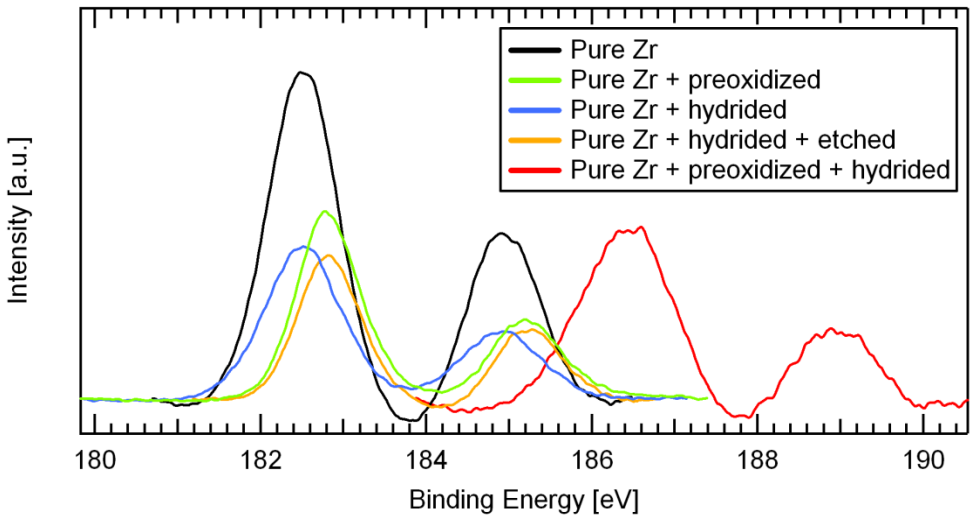

Fig 3.1. Zr 3d spectra of as received and prepared pure zirconium samples.

We also acquired the Zr 3d spectra for the treated Zircaloy-4 samples as noted in table 3.2. Fig. 3.2 illustrates the Zr 3d XPS for the treated (G2, G4, P2, P4) Zircaloy-4 samples. The Zr 3d states of the pre-oxidized samples, namely P2 (blue curve) and G2 (black curve), have an energy shift relative to the non-oxidized samples P4 (green curve) and G4 (red curve).

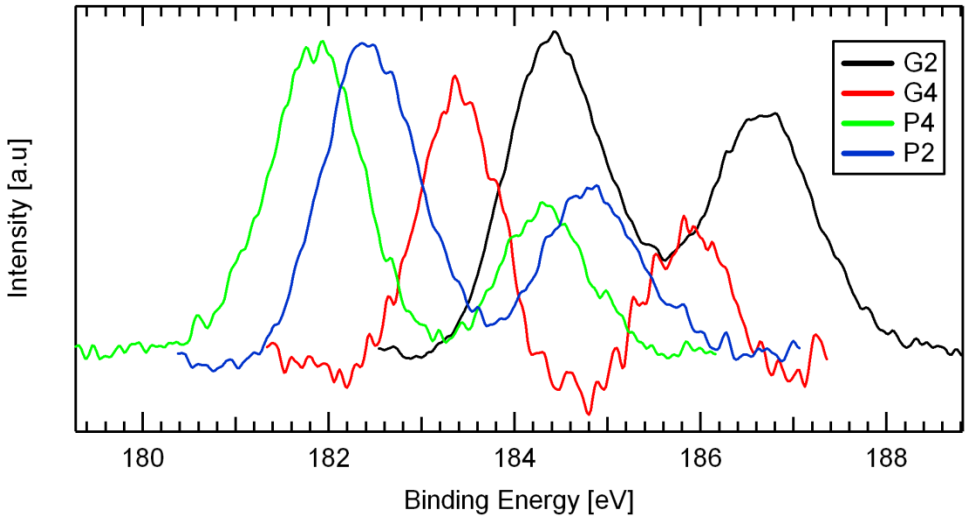

Fig 3.2. Zr 3d spectra of as received and prepared Zircaloy-4 samples.

To compare the Zr 3d doublet in pure Zr and Zr model alloy (Zircaloy-4), we measure the Zr 3d spectra for Zircaloy-4. Moreover, to illustrate the role of thin oxide layer in Zircaloy-4, we acquired XPS spectra of pre-oxidized Zircaloy-4. Fig. 3.3 illustrates the Zr 3d states of as-received and pre-oxidized (400˚C/1 hour) Zircaloy-4 samples. In Fig. 3.3.a, the spectra of the as-received sample are analysed by three sets of doublets. The former set was positioned at 179.6 and 181.0 eV, which is the characteristic Zr 3d doublet [51]. The latter set was shifted by about 3 eV (183 and 185.1 eV) and this shift is characteristic for ZrO_2. This is very close to the position that we measured for the pure Zr sample (Fig. 3.1). The middle doublet could be related to the formation of non-stoichiometric zirconium oxides. In contrast to these doublet sets, only one doublet presents in the pre-oxidized Zircaloy-4 sample (Fig. 3.3.b). Perhaps this can be related to the oxidation state of Zr^{4+} which will be discussed later in section 3.6.

As mentioned before, due to the surface sensitivity of the photoemission technique, even a very thin oxide layer of native ZrO_2 can be detected. This fact along with low oxidation resistance of pure Zr leads to shifted positions of Zr 3d in the pure Zr samples.

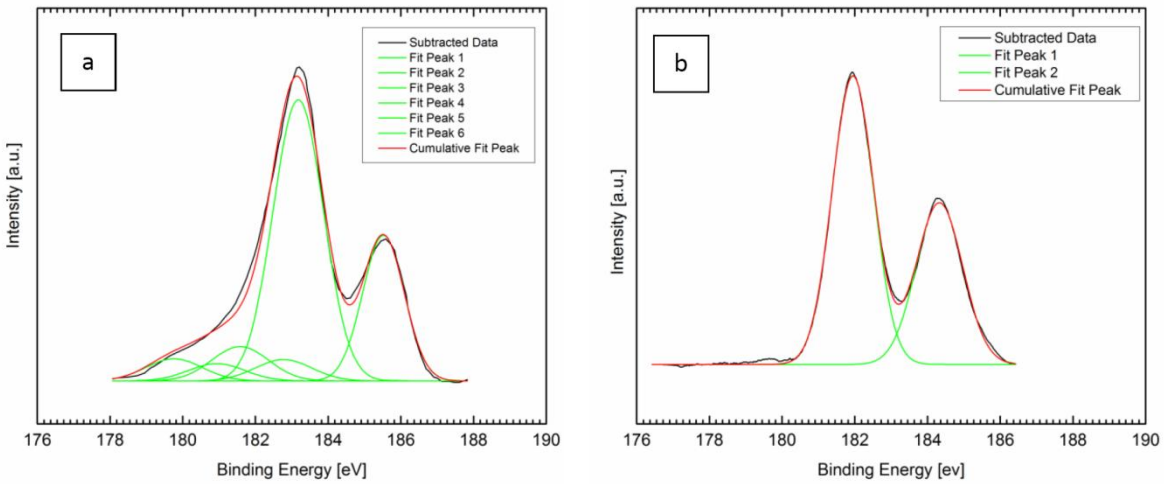

Fig 3.3. Experimental and fitted Zr 3d spectra of a) as-received and b) oxidized Zircaloy-4 sample

3.5.2. XANES analysis

X-ray absorption near-edge spectroscopy (XANES) is a technique that one may use to obtain detailed information about the chemical environment of a certain element within a material. XANES excites a core level electron into bound conduction states. As such, XANES directly probes the unoccupied partial density of states (pDOS) of the element being excited. We have employed the XANES technique to probe the Zr and O unoccupied pDOS by resonantly exciting on the Zr $M_{4,5}$ e and O K edges so that we may understand how oxidation and hydriding affect both Zircaloy-4 and Zr metal.

A XANES spectrum measures how efficiently a given sample absorbs X-ray photons at a particular energy. XANES spectra are typically measured indirectly via total electron yield (TEY) and total fluorescence yield (TFY). TEY measures the number of electrons ejected from the sample at a given energy, whereas TFY measures the number of photons ejected from the sample. Although both techniques ideally would produce the same spectrum, there is one important caveat: electrons have a very short mean free path length (10 to 15 nm) as compared to

photons (100 to 200 nm). Given that electrons can reasonably be expected to escape only if the atom is within 15 nm of the surface, TEY is much more surface-sensitive than TFY.

The results of the O K XANES experiment are shown below in Fig 3.4. Panels (a), (b), (c), and (d) in Fig. 3.4 show the experimental spectra measured from eleven samples: ZrO_2 powder as a reference, four samples of Pure Zr, and six samples of Zircaloy-4 were measured. The description of these samples is listed in the previous sections. Fig. 3.4.a and b show the TEY and TFY measurements from the Pure Zr sample set, respectively. Fig. 3.4.c and d show likewise for the Zircaloy-4 sample set.

The first pattern that emerges from a study of the displayed data is that the TEY spectra show a lot more variability between samples than the TFY spectra do. This statement is true for both the Pure Zr and Zircaloy-4 sample sets. This would suggest that it is the surface chemistry that is changing most strongly as a function of sample preparation. Given that the chemistry of each sample, except for the controls, was changed by post processing, the fact that it is the surface that experiences the most significant changes in electronic structure is expected.

The second pattern concerns relative peak heights. There are four peaks of interest here, namely peaks *a*, *b*, *c*, and *d*. Peak *d* is only seen in the spectra of the control samples (Pure Zr, Unpolished Zircaloy-4, and Polished Zircaloy-4); the nature of this feature will be discussed later. Peaks *a*, *b*, and *c*, on the other hand, exist in the spectra of all ZrO_2-based materials measured in this study. Generally speaking, an increase in spectral weight for c and *d* is accompanied by a decrease in relative weighting for *a*. This shift in spectral weight from *a* to *c* and *d* occurs most strongly for those samples that have been hydridized, which suggests a chemical shift for the O states in the presence of hydrogen.

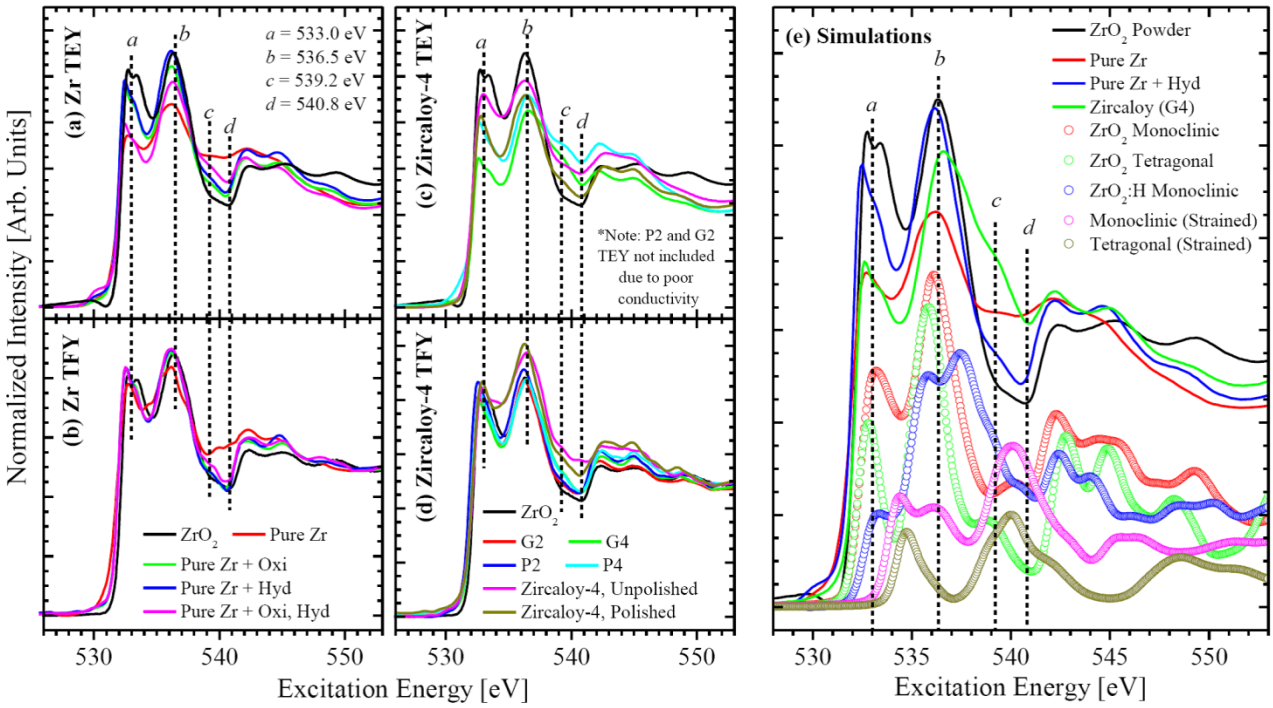

Fig. 3.4. O K XANES data of Pure Zirconium and Zircaloy-4 samples. Panels (a) through (d) show the measurements and highly four excitation energies of interest. Panel (e) compares the experimental XANES spectra with simulations from several different structures.

To uncover what is causing the change in relative intensity of the spectral features for samples that were prepared differently, we turn to density functional theory (DFT) simulations. As mentioned previously, we used the commercial DFT code WIEN2k [52] to simulate the electronic structures of a host candidate ZrO_y and ZrO_y:H_x structures, where $2.5 \leq y \leq 1.75$ and $x = 1$ or 2. For $y = 2$ (ZrO_2), different space group symmetries were also simulated, including monoclinic, tetragonal, cubic, and hexagonal.

The most successful calculations are shown in Fig. 3.4.e, where they are compared to a few selected experimental spectra from the panels on the left. The structures used in the simulations are detailed in Table 3.3.

Table 3.3. Unit cell parameters and atomic positions for all simulated structures

ZrO_2 Monoclinic				ZrO_2 Monoclinic (Strained)			
Space Group:		14 (P21/a)		Space Group:		14 (P21/a)	
a	5.317	α	90	a	4.808	α	90
b	5.151	β	90	b	4.657	β	90
c	5.212	γ	99.23	c	4.712	γ	99.23
Atom	x	y	z	Atom	x	y	z
Zr1	0.208	0.775	0.540	Zr1	0.208	0.775	0.540
O1	0.345	0.570	0.832	O1	0.345	0.570	0.832
O2	0.479	0.950	0.257	O2	0.479	0.950	0.257

ZrO_2 Tetragonal				ZrO_2 Tetragonal (Strained)			
Space Group:		P42/nmc		Space Group:		P42/nmc	
a	3.586	α	90	a	3.209	α	90
b	3.586	β	90	b	3.209	β	90
c	5.167	γ	90	c	4.623	γ	90
Atom	x	y	z	Atom	x	y	z
Zr1	0.250	0.750	0.250	Zr1	0.250	0.750	0.250
O1	0.750	0.750	0.546	O1	0.750	0.750	0.546

ZrO_2:H Monoclinic				ZrO_2:H_2 Monoclinic			
Space Group:		14 (P21/a)		Space Group:		14 (P21/a)	
a	5.317	α	90	a	5.317	α	90
b	5.151	β	90	b	5.151	β	90
c	5.212	γ	99.23	c	5.212	γ	99.23
Atom	x	y	z	Atom	x	y	z
Zr1	0.190	0.822	0.549	Zr1	0.219	0.779	0.536
O1	0.293	0.585	0.887	O1	0.354	0.565	0.835
O2	0.502	0.892	0.286	O2	0.463	0.964	0.242
H1	0.694	0.646	0.473	H1	0.536	0.637	0.395
				H2	0.583	0.693	0.523

Using the simulated X-ray spectra to help interpret the changes in the O pDOS, the increase in spectral weight of peaks *b* and *c*, with respect to peak *a*, can be well-modeled by ZrO_2:H with monoclinic symmetry. As one can see in Fig. 3.4.e, the simulated monoclinic ZrO_2:H spectrum adds significant spectral weight to peaks *b* and *c*. The reason for this is that the H atom bonds directly to one of the two oxygen non-equivalent sites that have only three pre-existing Zr-O

bonds. Thus, a high *b,c:a* peak ratio implies significant O-H bonding in the ZrO_2 lattice. Not surprisingly, G4 has the highest ratio of all the samples. As noted from the Figure, P2 and G2 conducted too poorly to provide a TEY spectrum. Recall that the G4 sample had very high surface roughness, which in turn would have increased the surface area of the sample and allowed for greater diffusion of H into the material than for the P4 sample. As such, the increased ZrO_2:H signature for G4, as compared to P4, is to be expected.

We thus have a model as to how monoclinic ZrO_2 hydridizes. However, there is a limit to how much H that it can absorb. The grip that the O site has on the hydrogen atom is tenuous, and if one attempts to put more hydrogen into the structure, the result is hydrogen molecule formation. Fig. 3.5 shows three unit cells of ZrO_2 in the monoclinic phase. The ZrO_2:H and ZrO_2:H_2 unit cells were allowed full force minimization. The H atoms in Fig. 3.5.c did not start in a molecular configuration; through the process of force minimization, the H atoms moved close to one another and the H-H bond was formed.

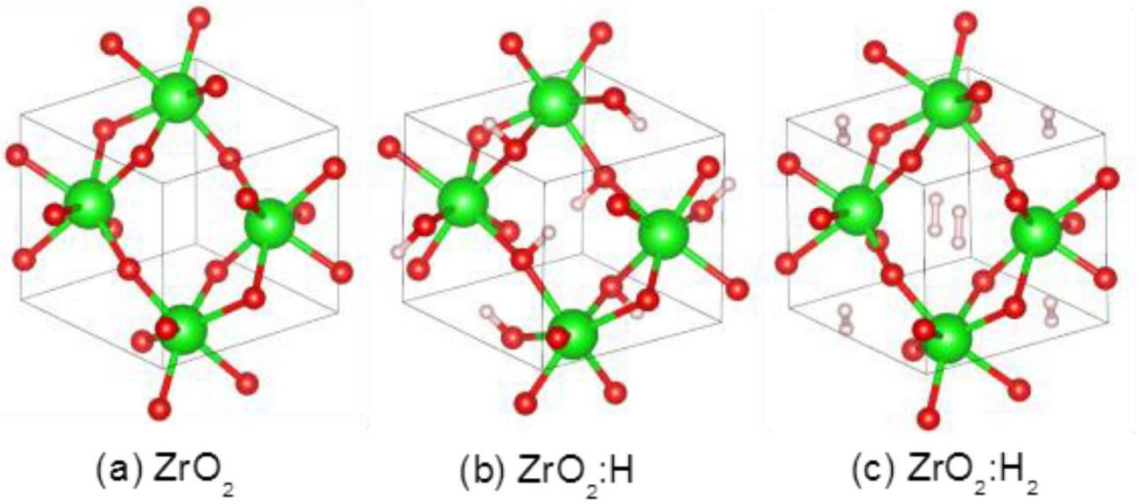

Fig. 3.5. Studying how hydrogen interacts with ZrO_2. (a) The base monoclinic unit cell, for reference. (b) Monoclinic ZrO_2 with four hydrogen atoms inserted to make ZrO2:H. (c) Eight hydrogen atoms inserted to make ZrO_2:H_2. For the unit cells in (b) and (c), the structures were allowed full force minimization.

We have also measured Zr $M_{4,5}$ spectra on all of the samples, shown in Fig. 3.6. In this Figure, the measurements are compared to WIEN2k DFT simulations. Unlike the O K edge, TEY measurements were not possible; only TFY was available for Zr.

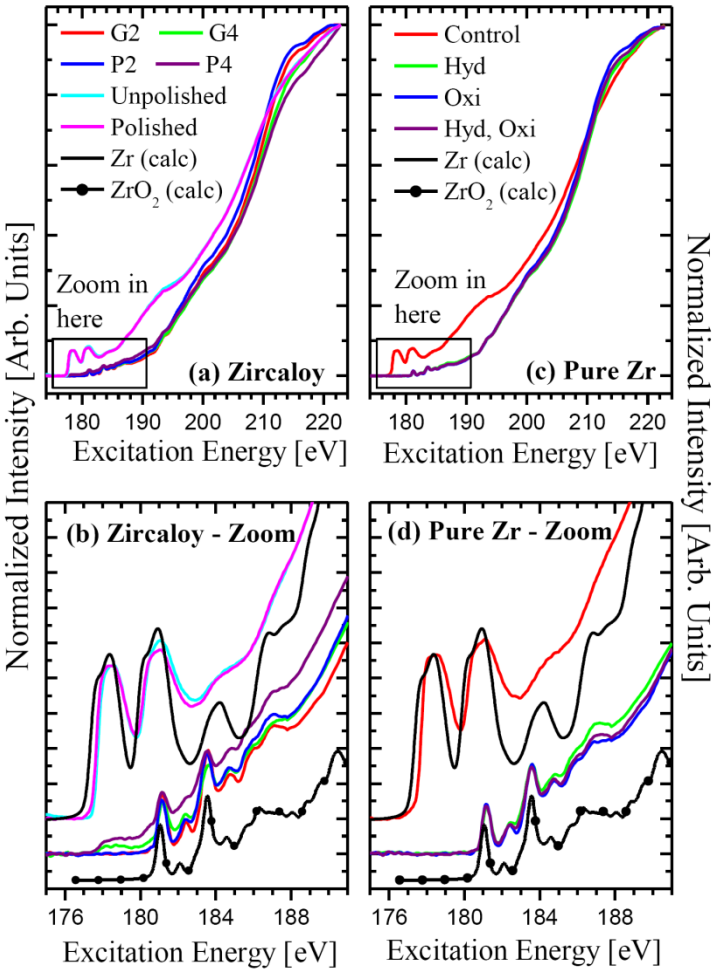

Fig. 3.6. Zr M4,5 XANES measurements on all samples. The left panels, (a) and (b), show the results measured from the Zircaloy-4 sample set; the top panel shows the entire spectrum, whereas the bottom one focuses on the near-Fermi bound states. Panels (c) and (d) function in a similar fashion for the Pure Zr sample set.

3.5.3. XRD analysis

The X-ray diffraction pattern of the as-received and oxidized samples of pure Zr is shown in Fig. 3.7. As can be seen, most of the changes in the XRD happened in the 25-40˚ 2theta angle range.

Thus, the detail view of this angular range is shown separately. This region has all the strong peaks for the Zr, ZrO_2 (both tetragonal and monoclinic) and possible Zr hydride allotropes ZrH_x (e.g. ZrH_2, $ZrH_{1.66}$, ZrH_{2-x}). As depicted in Fig. 3.7, upon peroxidation of pure Zr, the ZrO_2 peaks, mostly monoclinic, appear. Even in the hydride samples zirconia peaks are present. This is due to the presence of enough oxygen for oxidizing Zr in the hydriding procedure that is described in the previous section.

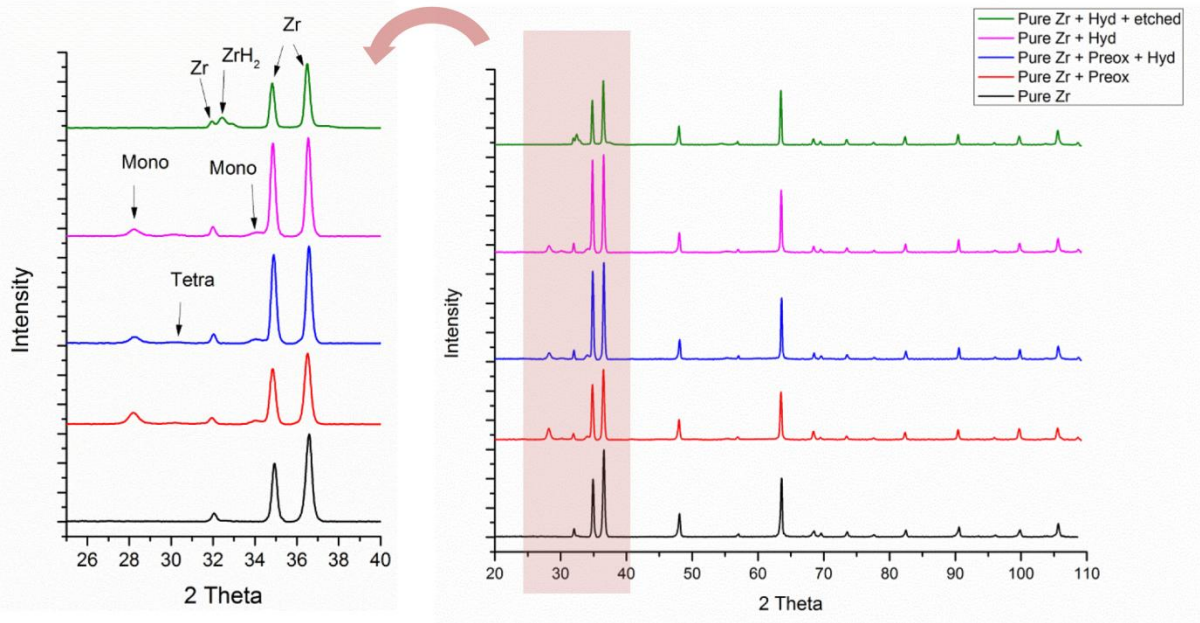

Fig. 3.7. X-ray diffraction patterns of as received and prepared pure zirconium samples.

There is no sharp peak of ZrH_x in the hydrided samples. However after etching, the hydride peak is revealed. We characterized the surface of the etched sample with Electron Backscattered Diffraction (EBSD). Fig. 3.8 shows that, ZrH_x is precipitated inside the Zr matrix grains. In some regions, the hydrides agglomerate, while in other regions, fine hydrides are dispersed. The main reason for this behavior lies in the orientation relationship between the Zr matrix and ZrH_x which is out of the scope of this paper and has been discussed in detail elsewhere [53].

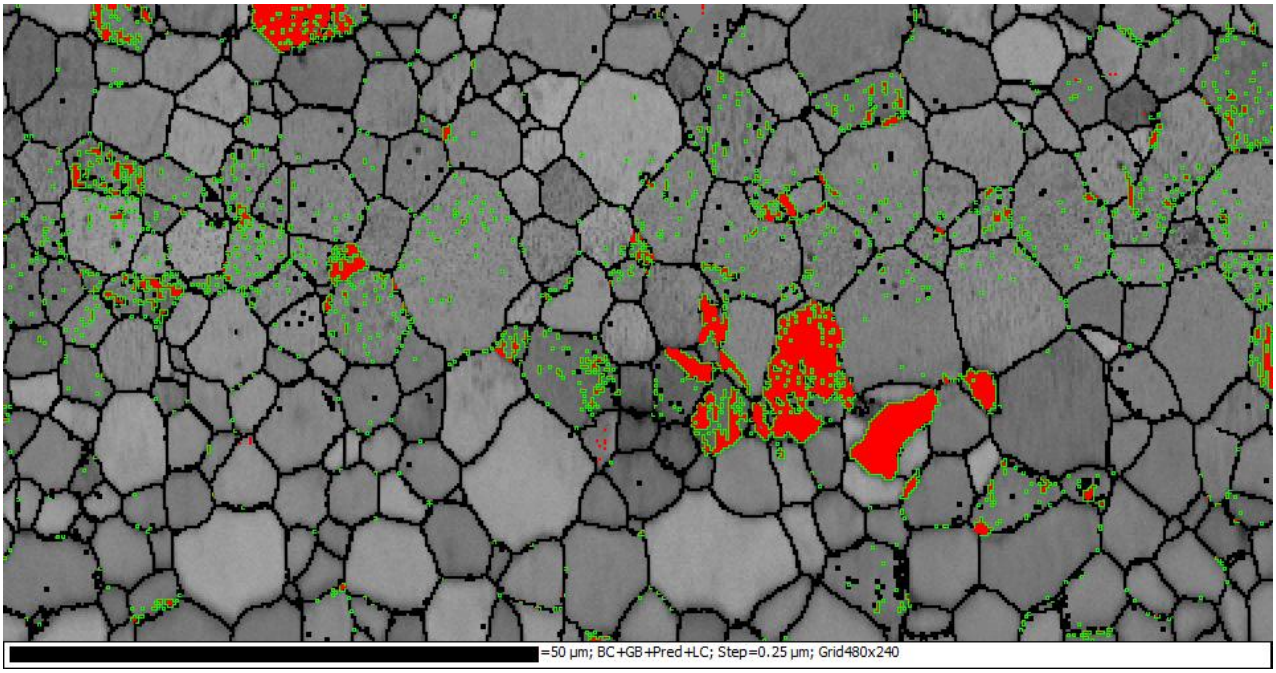

Fig. 3.8. EBSD grain and phase map of the pure Zr hydrided sample. (Hydrides and their boundaries are shown in red and green, respectively)

Fig. 3.9 illustrates the XRD diffraction pattern of the Zircaloy-4 samples. Pre-oxidized samples (P2 and G2) shows very strong oxide peaks, while solely hydrided samples (P4 and G4) pose very weak oxide peaks.

One reason for detecting no hydrides on the Zr surface without etching could lie in the hydride formation mechanism. Hydrogen diffuses to the Zr bulk structure at high temperature. Upon cooling, the solubility limit of hydrogen in Zr decreases, so the excessive amount of hydrogen will precipitate as hydride phases in the Zr microstructure. Regarding the kinetic and thermodynamics of this process, the hydrogen molecules absorbed on the surface or very close to the surface of the Zr can escape from the Zr structure prior to precipitation. Thus, statistically very few hydrides can be formed in these regions. Through the etching process, the Zr matrix and ZrH_x are removed selectively from the surface. As a result of this process and considering the X-ray penetration depth, the hydrides can be detected by the X-ray.

The higher surface roughness in G sample lead to higher oxidation, as a result stronger oxide peaks can be seen in G2 sample. This fact has been discussed in our previous work [46].

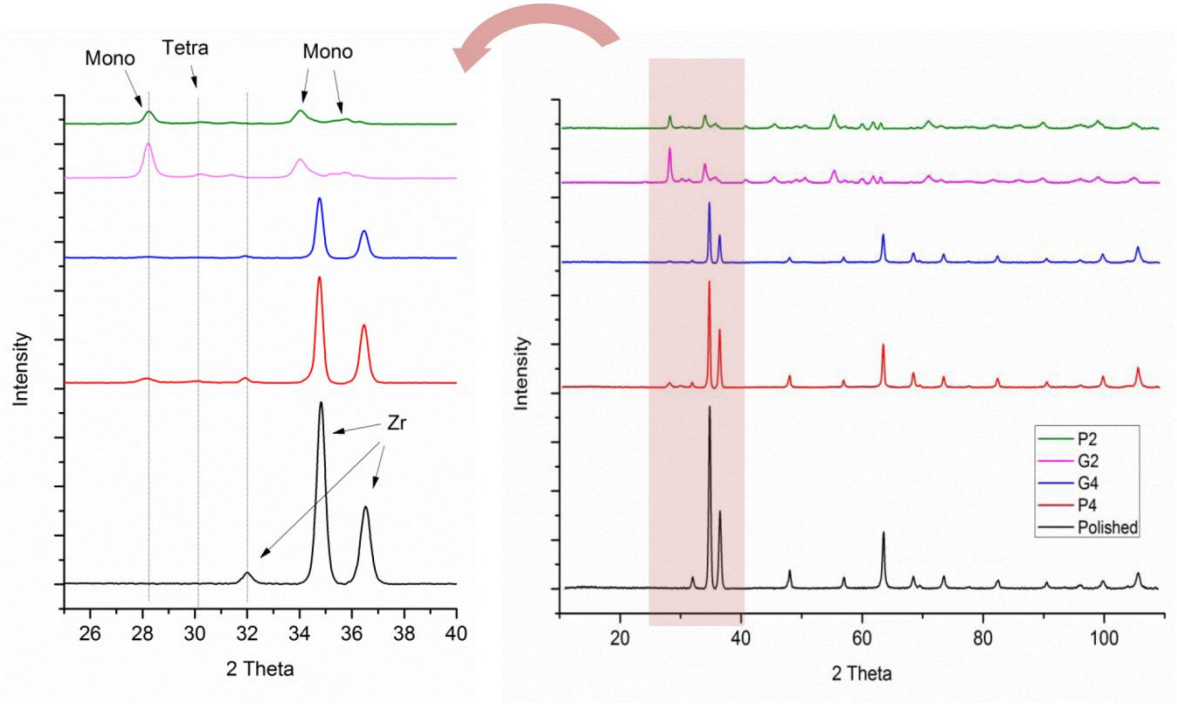

Fig.3.9. X-ray diffraction patterns of as received and prepared Zircaloy-4 samples.

3.6. Discussion

As depicted in Fig. 3.1, the Zr 3d XPS spectra for various treated Zr samples have different shifts in binding energy. Interestingly, the largest shift was for the pre-oxidized and hydrided sample. This large shift could be related to the interaction of hydrogen with the Zr oxide layer or formation of a complex hydroxide phase (e.g. $ZrHO_{2-x}$) on the surface [54]. This type of hydrogen contribution was also reported by Roustila et al. [49] and Wang et al. [50] in their studies on Zr interaction with hydrogen and oxygen. They claimed that the lattice distortion upon hydrogen absorption and H-O interactions on the surface of Zr may enhance the outward diffusion of oxygen which already exists in the bulk to the surface. Wang et al. [50] also suggested that the hydrogen diffusion can restructure the ZrO_x to ZrO_2. In addition, diffusion of hydrogen through the structure of ZrO_2 can alter the dielectric constant; therefore the electronic behavior of Zr could be changed. Gomez-Sanchez et al. [55] also observed the same binding energy shift for Zr when adding phosphorus during the anodizing.

It is necessary to mention that, due to hydriding procedure at high temperature, these samples might be oxidized slightly under the hydriding regime. This phenomenon has been validated by XRD which was shown in section 3.5.3.

For the Zircaloy-4 treated samples, the XPS spectra exhibit different amount of shift in the binding energy (Fig. 3.2). The pre-oxidation is the main reason for this shift. Moreover, the G samples show larger 3d binding energies than the P samples. To explain the higher binding energies of the G samples, recall from table 3.2 that the G samples have much rougher surfaces. A rougher surface has a higher oxidation rate so the oxide layer would be thicker on these samples. This fact has been discussed in our previous work (Chapter 2) [46]. Thicker and/or a more stoichiometric oxide layer might be the reason for a larger energy shift due to the oxide layer.

Comparing Fig.3.1 and Fig 3.3.a, one can observe that the Zr 3d doublet was located at 182.5/184.9 eV for pure Zr (Fig. 3.1) and 179.6/181 eV for the as received Zircaloy-4 sample (Fig. 3.3.a). These levels shift by around 0.6 to 4 eV compared to the standard pure Zr state [51]. The presence of a thin native Zr oxide layer on the surface would be responsible for these shifts towards higher binding energies. As Zircaloy-4 has higher oxidation resistance than pure Zr [56], the native oxide layer, which is formed at STP condition on the Zircaloy-4 samples, is thinner. The spectra of the as-received sample are analysed as three sets of doublets, as shown in Fig. 3.3.a. On the contrary, only one doublet presents in the oxidized sample (Fig. 3.3.b), and this can be related to the oxidation state of Zr^{4+}. As reported by Wang et al. [50], ZrO_2 can introduce different chemical shifts depending on its stoichiometric ratio. Non-stoichiometric oxide ZrO_x, where $0 < x < 2$, has smaller chemical shifts than stoichiometric ZrO_2 oxide. Therefore, the middle doublet in the pure Zircaloy-4 sample could be correlated to this non-stoichiometric zirconium oxide (ZrO_x). Consequently, part of the binding energy shift in the as-received Zircaloy-4 sample is correlated to the lower valence state of Zr in ZrO_x. Indeed, shifting toward higher binding energies due to oxidation has also been reported for pure Zr by other scholars [57–60]. Veal et al. measured about 4.2 eV chemical shift for Zr 3d core level in ZrO_2 with respect to pure Zr.

The other parameter than can be responsible for the different energy shifts, is the change in alloying elements. Most of the photoemission studies have been done on pure Zr [50,57,61]. However, similar energy shifts have been reported for Zr-Pd and Zr-Cu alloys; as 1.14 and 0.85 eV, respectively [50,62]. Thus, the presence of alloying elements (tin, iron and chromium) in Zircaloy-4 might be another reason for the observed shifts.

We now focus on the XANES spectra of the samples from section 3.5.2. The results showed in Fig. 3.4 panels and the unit cells in Fig. 3.5, would imply that ZrO_2 does not hydridize very easily, and attempting to fill the monoclinic ZrO_2 lattice with more H than the ZrO_2:H ratio allows, will result in mobile hydrogen. On the other hand, the monoclinic phase will hydridize at least somewhat with minimal distortion to the lattice; the tetragonal and cubic phases have no place for the H atoms to bond easily, and as such, they can only hydridize after strong distortions of their unit cells. If the tetragonal and cubic phases cannot bond with the hydrogen, then they also cannot hinder it from diffusing through to the Zr metal beneath. In terms of building an oxide barrier against hydrogen diffusion through to the core Zr metal, the monoclinic ZrO_2 phase would be the most effective. Other researchers have reported that ZrO_2 provides more effective protection against hydriding as the amount of tetragonal phase decreased [44,63].

As follows from the previous discussion in section 3.5.2 about Fig. 3.4, peak *a* is due to ZrO_2, and peaks *b* and *c* are due to a combination of ZrO_2 and ZrO_2:H. What then does the peak *d* at 540.8 eV represent? Through extensive simulations, we have found that the only plausible explanation is strained ZrO_2. Fig. 3.4.e shows two simulations, one of strained tetragonal ZrO_2, and one of strained monoclinic ZrO_2. In both cases, the base unit cell was compressed such that the average Zr-Zr bond length was equal to that of Zr metal. The results of the simulations are close because they both provide spectral weight approximately in the spot where it is needed, at peak *d*.

Given that peak *d* is explained only by ZrO_2 that has been compressed, the source of this peak is likely the interface between fully-developed ZrO_2 and Zr metal. It is therefore not surprising that Pure Zr has the highest weighting at peak *d*, with unpolished Zircaloy-4 taking second place and polished Zircaloy-4 sitting at a distant third. None of these three samples was treated in any way (e.g. ground, pre-oxidized, etc.), and as such, their oxidation would not be as advanced as the

other samples. Peak *d* is weaker for the Zircaloy-4 samples likely because Zircaloy-4 has a different oxidation mechanism than Pure Zr, which may explain why Zircaloy-4 is typically more resistant to oxidation than pure Zr metal.

Finally, the Zr $M_{4,5}$ results in Fig. 3.6 can be entirely explained by two model structures: Zr metal and ZrO_2 (monoclinic phase). The results show that the control samples – Pure Zr, as well as the polished and unpolished Zircaloy-4 samples – have a very strong metallic Zr signal. G4 and P4 show a mixture of ZrO_2 and metallic Zr states. All other samples show only ZrO_2 character. The fact that the Zr $M_{4,5}$ results can be explained so readily with just Zr metal and monoclinic ZrO_2 is to be expected, given that we only have TFY spectra from which we may draw conclusions. On the O K edge, the TFY spectra for all samples were very similar. It was only near the surface that can be measured more directly by TEY, the greatest changes were observed.

3.7. Conclusion

The present study demonstrates a qualitative analysis of Zr electronic structure at its oxide, hydride and alloyed states. Various oxidation, hydriding and surface roughness treatments were applied to the pure Zr and Zircaloy-4 model alloy samples. Upon these treatments binding energy shifts are clearly observable in the XPS spectra, which occurred due to different oxidation states. XANES measurements at the O K edge and Zr $M_{4,5}$ edge revealed strong differences between the samples, particularly in the surface O states as measured by TEY. In order to decipher the differences in XANES spectra, we applied DFT simulations. Upon using WIEN2k DFT simulations and comparing with the experimental spectra, we found that hydrogen preferentially bonds to one of two non-equivalent oxygen sites within the monoclinic ZrO_2 lattice, but only in a ZrO_2:H ratio. More hydrogen than this is unstable. From the perspective of protecting Zr metal from hydriding attack, the monoclinic phase of ZrO_2 offers the strongest barrier.

Moreover, we offer the perspective insight for using synchrotron-based techniques for characterizing the Zr compounds.

CHAPTER 4

EVOLUTION OF DEFORMATION AND ANNEALING TEXTURES IN INCOLOY 800H/HT VIA DIFFERENT ROLLING PATHS AND STRAINS

4.1. Overview of Chapter 4

In previous chapters 2 and 3, we addressed the two first objectives of the project concentrating on the current fuel cladding material and in the following chapters we focus on a future fuel cladding material. As mentioned in chapter 1, Incoloy 800H/HT is a candidate for fuel cladding materials in the Gen IV nuclear reactors. To elaborate the deformation and annealing textures of Incoloy 800H/HT and also to decipher the role of texture in the oxidation resistance of this alloy, a specific thermo-mechanical processing (TMP) was designed and employed to Incoloy 800H/HT. This chapter includes the detailed study of the texture and micro structure evolution of this alloy through the applied TMP. Moreover the deformation mechanism is studied by means of orientation imaging microscopy.

This chapter is presented as manuscript # 3 (Evolution of deformation and annealing textures in Incoloy 800H/HT via different rolling paths and strains). My contributions to the manuscript are: a) preparation and processing of the samples b) SEM, EDS and EBSD analyses c) Reviewing the relevant literature and writing the manuscript. Majid Nezakat was assisting in the sample processing and data analyzing.

The manuscript was published in Materials Science and Engineering A:

- H. Akhiani, M. Nezakat, and J. Szpunar, “Evolution of deformation and annealing textures in Incoloy 800H/HT via different rolling paths and strains,” Materials Science & Engineering A 614 (2014) 250–263.

The copyright permission to use the manuscript in the thesis was obtained and provided in the Appendix section. The references for this chapter along with references from other chapters are provided at the end of the thesis.

Evolution of deformation and annealing textures in Incoloy 800H/HT via different rolling paths and strains

Hamed Akhiani, Majid Nezakat, Jerzy Szpunar

Department of Mechanical Engineering, University of Saskatchewan, Saskatoon, Canada

4.2. Abstract

In this chapter, we characterize the deformation and annealing textures of Incoloy 800H/HT, following different rolling conditions that produced different textures in this material. Incoloy 800H/HT is an austenitic Fe-Ni super alloy and is considered to be a candidate material for Gen IV nuclear reactors. Fossil fuel plants have used this alloy for decades; however, as grain structure and texture parameters can strongly affect its physical and mechanical properties in-service, engineers should consider some structural modifications before using this alloy in nuclear reactors.

In this study, we used Thermo-Mechanical Processing (TMP) to alter the texture of Incoloy 800H/HT. We applied various thickness reductions (10, 30, 50, 70, and 90 %) to this alloy using two different rolling paths, followed by annealing. Our detailed study of the deformation and annealing texture evolution shows that upon different rolling paths, the final deformation texture and the annealing texture were different. Brass texture was the dominant component for the uni-directional rolled (UDR) samples, while a combination of brass (B) and ND-rotated brass (B_T) were the dominant components in the cross rolled (CR) samples. Annealing textures of UDR samples were mainly Goss, copper, S, recrystallized brass ($\{236\}<385>$) and minor copper twin $\{552\}<115>$ components. At lower deformations (<50 %), the annealed CR samples showed tilted cube, S, recrystallized brass ($\{236\}<385>$) and minor Goss twin $(113)<\overline{3}32>$. However, at higher rolling reductions, the $B+B_T$ deformation texture was retained for the CR samples.

Keywords: Incoloy 800H/HT, annealing texture, deformation texture, cross rolling

4.3. Introduction

Gen IV nuclear reactors use new concepts and designs to increase efficiency and improve safety. Very High Temperature Reactor (VHTR) and Super-Critical Water Reactor (SCWR) are among the designs selected for Gen IV reactors in the United States and Canada [1,4]. Both types are expected to work at high service temperatures (VHTR: 750-950˚C, SCWR: 550-650˚C) for a high thermodynamic efficiency [12]. Operating at high temperature/pressure requires materials with superior high temperature oxidation resistance. According to the Gen IV roadmap [1], Incoloy 800H/HT is one of the candidate materials for use as both cladding and structural components for the SCWR. It is notable that, in the very recent roadmap update (2014) [4], the candidate materials have been limited to austenitic steels with more than 20% chromium. Table 1.1 shows the chemical composition of Incoloy 800H/HT. Evidently this alloy with high chromium content still remains in this category.

Incoloy 800H/HT can be used for construction of various high temperature components in Gen IV reactors, including steam generators, intermediate heat exchangers, hot ducts, and fuel claddings [12,64,65]. Incoloy 800H/HT is a variant of the well-known austenitic Incoloy 800 family, which has chemical composition and heat treatment restrictions [66,67]. This alloy has been used widely in chemical processing, industrial heating and power generation units. Thus, there is a fairly good database on its behavior at high temperature. However, because of differences in the service conditions, some properties (e.g. grain boundary diffusion and corrosion resistance) should be improved. Several studies reveal that many important properties depend on grain boundary structure and texture [11,15,16,65].

Moreover, it is well known that the texture of FCC alloys has significant influence on mechanical properties, as well as oxidation resistance. Because the presence of strong texture can influence a wide range of mechanical properties, significant attention is paid to control of two critical processing parameters; strain path and deformation temperature, which are key in deciding the final deformation texture. While deformation temperature has been widely studied for a variety of alloys, the strain path effect studies are limited to a few publications [68–70]. These studies show that the strain path can govern the deformation texture and, accordingly, it might affect the recrystallization texture. The strain path can be changed by altering the rolling direction by some degrees about normal direction (ND) (e.g. 90˚ in cross-rolling) between the

reduction passes. Cross rolling will result in a different texture with lower anisotropy, intergranular misorientation, and fraction of low angle grain boundaries compared to unidirectional rolling in pure Ni and Cu [68,69]. In spite of these textural modifications, no serious attempts have been made at applying cross rolling in Incoloy 800H/HT.

Furthermore, Stacking Fault Energy (SFE) as an alloy characteristic factor can influence the deformation and annealing textures of FCC materials. In high SFE materials, dislocation slip is a dominant deformation mechanism, thus no twinning occurs. The typical deformation textures of the FCC materials consist of copper (Cu), Goss (G), S and brass (B) components. On the contrary, in low SFE alloys (e.g. 800H/HT), the B texture would be the dominant texture with weak Cu and S components [69,71,72]. Twinning also has a significant effect on texture in low SFE FCC materials [73–76]. The smaller the SFE, the higher the contribution from deformation twins [77]. In addition, large grains have a higher tendency to deform by twinning, compared with small grains [78,79]. As twinning occurs in the deformation and annealing stages, it might influence both the deformation and annealing textures. The effect of twinning on texture was first described by Wassermann [76]. In his model, the volume of the deformation twins is related to texture transformation. Based on this model, the Cu component transforms to the Cu twin component $\{552\}<115>$ via twinning, which can be further transformed to a G component $\{110\}<001>$ by slip [76,80,81]. However, Leffers [78,80], and Sekine and Wang [77] experimentally show that this theory does not agree with the microstructural studies. They claim that the volume fraction of twins is not high enough to have a direct effect on the texture. Consequently, a second theory was introduced regarding the indirect effect of twinning on texture. In a highly twinned sample, the fine twin lamellae make slip difficult, hence imposing a microstructural hardening. By increasing the deformation strain, a glide mechanism would be activated to accommodate the strain increase. In such a way, twinning could indirectly affect the texture. Therefore this theory is called the overshooting/latent hardening twinning effect [77–80].

Nevertheless, the twinning volume effect still can be responsible for the texture development in very highly twinned materials. In other materials, microstructural latent hardening or the overshooting effects of twin lamellae play a significant role in texture transformation [77,78]. Sekine and Wang [77] show that in Ag with low SFE, a large number of Cu $\{112\}<111>$ grains decay to the Cu twin component $\{552\}<115>$ by normal Wassermann's twinning mode. By

subsequent slip deformation, it can be transformed to $\{110\}<112>$ through G $\{110\}<001>$ orientation, resulting in a brass deformation texture. In addition, by comparing texture transition between very low SFE (Ag-Zn alloys) and low SFE (Ag) materials, these authors claim that the presence of $\{111\}<110>$ component shows that it is a characteristic deformation texture component that can be formed solely in very low SFE materials and results from overshooting/latent hardening in these materials [77].

Although there are rather controversial debates on the origin of deformation texture in low SFE FCC materials, the final textures are almost identical [73,78,81]. However, the recrystallization (annealing) textures of these materials show more discrepancy. Nucleation and growth competition play a significant role in the formation of the annealing texture. "Oriented nucleation" and "oriented growth" are the two distinct models used to describe the texture evolution upon annealing [73,79]. The dominant mechanism depends on many factors such as the materials deformation state (driving force for recrystallization), grain boundary structure (misorientation: high and low angle boundaries), dislocation density, twinning, size of the nuclei, etc. Based on these factors both of these mechanisms can act competitively and simultaneously [73,75,79].

High SFE materials (e.g. Al, Cu) that show copper deformation texture form a dominant cube recrystallization texture. This has been related either to selective/oriented growth or oriented nucleation mechanisms [73,79,82]. For low SFE materials exhibiting brass deformation texture, various recrystallization components regarding the SFE have been reported. However, one of the most common recrystallization texture components is $\{236\}<385>$ known as recrystallization brass (R-brass) [83–87]. As Lucke states [88], this component in annealing texture intensifies as the SFE decreases. Sztwiertnia [83] claims that this orientation forms mainly upon oriented growth and favors materials with brass deformation textures.

Most of the aforementioned textural studies were performed on model copper, brass and silver alloys. To our knowledge, there is no comprehensive study on the texture evolution of Incoloy 800H/HT. A few studies focus on the Grain Boundary Engineering (GBE) of this alloy, however only very low deformations with normal unidirectional rolling were studied [11,66]. In recent years, following the devolvement of TWIP steels in the automotive industry, some studies have

been done on these steels [81,85]. Although the texture evolution of TWIP and iron-based super-alloys (i.e. Incoloy 800H/HT) share some common features, the strain-induced martensite in TWIP steels would alter the deformation and annealing textures [85].

In this paper (chapter) we report the texture evolution of Incoloy 800H/HT via unidirectional and cross-rolling in both deformation and annealing states. Understanding the deformation and recrystallization behavior of this alloy under low and heavy deformation through different strain paths would be of significant value in optimizing its properties to suit prospective new applications (e.g. as a nuclear structural material).

4.4. Experimental procedure

For this study we used commercial Incoloy 800H/HT, which is a variant of Incoloy 800 [67]. Table 1.4 lists its chemical composition. The alloy was fully annealed at 1420˚C and water quenched in as-received condition. We performed Thermo-Mechanical Processing (TMP) on the as-received sample by a series of cold rolling operations followed by annealing at 1050˚C for a time period of 25 min/cm thickness of the samples. We applied a true strain of 0.2 per rolling pass for all the samples, which were rolled to 10, 30, 50, 70 and 90% thickness reduction with two different strain paths. We designed the experiments to allow us to decipher the roles of reduction percentage and strain path on the deformation and annealing textures. From the same plate we cut samples of 50x50x13.25 mm and 50x25x13.25 mm and subjected them to two modes of rolling with a laboratory roll machine to produce the thickness reductions. Fig. 4.1 illustrates the schematic of unidirectional rolling (UDR) and two-step cross rolling (TSCR/CR) modes.

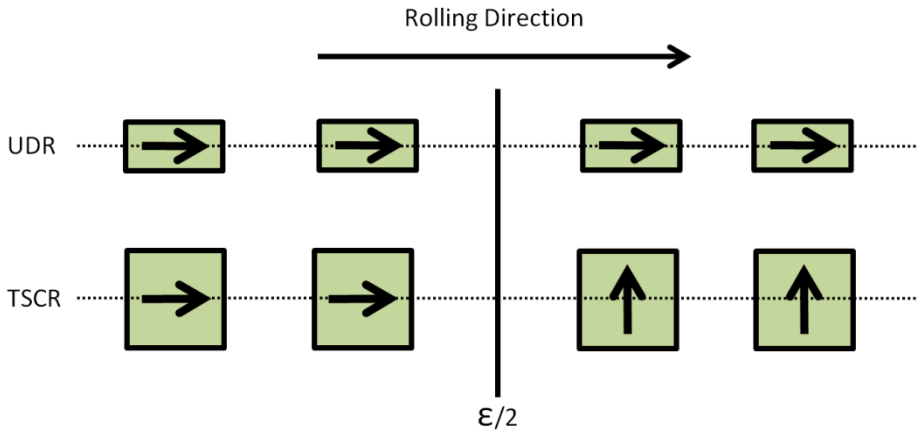

Fig. 4.1. Schematic graph showing the UDR and CR modes.

For textural studies we employed a Bruker D8 X-ray diffractometer with Eulerian cradle using Cr-Kα, and Vantec-500 detector with 0.8 mm collimator. We used incomplete pole figures to calculate Orientation Distribution Function (ODF) as well as the texture component, by means of ResMat® software. The volume fractions of various texture components were calculated within 15˚ tolerance around their ideal position in the Euler space, both in micro and macro texture. We performed the micro texture measurements using an Oxford Electron Back Scatter Diffraction (EBSD) setup fitted on a Hitachi SU6600 Field Emission Gun Scanning Electron Microscope. The SEM was operated at 30 kV with the automatic EBSD scan. We performed EBSD on the TD plane as the planar features of cold-rolled microstructures can be better detected in this plane than on any other specimen plane. We used the HKL Technology Channel-5 software to carry out data analysis.

4.5. Results and discussion

4.5.1. Deformation texture

Fig.4.2 shows the macro and micro textures of the as-received Incoloy 800H/HT. For ease of comparison between the textures of all samples only the 3 important sections of ODF are illustrated and discussed here. We selected ODF sections at φ2 = 0, 45 and 65˚ since they demonstrate the common FCC deformation and annealing texture features: α, β fibers and S component. Fig. 4.3 illustrates the major components and their positions where B, G, S, and Cu

stand for brass, Goss, S and copper components. Similarly B_T, G_T, S_T, Cu_T show the ND rotated components. As Fig. 4.2 illustrates, both macro (XRD) and micro (EBSD) textures of Incoloy 800H/HT show a weak texture with no preferred orientations. Coarse grains and twinning have resulted from the hot rolling deformation history of the alloy.

Textures of the UDR and CR samples are depicted by pole figures (PF) and selected ODF sections. Fig. 4.4 shows the (111) PF for these samples at different rolling reductions. It is well-known that FCC materials develop two different types of rolling textures based on the materials structure (e.g. SFE, grain size, etc.) and the processing parameters (e.g. strain rate, strain path, rolling temperature, etc.) [75,78]. In general, low SFE materials tended to form the brass-type texture while high SFE materials favored the copper-type texture upon rolling. Similarly, it was found that low and high strain rates would encourage copper-type and brass-type textures, respectively [78].

Incoloy 800H/HT has low stacking fault energy (<100 mJ/m^2) due to its alloying elements [89]. Therefore it is expected to have the FCC "alloyed" or brass-type texture rather than "pure metal" or copper-type [90]. Comparing the initial (111) PF (Fig. 4.2) with the rolled samples, one can observe the differences. More or less, all samples show typical brass-type texture, although there are some differences in the strength of maxima in UDR and CR, particularly at higher reductions (e.g. 90%UDR vs. 90%CR), which will be addressed later. We have extracted selected ODF sections to give a better illustration and more precise comparison between the samples, as previously mentioned. Figs. 4.5 and 4.9 show these ODF sections for the UDR and CR processed samples.

In order to characterize the deformation texture, we first focused on the UDR samples. As Fig. 4.5 illustrates, upon applying 10% deformation by UDR, we observed a weak texture with a combination of G, B, Cu and S components. This can be identified by φ_2 = 0, 45 and 65˚ODF sections. After 30% reduction, the texture, represented by the same components, was strengthening. The $(221)<2\bar{3}2>$ component, which was very close to the S component is moving toward the brass component (φ_2 = 45˚ODF section). Upon further reduction to 50%, we observed a strong texture consisting of B and G components. By increasing the rolling strain to 70%, Cu and G components gradually diminished while B component was strengthened. This

trend continued to 90% reduction, where B component proposed itself as the dominant texture. Consequently, the final texture after 90% reduction was the typical brass type $(110)<1\bar{1}2>$ rolling texture.

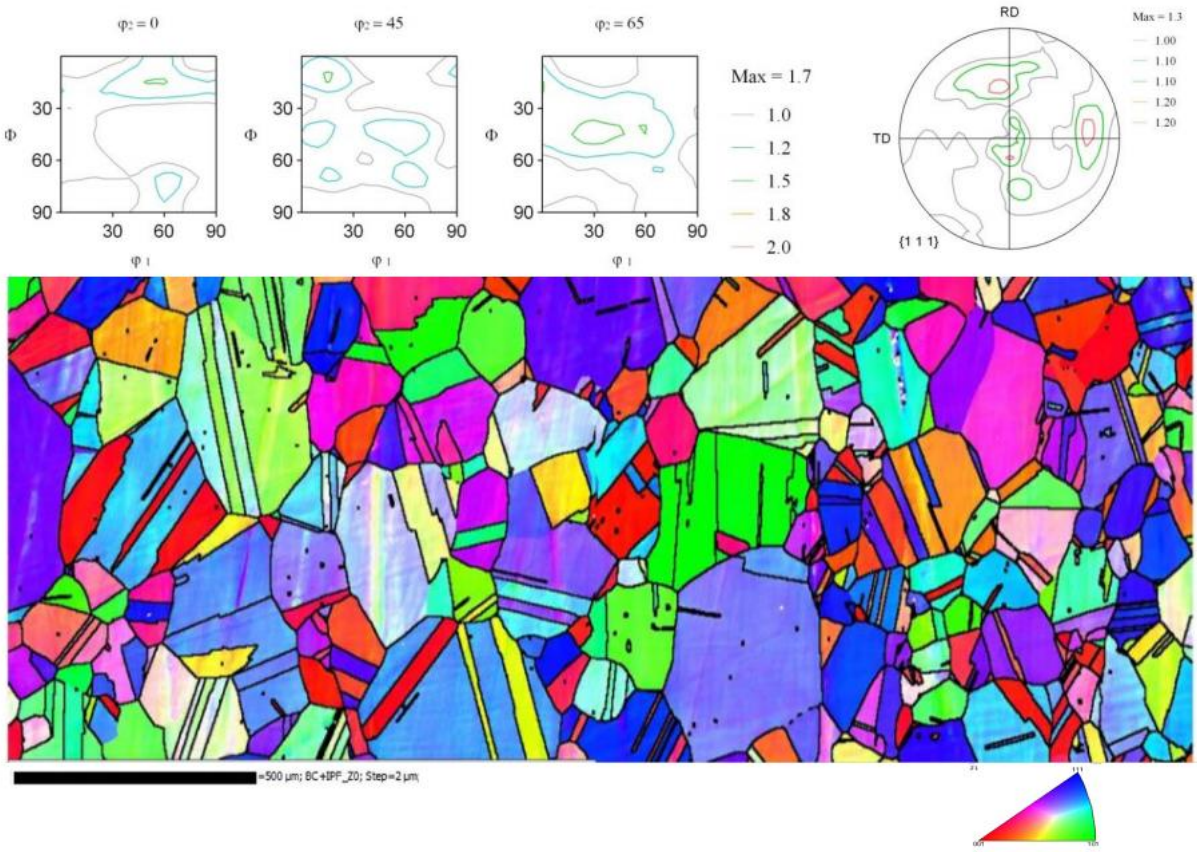

Fig. 4.2. ODF sections and Inverse Pole Figure (IPF) EBSD map of the starting Incoloy 800H/HT showing grain morphology and orientations.

The transition of the near S component $(221)<2\bar{3}2>$ is clearly depicted in the β fibre (Fig. 4.6). By increasing the rolling strain, B component gradually intensified. Particularly, comparing the 50% and 70% processed samples one can observe the transition between near S components towards B component. In order to compare these components quantifiably, Fig. 4.7 shows the volume fraction of rolling texture components as a function of deformation strain. As discussed earlier, B and G components gradually increased in strength while Cu component decreased. The $(112)<1\bar{1}1>$ component increased up to 50% and then, upon the transition to B component, it

reduced. This is in accordance with Wassermann`s model that also has been reported elsewhere [76,87,91]. Due to the high multiplicity factor of S component, produced by slip at early deformation stages [92], we did not include its volume fraction in the figures. Fig. 4.5 depicts how S components are presented strongly in the φ_2 = 65 ODF section at 10% and 30 % deformations. However by increasing the rolling strain beyond 30%, S component was weakened. It is significant that the relatively low intensity in macro texture is in agreement with the measurements of Saleh et al. [81] and Bracke et al. [85].

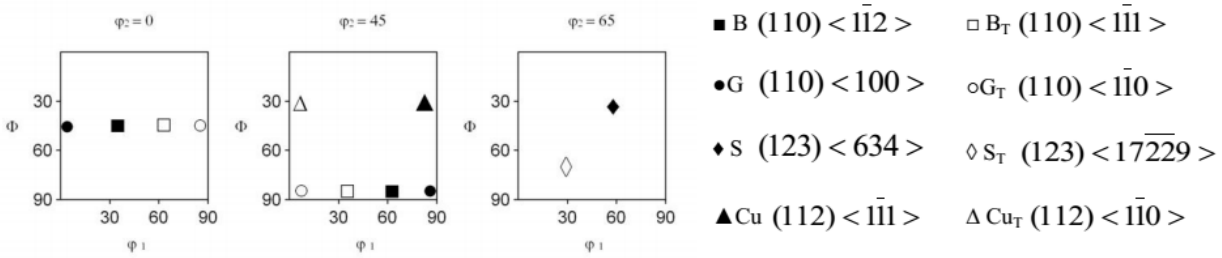

Fig. 4.3. Incoloy 800H/HT major texture components and their positions in the ODF sections.

In their comprehensive review on brass-type texture, Leffers and Ray [78] state that deformation twinning is mainly responsible for the formation of brass-type texture. Other researchers also state that all materials showing brass-type texture exhibit extensive twinning [78,92]. In order to validate this for Incoloy 800H/HT, we analyzed the deformed samples by EBSD. Fig. 4.8 shows the orientation map of a 10% deformed sample. The most favorable orientation for twinning required to accommodate rolling strains is $(110) < 1\bar{1}2 >$ [77]. As documented [78], at the earlier stages of deformation, twinning was typically restricted to a (111) plane. This fact can be clearly observed in Fig. 4.8 where twins were elongated in the grains with (111) and (112) planes (blue and purple colors). On the contrary, the annealing twins in other grains can be distinguished as they were generally singular, wider and elongated in all grain widths. Comparing this observation with Fig. 4.2, we see that some of the twins were present in the as-received structure. To elucidate the orientation relationship between the twins and the parent grains, we prepared two subsets from two different grains. The (111) pole figure of the first subset in the (111) blue grain shows a common pole between the twins and the parent grains. The primary twin in FCC structure exhibits a 60˚ rotation around <111> crystal axis [79]. In order to consider a boundary

as a coherent twin boundary not only should the rotation be correct but also a boundary should coincide with the twinning plane. This will result in having a common pole in (111) PF on the subsets consisting of twins and parent grains. Similarly, this rotation will result in 3 common poles in (110) PF. The second subset in (100) red grain had a slightly different twinning occurrence. As can be seen in the subset region and associated PFs, there was a third orientation between the twin and the parent grain (yellow color). It seems that here the Schmidt factor of the grain was not appropriate for twinning so slip occurred first, and then twinning took place. In addition, the number of twins in this region was not as large as the previous case. Again this could be related to the difference in orientation of the grains. Most of the deformation twins are seen in or near Cu oriented grains (blue and purple colors), which is in accordance with the fact that Cu-oriented grains are the most favorable grains to accommodate the strains with twinning [77,78].

Although some studies report the strong (111)// ND component in rolling texture of FCC alloys [77,78,80], here it is not the case. A very high degree of latent hardening is attributed to the presence and formation of this component [77,78]. Perhaps the reason for the absence of this component in Incoloy 800H/HT TMP is that the twinning deformation is not sufficiently dominant to impose the latent hardening. The absence of this component has also been reported in other materials (e.g. Ag) [77,78]. By comparing various alloys with different SFE, Sekine and Wang [77] claim that the (111) component can only be present in very low SFE materials. In addition, they state that fine twin lamellae, which are responsible for (111) grains formation, are more predominant in very low SFE materials with fine grains. This is clearly not the case for Incoloy 800H/HT. However, TEM observation needs to be done for better clarifying this.

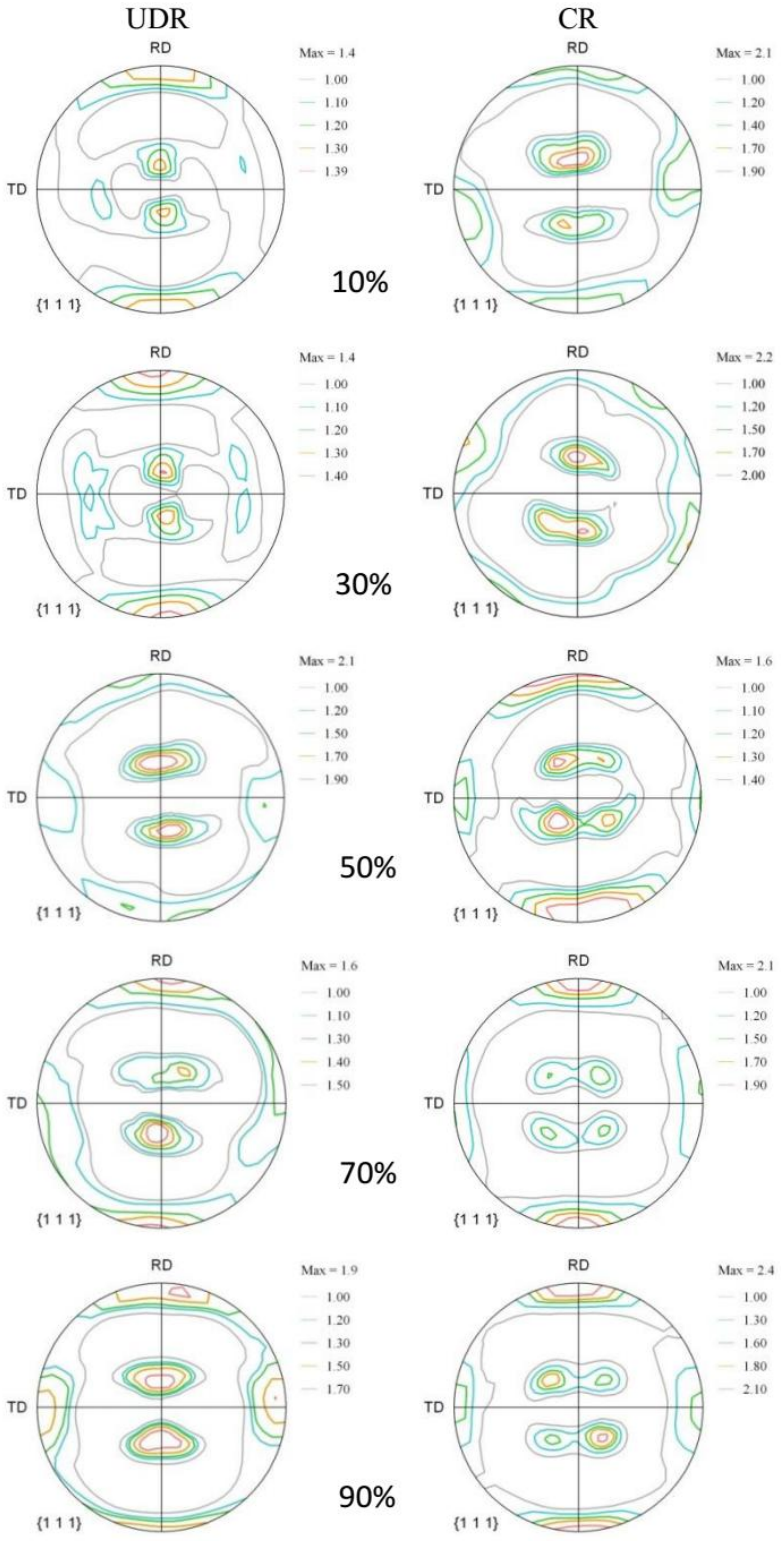

Fig. 4.4. (111) PFs of the CR and UDR samples.

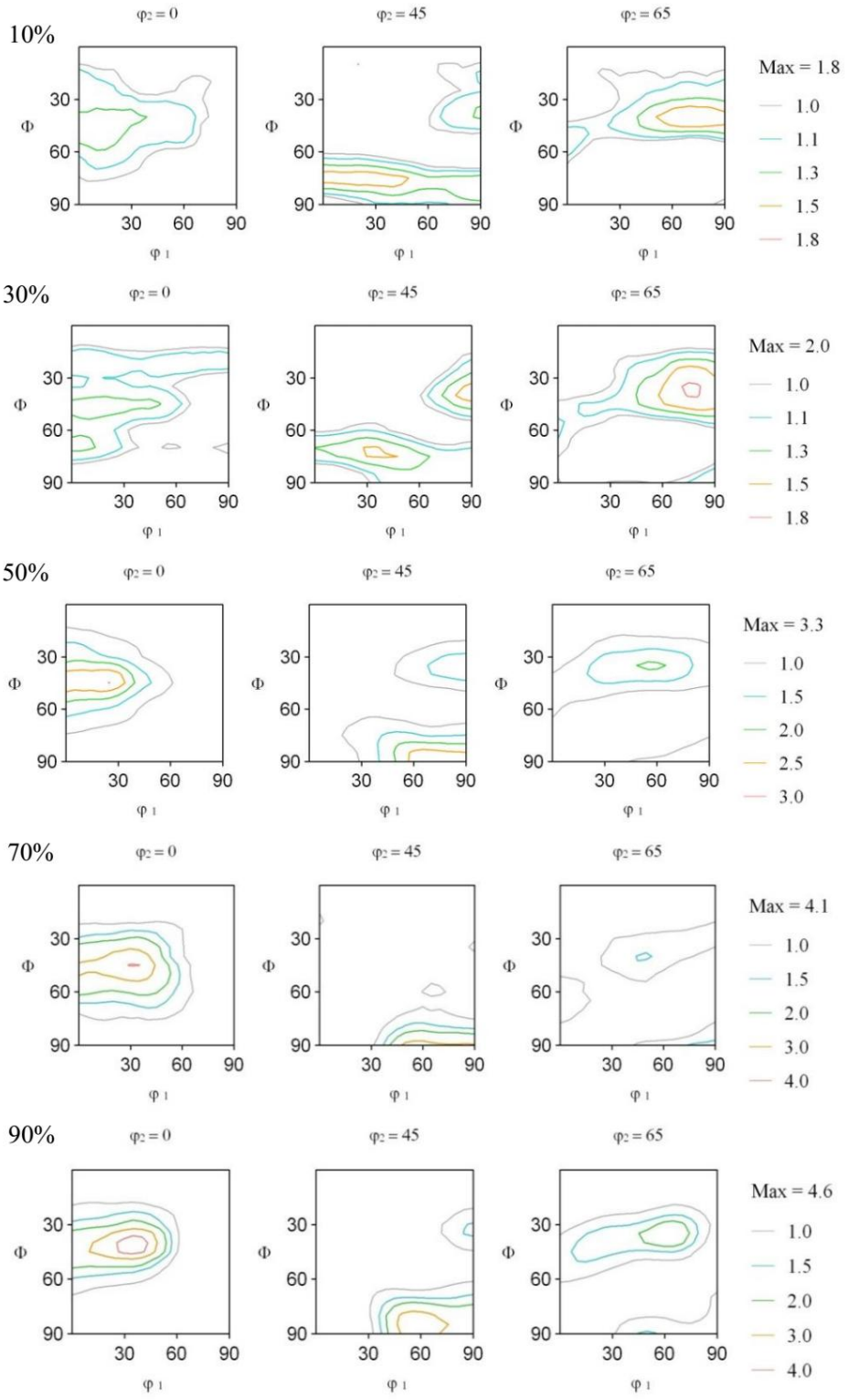

Fig. 4.5. ODF sections at φ_2 = 0, 45 and 65° of the UDR samples.

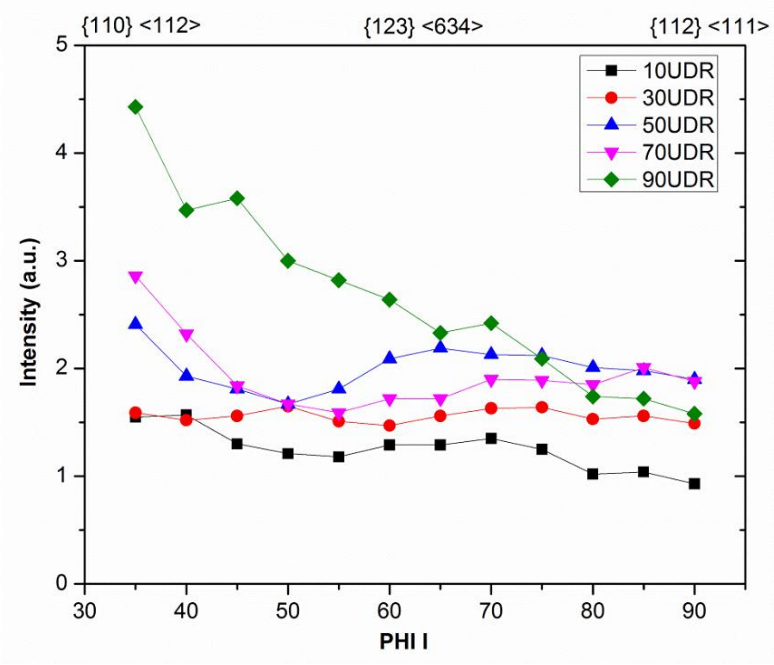

Fig . 4.6. β fibers for the UDR samples.

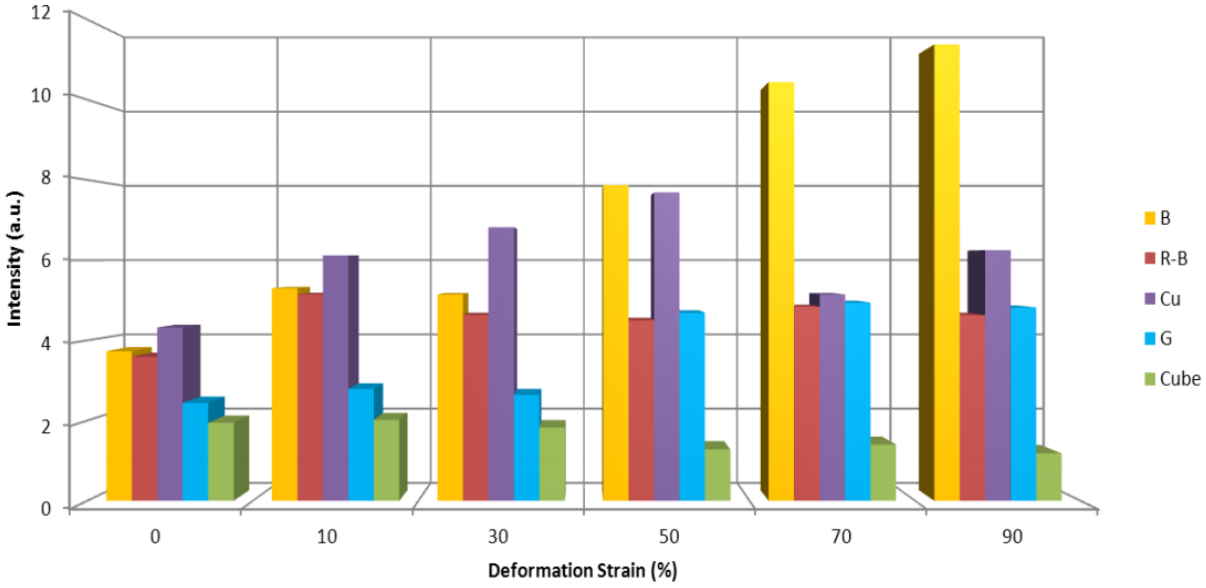

Fig. 4.7. Volume fractions of texture components in UDR samples at different deformation strains.

In contrast to the UDR samples, the CR samples show slightly different texture after the sequential rolling deformation. Fig. 4.9 depicts the ODF sections of CR samples at different rolling reductions. Compared to UDR after 10% reduction, the CR sample shows a strong brass

texture. As the deformation increased, the dominant texture component oscillated between B and B_T. Comparing the φ_2 = 45˚ sections for CR samples, we found that the strength of the texture components gradually moved from B to B_T. Bhattacharjee et al. suggest that the two stable texture components for the cross-rolling deformation would be $(110)<1\bar{1}2>$ (B) and $(110)<1\bar{1}1>$ (ND rotated B) [69]. Upon unidirectional rolling, the grains will move to B component [69,93]. By further rotating the strain path around ND by 90˚ in a cross-rolling condition, the rotated B component will be driven. Therefore, the dominant texture of the cross-rolled samples would oscillate between B and ND rotated B.

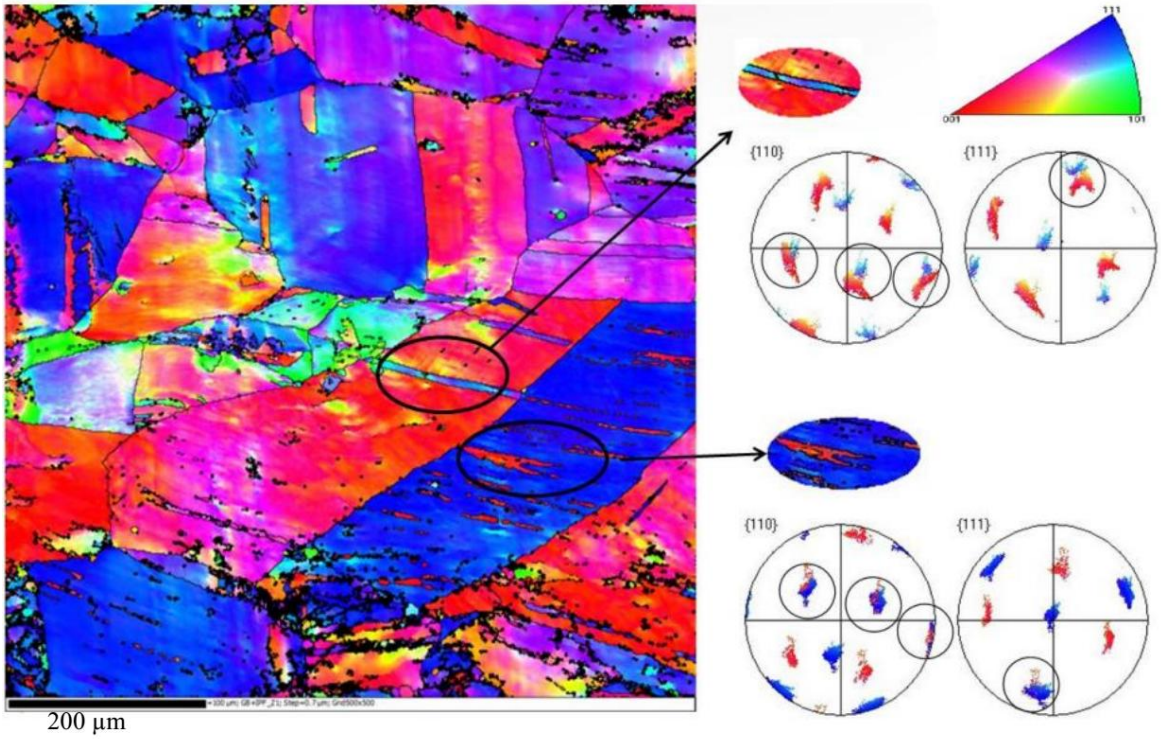

Fig. 4.8. Orientation map of 10% deformed sample showing extensive twinning in (111) grains.

Fig.4.10 shows β fiber evolution in CR samples. Comparing this figure with Fig. 4.6, we observe that β fiber is unstable at CR condition. This result is in agreement with studies by Bhattacharjee et al. [69] and Huh et al.[70], where they observed the same textural differences in CR and UDR samples.

In order to clearly demonstrate texture component changes in CR condition, Fig. 4.11 illustrates the volume fraction of rolling texture components as a function of deformation strain. As discussed earlier, B and B_T components gradually increased in strength while Cu and cube components decreased. G and S components remained almost unchanged. Therefore the deformation texture of Incoloy 800H/HT under the current CR condition at high deformation strains was a combination of B and B_T. After 90% deformation, B_T was the dominant texture. It is noteworthy that, depending on the last rolling path sequence, the final deformation texture of the CR samples at higher reductions is either B_T and Cu_T or normal B and Cu.

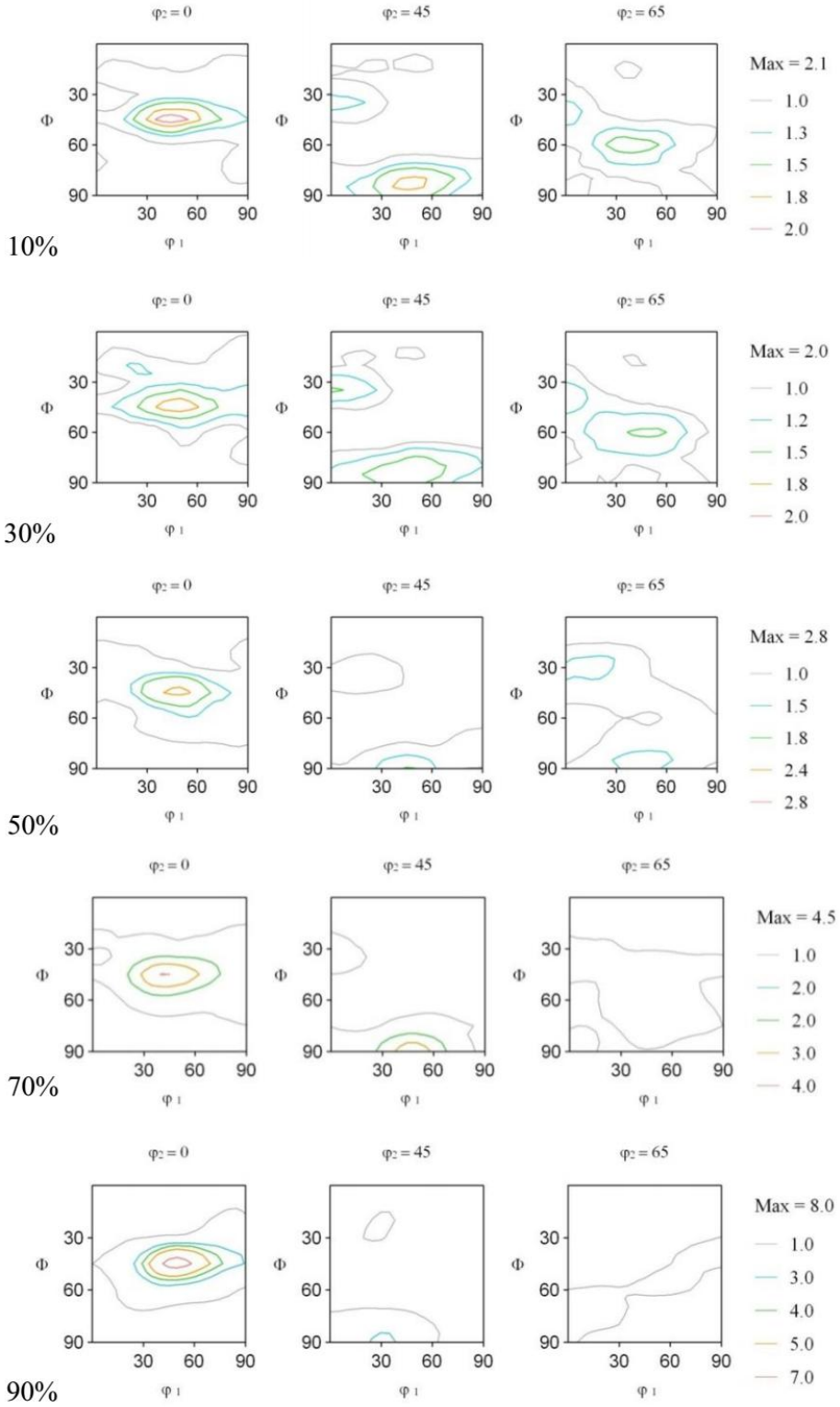

Fig. 4.9. ODF sections at φ_2 = 0, 45 and 65° of the CR samples.

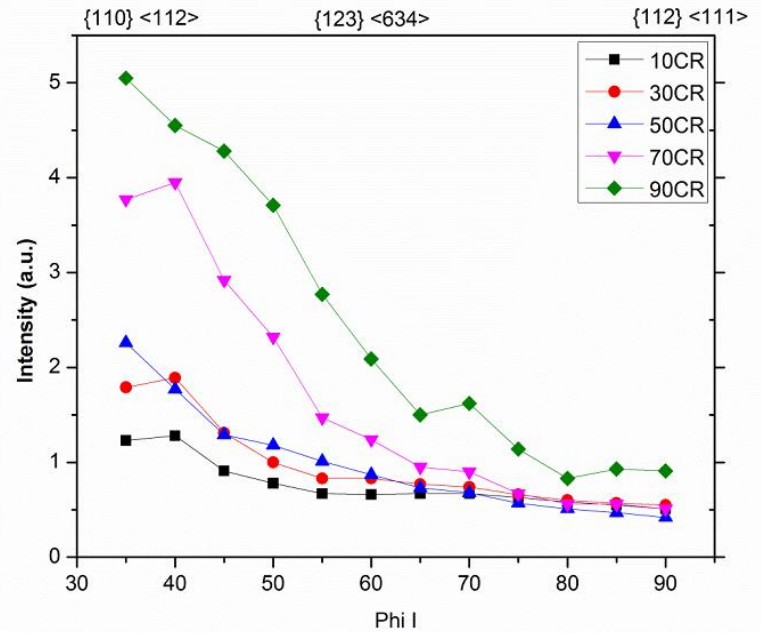

Fig. 4.10. β fibres for the CR samples.

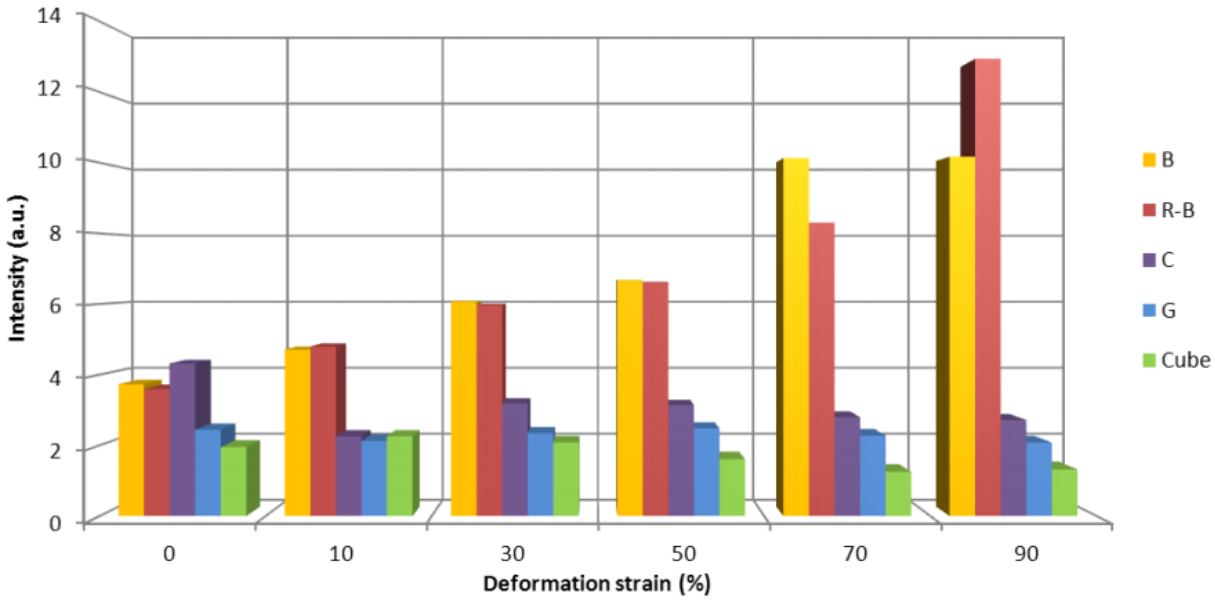

Fig. 4.11. Volume fractions of texture components in CR samples at different deformation strains.

4.5.2. Annealing texture

We measured the textures of both UDR and CR samples after the recrystallization annealing and used a similar strategy to compare the textures. Fig. 4.12 illustrates the (111) pole figure of the

annealed UDR and CR samples (UDRA and CRA). Compared to the deformed samples, the overall intensity of the pole figures was reduced. The PFs of UDRA and CRA samples show no significant differences up to 50% reductions. However in higher deformation regimes (i.e. 70% and 90%), we found sharp changes. These changes are clearer in ODF sections, which are shown in Figs. 4.13 and 4.14. In the annealed samples that were rolled up to 50% before annealing, $(013)<0\bar{3}1>$ and $(212)<0\bar{3}1>$ were the main components, although they are weak. The former and latter components were close to cube and S components, respectively. At low deformation stages, cube texture can be observed. This is in agreement with Sztwiertnia [83] who reports the minor cube component in a recrystallized Ag with low SFE. As noted from the PFs comparison, the main changes in annealing texture of the samples occurred at high deformations (i.e. 70% and 90%). The texture of the 70% UDR annealed sample was similar to the 50% UDR while the maxima were concentrated around G and $(001)<1\bar{1}0>$. By increasing the rolling strain to 90%, the texture was mainly B, G, and Cu with minor $(001)<1\bar{1}0>$ and S components. In contrast, annealed CR samples at 70% and 90% reductions depicted strong B with minor Cu and S components texture. This strong texture is also reported by Zhang and Sekine [94] in annealed pure silver that was cold rolled to 95% and also by Chowdhury et al. [91] in the recrystallization texture of cold rolled 304 austenitic steel. As stated by Chowdhury et al., if the deformation texture was close to brass, due to second order twinning, the recrystallization texture was likely to be close to copper component. It is evident that, depending on the rolling texture of the CR samples, the annealing texture at higher reductions is either B_T and Cu_T or normal B and Cu.

Most of the minor components that were observed in the recrystallized samples, such as $(326)<83\bar{5}>(\{236\}<385>$ known as Recrystallized Brass: R-B), $(013)<0\bar{3}1>$ and $(114)<\bar{1}\bar{2}1>$, could be driven from certain rotations (e.g. 40˚ <111> twin rotations) of the deformed texture components. A detailed discussion on this can be found elsewhere [73,86]. The small differences between the positions of the assigned texture components could mainly be raised from various alloying elements in different studies, as declared by Schmidt and Lucke [86].

To elucidate the texture components differences in annealed UDR and CR samples, we acquired EBSD maps. Fig. 4.15 shows the differences between B and Cu components in the annealed

90%CR and 90%UDR samples. These images were taken to include about 2000 grains to obtain reasonable grain statistics. As illustrated in Figs. 4.13 and 4.14, the texture of 90%UDRA samples is a combination of G, Cu and R-B, while 90%CRA samples exhibit a strong brass texture. The results from macro texture measurements could be validated by micro texture (EBSD) measurement. Fig. 4.15 illustrates the EBSD orientation maps for 90%UDRA and 90%CRA samples highlighting two major components: B and Cu. As shown, the 90%CRA sample has a high number of B-oriented grains (~25%) while 90%UDRA has fewer (~ 15%). However, 90%UDRA exhibits about 23% Cu-oriented grains in contrast with only ~9% in 90%CRA. R-B and G components show similar trends to Cu. The R-B and G oriented grains fraction was about 16% and 12% for UDRA whereas the contribution of these components was reduced to 8% and 6% for the 90%CRA sample. Therefore, as a result, two different annealing textures have formed upon rolling after different strain paths.

The retention of B component in recrystallization texture is reported in other studies on austenitic steels [81,85]. This texture retention could be attributed to nuclei growing inside the deformation grains, which would result in some B-oriented grains upon annealing [81]. Moreover, it is suggested that homogeneous distribution of deformation in the structure would make no preferable orientation for nucleation. Therefore with random nucleation, rolling texture can be retained [85]. This behavior is only observed for Incoloy 800H/HT CR samples and it could be related to the cross rolling process and its effect on the nucleation and growth. The mechanism of grain nucleation and growth in annealing CR and UDR samples will be discussed in the next chapter.

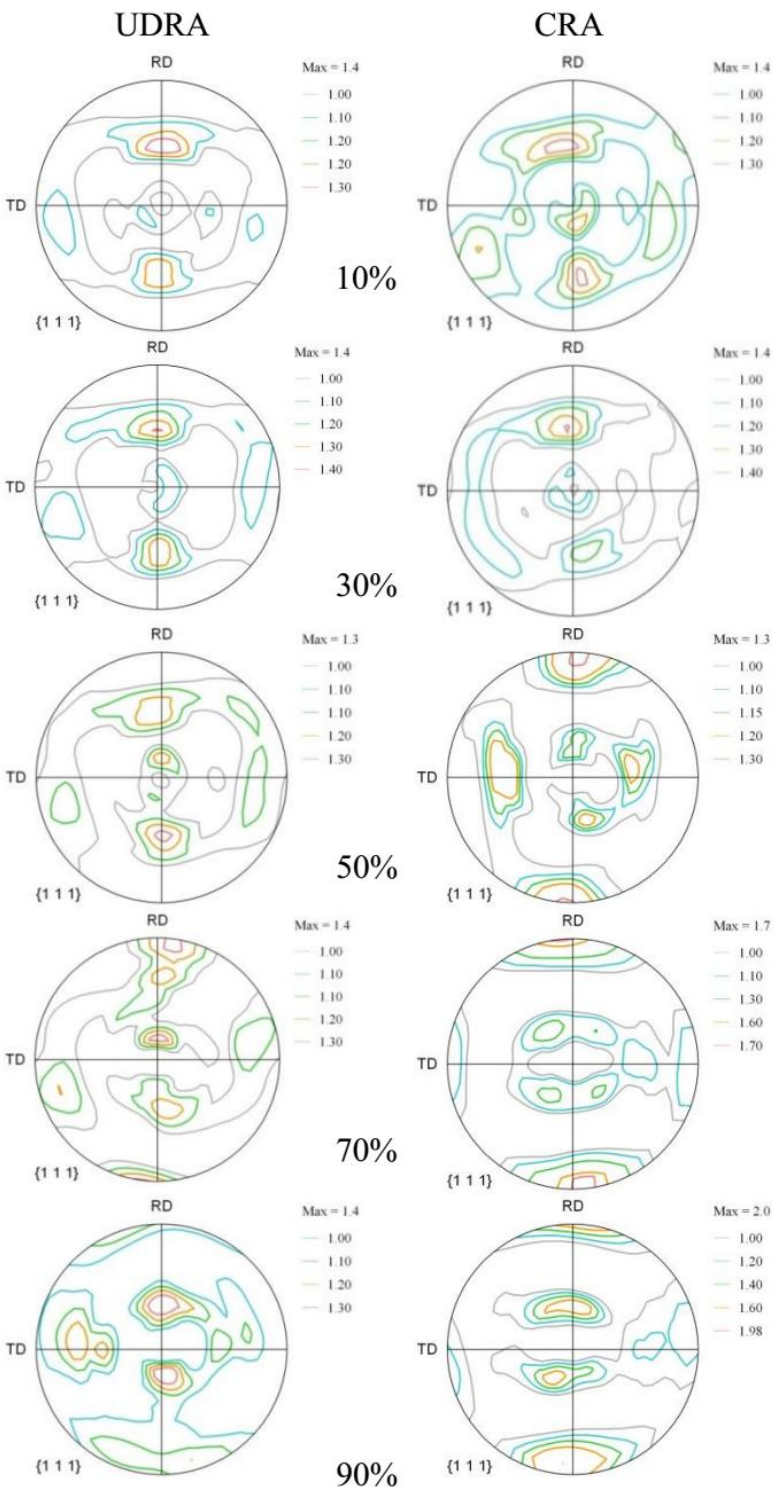

Fig.4.12. (111) PFs of the CR and UDR samples.

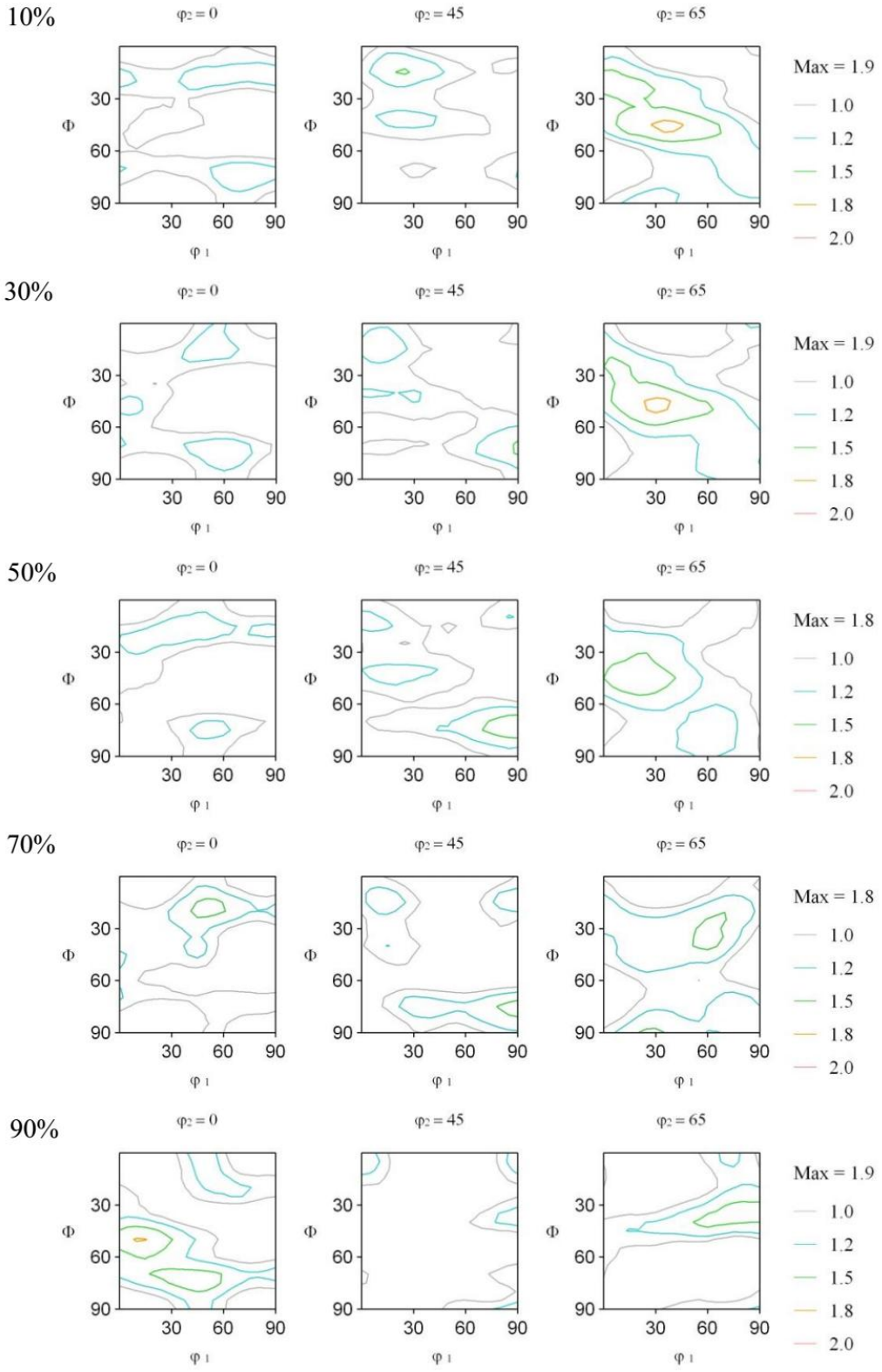

Fig. 4.13. ODF sections at φ_2 = 0, 45 and 65° of the UDRA samples

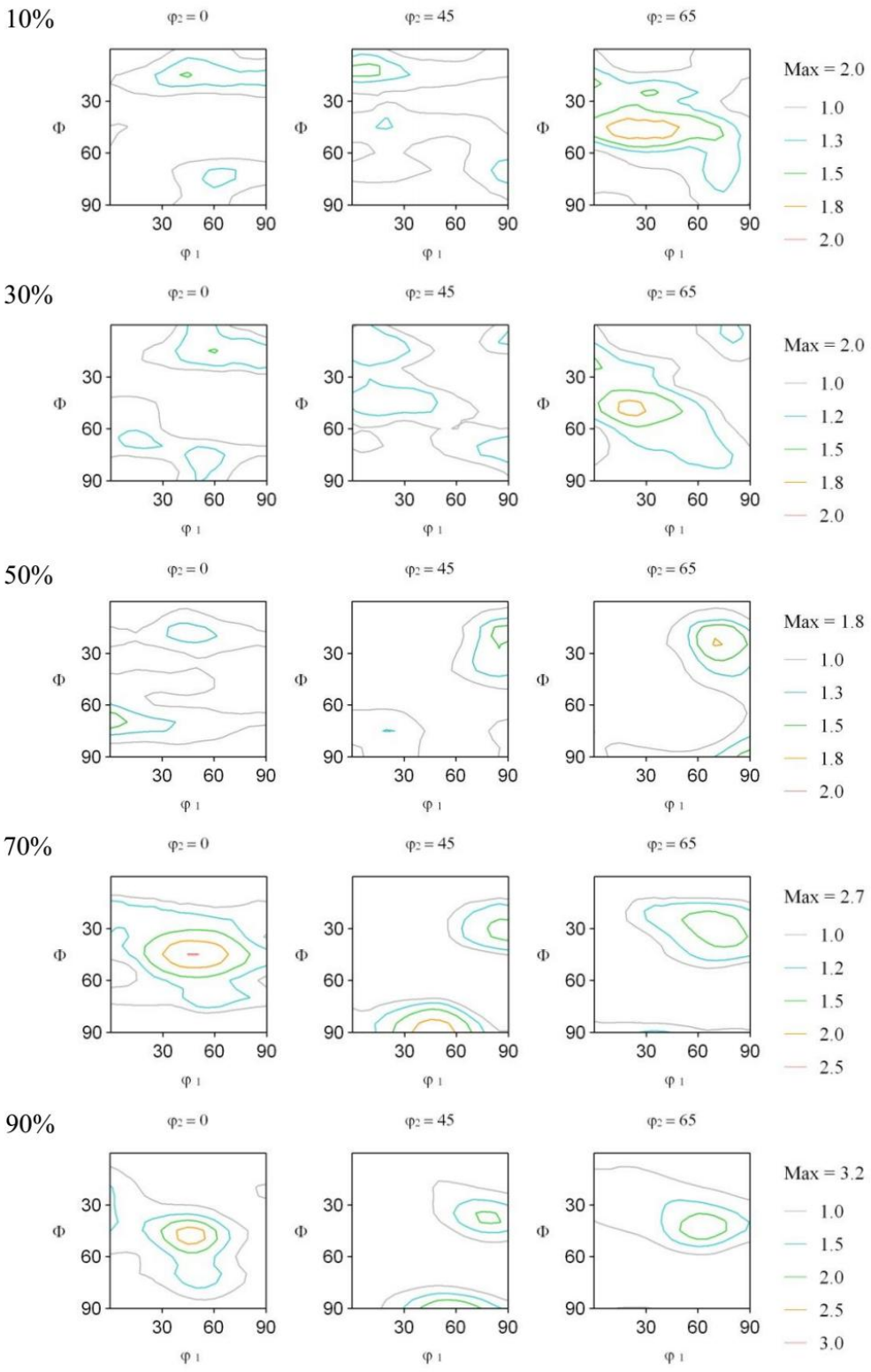

Fig.4.14. ODF sections at φ_2 = 0, 45 and 65° of the CRA samples

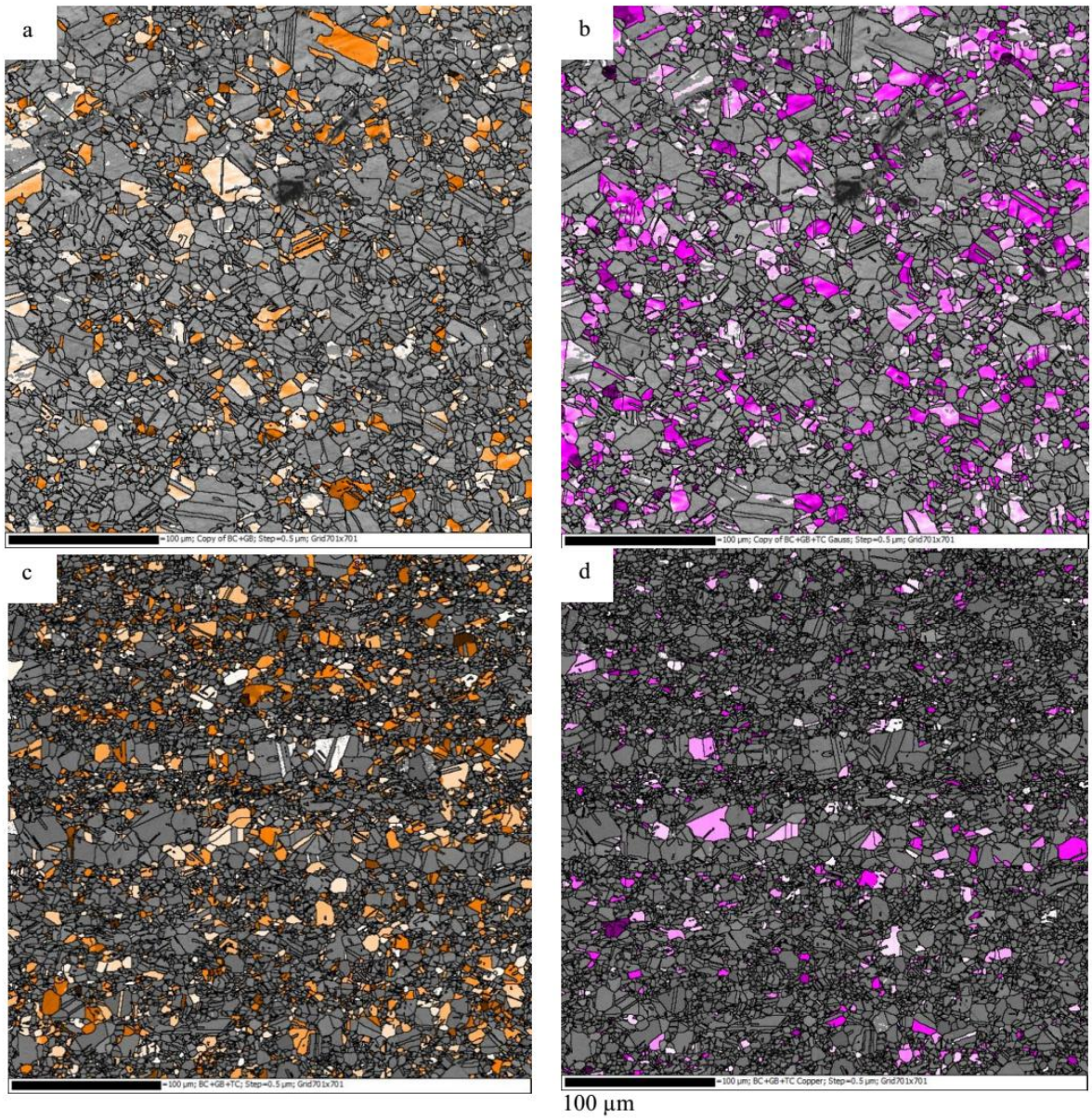

Fig.4.15. Grain orientation maps of a,b) 90%UDRA c,d) 90%CRA samples showing a,c) brass-oriented grains, b,d) copper-oriented grains (TD plane).

The manufacture of Incoloy 800H/HT with different textures would be of great interest to those who design and fabricate with this material. Texture can influence a wide range of material properties including formability, weldability, creep, oxidation and radiation damage [71,75,79]. We are currently investigating the oxidation resistance of the processed samples in super-critical

water and preliminary results indicate that texture optimizing can improve the alloy's oxidation resistance.

4.6. Conclusion

We carried out a comprehensive textural study of the deformed, through various rolling strains with two different rolling modes, and annealed samples of Incoloy 800H/HT. We draw the following conclusions based on our present results:

- The final deformation texture for UDR samples, upon rolling to 90% reduction, was a typical brass texture while the dominant texture of the cross rolled samples oscillated between B and ND rotated B.
- Deformation twinning influenced the texture from the early stages of deformation. Micro texture analysis showed the important mechanisms of twinning and slip. The twinning can be traced at different stages of the transformation of texture.
- The final recrystallized texture depends on the deformation mode applied before annealing: for UDR samples, a combination of G, Cu and R-B textures was dominant, while the recrystallization texture of CR samples after 90% rolling, retained the brass texture. In addition to the texture differences, CR samples have smaller grain size. Randomization of nucleation sites upon cross-rolling is one possible reason.
- The retained B deformation texture in the annealing texture of CR samples at higher rolling reductions is related to a more homogeneous distribution of nucleation sites upon cross-rolling. Detailed studies are performing to elucidate the role of strain path on the nucleation and growth mechanism.

CHAPTER 5

THE ORIGIN OF ANNEALING TEXTURE IN A COLD-ROLLED INCOLOY 800H/HT AFTER DIFFERENT STRAIN PATHS

5.1. Overview of Chapter 5

In the previous chapter, the evolution of deformation and annealing textures of Incoloy 800H/HT via the designed thermo-mechanical processing including different deformation strains and two rolling modes was explained. It was shown that changing the strain path led to a different deformation and annealing texture. The present chapter aims to address the origin of different annealing textures via textural and orientation imaging microscopy (OIM) analyses. Understanding the process of nucleation and growth during recrystallization of this material and the way this process is affected by the local microstructure and texture will contribute to decipher the formation of the final recrystallization texture.

This chapter is presented as manuscript # 4 (The origin of annealing texture in a cold-rolled Incoloy 800H/HT after different strain paths). My contributions to the manuscript are: a) preparation and processing of the samples b) SEM, EDS and EBSD analyses c) Reviewing the relevant literature and writing the manuscript. Majid Nezakat and Ali Sonboli were assisting in analyzing the results.

The manuscript is published in the Materials Science and Engineering A:

- H. Akhiani, M. Nezakat, A. Sonboli and J. Szpunar, “The origin of annealing texture in a cold-rolled Incoloy 800H/HT after different strain paths”, Materials Science & Engineering A 619 (2014) 334-344.

The references for this chapter along with references from other chapters are provided at the end of the thesis.

The copyright permission to use the manuscript in the thesis was obtained and provided in the Appendix section. The references for this chapter along with references from other chapters are provided at the end of the thesis.

The origin of annealing texture in a cold-rolled Incoloy 800H/HT after different strain paths

Hamed Akhiani, Majid Nezakat, Ali Sonboli and Jerzy Szpunar

Department of Mechanical Engineering, University of Saskatchewan, Saskatoon, Canada

5.2. Abstract

In this paper, we examine the nucleation and growth behavior of a highly deformed Incoloy 800H/HT. We also investigate the effect of rolling path (i.e. unidirectional and cross rolling) on the recrystallization mechanism and subsequent annealing texture of Incoloy 800H/HT. We used micro and macro texture measurements to investigate the evolution of texture components in various nucleation and growth stages. We studied the recrystallization kinetic by means of isothermal transformation plots based on recrystallized and softened fractions drawn from orientation imaging microscopy and micro hardness measurements.

Results show that the recrystallization kinetic after Cross Rolling (CR) is slower than after the Uni-Directional Rolling (UDR) deformation. Due to different nucleation and growth mechanisms, these samples showed different recrystallization textures. CR samples exhibited a strong brass recrystallization texture while UDR samples showed a combination of Goss, copper and recrystallized brass $(326)<83\bar{5}>$ components.

Keywords: Incoloy 800H/HT, annealing texture, cross rolling, oriented nucleation, oriented growth

5.3. Introduction

Researchers have often discussed the deformation and annealing textures of FCC alloys [75,78,79,86,95]. Many studies have focused on the transition mechanism and correlations between the deformation and annealing textures and there is a general agreement on primary factors influencing the recrystallization texture [73,79]. These factors, which determine the orientation of new recrystallized grains, are based on relative differences in nucleation and growth rate of grains during the recrystallization. In fact, nuclei orientations and their growth

rates in the deformed matrix dictate the final recrystallization texture. In other words, the most preferred nucleation or preferred growth of a certain orientation will decide the recrystallization texture. We can find the assumptions on the importance of these processes in the commonly accepted models, which describe the recrystallization textures known as oriented nucleation and oriented growth models [79,96]. The former model states that a certain orientation that has higher nucleation kinetics will dominate the recrystallization texture. The latter model emphasizes a higher growth rate of a certain orientation in the recrystallization stage. According to this model, the recrystallization texture is determined by the component that has the faster growth kinetic. Indeed, after the recrystallization, the texture may still change upon further grain growth [73,79].

Despite all controversies, scientists commonly accept that the deformation texture influences the recrystallization texture. Deformation texture of FCC materials depends strongly on Stacking Fault Energy (SFE), initial texture and microstructure, purity of the material, strain amount, path of deformation and temperature [68,75,78,79,95]. Consequently, deformation-processing parameters like the strain amount and path also influence the final deformation and subsequent annealing textures. The classic example is the effect of strain path in reversing uniaxial deformation, known as the Bauschinger effect [95]. Indeed, changing the strain path can also be done by changing the rolling direction in deformation processes. Accordingly, various rolling methods were employed to study the effect of strain path on the texture and microstructure of the produced sheets [68,95]. Two-step, multi-step, and pseudo cross rolling, clock, reverse and angular rolling are among these methods [68,95]. In fact, altering the texture of a material through the manufacturing process could be of great interest for secondary processing steps. Changing the aluminum texture for deep drawing process to avoid the earing problem, is the well-known industrial example [75,95]. Moreover, different rolling paths could influence the special grain boundaries after recrystallization [95]. A higher fraction of these special boundaries can efficiently enhance the materials mechanical and physical properties [18,79]. Therefore, many attempts have been made to utilize the strain path alteration for obtaining a desired texture in a wide range of materials, particularly for new engineering applications [68,69,95,97]. One of the new challenging applications is development of structural materials that can be used in the future generation of nuclear reactors known as Gen IV [1]. According to Gen IV road maps [1,4], Incoloy 800H/HT is one of the promising materials for use as both cladding and structural

components of these reactors. Incoloy 800H/HT is a variant of a well-known Incoloy 800 super alloy family, which has excellent high temperature properties [1,4,12,67]. Indeed, construction of different parts and components requires a comprehensive knowledge of the alloy formability. As the texture and anisotropy strongly influence the formability of an FCC material [98], it is important to characterize the different textures that can be obtained from various manufacturing routes. This will allow manufacturers to select the appropriate texture for the secondary forming/processing step, such as pilgering or extrusion in making fuel cladding.

Our previous study examined the effect of strain amount, with two rolling methods, on the deformation and annealing textures of Incoloy 800H/HT [97]. We show that changing the strain path led to a different deformation and annealing texture. We also obtained same grain structures having different textures by applying cross and unidirectional rolling. In fact, it would be very useful to isolate the effect of texture from microstructure, since altering the texture through common processes inevitably changes the microstructure [95]. However, we were to address the differences in annealing textures there [97]. Thus, in the present study, we investigated the origin of different annealing textures via textural and Orientation Imaging Microscopy (OIM) analyses. Understanding the process of nucleation and growth during recrystallization of this material and the way this process is affected by the local microstructure and texture will contribute to decipher the formation of the final recrystallization texture. From a technological viewpoint, we aimed to explore the origin of recrystallization texture in differently rolled Incoloy 800H/HT in the present study.

5.4. Experimental procedure

We used a commercial Incoloy 800H/HT from Special Metals Co. in this study. Table 1.4 shows in detail the alloy composition of Incoloy 800H/HT. We cut samples with the dimensions of 50x50x13.25mm and 50x25x13.25mm from the same plate and subjected them to Uni-Directional Rolling (UDR) and Cross Rolling (CR), respectively. We used a laboratory roll machine to perform deformation up to 90% reduction. The rolling modes are described in detail in references [95,97]. In order to study the nucleation and growth behaviors, we annealed the 90% deformed samples at discreet periods of time (5, 10, 30, 60, 120, 240, 480 and 960 seconds) at 1050° C, and then subjected them to macro and micro textural studies to reveal the recrystallization texture evolution. We employed a Bruker D8 diffractometer utilizing Eulerian

cradle and 2D detector to measure the macro texture. We acquired diffraction patterns with a Cr Kα target with a 0.8 mm collimator. We used incomplete pole figures to calculate Orientation Distribution Function (ODF) as well as the texture components, by means of ResMat® software. The micro texture measurements were carried out using an Oxford Electron Back Scatter Diffraction (EBSD) setup fitted on a Hitachi SU6600 Field Emission Gun Scanning Electron Microscope. We operated the SEM at 30 kV with the automatic EBSD scan and EBSD was performed on the TD plane as the planar features of cold-rolled microstructures can be better detected in this plane than any others. We utilized HKL software to extract and analyze the EBSD data. For XRD and EBSD measurements, samples were mechanically polished and then subjected to vibratory polishing using a Beuhler Vibromet® with 0.04 Silica to remove the deformation layer.

We calculated the volume fractions of various texture components within 15˚ tolerance around their ideal position in the Euler space both in micro and macro textures. We made both of these measurements on the TD plane of the samples. We employed a Mitotoyu Vickers micro hardness tester with 200gf to measure the softened fractions upon recrystallization. We used an average of 10 points to determine the hardness of each sample. We explored the recrystallization kinetics, employing two different methods for calculation of recrystallized fractions. In the first method, we obtained the recrystallized fraction from EBSD maps considering that a grain orientation spread threshold equal to 1˚ characterizes the recrystallized structure. The recovered and deformed fractions were also distinguished by assuming an internal misorientation threshold of 6.5˚. Other researchers have previously used these threshold values [81,96]. The second approach was the classic hardness measurement method, in which we derived the recrystallized fraction from Vickers micro hardness measurements [85].

5.5. Results

5.5.1. Macro texture

ODF presents comprehensive texture data that offer a quantitative comparison between different textures [95]. Therefore to compare the textures of different samples, we used the three important sections of ODF. The ODF sections at φ2 = 0, 45 and 65˚ were selected since they demonstrate the common FCC deformation and annealing texture features; α, β fibres and S component. As

we showed in our previous paper (chapter 4) [97], both macro (XRD) and micro (EBSD) textures of Incoloy 800H/HT show a weak texture with no preferred orientations.

Fig. 5.1 shows the texture evolution of the UDR samples after different annealing time periods. The starting deformed sample (0s) exhibited strong brass (B) deformation texture with minor Goss (G) component. This texture remained almost intact, as annealing time increased to 10s. However, after 20s annealing, the ODF (texture) intensity decreased dramatically, which marked the start of recrystallization. By increasing the annealing time from 20 to 60s, the brass component was progressively decreased. While the brass component decreased, upon the annealing, Goss (G) and copper (Cu) components formed, particularly at this time period (20-60 s). This trade-off trend suggests that recrystallization had started in this period. We performed the micro texture analysis in order to validate this, and will discuss it later in section 3.2. The texture of the samples after 60s remained almost identical considering the intensity and texture components. Consequently, after 960s, the Cu became the dominant annealing texture component. Indeed, minor G and a trace of B components could still be observed at that point.

Fig. 5.2 illustrates the texture evolution of the CR samples with different annealing time periods. The deformed CR sample (0s) showed a strong B texture, which is slightly shifted towards ND-rotated brass ($(110)<1\bar{1}1>$). As in the UDR samples, before 30s, the texture had no major change in both component positions and intensity. However from 30s, the ODF intensity dropped and remained almost the same up to 960s. Unlike the UDR samples, no new texture components formed upon recrystallization in the CR samples, although the intensity decreased by half. As a result, after 960s annealing, B component was still the dominant texture in the recrystallized sample. It seems that the annealing texture of the CR samples was a weakened deformation texture. In other words, the deformation texture of CR samples was retained following all annealing stages.

Fig. 5.3 elucidates the evolutions of various texture components in all samples. In UDR samples, B component was dominant up to 10s of annealing; however as annealing time increased this component dramatically weakened and Cu gradually intensified. The other intensifying component was $(326)<83\bar{5}>$ or $(236)<\bar{2}\bar{5}3>$, also known as recrystallized brass (Rex-B). The intensity of Rex-B was higher due to its having the highest multiplicity factor compared with the rest of the components. Therefore, as its intensity is irrational, only this evolution trend should be

considered for comparison with the other ones. As Fig. 5.3 shows, the Rex-B, like Cu, intensified just after the B component weakened.

In the CR samples, the component evolution trend was different to some extent. First, the overall intensity of the CR deformed texture components was lower than in the deformed UDR (about ~ 25%). The ND-rotated brass (R-B) was stronger in CR samples due to the nature of cross rolling which has applied to the samples. In addition, G component was stronger in UDR samples, particularly before starting the recrystallization (<10s). This can also be observed from the $\varphi 2 = 0$ section in Figs. 5.1 and 5.2.

Although the CR sample showed a similar drop in the overall intensity after 10s, the drop was smaller than the UDR samples: about 20% and 40% descent in the intensity of B component in CR and UDR samples respectively. Unlike the UDR samples, Rex-B component had not changed significantly in the CR samples, even after longer annealing times. Consequently, B with ND-rotated B (R-B) components were the final annealing textures for the CR samples.

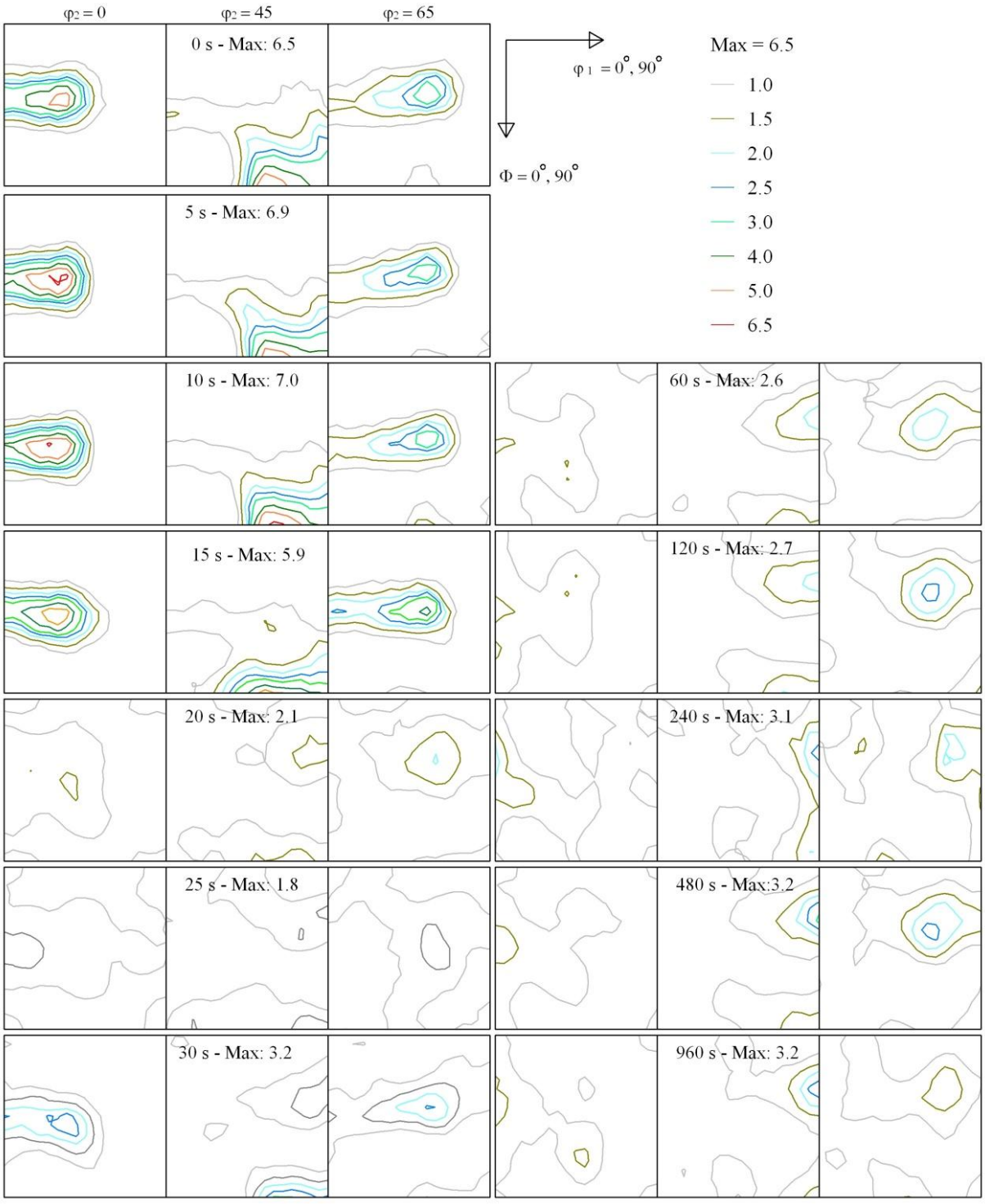

Fig. 5.1. ODF evolution of the UDR samples as a function of annealing time.

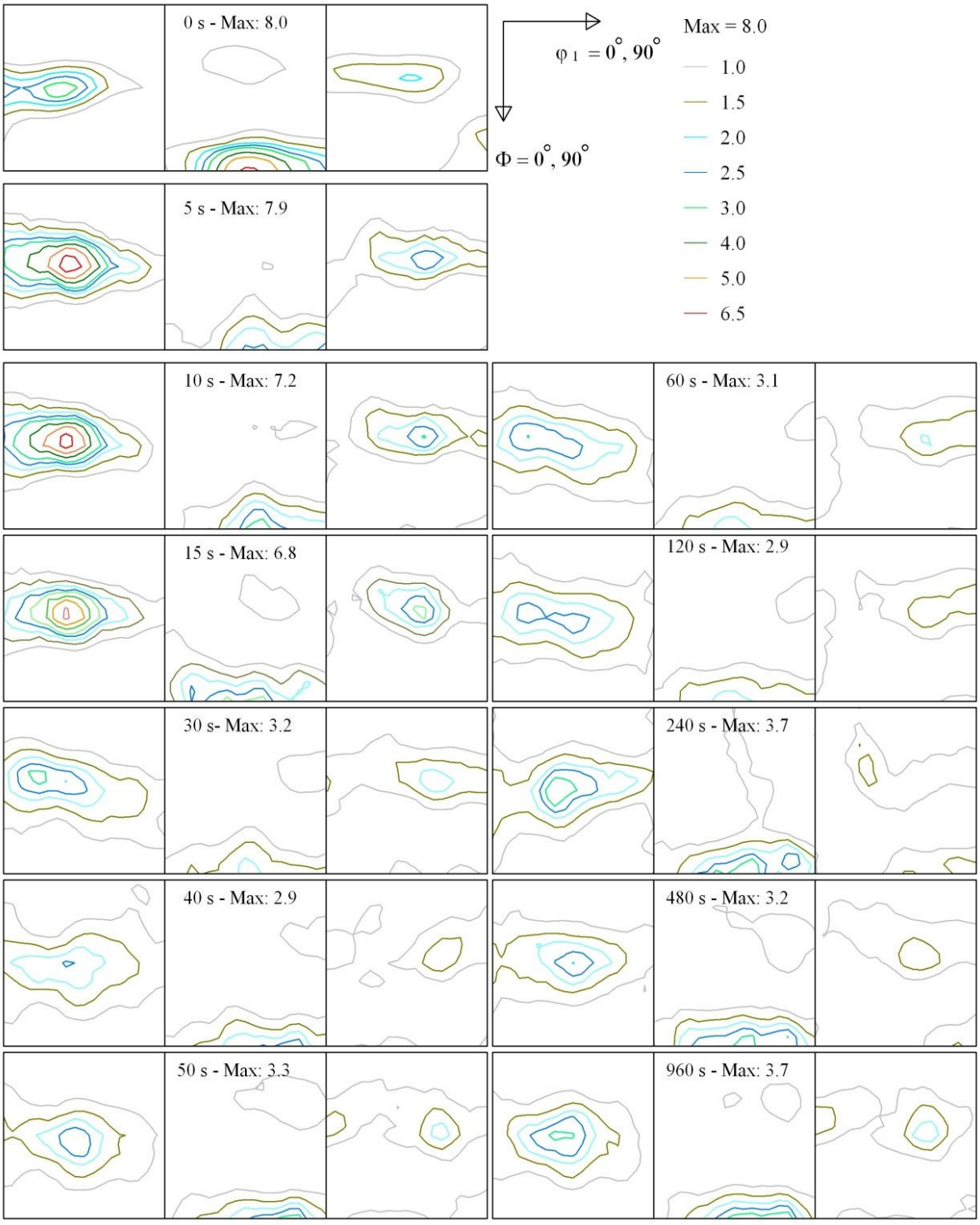

Fig. 5.2.ODF evolution of the CR samples as a function of annealing time.

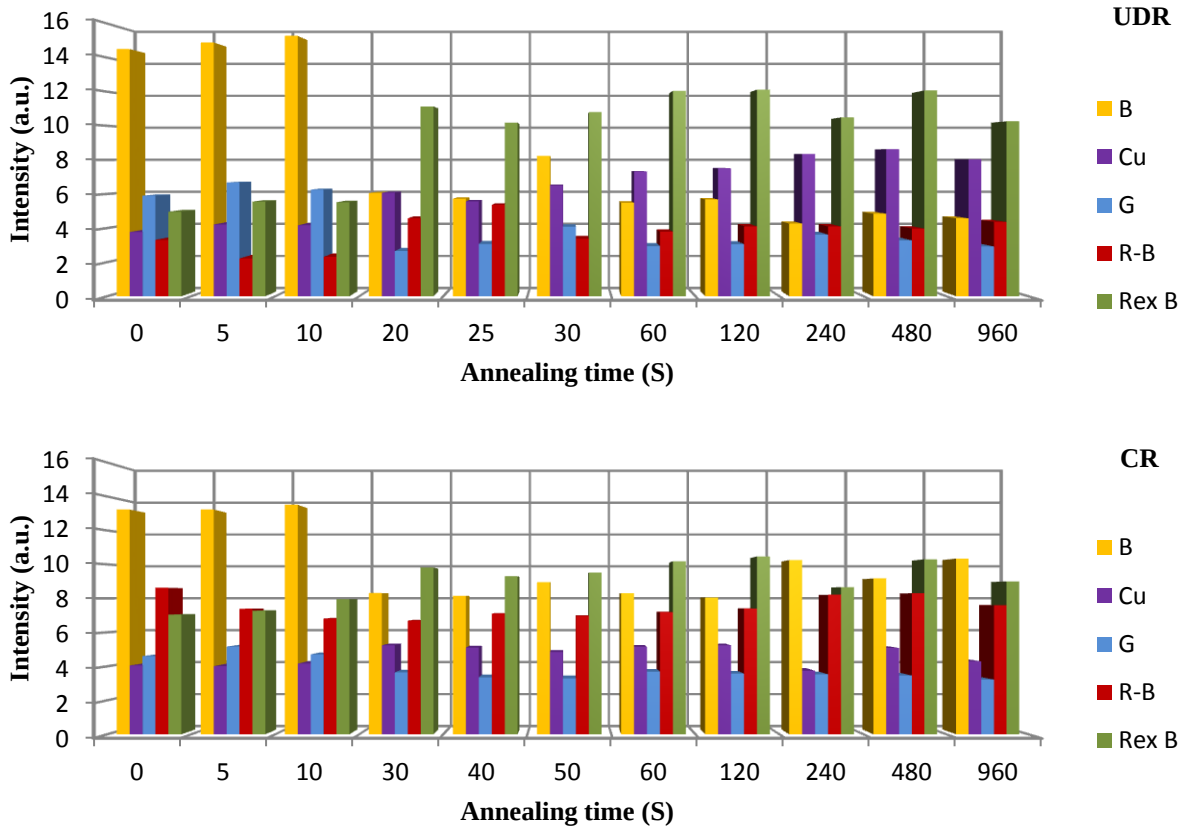

Fig. 5.3. Texture components of the a)UDR and b)CR samples as a function of annealing time.

5.5.2. Micro texture

All the samples were subjected to EBSD to investigate the nucleation and growth stages. Selected EBSD maps including B, G and Cu components are shown in Fig. 5.4 (UDR) and Fig. 5.5 (CR). After 30s, the microstructures of UDR and CR samples showed recrystallized grains with different grain size distributions. As we increased the annealing time, the grain sizes increased. At higher annealing times, coarse annealing twins appeared. These features were in common for both UDR and CR samples. However, the grain sizes of the CR samples were smaller than those in the UDR samples in each time period. The interesting differences are apparent when comparing the texture components. As shown in Fig 5.4.a, the UDR sample contained a combination of B, G and Cu texture components. Quantification of these components shows that Cu was the dominant one while B was the lowest. This trend remained nearly similar for the UDR-60s sample, although the grain size was smaller. Indeed, Fig. 5.4.c

shows the transition stage between the deformed and the recrystallized states in the UDR-10s sample. The elongated deformation grains showed strong G and B textures, while Cu and some G components appeared in deformation twins and shear bands regions, as marked by arrows. Fig. 5.4.d. illustrates the fully deformed UDR sample, which showed B and G textures. It is noteworthy that, due to high strain in the 90% deformed samples, many regions could not be indexed well (index rate ~ 45%). However, the indexed regions still reveal the deformation texture components. Two indicated subsets from different regions are shown in Figs. 5.4.e and f. The main deformation textures were B and G, which is in agreement with the macro texture measurements in Fig. 5.1.

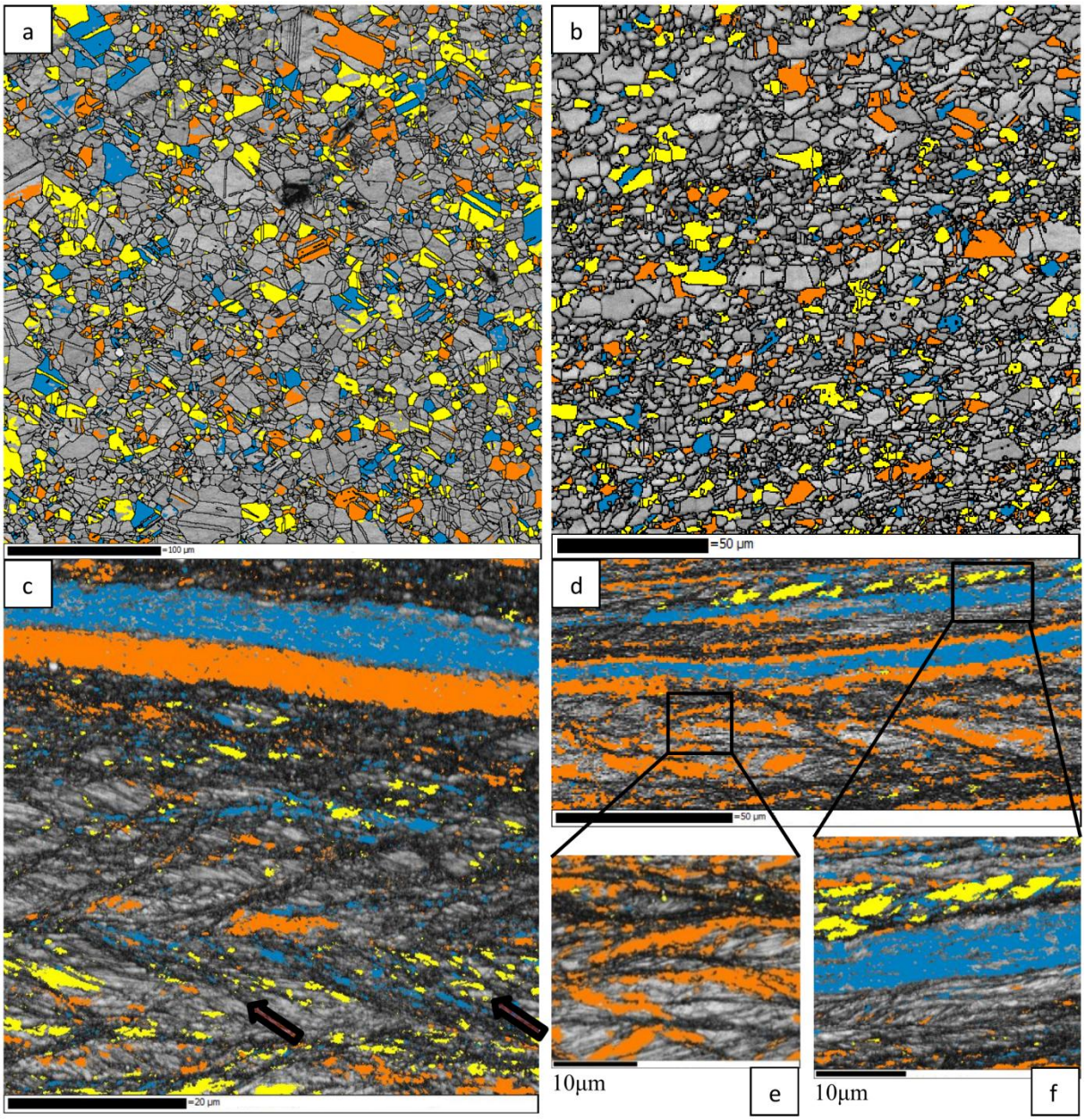

Fig. 5.4. EBSD maps showing the brass (orange), Goss (blue) and copper (yellow) components in UDR samples. a) 240s, b) 60s, c) 10s, d, e, f) deformed.

Fig. 5.5 illustrates the evolution of the microstructure and texture components in CR samples. Figs. 5.5.a and b demonstrate the microstructure and micro texture of the CR samples after 240s and 60s annealing. CR-240s (Fig. 5.5.a) exhibited a strong brass texture and CR-60s showed a similar components distribution with smaller grain size. The brass grains were dominant at both annealing times, which is in agreement with XRD macro texture measurements (Figs. 5.2 and 5.3.b). The 10s annealed sample showed a deformed micro structure with some small

recrystallized regions. Figs. 5.5.d and e illustrate the 90% CR fully deformed sample, which showed a deformed microstructure with mostly brass-oriented grains.

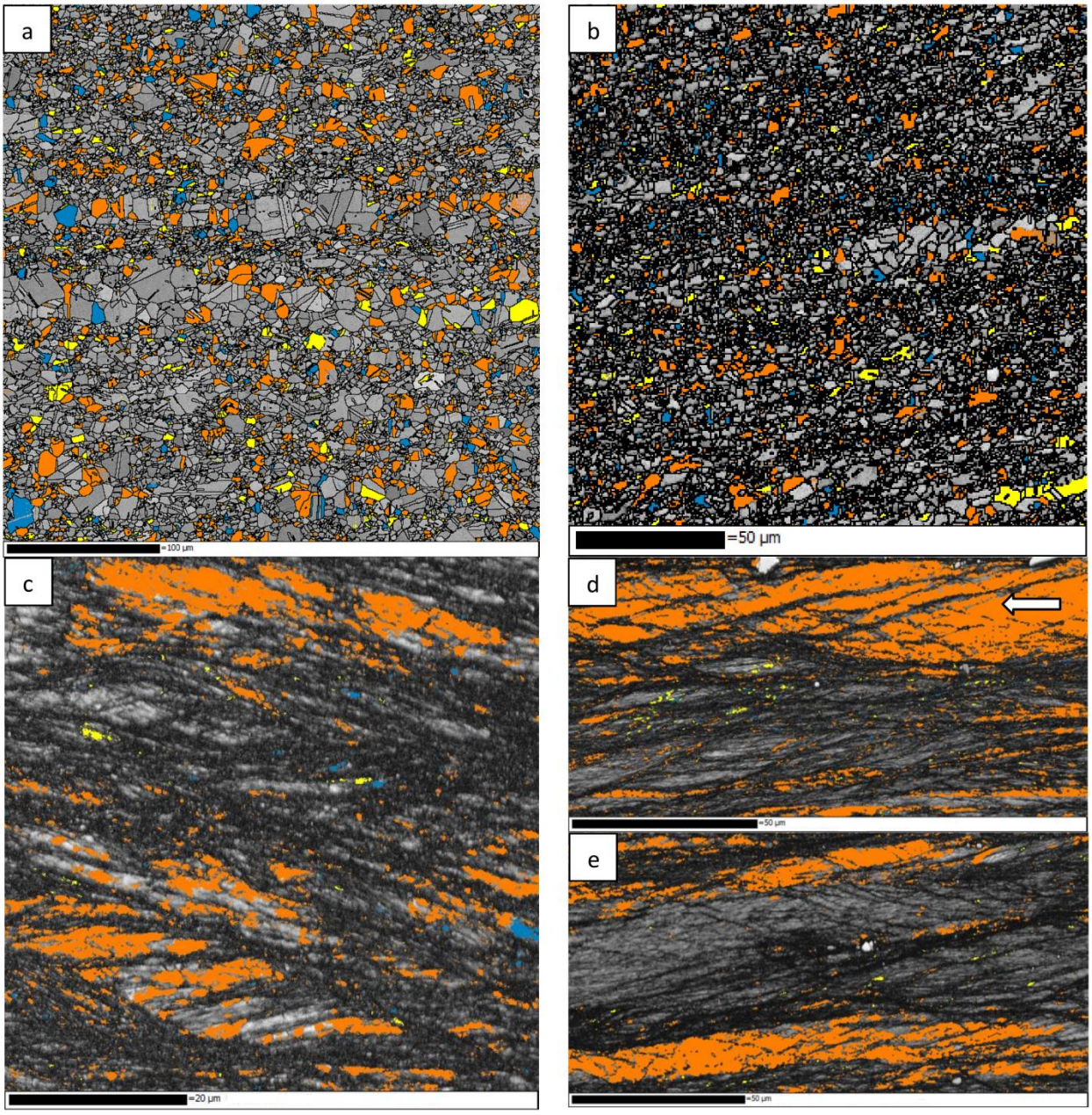

Fig. 5.5. EBSD maps showing the brass (orange), Goss (blue) and copper (yellow) components in CR samples. a) 240s, b) 60s, c) 10s, d, e) deformed.

As mentioned before, due to high deformation strain and high stored energy in 90% rolled samples, the image quality (IQ) and indexing percentage are not ideal. Our previous study shows there is no major difference in reductions between 70% and 90% in terms of texture components

[97]. Therefore, to elucidate the deformation microstructure and texture differences between UDR and CR samples more clearly, EBSD maps of 70% rolled samples are shown in Fig. 5.6. The 70% UDR sample exhibited a combination of (111) and (110) // ND grains while the CR sample mostly showed (110) grains. This is also in agreement with 90% deformed samples. Section 5.6 presents a more detailed discussion.

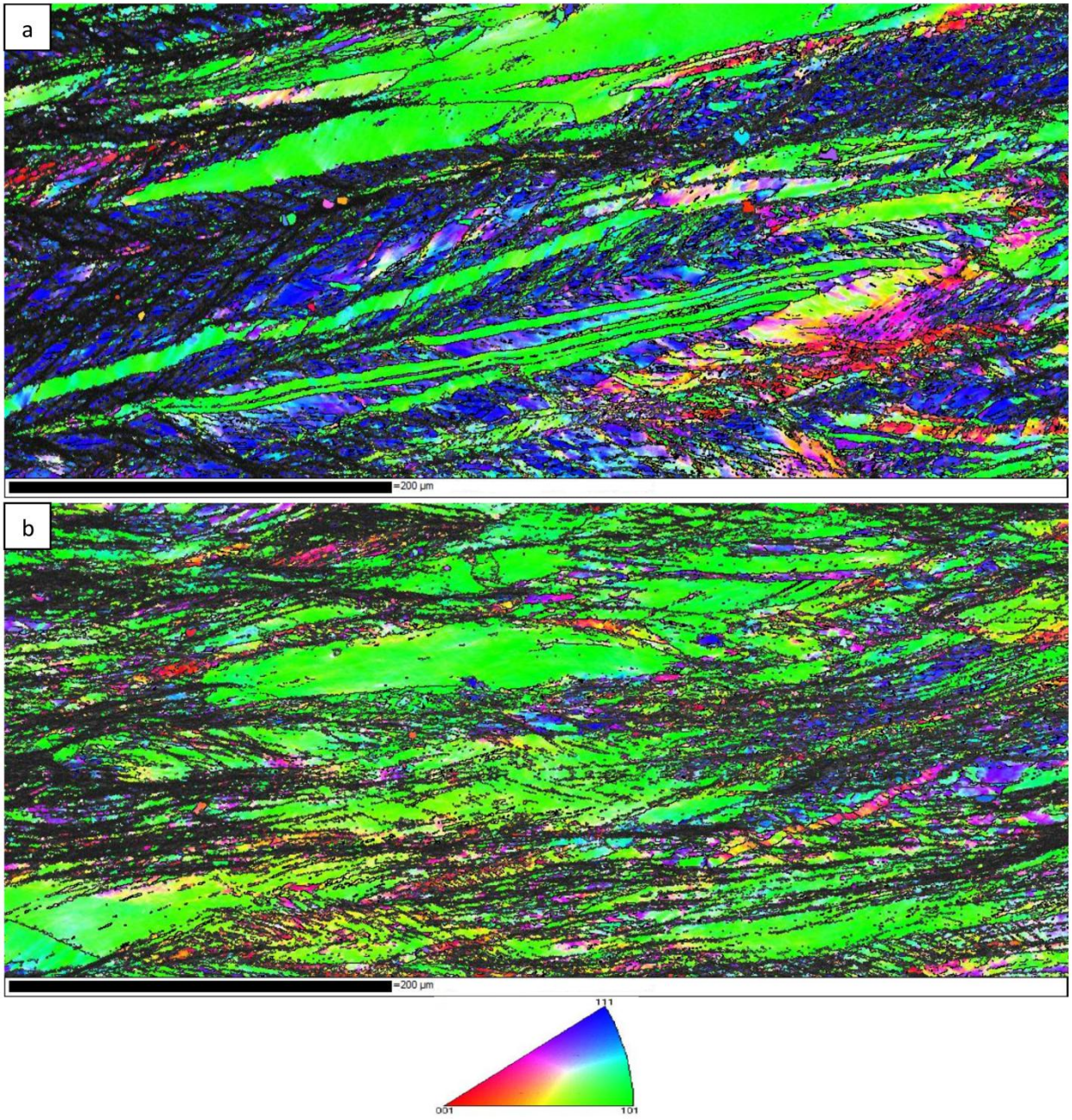

Fig. 5.6. ND-IPF EBSD maps of 70% deformed samples a) UDR, b) CR.

5.5.3. Recrystallization kinetics

Fig. 5.7 illustrates the recrystallization kinetics during annealing treatment at 1050˚C, which we analyzed with two different methods. There is good agreement among the curves produced by the different methods and all four curves roughly depict a typical Johnson-Mehl-Avrami-Kolmogorov (JMAK) curve. The fast kinetics observed here are in agreement with those of similar alloys at the same temperature [85]. The recrystallization kinetic of the CR samples was slower than the UDR samples. Although it appears that the beginning of recrystallization is about the same for both UDR and CR samples, Fig. 5.7 shows a lower slope for the CR sample, which indicates a slower recrystallization rate compared with the UDR samples.

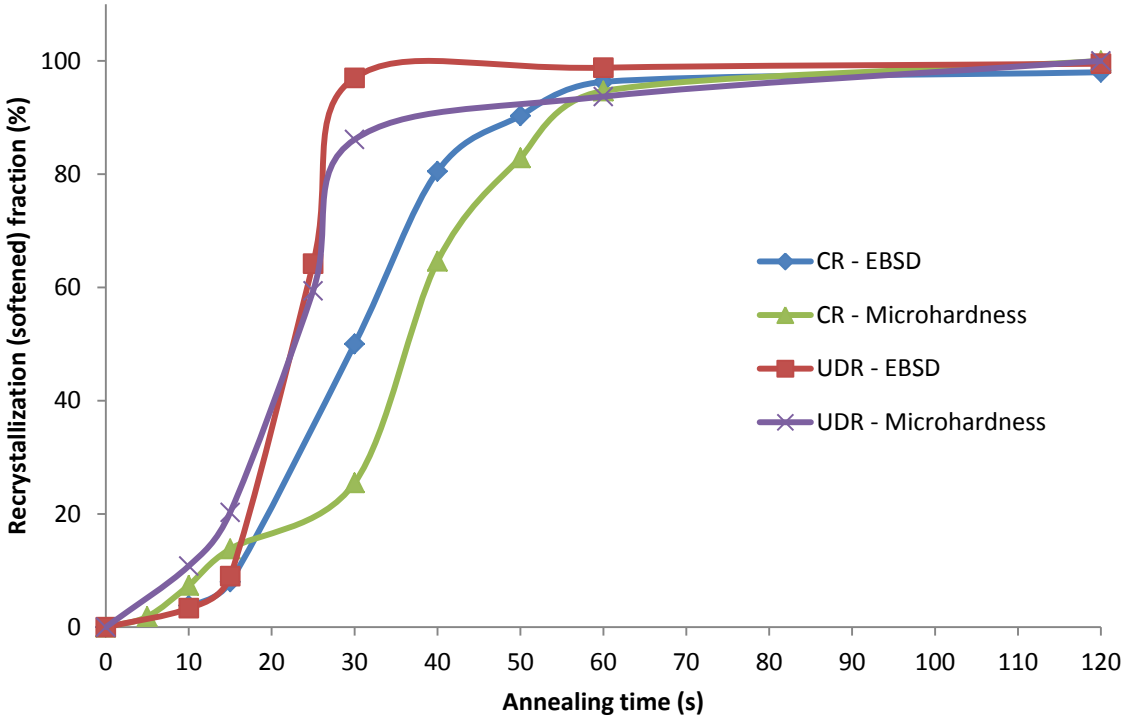

Fig. 5.7. JMAK curves for UDR and CR samples with the recrystallization (softened) fractions were obtained based on EBSD and micro hardness.

5.6. Discussion

In our previous study, the effect of rolling path on the deformation texture of Incoloy 800H/HT is discussed in detail [97]. However, we were unable to address the differences in annealing textures. Therefore in the present study, we firstly aimed to analyze the texture evolution of

Incoloy 800H/HT from the deformed to the annealed states. Figs. 5.1 and 5.2 depict the aforementioned texture evolutions for the UDR and CR samples, respectively. By comparing these two figures, we see that the texture evolutions were different for each of these rolling regimes. Indeed the deformation textures of these samples were different as well. First we focused on the UDR samples. In UDR, the deformation texture was G and B with a trace of γ fibre. However in our previous study, we did not observe the γ fibre from the ND plane macro texture measurement, but in the present study the macro texture measurement from the TD plane reveals a weak γ fibre. This is in agreement with many low SFE FCC rolled textural studies [75,78,99]. Considering Fig. 5.1, after 15s annealing there were no major changes in the intensity or position of the texture components. However, continuing the annealing to 20s, the overall texture intensity diminished, while Cu component appeared. This trend continued in such a way that B and G were consumed as an expense of strengthening the Cu component. To this point, from the ODF intensity and component positions, we can suggest that the recrystallization occurred between 15s and 30s. To validate this hypothesis, the EBSD maps in Fig. 5.4 are useful. Figs. 5.4.a and b illustrate recrystallized grains that formed after annealing for 240s and 60s. The texture components visible in this map are in agreement with their XRD macro texture measurements in Fig. 5.1. Fig. 5.4.c, which shows the 10s annealed sample, is interesting since it shows both B and G deformation grains with fine Cu and G recrystallized grains together. Most of the Cu and G recrystallized grains were formed in the shear bands as indicated by arrows.[2] This map implies that Cu and G components were mainly nucleated preferentially from the shear bands of the deformed matrix. In other words, orientated nucleation could be the primary origin for the recrystallization texture. As confirmed from Fig. 5.1 and Fig 5.4.d, the dominant deformation texture for UDR samples is B and G. Although in some regions Cu grains are also visible, the quantity of these Cu oriented grains was not high enough to be traced in XRD macro texture measurement. As these grains were observed adjacent to G grains, they might be transformed to G upon further reduction, according to Wassermann's theory [76]. This suggestion is in agreement with the volume fraction of the texture components shown in Fig. 5.3.

[2] Due to the EBSD resolution and small size of some of the shear bands/twins, in some cases we are unable to confirm that these are shear bands or twin lamellae. Indeed, shear bands can also contain deformation twins [84]. Although many researchers report the micro twin lamellae and twin bundles formation in low SFE FCC metals [75,77–79], still it needs to be confirmed in the Incoloy 800H/HT with TEM. Therefore, in those cases (e.g. very small features) we use shear band terminology from now on.

The CR samples texture evolution and recrystallization behavior was different. The deformation texture showed a strong maxima in a position between B and ND-rotated B (R-B), which refers to $(110)<322>$ in most of the literature related to cross rolling [69,93,95]. Unlike UDR samples, there was no trace of γ fibre in CR samples. Therefore, comparing Figs. 5.1 and 5.2, we can conclude that the mechanism of recrystallization was different for UDR and CR samples. As depicted in Fig. 5.2, CR samples showed almost no texture component changes through the annealing process. The ODF intensity decreased as recrystallization occurred, though. In other words, CR samples showed deformation texture retention upon annealing. Consequently, B (with a spread towards R-B and $(110)<322>$) presented as the final annealing texture for the CR samples. Fig. 5.5 shows EBSD maps for selected CR samples at different annealing times. Similar to the UDR sample, we suggest that the recrystallization started between 15s and 30s (Fig. 5.2). This assumption is rational since the EBSD maps in Fig. 5.5 validate it to some extent. As Fig. 5.5.c shows, there was no new orientation formation in recrystallization of CR samples, except some minor G and Cu. Indeed the volume fractions of these components were so small they are not visible in XRD macro-texture measurements (Fig. 5.2). It is notable that the morphology of nuclei, seen in Figs. 5.4.c and 5.5.c, is not a typical equiaxed nuclei as it forms for cube texture [79,86,96,100]. Moreover, as suggested by several studies [73,79,86], *nuclei* are the small pre-existing volumes in the deformed matrix rather than the classic thermodynamically defined one. In other words, no new orientations form upon recrystallization except in the case of twin formation [73,79,86]. Burgers [101] was the first to suggest that the recrystallization might start from the crystallite present in the deformed matrix. This hypothesis is now confirmed as dislocation cells, sub grains, deformation and shear bands would serve as heterogeneous nucleation sites [73,79,86]. This definition is in agreement with our results.

Furthermore, comparing the UDR and CR EBSD maps (Figs. 5.4 and 5.5) some interesting differences can be observed. First, there is a remarkable difference between the brass-oriented grains in UDR and CR samples. Deformation twins mainly occurred on (111) and (112) // ND grains as was reported before [102,103]. Twinning usually is not observed in brass-oriented grains due to low Schmidt factor, as was the case for UDR samples here. However, we can observe intersecting twin bands in CR samples, as marked in Figs. 5.5.d and e. At first, these bands appear to be shear bands but in our previous work with the help of the crystallographic

orientation relation, we confirm that these are twins not shear bands [97]. In addition to primary twinning, secondary twinning was also activated in CR samples, which resulted in twins intersections. These intersections have also been reported by other researchers [93,102,103]. These twins and their intersections could act as preferential nucleation sites in brass-oriented grains. This might encourage the brass-oriented nucleation, which might be responsible for the strong brass recrystallization texture. It is noteworthy that there was no such twinning in the brass-oriented grains in UDR samples (Fig. 5.4.c).

Besides the 90% samples, EBSD maps of the 70% deformed samples elucidate the texture component differences better. The Inverse Pole Figure (IPF) map of ND plane for the UDR sample (Fig. 5.6.a) shows (110) and (111) grains that were elongated towards the rolling direction. Almost no twinning occurred in (110) grains; indeed most of the twins were formed in the (111) and (112) grains (blue and purple color grains) due to the higher Schmidt factor [76,77,79,104]. However, IPF map of the CR sample (Fig. 5.6.b) exhibits the dominancy of (110) grains. Compared to the UDR sample (Fig. 5.6.a), fewer (111) grains can be found. This difference was also present in 90% rolled samples and can be validated by macro texture (Figs. 37-39) and micro texture (Figs. 5.4 and 5.5) measurements. The presence of (111) and (112) // ND orientations in UDR samples resulted in extensive twinning. The consequence of the formation of these twins was the formation of Cu, Cu-twin and G components. During the recrystallization stage, the nucleation could have started from these grains. On the other hand, there was less inhomogeneity in (110) grains in the UDR samples, since no twinning or shear bands was observed in these grains. Therefore, there were more nucleation sites available for Cu and G to be formed in the recrystallization. However, in the CR samples the story is different since the majority of grains were brass–oriented $(110)<112>$. As mentioned previously, the brass-oriented grains in the CR samples showed twinning and shear banding, and in some cases even exhibited the intersecting bands. These features could be favorable sites for nucleation during subsequent annealing.

Humphreys and Hatherly [79] state that UDR samples have higher stored energy in comparison with CR samples. UDR applies the compressive force and strain in the rolling direction [79]. In such a way, material flow begins by dislocation movement; however dislocation movement can be impeded upon facing some obstacles such as precipitates in the movement path.

Consequently, a dislocations jungle would be formed and the energy of the material increased. For the CR samples, changing the strain path by 90˚ would have released the dislocation back-force, so that dislocations that had become sessile by facing an obstacle could have been made mobile again. Therefore, the stored energy would have been less than UDR [79]. However, there are some controversial observations that suggest higher CR stored energy due to tangled dislocations [95,105]. Nevertheless, there is general agreement in most of the literature that lower anisotropy is obtained through CR [69,79,93,95,105]. Reduced anisotropy combined with an energetically homogenized structure in the CR samples could have led to fewer preferred nucleation sites for recrystallization. The lack of preferred nucleation sites would have increased the nucleation rate, which would eventually have resulted in smaller grain sizes [69,79,85]. Moreover, as mentioned earlier, the interesting twins/shear bands in brass-oriented grains might also have played a role in the nucleation of brass components. These results suggest that oriented nucleation played a significant role in determining the final annealing texture, particularly for the CR samples as most of the new grains, formed in the annealing procedure, reproduced the deformation texture. However, Cu component in the UDR samples is an exception since we show that it mostly formed upon the onset of recrystallization. In addition, as depicted in Figs. 5.3 - 5.5, no significant changes in texture components were observed after the recrystallization started, in contrast with the orientation growth model. Nevertheless, researchers also propose that orientation growth has a strong effect on the recrystallization texture of Rex-B through annealing twins [84,86]. The sharp increase of Rex-B component, which is very close to Cu, for the UDR sample in Fig. 5.3.a, implies that orientated growth can also influence the recrystallization texture. Moreover, very weak brass texture in the annealed UDR samples could be correlated to the presence of G in the deformation texture of these samples [86]. Schmidt and Lucke [106] report that G component inhibits and suppresses the B growth and instead it leads to the formation of Rex-B component in such a way that the Rex-B appears in the recrystallization texture only if B and G were present in the deformation texture [86]. Hence, considering the present results and previous studies, it appears that orientated nucleation mainly governs recrystallization texture. However orientated growth, particularly as mentioned for Rex-B and Cu formation in the UDR regime, might facilitate the recrystallization texture evolution.

As shown in Fig. 5.7, altering the rolling path can also change the recrystallization kinetics. The higher recrystallization rate in UDR samples also can be traced to the presence of γ-fibre (111//

ND) in these samples. Researchers state that nucleation in steels preferentially starts at shear bands and deformed grains with γ-fibre orientation. This preferential nucleation is a result of higher stored energy in γ-fibre orientation [79,96,107]. Moreover, the Taylor factor for γ-fibre orientations was higher than other present texture components. Therefore, the tendency of shear band formation would be higher in this orientation [96]. Consequently, these shear bands can act as preferential nucleation sites and increase the recrystallization rate. In other words, the presence of γ-fibre, although it is weak, in UDR samples contributed to a higher recrystallization rate when compared to CR samples.

It is notable that the JMAK model is not comprehensive enough to quantify the recrystallization phenomena, since it is based on homogenous nucleation [73,79]. In contrast, it is well known that the recrystallization starts from preferred nucleation sites, such as grain boundaries, transition bands and shear bands in metals. However, due to the complex phenomena of inhomogeneous nucleation, the recrystallization kinetic was mostly studied with the classic Johnson-Mehl-Avrami-Kolmogorov (JMAK) model, which is based on random distribution of nucleation sites [79,108]. Although Microstructural Path Methodology (MPM) implements a more realistic model, which gives a better analysis of site-saturated nucleation, it is still based on homogenous nucleation. Thus, no commonly accepted analytical model for preferred nucleation sites was available [79]. Although the aforementioned preferential sites alter the random distribution of nuclei, the different recrystallization behaviors of various texture components would also increase the heterogeneity of this process. As different slip/twinning systems operated on different crystallographic orientation planes, the density of dislocations and the corresponding stored energy would be strongly orientation dependent. Thus the preferred nucleation sites and growth rate are strongly influenced by grain orientation [79,108]. Strain path can also influence the slip/twinning systems, which in turn can lead to different deformation and recrystallization textures [79,95]. Bracke et al. [85] report a high kinetic of recrystallization, which we observed here, for an austenitic iron based alloy with almost similar SFE. Since the recovery is not prevalent in low SFE FCC metals, there is a higher driving force for recrystallization in these materials [75,79]. Moreover, the heterogeneous distribution of stored energy in different texture components could also influence the kinetic and the mechanism of recrystallization [73,79]. In general, the recrystallization rate is a function of strain amount, deformation mode, annealing mode, grain orientation and initial grain size. All of these factors

can affect the recrystallization kinetics. In our study the strain amount, initial grain size, and annealing modes were identical; thus the recrystallization kinetic mostly influenced by the deformation mode and its subsequent grain orientation. It is stated that B component has 50 times less recrystallization rate than G component [79]. With this in mind, the strong B texture in CR samples could have been responsible for the slower recrystallization kinetic. Similarly, the presence of G component in UDR deformed texture would have accelerated the recrystallization rate for the UDR samples.

5.7. Conclusion

In this chapter, we have investigated the macro and micro texture evolution and kinetics of recrystallization in highly deformed Incoloy 800H/HT along with two different rolling paths. We summarize the main conclusions of the study as follows:

- Different rolling paths not only led to different deformation textures, but also altered the subsequent annealing textures. B and G were the dominant texture components for unidirectional rolling, while strong B with a slight shift towards ND-rotated B was the texture for cross rolling after 90% deformation. The annealing texture of UDR consisted mainly of Cu and G. In contrast, cross rolled samples showed a retained deformation texture.
- EBSD investigations show that the presence of (111) // ND grains in UDR led to extensive twin formation, which mainly resulted in Cu and G formation. These components nucleated and grew in the annealing stage and consequently formed the final annealing texture.
- Oriented nucleation played a significant role in determining the final annealing texture, although clear footprints of oriented growth can be tracked in the formation of Cu and Rex-B components.
- The strain path also influenced the annealing grain size. Cross rolled samples exhibited a smaller grain size, which could be correlated to a lower degree of anisotropy compared to unidirectional rolling in their deformed states.
- UDR samples exhibited a faster recrystallization kinetic. The presence of γ-fibre with a higher stored energy was found to be responsible for altering the recrystallization rate upon changing the rolling mode.

CHAPTER 6

THE EFFECT OF THERMO-MECHANICAL PROCESSING ON GRAIN BOUNDARY CHARACTER DISTRIBUTION IN INCOLOY 800H/HT

6.1. Overview of Chapter 6

In chapters 4 and 5, the evolution of deformation and annealing textures as well as the origin of different textures through the proposed thermo-mechanical processing was discussed. Grain boundary character distribution (GBCD), including the presence of coincidence site lattice (CSL), can strongly affects the materials physical and mechanical properties. Besides, it is found that the TMP can alter the grain boundary character distribution. Therefore, this chapter focuses on the evolution of GBCD through the employed TMP.

This chapter is presented as manuscript # 5 (The origin of annealing texture in a cold-rolled Incoloy 800H/HT after different strain paths). My contributions to the manuscript are: a) preparation and processing of the samples b) SEM, EDS and EBSD analyses c) Reviewing the relevant literature and writing the manuscript. Majid Nezakat and Mohsen Sanayei were assisting in the sample processing and data analyzing. The manuscript is published in the Materials Science & Engineering A:

- H. Akhiani, M. Nezakat, M. Sanayei and J. Szpunar, "The Effect of Thermo-Mechanical Processing on Grain Boundary Character Distribution in Incoloy 800H/HT", Materials Science & Engineering A, 626 (2015), 51-60.

The references for this chapter along with references from other chapters are provided at the end of the thesis.

The Effect of Thermo-Mechanical Processing on Grain Boundary Character Distribution in Incoloy 800H/HT

Hamed Akhiani, Majid Nezakat, Mohsen Sanayei and Jerzy Szpunar
Department of Mechanical Engineering, University of Saskatchewan, Saskatoon, Canada

6.2. Abstract

In this chapter, we applied a thermo-mechanical process to alter the grain boundary characteristic distribution (GBCD) with a view to the feasibility of grain boundary engineering in Incoloy 800H/HT. In order to optimize the GBCD through increasing the low Σ coincidence-site lattice (CSL) boundaries, we applied various thickness reductions with two different rolling modes followed by annealing. We used Electron Backscattered Diffraction (EBSD) to analyze the GBCD and CSL boundaries. We found that the coincidence-site lattice boundaries, particularly Σ3 and its variants, increased with the pre-deformation level in cross-rolled (CR) samples. In the contrast, for uni-directionally rolled (UDR) samples, the fraction of these CSL boundaries had an optimum in 50% reduction. In fact, different $\Sigma 3^n$ interactions led to different GBCD in UDR and CR processed samples. Low to medium deformation with UDR and medium to high deformation with CR on the Incoloy 800H/HT samples showed some potential for grain boundary engineering.

Keywords: Incoloy 800H/HT, cross-rolling, grain boundary engineering, grain boundary character distribution.

6.3. Introduction

Incoloy 800H/HT is an austenitic Fe-Ni super alloy, which is currently used in industrial chemical processing and power generation units due to its high resistance to high temperature oxidation and corrosion [13,14]. With these properties, application of Incoloy 800H/HT in other industries, such as nuclear power generation with its severe operating conditions, appears to be feasible. Recently, new approaches and designs have been implemented in Gen IV nuclear reactors to enhance their performance and safety. Two of the seven types of Gen IV reactors, the

Very High Temperature Reactor (VHTR) and Super-Critical Water-cooled Reactor (SCWR), are being developed to work at high temperature (VHTR: 750-950˚C, SCWR: 550-650˚C) for a higher thermodynamic efficiency [12]. Moreover, improvement of the high temperature properties of construction materials is an enduring interest for materials scientists and engineers. This interest would become more focused by introducing these materials in new challenging industrial applications such as structural components in Gen IV nuclear reactors. According to the Gen IV roadmap [1] Incoloy 800H/HT is being considered as one of the candidate materials to be employed in construction of different components of Gen IV reactors such as the intermediate heat exchanger, hot duct, steam generator and fuel cladding [64]. However, to be suitable as a nuclear structural material in the Gen IV designed environment, some modifications of the material's structure should be considered [12,13]. Several studies state that grain boundary characteristics strongly influence the alloy's physical and mechanical properties [11,15,16,79].

Based on the misorientation of the adjoining grains, grain boundaries can be categorized as low-angle grain boundaries (LAGBs), high-angle (random) grain boundaries (HAGBs) and special/coincident-site lattice (CSL) boundaries [109]. Different CSLs can be categorized by Σ value, which is defined as the inverse of common lattice points in the boundaries that coincide between the two adjoining grains or crystals. The relative fraction of CSL and random boundaries as well as the deviation of the special boundaries from the exact CSL boundaries and connectivity between these boundaries can be derived from the grain boundary character distribution (GBCD) [75,79,110–113]. Altering the GBCD, as a relatively new microstructural feature, can effectively change the material's properties. This fact was initially proposed by Watanabe in the early 1980s as "grain boundary design and control" which has been referring to Grain boundary engineering (GBE) afterwards [18,114]. Since then, many attempts have been made to improve the physical and mechanical properties of various materials by this method. In most studies, the GBE process is comprised a combination of deformation and consequent annealing, which is known as Thermo-Mechanical Processing (TMP) [75,79,110,115]. Fundamentally, the main concept of GBE is to generate and increase the low Σ CSL density through changing the geometry of grain boundaries, which consequently improves various material properties [14–16]. Several investigations show that low- Σ CSL boundaries (e.g., $\Sigma 3^n$) exhibit higher resistance to various types of intergranular degradation compared with random

boundaries [114]. Consequently, the presence of a high concentration of CSL boundaries enhances the properties of the materials in various aspects including: lower rates of grain boundary sliding during creep [116], resistance to high temperature fracture [15], resistance to solute segregation, precipitation, and intergranular embrittlement [117], weldability [118], resistance to corrosion and stress corrosion [15,119], resistance to intergranular corrosion [120], and resistance to radiation damage [92,117]. The most successful experiments were done in low Stacking Fault Energy (SFE) materials [75,121] and some of them are now commercially employed [122,123].

In our previous papers, in addition to deformation and annealing textures evolution, we discussed in detail the recrystallization behavior of Incoloy 800H/HT during the proposed TMP [97]. In the present study, we aim to characterize the GBCD evolution with the same TMP procedure (different strain path with various deformation strains) as we performed before. Studies investigating the effect of deformation path on the CSL boundaries are scarce. Lee et. al [30] reported an improvement in the CSL density due to applying CR in comparison with UDR deformation. However, they did not address the reason for this improvement when they changed the strain path. Understanding the role of deformation mode and strain in manipulating the GBCD would strongly contribute to the low Σ -CSL fractions and consequently improving the material's properties.

6.4. Experimental procedure

A commercial Incoloy 800H/HT from Special Metals® with the chemical composition listed in table 1.4, was used in this study. The alloy was fully annealed at 1420˚C and water quenched in the as-received condition. We performed thermo-mechanical processing (TMP) on the as-received sample by a series of cold rolling followed by annealing at 1050˚C for a time period of 25 min/cm thickness, commensurate with the size of the samples. A true strain of 0.2 was applied per rolling pass for all the samples using a laboratory roll machine. We employed two different rolling modes, Unidirectional Rolling (UDR) and Cross-Rolling (CR) to decipher the role of strain path in altering the grain boundary structure. We cut samples with the dimensions of 50x50x13.25 mm and 50x25x13.25 mm from the same plate for UDR and CR, respectively.

In order to study the effect of strain amount, we rolled the samples with 10, 30, 50, 70 and 90 % thickness reductions.

In pursuance of investigating the grain orientations and grain boundary character distribution (GBCD), we used Electron Backscattered Diffraction (EBSD). We prepared the samples with a general metallographic procedure to a mirror-like surface followed by the final polishing step with 50 nm colloidal silica on a Beuhler Vibromet® for 24 hours. We employed an Oxford Electron Backscatter Diffraction (EBSD) setup interfaced to a Hitachi SU6600 Field Emission Gun Scanning Electron Microscope (SEM) to carry out Orientation Imaging Microscopy (OIM). We operated the SEM at 30 kV with the automatic EBSD scan on the TD plane of the samples. We utilized HKL AzTech and Tango software to acquire and analyze the EBSD data, respectively. The Brandon criterion was adopted for the classification of Σ boundaries. For the fraction of CSL boundaries, we reported the average of 5 random locations on the TD surface of the samples. Coherent and non-coherent twins were separated using a misorientation threshold of 2˚, which was successfully used before [115]. In measuring the grain sizes, twins were not counted as grains. The Vickers hardness was measured using a Mitutoyu Vickers hardness testing machine with a load of 500 gf.

6.5. Results

Fig. 6.1 shows the microtexture, microstructure and grain boundary structure of the as-received Incoloy 800H/HT. The inverse pole figure (IPF) EBSD map illustrates a weak texture and a random dispersion of differently oriented grains. Coarse grains and twinning resulted from hot rolling deformation and solution annealing. High Angle Grain Boundaries (HAGB: $\delta>15$), Low Angle Grain Boundaries (LAGB: $5<\delta<15$) and CSL boundaries: Σ3, Σ9, and Σ27 are respectively shown in black, grey, violet, blue and green lines.

Fig. 6.2 and Fig. 6.3 illustrate the EBSD maps of the processed samples after two different rolling modes with various rolling strains. In order to obtain statistically reliable data from EBSD images, the scan areas were selected in a way to contain a certain number of grains. Therefore, the scan areas varied based on the grain size range of the samples. To focus on the grain boundary character distribution and ease of comparison between the samples, an EBSD grain boundary map including the HAGB, LAGB, Σ3, Σ9 and Σ27 CSL is shown for each sample.

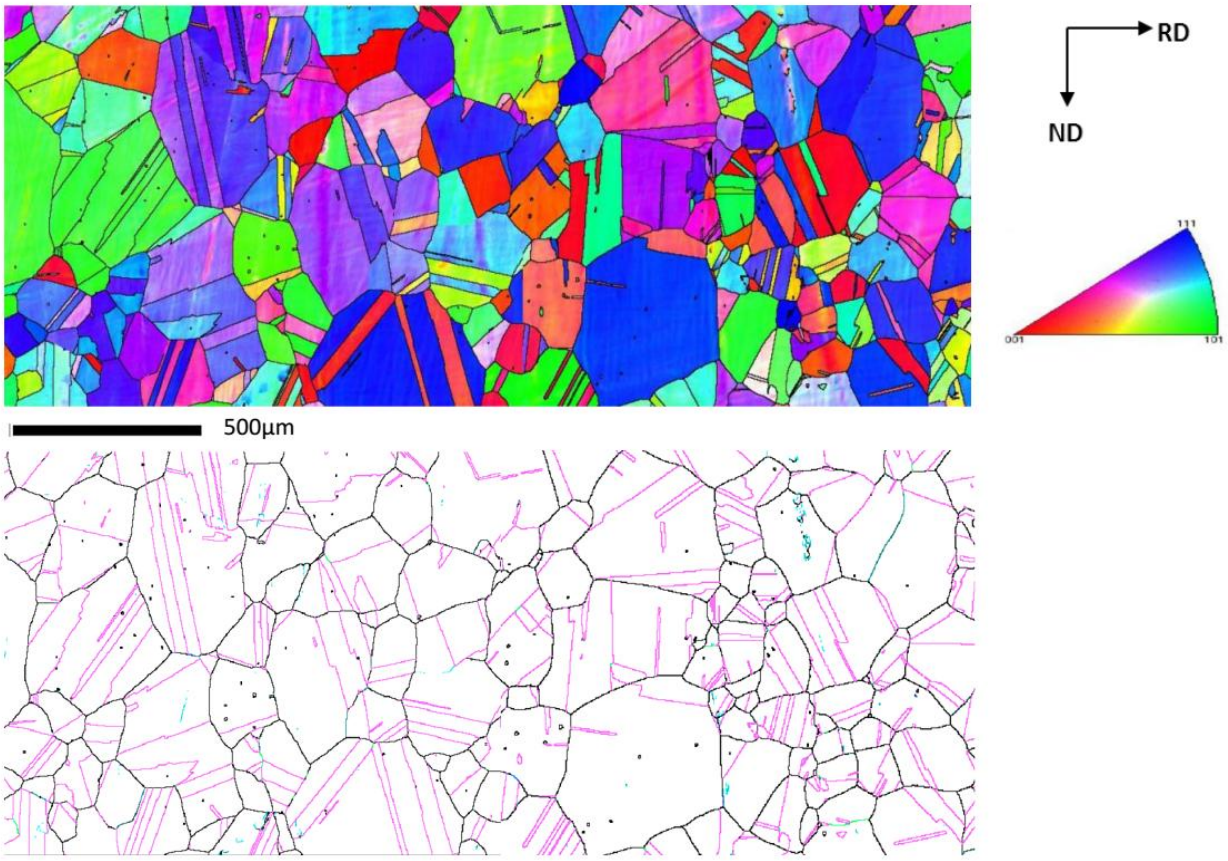

Fig. 6.1. The starting Incoloy 800H/HT grain morphology, orientations and grain boundaries in EBSD (IPF ND) and grain boundary maps (HAGB: black, LAB: gray Σ3: violet, Σ9: blue, and Σ27: green).

Fig. 6.2.a shows the EBSD grain boundary map of the annealed samples after 10% UDR deformation. The grain size decreased by almost half its size in the starting material. The microstructure of the 10%CR sample (Fig. 6.3.a) resembles the starting sample; the grain size decreased by about 30% from the as-received sample. By increasing the rolling strains to 30%, the grain size was dramatically decreased, particularly for the UDR sample. The trend of decreasing the grain size continued as the prior deformation strain increased until the grain size finally reached about 10 and 17 µm for the 90% UDR and CR samples, respectively. The evolution of the grain size of the samples and their associated hardness with increasing the rolling strain is depicted in Fig. 6.4. The major difference in grain size evolution was that below 50% reduction; UDR samples had smaller grain size while after this deformation strain the CR samples exhibited lower grain sizes. This point can also be observed by comparing 50% UDR

(Fig. 6.2.c) and 50%CR (Fig. 6.3.c) samples, where both show almost the same average grain size. In general, the CR samples possessed higher hardness when compared to UDR samples. This has been referred to as dislocation tangling, resulting from changing the strain path in CR [95,105]. Indeed, we previously discussed in detail the evolution of deformation and annealing texture, the texture differences between UDR and CR, as well as the recrystallization behavior of these samples [97,124]. Despite the difference in hardness number of UDR and CR samples, they both demonstrated an increasing trend upon decreasing the grain size. This is in agreement with the Hall-Petch relationship in the current grain size range [79].

Furthermore, we made subsets of the grain boundary maps in the order/range of the average grain size of each sample, in the interest of analyzing grain boundary connectivity and twins' morphology. Examples of these subsets are shown in Fig. 6.5. In the UDR samples, $\Sigma 3^n$ boundaries were incorporated to the high angle grain boundary network as convoluted boundaries, particularly at lower deformation strains (<50%). Apparently, increasing the strain beyond this limit led to a decrease in $\Sigma 3^n$ boundaries in UDR samples. In contrast, the $\Sigma 3^n$ boundaries incorporation was different in the CR samples. The twins in CR low strain samples (<50%) consisted mainly of straight boundaries, which are in accordance with annealing twin boundaries. However, by increasing the strain level, convoluted $\Sigma 3^n$ boundaries substituted these straight twins. Concurrent to these morphology changes, it appears that the connectivity of the high angle grain boundaries network became disrupted.

In addition to the GB morphology, we analyzed the GBCD as a function of the change in misorientation angle for all the samples. Figs. 6.6.a and 6.6.b illustrate the misorientation distributions for UDR and CR samples with their respective strains. To compare the misorientation distributions of the processed samples, Fig. 6.6 also shows a random (McKenzie) distribution. The as-received sample had a lower internal misorientation grain, which was inherited from the hot deformation processing route. However, a 60˚ misorientation angle is associated with the FCC Σ3 boundaries (60˚ <111>) [79]. Apart from the low angle and 60˚ misorientations, the frequency of the remaining misorientation angles was very small. Following UDR processing, the low misorientation fraction decreased as the 60˚ misorientation fraction increased. Nevertheless, the 60˚ misorientation (Σ3) was at a maximum in 50% UDR.

Fig. 6.6b depicts the misorientation profiles for the CR samples. This misorientation distribution was slightly different from the UDR samples, particularly at lower strain levels (<50%). However, after 50% reduction, the similar counter swing of low angle and 60˚ misorientations occurred in the CR sample as well. Moreover, comparing Fig. 6.1 to Fig. 6.2 and Fig. 6.3, it appears that the number of CSL boundaries (Σ3, Σ9 and Σ27) was increased, while the grain size decreased. We measured the number of these boundaries and the results are shown in Figs. 6.7 and 6.8. In addition to Σ3, Σ9 and Σ27, we also calculated Σ3/ Σ(9+27) and Σ9/ Σ3 fractions, which can be used as a general indication of grain boundary engineering.

First, we focus on the CLS boundaries in the UDR samples. Fig. 6.7.a demonstrates that the Σ3 fraction of the UDR samples increased dramatically by increasing the pre-strain. However, this fraction reduced slightly for higher deformation samples (70% and 90% UDR). Although the number of coherent Σ3 boundaries is less than the total number of Σ3 boundaries, it followed a similar trend. Due to the lower intensity of Σ9 and Σ27 in comparison with Σ3 in Fig. 6.7a, we plotted them separately in Figs. 6.8.a and 6.8.b. Both Σ9 and Σ27 fractions showed a similar trend to Σ3 in UDR samples: They increased up to 50% and then slightly decreased. In addition, Σ3/ Σ(9+27) and Σ9/ Σ3 fractions demonstrated a trend similar to Σ9 and Σ27, although they indicated the interactions between CSL boundaries, which will be discussed later.

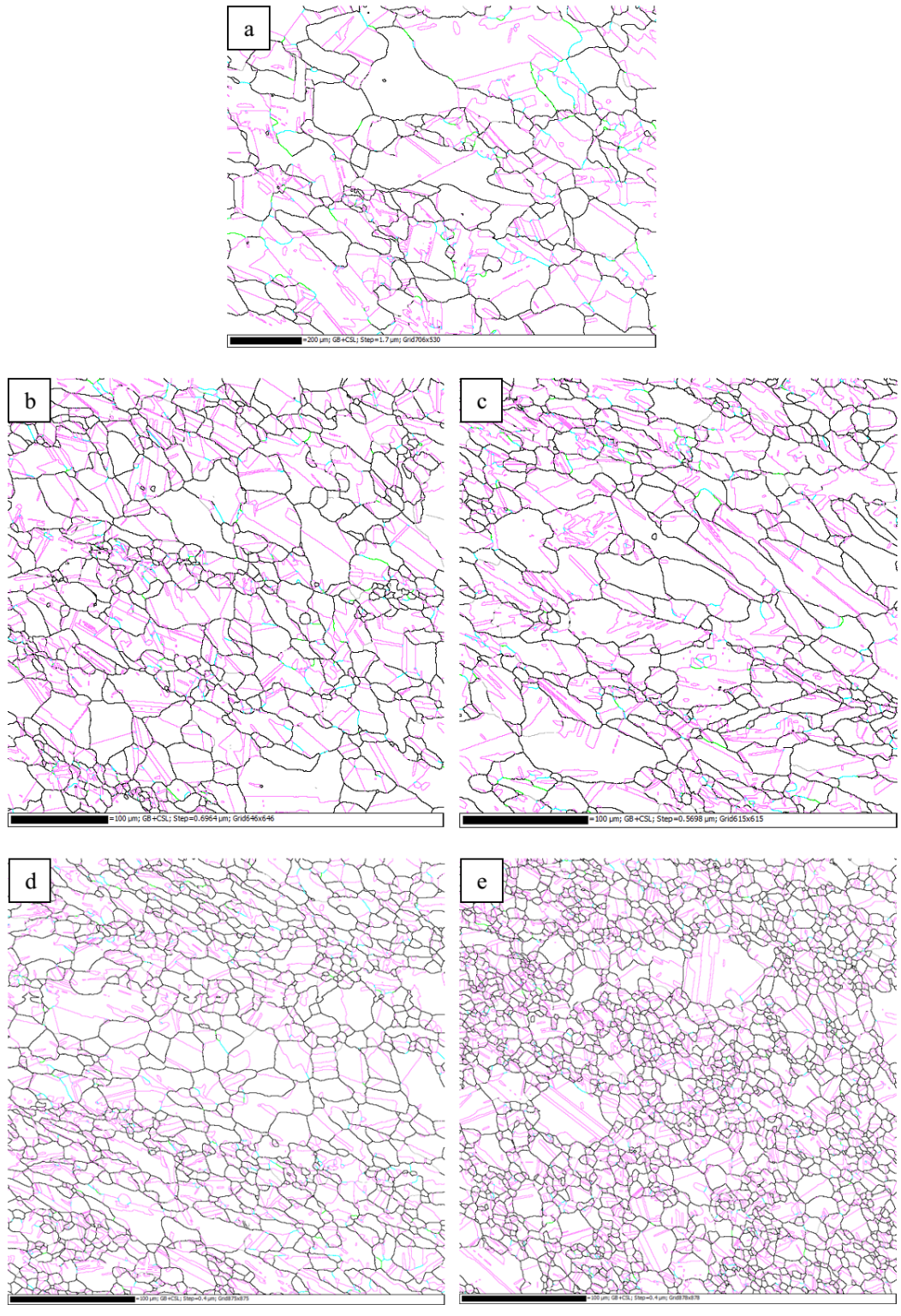

Fig. 6.2. EBSD GB maps (including LAGB, HAGB, Σ3, Σ9 and Σ27) showing microstructures of the UDR annealed samples after: a) 10%, b) 30%, c) 50%, d) 70%, and e) 90% reduction. HAGB: black, LAB: gray Σ3: violet, Σ9: blue, and Σ27: green. (Note that the scales are different in some cases.)

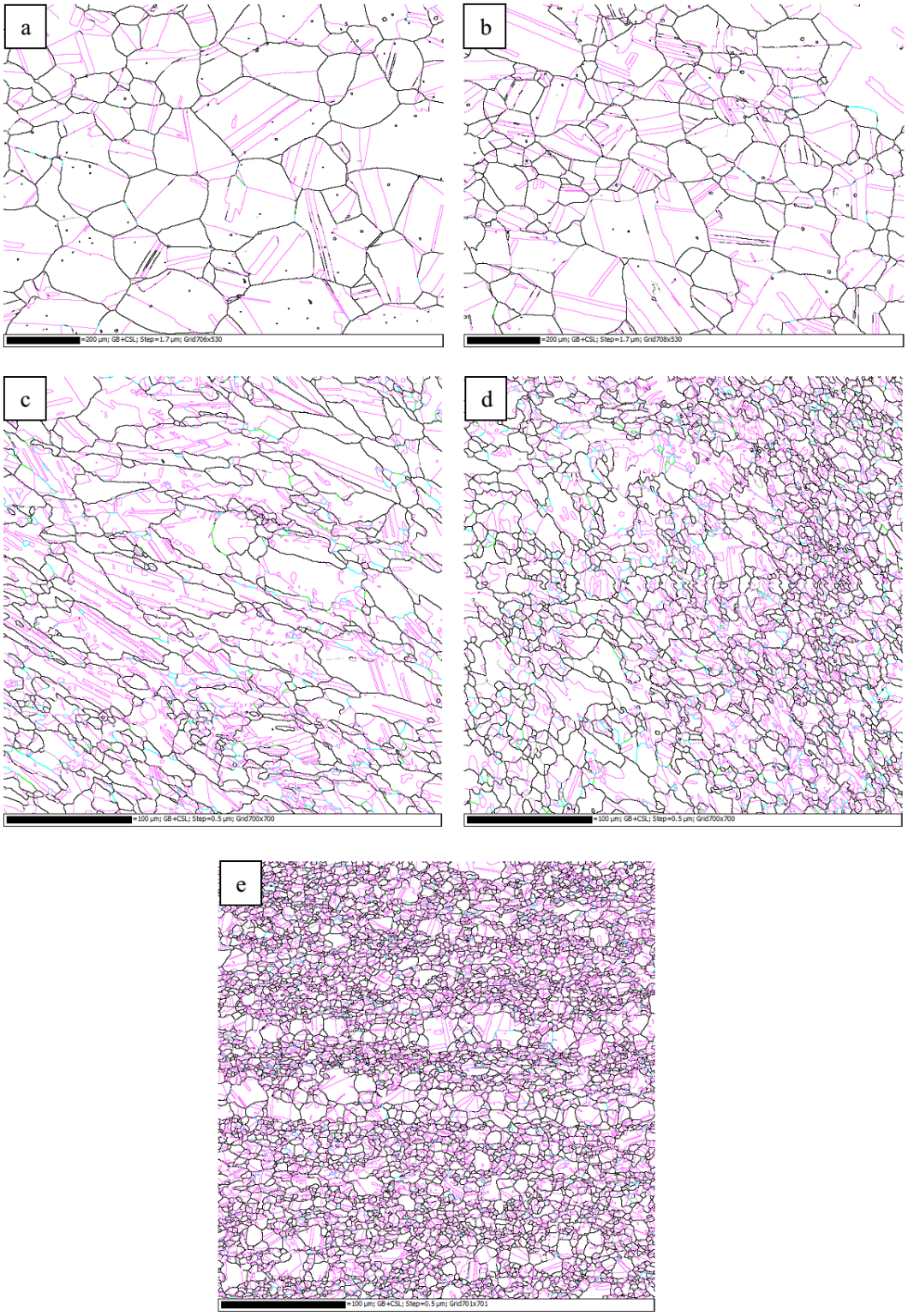

Fig.6.3. EBSD GB maps (including LAGB, HAGB, Σ3, Σ9 and Σ27) showing microstructures of the CR annealed samples after: a) 10%, b) 30%, c) 50%, d) 70%, and e) 90% reduction. HAGB: black, LAGB: grey, Σ3: violet, Σ9: blue, and Σ27: green. (Note that the scales are different in some cases.)

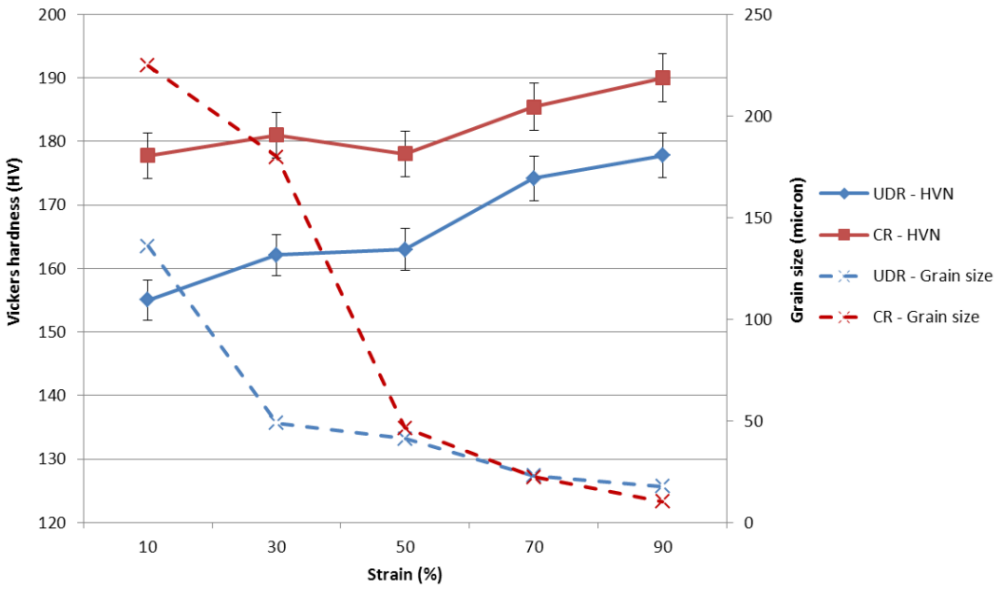

Fig.6.4. Hardness and the grain size of the processed samples as a function of rolling modes for various reductions.

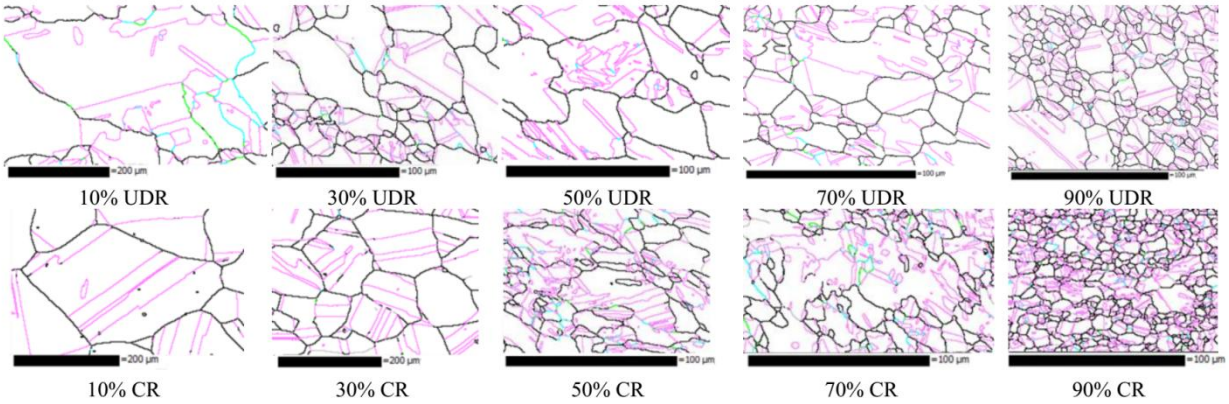

Fig.6.5. The effect of two rolling modes with various reductions on the grain boundary network topology and twins morphology in the scale of average grain size for each sample.

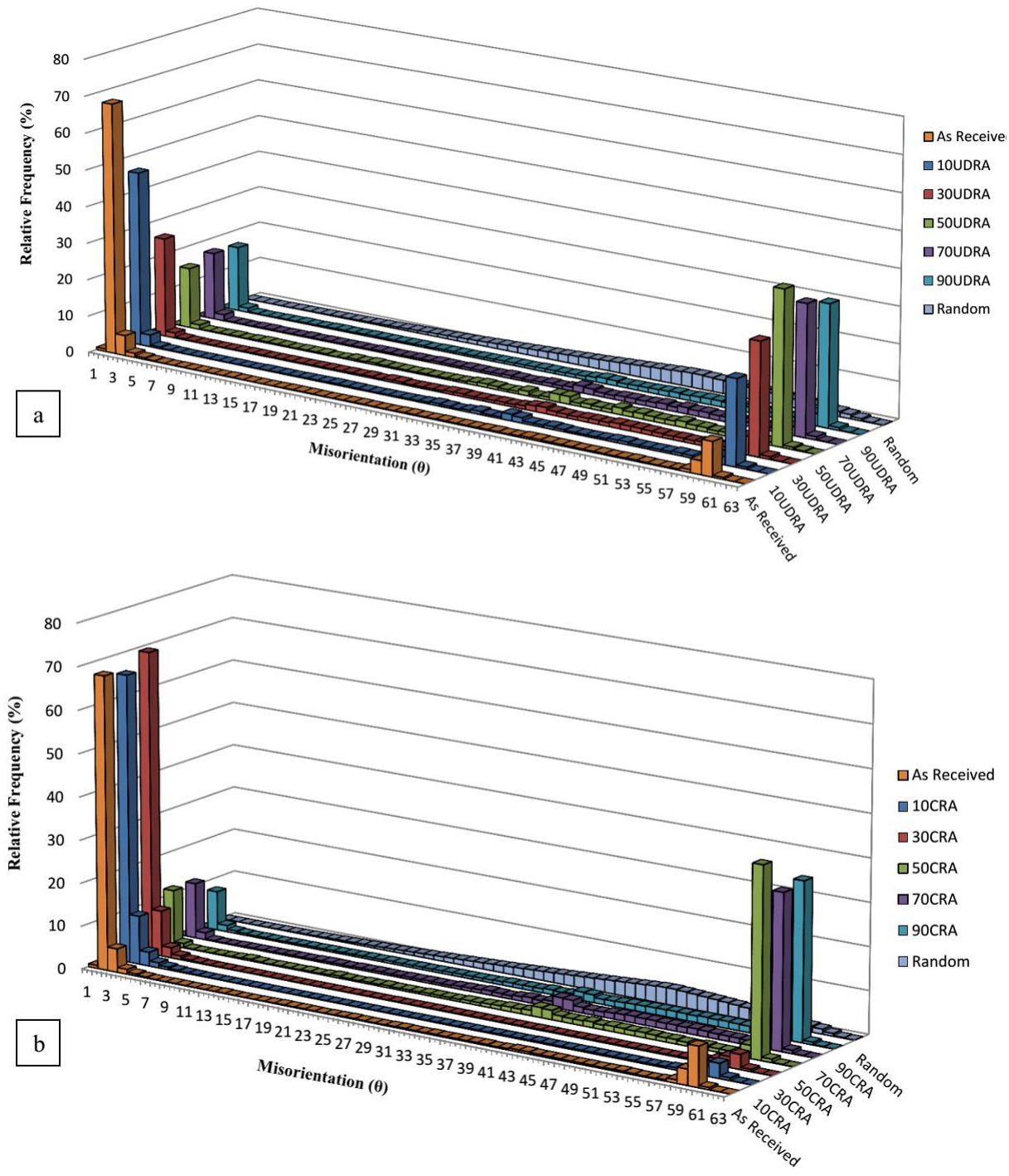

Fig.6.6. Grain Boundary Character Distribution (GBCD) of the annealed samples after: a) UDR, and b) CR for various reductions.

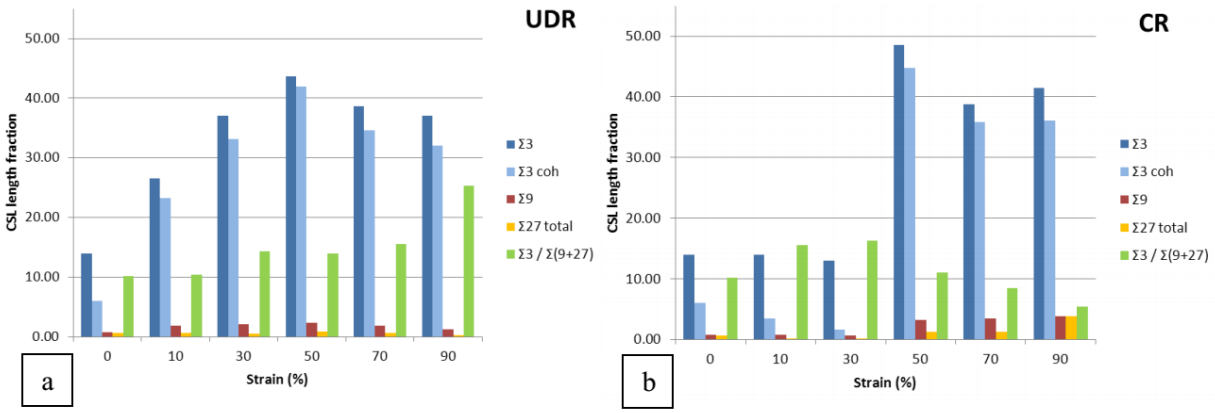

Fig.6.7. CSL fraction of the starting and processed (annealed) samples versus reduction pct for: a) UDR and b) CR.

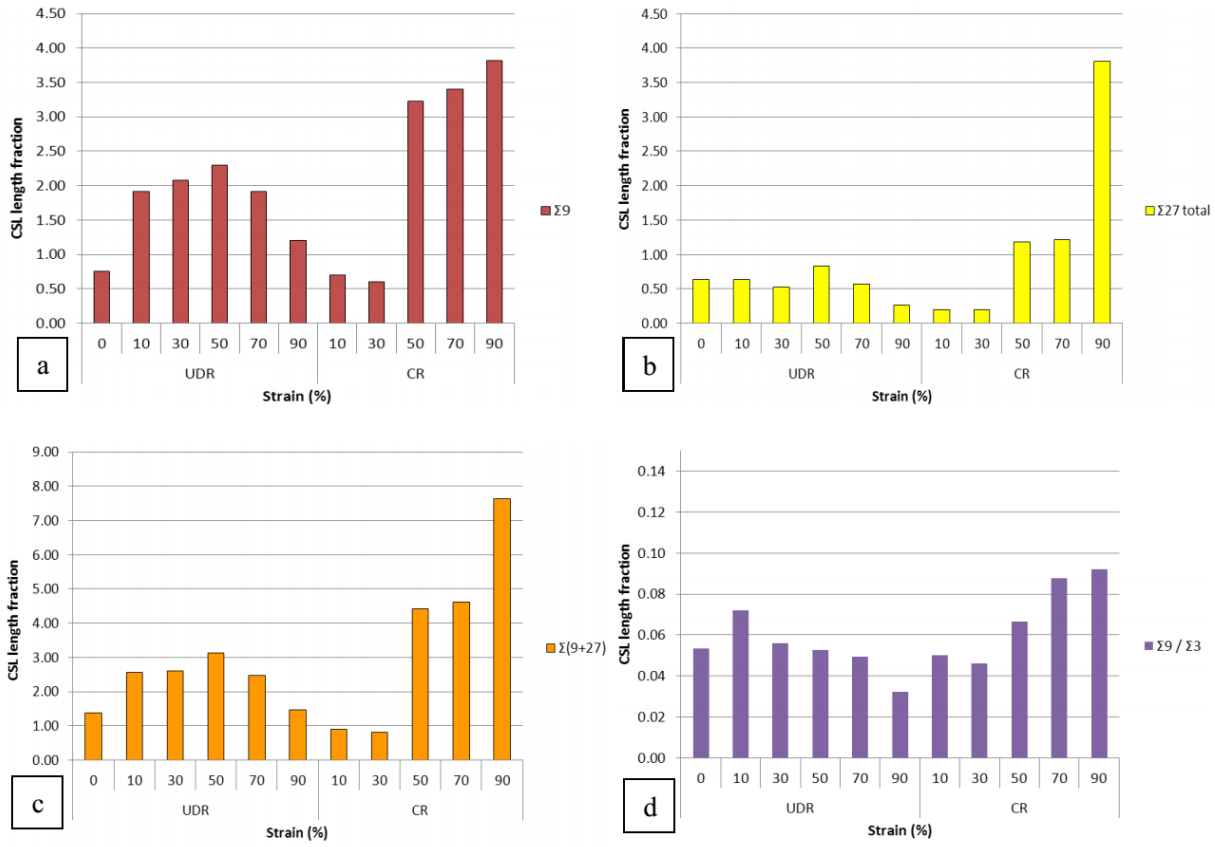

Fig.6.8. Fractions of: a) Σ9, b) Σ27, c) Σ(9+27), d) Σ9/Σ3 for the starting and processed (annealed) samples after various reductions.

6.6. Discussion

Figs. 6.2 and 6.3 depict the HAGB and CSL boundary evolution in UDR and CR samples, respectively. The increase in the number of CSL boundaries (particularly Σ3) is observable. Σ9 and Σ27 boundaries mostly had short segments as can be seen in Fig. 6.2 and Fig. 6.3. Randle [115] also reported that these boundaries could be in the order of 1μm, particularly when they were formed by the interactions of $\Sigma 3^n$. Due to the small sizes of these boundaries, it was difficult and inaccurate to measure them and calculate the associated number fractions. Therefore, it is more appropriate in our case to use length fractions. As stated by Randle, length fractions often possess a smaller value than the number fractions but the trends for comparison purposes are the same [112,115]. Considering Figs. 6.2 and 6.3, it appears that concurrent with the progressive grain size refinement, the density of low energy CSL boundaries was increased. We could attribute grain size refinement to the amount of strain and preferential nucleation sites; as the level of deformation strain increased, more preferential (high dislocation density) sites would have been available for nucleation, thus more grains would have been nucleated, which in turn resulted in a finer grain microstructure.

Furthermore, increasing the prior deformation led to a decrease in the low angle misorienation frequency and an increase in the frequency of about 60˚ misorienation (Σ3), as illustrated in Fig. 6.6. This is in accordance with the relation of the prior deformation and stored energy. In fact, as deformation reduction increased, the stored energy would have amplified and served as a driving force for grain boundary migration and subsequent recrystallization [79]. In other words, increasing the rolling strain would have increased the grain boundary mobility. During annealing, boundaries move or migrate in such a way to minimize the internal energy. Hence, the higher the stored energy, the higher will be the migration of grain boundaries. Consequently, by increasing the deformation strain followed by annealing treatments, grain boundaries become capable of migration towards specific misorientation (e.g. Σ3) to lessen/minimize the stored energy [79,125]. The tendency to minimize the energy is seen through formation of Σ3 boundaries [79,125]. Therefore, increasing the deformation strains is the reason we observed such a misorientation distribution profile.

We addressed the texture transition from deformation to annealing as well as the recrystallization behavior of Incoloy 800H/HT in detail before (chapter 4 and 5) [97,124].

Analysing the EBSD maps and quantifying the length fractions of these boundaries reveals their evolution trend precisely as illustrated in Fig. 6.7 and Fig. 6.8. The number of $\Sigma3^n$ boundaries progressively grew by increasing the prior deformation strain up to 50% in UDR samples (Fig. 6.6.a). There is a controversy in the literature about the large prior deformation (>50%) effect on the CSL density. The large prior deformation is reported to have been detrimental in Ni alloys [115] while it enhanced the CSL density in Pb alloys [126]. For the present study, not only the deformation strains but also the deformation (strain) paths might have affected the CSL boundaries. In addition to total Σ3 (coherent and non-coherent twins) numbers, we illustrate the coherent ones in Fig. 6.7. Coherent twins have less free volume and very low mobility compared with non-coherent ones. Although both of these twin types have different characteristics from other boundaries, in some cases coherent twins show better improvements in materials' mechanical properties [115]. Nevertheless, the coherent and non-coherent Σ3 boundaries in the present study show exactly the same trend; therefore we cannot suggest which one is more effective in altering the Incoloy 800H/HT physical and mechanical properties.

Although the main mechanism for GBE depends on proliferation of twinning (as a type of Σ3 boundary) in low SFE materials, the interactions of other Σ3 variants such as Σ9 and Σ27 could further alter the GB structure [112]. For many years, enhancing the materials' properties via GBE was solely linked to the increase of Σ3 boundaries. However, recent studies show that twin/grain boundary planes and the connectivity of random/HAGB strongly influence these properties as well [110,112,127]. Some of these factors (e.g. connectivity of GB networks) rely on the $\Sigma3^n$ quantity and interactions. First we focus on the $\Sigma3^n$ quantity here. Comparing Fig. 6.7.a, Fig. 6.8.a and Fig. 6.8.b, we observe that the trend of Σ3 was very similar to Σ9 and Σ27 in UDR. However, the number of these boundaries was in different levels: $\Sigma3 >> \Sigma9 > \Sigma27$. The drop in the number of these boundaries after 50% reduction also showed similar trends. Drabble et al. [128] report the same behavior of $\Sigma3^n$ in GBE of 800H. On the other hand, the trend of Σ3 in CR samples was different from the associated Σ9 and Σ27. Although Σ3 slightly decreased after 50% in CR samples, Σ9 and Σ27 were mainly increased by deformation strain. This different drift of Σ3 versus Σ9 and Σ27 would suggest that different interactions were occurring in UDR and CR samples.

The increase in $\Sigma 3^n$ boundaries could be a consequence of two main mechanisms: formation of new annealing twins and regeneration (geometrical interactions) of pre-existing twins or other $\Sigma 3^n$ [112]. After analysing several successful GBE studies, Randle suggested that $\Sigma 3/ \Sigma(9+27)$ ratio can be efficiently used to determine the twin proliferation mechanisms [112,115]. This ratio has also been used by other scholars in their GBE studies [113,129]. A lower $\Sigma 3/ \Sigma(9+27)$ ratio would suggest that the $\Sigma 3$ regeneration mechanism is more active than new twinning formation. This is due to higher interactions of $\Sigma 3^n$ boundaries, which in turn incorporate the $\Sigma 3^n$ boundaries to the grain boundary network. On the other hand, a higher $\Sigma 3/ \Sigma(9+27)$ ratio defines the new twin formation mechanism, which usually does not influence the grain boundary network. Despite these criteria, both of the mechanisms can contribute to the number of $\Sigma 3^n$ boundaries but normally one of them would be dominant [112]. In addition to the aforementioned ratio, the morphology of twins that form by each of these mechanisms is also different. In the former mechanism, twins mainly possess a convoluted morphology while in the latter mechanism, new annealing twins mostly form in long, straight parallel pairs/multiples [75,79,112]. Many factors such as SFE, strain path, strain amount, annealing time/temperature and grain size could concurrently define which mechanism would be activated. In the present case, we designed the experiment in such a way to enable us decipher the role of strain path with UDR and CR. Comparing Fig. 6.7.a and Fig. 6.7.b, we can analyse the twinning mechanisms in UDR and CR samples. The $\Sigma 3/ \Sigma(9+27)$ ratio was progressively increased for UDR samples by deformation strains. This could suggest that the main twinning mechanism for UDR samples is likely to be new twins generation. In contrast, the declining $\Sigma 3/ \Sigma(9+27)$ ratio for CR samples elucidates the predominance of regeneration and interactions between $\Sigma 3^n$ boundaries. There is an interesting point in the counter swing of $\Sigma 3$, $\Sigma 9$ and $\Sigma 27$ in CR samples. Fig. 6.8 shows that $\Sigma 9$ and $\Sigma 27$ were increasing with increasing the strain in CR samples. Nevertheless, the $\Sigma 3$ slightly decreased after 50%. This counter swing of $\Sigma 3$, $\Sigma 9$ and $\Sigma 27$ suggests that more $\Sigma 9$ and $\Sigma 27$ boundaries were forming at the expense of decreasing $\Sigma 3$ boundaries. This would imply that the main mechanism for increasing the $\Sigma 3^n$ boundaries in CR samples is the regeneration and interactions of $\Sigma 3^n$ boundaries. Moreover, the $\Sigma 9/ \Sigma 3$ ratio proposed by Randle [130], demonstrates a similar trend to $\Sigma 9$, $\Sigma 27$, $\Sigma(9+27)$, and $\Sigma 3/ \Sigma(9+27)$, which validates the interaction of $\Sigma 3^n$ boundaries. Some of these interactions can be observed in the EBSD maps

in Fig. 6.2 and Fig. 6.3. We illustrate several examples of these types of triple junction interactions ($\Sigma3^n + \Sigma3^{n+1} \rightarrow \Sigma3^{n+2}$ and $\Sigma3^n + \Sigma3^{n+1} \rightarrow \Sigma3$) within subsets in Fig 6.9. Most of these interactions led to an increase in the number of Σ9 and Σ27 boundaries as depicted in Fig. 6.6.b. The increase in overall CSL boundaries in CR samples is in agreement with Lee et. al [126] who reported an improvement in the CSL density with application of CR as compared with UDR.

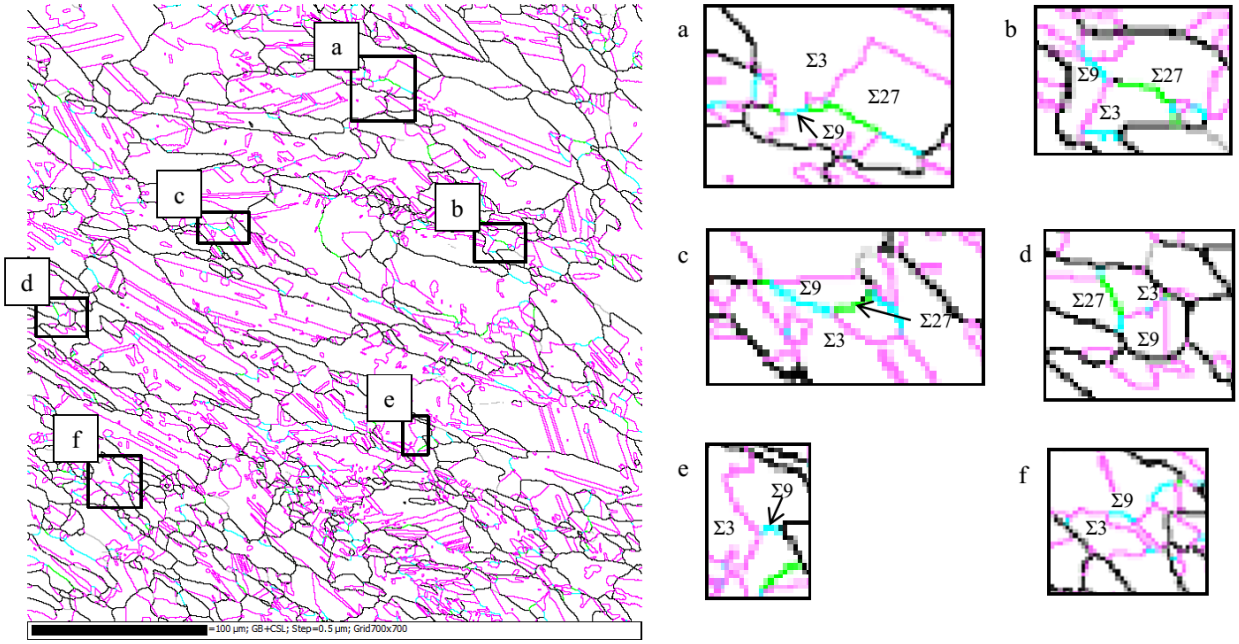

Fig. 6.9. EBSD GB map (including LAGB, HAGB, Σ3, Σ9 and Σ27) of the 50% CR sample showing $\Sigma3^n$ boundaries interactions. (Reproduced from Fig. 6.3c: HAGB: black, LAGB: grey Σ3: violet, Σ9: blue, and Σ27: green)

In addition to amplifying the $\Sigma3^n$ boundaries, Fig. 6.5 illustrates that these boundaries effectively disrupted the high angle grain boundaries network particularly in UDR and CR at low strains (<50%) and high strains (≥50%), respectively. Moreover the twins morphology of these samples was in agreement with those predicted by the Σ3/ Σ(9+27) ratio. As mentioned before, the Σ3/ Σ(9+27) ratio could suggest the $\Sigma3^n$ boundaries morphology. A lower ratio leads to formation of mainly convoluted $\Sigma3^n$, while mostly long and straight pairs of $\Sigma3^n$ would be expected at a higher ratio [112].

A higher density of CSL boundaries and disruption of the HAGB network could improve various materials' properties, regardless of the mechanism of $\Sigma3^n$ proliferation. However, to ascertain the decisive effect of each mechanism on the material's properties, further experiments are required [112]. Accordingly, these samples with different $\Sigma3^n$ interaction mechanisms should be subjected to certain tests to evaluate the effectiveness of each $\Sigma3^n$ mechanism/variant on a particular property such as oxidation resistance. We expect that the GBE samples would exhibit better oxidation resistance in comparison with the conventional Incoloy 800H/HT. Thus, we are currently examining the oxidation resistance of these processed samples in super-critical water (SCW) for future application in SCW reactors. The outcome of this research will allow us to make recommendations for choosing the appropriate microstructure with optimum GBCD for Incoloy 800H/HT in future SCW reactors.

6.7. Conclusion

In the present study, we investigated the evolution of grain boundary character distribution of thermo-mechanically processed Incoloy 800H/HT. We also studied the feasibility of engineering the grain boundaries for Incoloy 800H/HT with the proposed TMP. The main conclusions of the study are as follows:

- Different grain boundary character distributions in terms of low Σ CSL boundaries ($\Sigma3^n$) boundaries were achieved through TMP.

- Unidirectional rolling mode initially led to enhanced Σ3 boundaries up to 50% deformation. However by increasing the strain, the number of Σ3 boundaries slightly declined.

- Cross-rolled samples possessed a higher fluctuation in the Σ3 boundaries particularly at lower deformation strains (<50%).

- Different rolling paths led to different interactions between grain boundaries and number of $\Sigma3^n$ boundaries. Moreover, the mechanism for twinning proliferation was found to be different in UDR and CR samples. For UDR samples, new twin formation was the main mechanism, while twin regeneration and interactions with $\Sigma3^n$ boundaries was the dominant one for the CR samples.

- We mainly observed proliferation of $\Sigma 3^n$ boundaries and connectivity disruption of HAGB networks in low to medium deformation (<50%) with UDR and medium to high deformation (≥50%) with CR. Hence, the proposed TMP in the aforementioned criteria show the potential for GBE of Incoloy 800H/HT.

CHAPTER 7

OXIDATION OF INCOLOY 800H/HT IN SUPERCRITICAL WATER

7.1. Overview of Chapter 7

A comprehensive study of microstructure, texture and GBCD of Incoloy 800H/HT through the specific thermo-mechanical processing, was discussed in chapter 4, 5 and 6. This chapter focuses on the oxidation resistance of thermo-mechanically processed samples in super-critical water. The oxide scale formed on the Incoloy 800H/HT was characterized by means of SEM, EDS and EBSD. Moreover, the roles of various microstructural parameters (e.g. texture, grain size, GBCD) are investigated in detail.

This chapter is presented as the manuscript # 6 (The oxidation resistance of thermo-mechanically processed Incoloy 800H/HT in Supercritical water). My contributions to the manuscript are: a) preparation and processing of the samples b) SEM, EDS and EBSD analyses c) Reviewing the relevant literature and writing the manuscript. Sami Penttilä performed the SCW oxidation exposure tests at VTT Finland and Majid Nezakat assisted in the sample processing and data analyzing.

The manuscript is submitted to the Journal of Supercritical Fluids.

The references for this chapter along with references from other chapters are provided at the end of the thesis.

The oxidation resistance of thermo-mechanically processed Incoloy 800H/HT in supercritical water

Hamed Akhiani[1], Majid Nezakat[1], Sami Penttilä[2] and Jerzy Szpunar[1]

[1] Department of Mechanical Engineering, University of Saskatchewan, Saskatoon, Canada
[2]VTT Technical Research Centre of Finland, Espoo, Finland

7.2. Abstract

In this chapter, we evaluate the oxidation behavior of thermo-mechanically processed Incoloy 800H/HT with a view to its feasible application in the Gen IV supercritical water- cooled reactor. In order to evaluate the role of microstructural characteristics such as texture, grain size and grain boundary character distribution, we implemented a specific thermo-mechanical treatment to process Incoloy 800H/HT. The processed samples with different microstructures were exposed to supercritical water, for 100, 300 and 1000 hours. In addition to weight changes, we used scanning electron microscopy, energy dispersive X-ray spectroscopy and orientation imaging microscopy to analyze the oxide scale formed on the samples. We found that the thermo-mechanical processing significantly improved the oxidation resistance. Also while in the as-received alloy oxide scale exfoliation and spallation was observed even at 100 hours SCW exposure, the processed samples showed no sign of such a behavior. Moreover, cross-rolled samples showed a better oxidation resistance compared to unidirectional rolled samples due to favorable texture. However, the results demonstrated that grain size has stronger effect, in compare with texture, on the oxidation resistance of Incoloy 800H/HT in supercritical water.

Keywords: Incoloy 800H/HT, Supercritical water, Oxidation, grain boundary engineering, grain boundary character distribution.

7.3. Introduction

Water transforms to a supercritical state upon passing its thermodynamic critical point (374.2˚C and 22.1 MPa). The supercritical water (SCW) exhibits unique thermo-physical properties in terms of specific heat and thermal conductivity. Therefore, SCW is considered to serve as cooling and heat transfer medium for future generation of nuclear reactors [8,131]. Accordingly,

a supercritical water-cooled reactor (SCWR) was selected as one of the Generation IV nuclear reactors design concepts to be developed [1,4]. One of the major challenges for implementing the SCWR is to find the reactor structural materials such as fuel cladding. SCW environment is highly corrosive so that it could dramatically degrade the exposed materials. In addition, higher fuel burn up in SCWR results in a higher fuel cladding temperature. Conventional zirconium alloys used in Gen II and III nuclear reactors are no longer appropriate choices for Gen IV-SCWR due to their higher corrosion rate and cladding peak temperature in SCW [1,132]. As a result, an international quest, managed by the Generation IV International Forum (GIF), was initiated with the task to find appropriate materials which can tolerate the exposure to SCW that the reactor core components will experience in service [1]. Nickel and iron base super-alloys, due to their superior high temperature properties (e.g. oxidation, creep) would be good choices. However, their neutron transparency are respectively about 14 and 24 times lower than zirconium [3]. Consequently, despite the excellent high temperature properties of nickel alloys, their higher neutron absorption coupled with swelling and embrittlement make Ni base alloys less favorable as fuel cladding material [4].

Among iron based super-alloys, Incoloy 800H receives more attention due to its superior properties [1,133,134]. The Incoloy 800H is an austenitic Fe-Ni super-alloy which has been used in fossil fuel plants for decades. The alloy exhibits high temperature strength, due to solution hardening and precipitation hardening with Ti and Cr carbides, as well as high resistance to oxidation and other types of high temperature degradation (e.g. creep). Based on these properties, Incoloy 800H has been selected as a fuel cladding material candidate for SCWR by GIF [1,4]. Nevertheless, to serve as a nuclear structural material in the Gen IV reactors condition, some modifications on Incoloy 800H structure should be considered [12,13]. The few available literature on SCW oxidation of austenitic stainless steels reported that Incoloy 800H alloys family, generally exhibit a lower oxidation rate and weight gain compared to other iron based/stainless steel alloys [133,135]. However, in most of these studies Incoloy 800H shows oxide scale exfoliation and spallation particularly above 500˚C [11,135–137]. It is worthy to mention that most of these studies have been done using a static autoclave which often leads to lower oxidation and less spallation than dynamic/recirculating autoclaves. Nevertheless, a few

studies stated the oxide scale spallation can be effectively mitigated by altering the grain boundary characteristics [11,15,79].

We have implemented a specific Thermo-Mechanical Processing (TMP) to alter the Incoloy 800H/HT microstructure. In our previous papers (chapters 4-6), we described the evolution of the deformation/annealing textures, grain boundary character distribution (GBCD) as well as the recrystallization behavior of Incoloy 800H/HT during the proposed TMP, in detail [97,124]. In the present chapter, we assess the SCW oxidation resistance of the thermo-mechanically processed Incoloy 800H with the same TMP procedure as we performed before [97]. Moreover, we focus on the the heterogeneous oxide surface morphology including iron oxide islands and their origin, which has not been addressed in the previous studies on SCW oxidation of Incoloy 800H/HT [133,134,137,138].

Evaluating the oxidation resistance of the TMP samples would help us to decipher the role of texture, grain structure and GBCD in SCW oxidation of Incoloy 800H/HT. This could significantly contribute to tailor the optimized structure for enhancing the oxidation resistance of Incoloy 800H/HT in SCW.

7.4. Experimental procedure

The composition of Incoloy 800H/HT used in this study is listed in table 1.4. The as-received alloy was fully annealed at 1420˚C and water quenched. TMP was performed on the as-received sample by a series of cold rolling followed by annealing at 1050˚C as reported previously[97].

Prior to SCW exposure, the samples were polished at the final stage with 1200 grade emery paper. The supercritical water oxidation experiments were performed at 600 ºC and 25 MPa for 100, 300, and 1000 hours in an autoclave with a recirculation water loop, as illustrated in the reference [139]. The SCW properties such as temperature, pressure, inlet and outlet water conductivity, oxygen content and flow rate were monitored and controlled as stated in table 7.1. The samples were electrically insulated from the sample holding rack and the autoclave body. The weights of the specimens were measured before and after each exposure period in order to calculate the weight changes per unit area using an electronic balance with a ±0.01 mg precision.

Table 7.1. Targeted and recorded values for the supercritical water test environment

Parameter	Target value / range	Notes/ values (recorded mean ± standard deviation)
Temperature	600 ºC	599 ± 1.0 ºC
Pressure	250 bar	250 ± 0.9 bar
Inlet conductivity	0.1-0.5 µS/cm	0.053 ± 0.001 µS/cm
Outlet conductivity	1.0-3.0 µS/cm	0.29 ± 0.11 µS/cm
Inlet dissolved O_2	150 ppb	150 ± 0.5 ppb
pH of the inlet water	7.0	(Pure water)
Flow rate	~5 ml/min	Full renewal about every 2 h

To investigate the oxide scale structure, we used a SEM equipped with EDS and Electron Back-Scattered Diffraction (EBSD). We prepared the samples using general metallographic procedure to a mirror like surface followed by the final polishing step with 50 nm colloidal silica on a Beuhler Vibromet® for 24 hours. We used an Oxford EBSD setup interfaced to a Hitachi SU6600 Field Emission Gun Scanning Electron Microscope to carry out Orientation Imaging Microscopy (OIM) measurements. We operated the SEM at 20 kV with the automatic EBSD scan on the TD plane of the samples. We utilized HKL AzTec, Tango and Mambo software to acquire and analyze the EBSD data.

7.5. Results

7.5.1. Weight change

Fig. 7.1 illustrates the weight change of all the tested samples at 100, 300 and 1000 hours SCW exposure periods. As-received (control) sample shows a negative weight change at 100 and 1000 hours exposure. In the contrast, all the processed samples exhibit a positive weight change. As expected, the weight changes of the processed samples increased by the exposure time. However, the weight change observed in few samples (e.g. 90UDR) suggested oxide spallation. This would be clarified in section 7.5.2 through investigation of the oxide surface. Due to the spallation of the oxide scale, we mostly focus on the 1000 hours exposed samples to have a more realistic evaluation of SCW oxidation resistance of Incoloy 800H/HT. The average weight change of the samples exposed to SCW was about 4 times higher than the same temperature at atmospheric pressure in air. Nevertheless, the weight change is still very low compared with other austenitic

alloys. For instant, the weight change of 316L stainless steel is about 40 times higher than Incoloy 800H/HT at the identical exposure conditions [140].

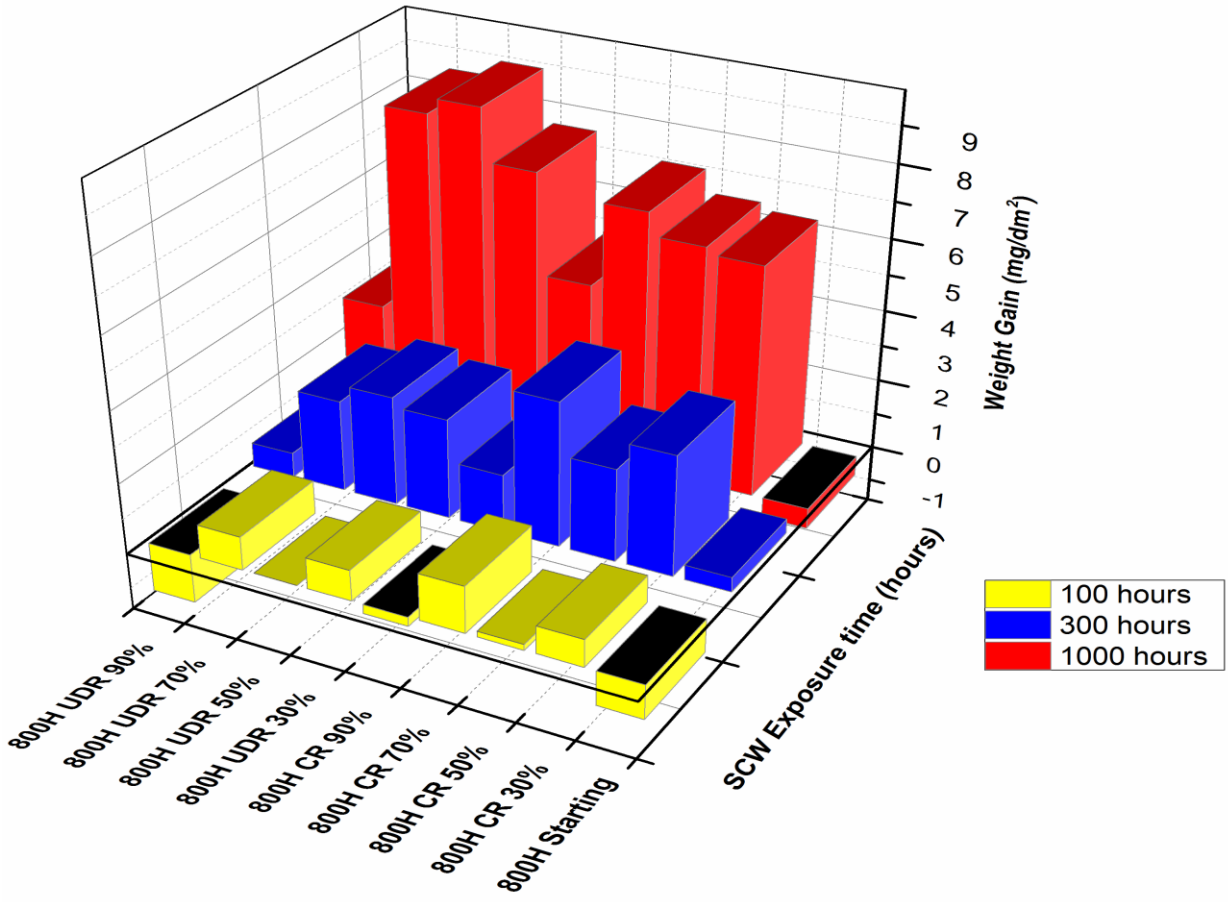

Fig. 7.1. Weight change of Incoloy 800H/HT samples at 100, 300 and 1000 hours of SCW exposure.

7.5.2. Oxide structure

All of the tested samples were characterized in terms of oxide appearance, surface morphology, oxide scale thickness, and oxide microstructure at the cross-section. For the ease of comparison and to avoid repetition, we report the important features and differences. Fig. 7.2 shows the images of the as-received and some of the exposed samples. The as-received sample exhibits a strong discoloration due to oxidation even after 100 hours. Upon increasing the exposure time, the oxide scale exfoliation and spallation are clearly visible in these samples. In the contrast, the UDR90 and CR90 samples show less discoloration and the oxide scale seems to be more

integrated. Although there are some spallation zones in UDR90 samples as indicated by the arrows (Fig.7.2.g), the CR90 samples have a uniform and cohesive oxide scale (Fig.7.2.j).

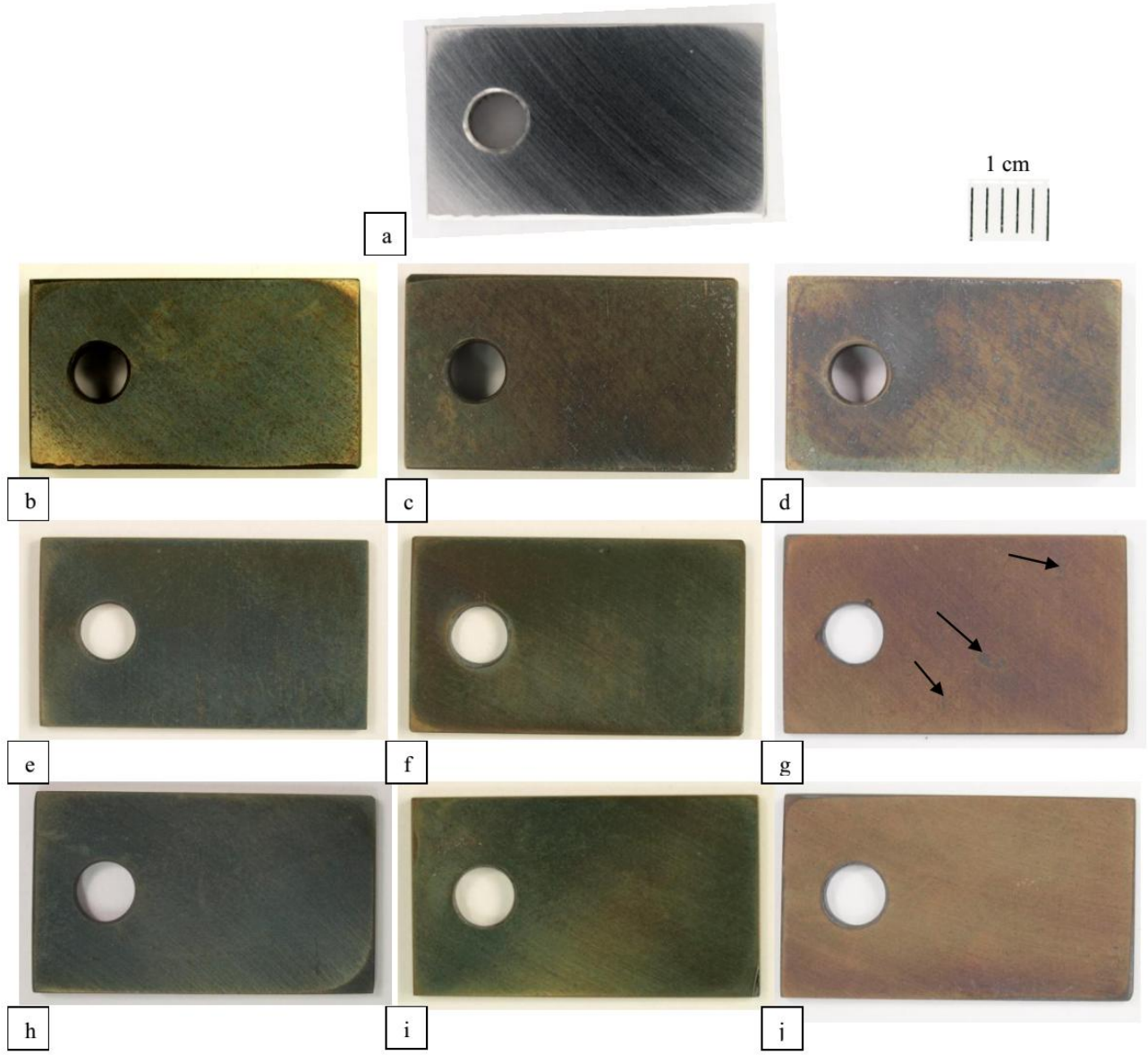

Fig. 7.2. Images of: a) starting (as received) before exposure, b, c, d) starting e, f, g) UDR90, h, i, j) CR90 after 100, 300 and 1000 hours of SCW exposure respectively.

In terms of oxide morphology, all the samples exhibit very similar typical features including Fe, Cr, Mn spinel and iron oxide islands. Fig.7.3 shows the surface morphology of the as-received and CR90 samples after 100, 300 and 1000 hours of SCW exposure. By increasing the SCW exposure time up to 1000 hours the iron oxide islands dramatically grow larger. However, for

most of the processed samples, the growth rate of these islands is significantly lower than for the as-received sample. These islands along with spinel matrix are the most frequent observed features on the oxide surface of Incoloy 800H/HT after exposure to SCW. These morphological differences suggest that these oxides might have different composition/structure. Fig. 7.4 illustrates these features with their associated elemental EDS maps. The presence of Ti beneath the iron oxide island implies that the titanium carbides might have some effects on the formation of these islands. The cross section of these typical features will be presented and discussed later.

In addition to iron oxide islands, there are other regions; including titanium carbides surrounded by chromium oxide (Fig. 7.4). These regions are associated with the titanium carbides in Incoloy 800H/HT which was exposed to SCW. Fig.7.5 illustrates the morphology and the elemental EDS maps of this type of regions at 100, 300 and 1000 hours of SCW exposure. After 100 hours, the titanium carbide is partially covered by chromium oxide. By increasing the exposure time up to 1000 hours, the surrounding chromium oxide grows larger in a volcano-shaped morphology and the carbides are gradually buried under the chromium oxide.

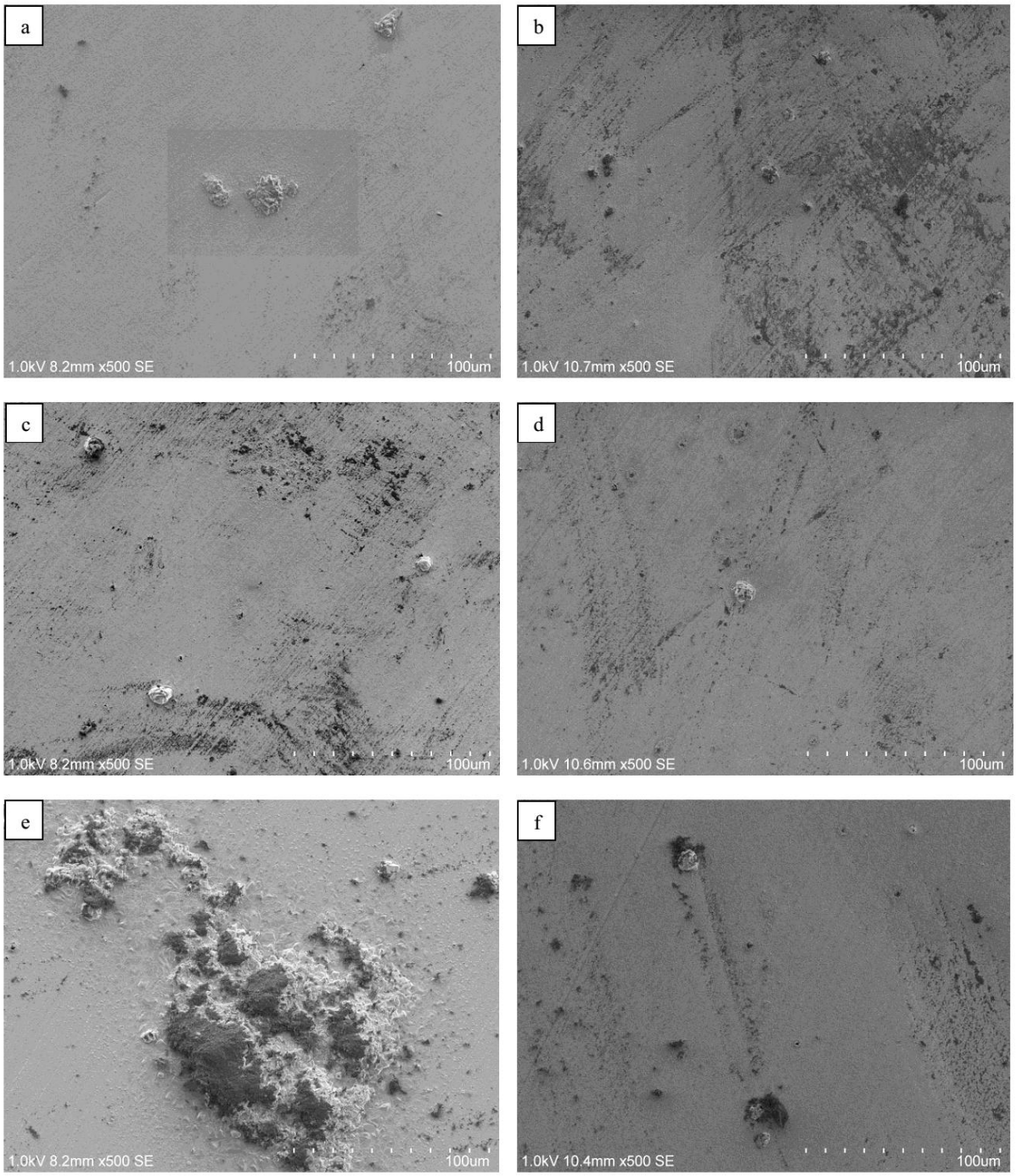

Fig. 7.3. SEM images of: as received at : (a)100, (c)300, (e)1000 hours and CR90 at: (b) 100, (d)300, (f)1000 hours of SCW exposure.

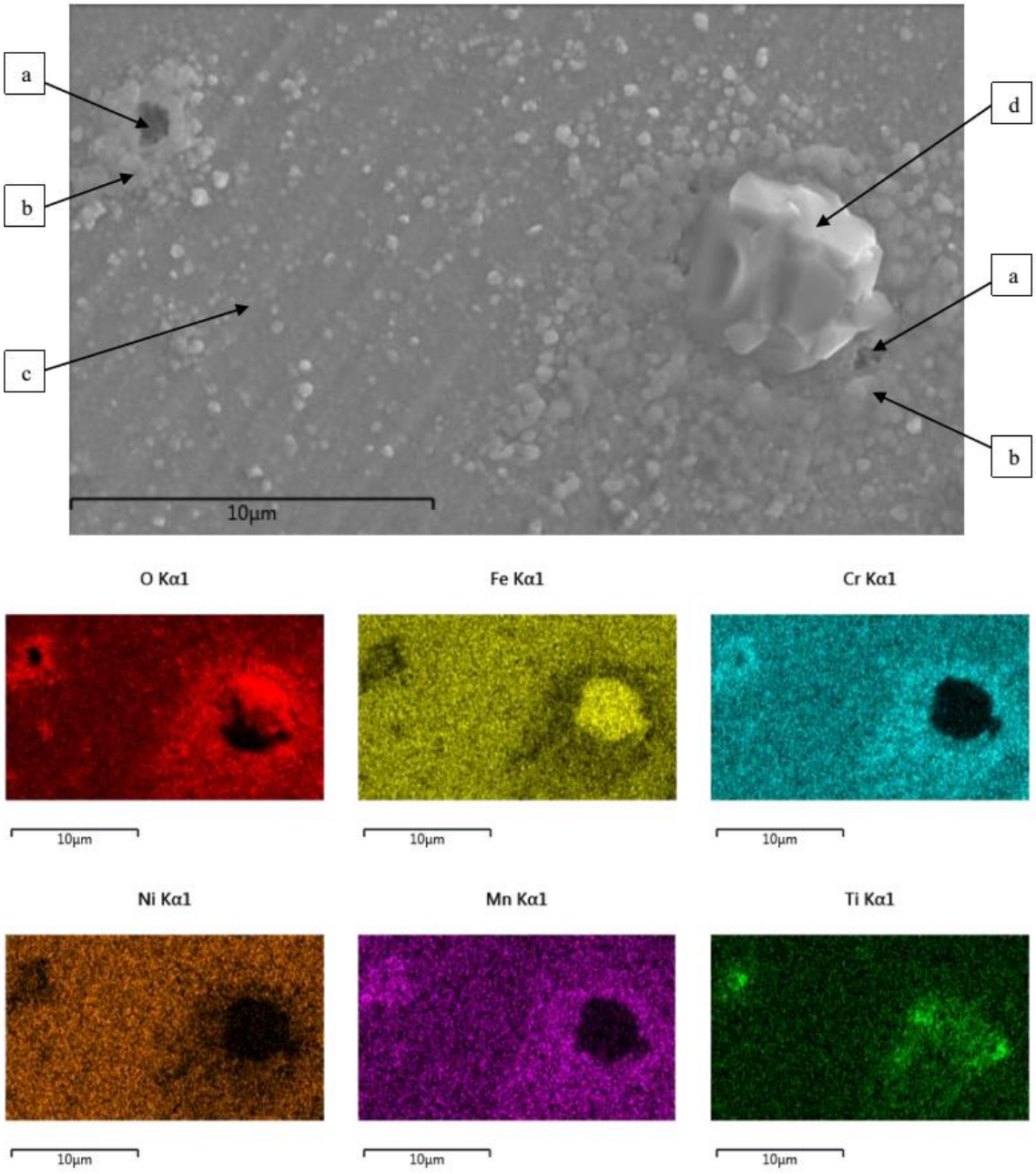

Fig. 7.4.SEM image with EDS maps showing different regions which formed during SCW oxidation of Incoloy 800H/HT: (a) titanium carbide precipitate, (b) enrich chromium oxide, (c) Fe, Cr, Ni spinel, (d) Fe oxide island.

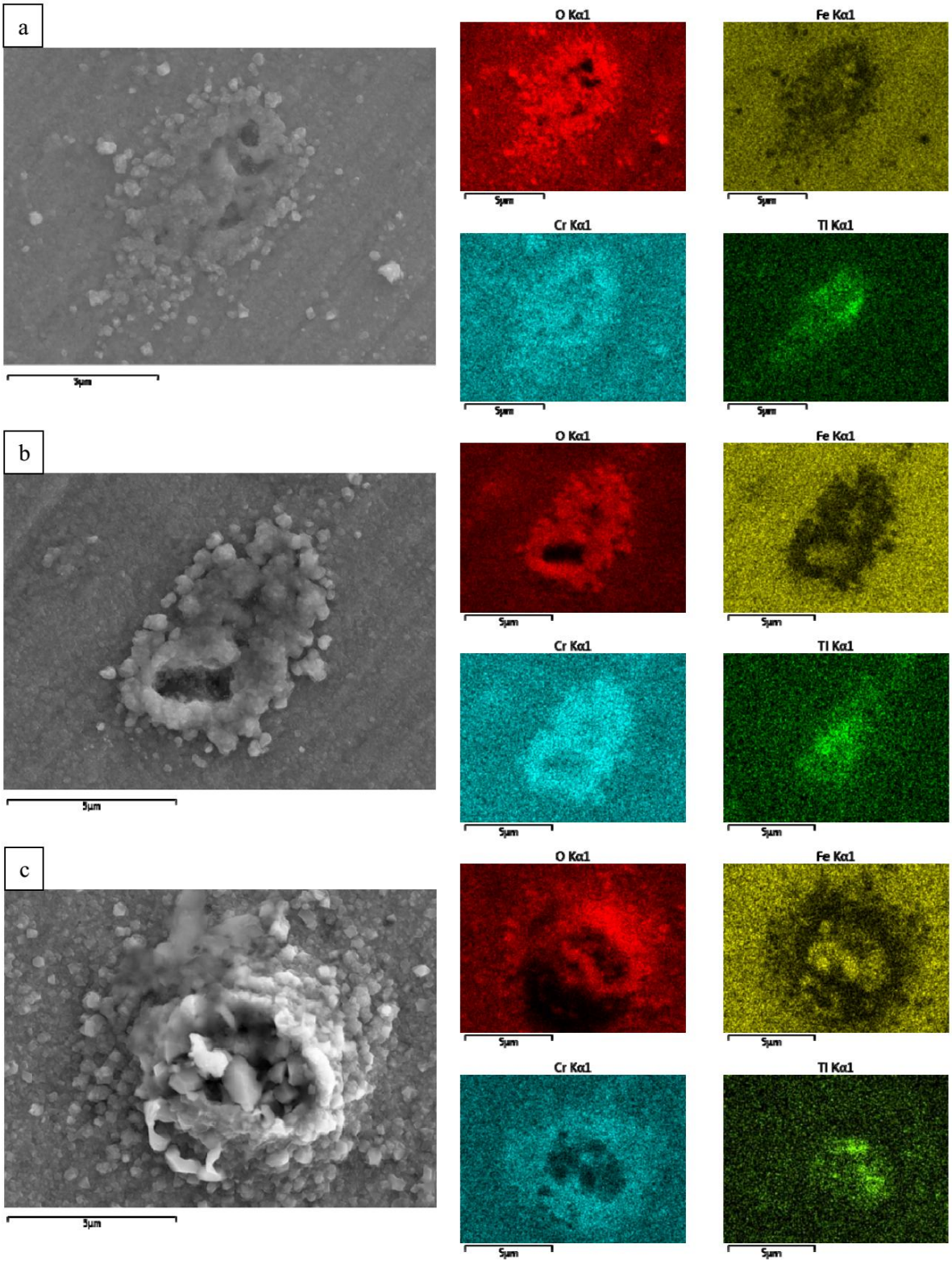

Fig. 7.5. SEM images of titanium containing regions after: (a) 100, (b) 300 and, (c) 1000 hours of exposure to SCW.

Furthermore, in order to clarify the role of carbides in the oxide scale, we investigate the cross-section of the oxides layer. We have studied several zones on the cross-section of the oxide layers particularly around the oxide islands. Fig. 7.6 and Fig. 7.7 illustrate two different types of islands cross-section that we observed on all of the SCW oxidized Incoloy 800H/HT samples, with their associated EBSD (band contrast, phase map, ND inverse pole figure, and Kernel misorientation map) and EDS maps. Comparing the EDS and EBSD maps, four phases could be identified; austenite (Incoloy 800H/HT), hematite (Fe_2O_3), TiC and magnetite (Fe_3O_4). Although EBSD is incapable of differentiating between magnetite and austenite due to their similar FCC structure, EDS maps play a complementary role in identifying them. The red arrows in Fig. 7.6.b and c and Fig. 7.7b and c indicate that the magnetite phase is beneath hematite. The first and most frequent case is that we found relative high Ti concentration adjacent to Mn,Cr spinel in the sub surface of the iron oxides (Fe_2O_3 and Fe_3O_4) scale (Fig.7.6). In the second case, we found internal mushroom-shaped islands of chromium oxide beneath the external iron oxide islands (Fig. 7.7).

We have also studied the oxide texture in the aforementioned cases. The pole figures of the oxide layer consisting of magnetite and hematite are presented in Fig. 7.8. There is a common maxima in (111) pole figure of FCC magnetite and (0001) pole figure of trigonal hematite. This is a commonly known relationship between the magnetite and hematite [141]. This relationship is also identified for the iron oxide layer in Fig. 7.7. Fig. 7.8 similarly shows the pole figures of magnetite and hematite from Fig.7.7. With respect to the oxide scale in Fig.7.6, magnetite and hematite orientation relationship are still the same, although the orientation of hematite has been changed. The presence of different carbides in each of these cases might be responsible for different oxide orientation.

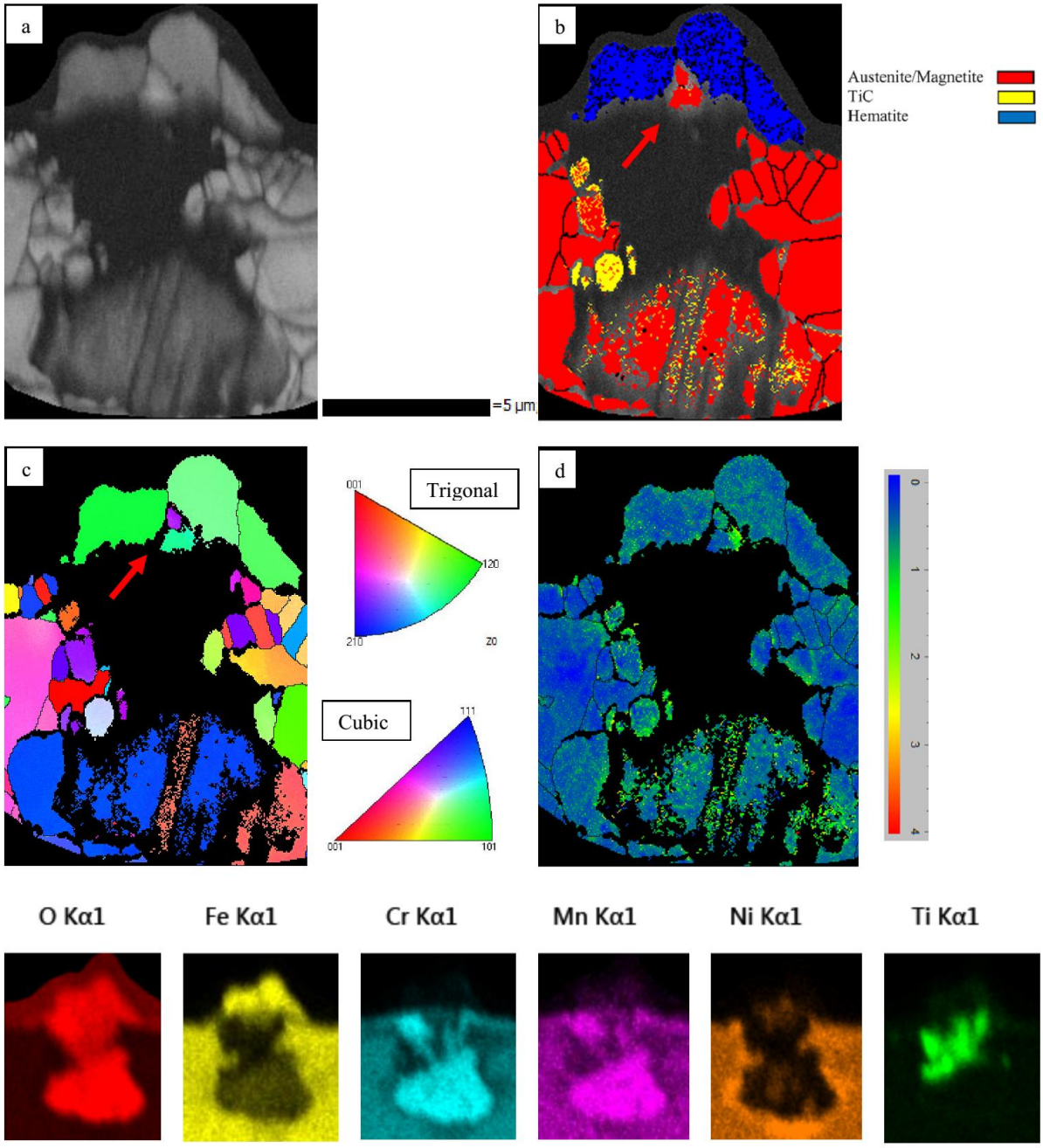

Fig. 7.6. EBSD (a) band contrast, (b) phase map, (c): IPF Z, (d) Kernel misorientation and EDS maps of iron oxide islands on the cross-section.

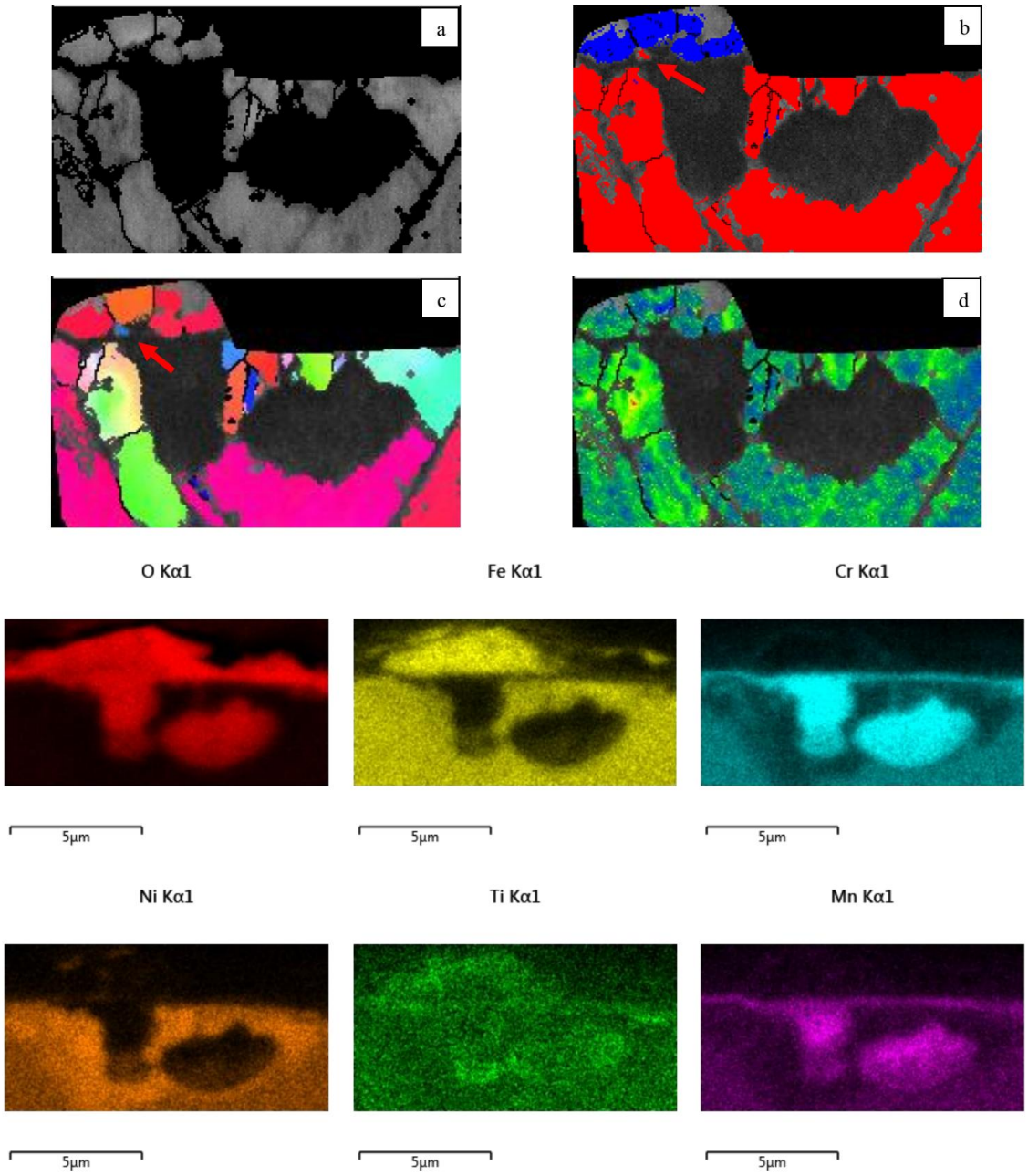

Fig. 7.7. EBSD and EDS maps of iron oxide islands on the cross-section without major titanium carbides (the legends are the same as Fig.58)

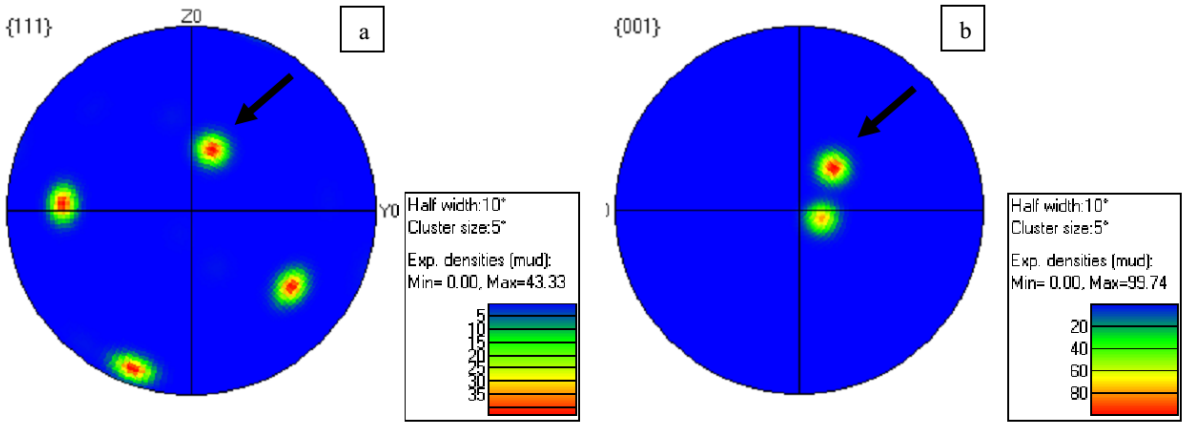

Fig. 7.8. Inverse pole figures of (a) magnetite (Fe_3O_4) and (b) hematite (Fe_2O_3) showing their orientation relationship of the oxide scale presented in Fig. 7.6.

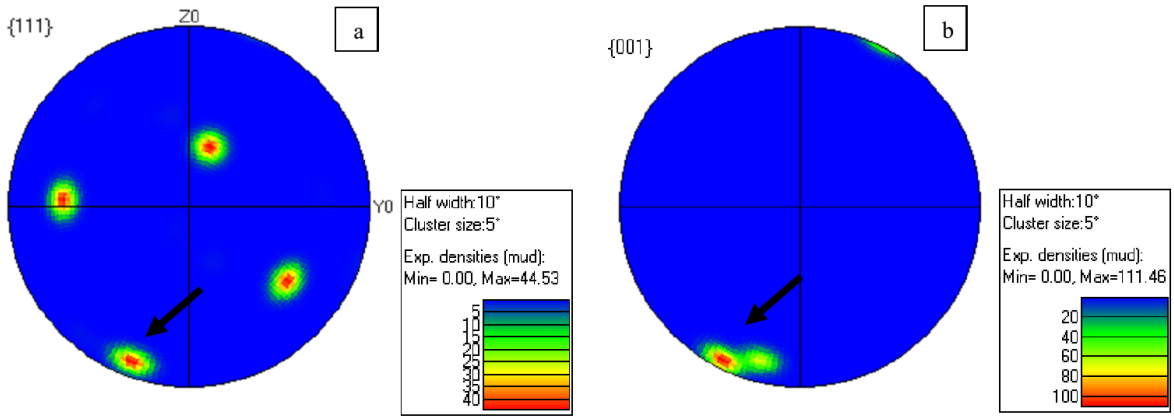

Fig. 7.9. Inverse pole figures of (a) magnetite (Fe_3O_4) and (b) hematite (Fe_2O_3) showing their orientation relationship of the oxide scale presented in Fig. 7.7.

7.6. Discussion

7.6.1. Effect of carbides

The oxidation of Incoloy 800 alloy family in SCW was reported in few studies [133,134,137,138]. In most of the available studies, the heterogeneous oxide surface morphology including iron oxide islands has been observed. However there is no explanation for their

formation in the available literature. Hence, we emphasize the results on the island formation and carbides presence in this study. As stated previously, upon analysing various areas on the cross-section of the oxide scale of the samples, we observed two different island formation cases. Fig. 7.6 and Fig. 7.7 represent these two cases respectively.

The EDS maps in Fig.7.6 suggest the presence of Cr,Mn spinel phase beneath the surface; however due to the small grain size of this oxide, EBSD technique was not able to detect it. The Mn map is almost identical to Cr maps which suggest the formation of $MnCr_2O_4$ spinel. This observation is in agreement with Mahboubi et al.[138] study on the oxide layer of Incoloy 800H after exposure to SCW. However these authors did not report any titanium content changes in the islands area. The presence of titanium precipitates between the $MnCr_2O_4$ spinel and iron oxides (Fe_2O_3 and Fe_3O_4) are clearly visible in the EDS maps of Fig. 7.6. In addition, EBSD phase map (Fig. 7.6.b) also depicts some of the titanium carbides grains. We have studied several cross-sections of these islands areas; all of them could be categorized in two different cases. The first and most frequent case is where a relatively high Ti concentration adjacent to $MnCr_2O_4$ in the sub surface of the iron oxides (Fe_2O_3 and Fe_3O_4) scale is present (Fig.7.6). In the second case, we found internal mushroom-shaped islands of chromium oxide beneath the external iron oxide island. Fig. 7.7 represents the case where an iron oxide island was formed on top of two internal chromium oxide islands. Indeed, Ti still exists in this region but its quantity is very less than the first case. Actually, the presence of titanium and chromium carbides together is rational since the larger carbides can act as nucleation site for other carbides in their forming stages [66,142]. Tan et al.[134], Fulger et al.[133,137] and Mahboubi et al.[138] observed the same mushroom-shaped oxide islands in SCW oxidation; however none of them addressed the origin of these islands. Fulger et al.[133] reported that there are no such islands at 450˚C; however by increasing the SCW temperature to 500˚C, 550˚C and 600˚C , the islands form and grow very fast. In other words, the higher the temperature, the larger the islands. Their observation implies that most likely the outward diffusion of iron and chromium along with inward diffusion of oxygen controls the formation of these islands. Nevertheless, still an important question remains unsolved; what makes the islands to form on specific spots? In other words, are we able to predict the islands location? Since the islands are formed on the surface and they grow larger with temperature, there should be a fast diffusion path for the species i.e. O, Cr, and Fe. The

observation of higher concentration of Ti and Cr close to the islands would suggest that Ti and Cr play important roles in the formation of $MnCr_2O_4$ spinel and iron oxide islands.

Incoloy 800H/HT is mainly strengthened by solution hardening as well as precipitation hardening with Cr and Ti carbides [14,66]. The presence of carbides can strongly influence the oxidation behavior of alloys [32,35,142–146]. The carbides which are located near to the oxidation surface can be oxidized by the inward diffusion of oxygen [142]. The oxidation of these carbides depends on the thermodynamics of their oxidation reaction at the exposure temperature, partial pressure of the oxygen in the oxidation media and their position at the oxidation front [145,147]. Selective oxidation of these carbides would result in a volume increase e.g. $TiO_2/TiC = 1.28$ [142]. Upon this volume increase, an expansion would be imposed to the oxide layer on the top of the carbide [142]. As a result, protective Cr_2O_3 and spinel layer may crack, providing fast diffusion path for the elements with outward diffusion tendency. This seems to be happening for the first case (Fig. 7.6). Similar scenario could happen for the Cr carbides (second case: Fig. 7.7) which are close to the oxidation front. Fig. 7.10 depicts these occurrences schematically. Regarding the partial pressure of oxygen in our SCW test set up, chromium carbide could convert to chromium oxide. This conversion, which is mostly occurred at the oxidation front, would form the internal mushroom-shaped islands of chromium oxide. Due to higher concentration of Cr in these islands, their surrounding region would be relatively depleted from Cr and concurrently concentrated with other alloying elements e.g. Ni and Fe. As a result, the amount of Cr is not enough to form a protective Cr oxide layer on the surface anymore. Therefore, Fe could easily diffuse to the surface and form the iron oxide islands. It is worthy to say that higher concentration of Ni nearby the internal Cr islands would also assist the Fe outward diffusion since $D_{Fe} \approx 4D_{Cr}$ in Ni [148]. Furthermore, due to the low solubility of Ni in Cr oxide, formation of $MnCr_2O_4$ islands would expel the Ni to the surroundings; which results in the slight enrichment of Ni, adjacent to the mushroom-shaped $MnCr_2O_4$ islands. At this point, Ni would act as a relative diffusion barrier for Cr and fast diffusion path for Fe since $D_{Fe} \approx 4D_{Cr}$ in Ni. Due to $D_O \approx 10^5 D_{Fe}$ in Ni [149], these Ni-enriched regions could also facilitate the inward diffusion of O which can promote the inner formation of $MnCr_2O_4$ islands.

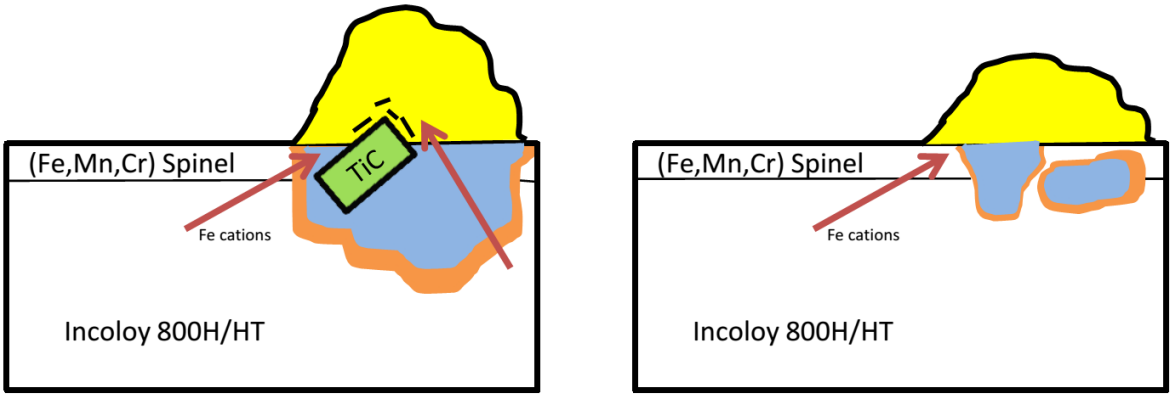

Fig. 7.10. Schematic figures showing the iron oxide islands cross-sections.

This phenomenon happens locally on the internal carbides region at the oxidation interface, consequently external islands of iron oxide are also formed locally. Indeed, at the beginning of the oxidation; selective oxidation of the carbides are limited to the surficial ones, however by proceeding the oxidation front, the lower depth carbides would be also exposed.

The smaller islands in CR90 sample particularly at higher SCW exposure periods (e.g.1000 hours) compared with the as-received sample (Fig.7.3), could be associated with smaller grain size. The smaller grain size provides higher grain boundary surface fraction which facilitates the diffusion of alloying elements. Cr has the highest diffusion coefficient in the Fe-Ni-Cr alloys; whereas $D_{Cr} > D_{Fe} > D_{Ni}$ [150]. Due to higher diffusion coefficient of Cr, chromium oxide would diffuse faster through any diffusion path (e.g. grain boundaries) and form the protective chromium oxide layer. This is consistent with mitigation of oxide weight change and exfoliation by decreasing the grain size as shown in Fig.7.1 and 7.2.

Furthermore, there is another interesting difference between two cases shown in Fig. 7.6 and 7.7. The kernel misorientation maps (Fig.7.6.d and Fig 7.7.d) depict the strain localization near the mushroom-shaped islands. In the former one, where the titanium carbides are present, there is less strain in nearby region. In the contrast, relatively higher strain is obserevd around the carbides in the latter case (Fig.7.7.d). Tan et al.[66] studied the precipitation of titanium and chromium carbides in Incoloy 800H in some details. They found that chromium carbides mostly precipitate on random/ high angle grain boundaries (HAGB) but most of the titanium carbides

tend to precipitate on special coincidence site lattice (CSL) boundaries. As CSL boundaries generally possess lower energy, it is expected to have less strain in the presence of titanium carbides (Fig. 7.6.d) than chromium carbides (Fig. 7.7.d). Due to oxidation and coarsening of grain boundaries at the oxidation front, we could not clearly identify the special grain boundaries here.

7.6.2. Effects of grain size

Grain boundaries are fast diffusion paths for cations and anions. Therefore the oxide growth strongly relies on the grain boundaries. Smaller grain size has more grain boundary surface which allows faster diffusion of oxide forming elements. Indeed, lowering the grain size would affect the oxidation in two potential offsetting effects; smaller grains allow faster diffusion of Cr and Mn to form the protective spinel layer. Concurrently, oxygen can also diffuse through these fast paths and enter the bulk metal to form internal oxides, which is not desirable. Typically, the amount of protective oxide-forming elements (e.g. Cr) in the bulk metal determines whether smaller grains are beneficial to mitigate oxidation. According to Incoloy 800H/HT composition, the Cr concentration is above the critical value of 17-20% to form a protective oxide layer [32].

Furthermore, hematite formation could be also assisted with decreasing the grain size. The higher grain boundaries surface would act as fast diffusion path for Fe cations to transfer to the oxidation interface. Providing more Fe at the interface with oxidizing media (i.e. SCW) would increase the tendency of hematite formation. Hematite typically has a more compact morphology and crystal lattice structure compared to magnetite [32].

7.6.3. Effects of GBCD

In order to characterize the role of grain boundary character distribution (GBCD) on the oxidation of Incoloy 800H/HT in SCW, we focused on some regions away from the oxidation front. We also compare the GBCD of the thermo-mechanically processed samples before and after SCW exposure to investigate the CSL boundaries stability upon aging at SCW environment. We found that there are no major changes in the GBCD after 1000 hours exposure to SCW. This could imply that the obtained CSL boundaries via thermo-mechanical processing were stable during the SCW testing condition. In addition to the GBCD of the samples that we

reported previously [151], we investigate some random regions approximately 300-500 μm away from the oxide interface. Fig. 7.11 illustrates a crack which has been formed after 1000 hours SCW exposure in the starting (as-received) sample. The crack propagation path is along the HAGB as an intergranular crack. The strain level around the HAGB is clearly higher than the CSL boundaries. Furthermore, it seems that some of the cracks are initiated from the incoherent titanium carbides interfaces. Interestingly, we can observe that there are some points at which the crack has been arrested by a secure triple junction[3] which has two CSL boundaries. This is clearer in the 50UDR sample (Fig. 7.12) with more visible titanium carbides. The secure triple junctions are indicated by arrows. Although not all the junctions could be indexed due to oxidation and grain boundary coarsening, still we can see that the number of these junctions in the 50UDR sample is significantly higher than the starting (as-received) one. Moreover, the average kernel misorientation is lower in the thermo-mechanically processed sample, which makes it less vulnerable to crack propagation.

[3] A secure triple junction, which is a triple junction which resist against further propagation of a crack, two of the three connected boundaries should be low energy boundaries (e.g. CSL). When the crack reach the secure junction, further crack propagation would be arrested by the two CSL boundaries, even though the third boundary is random [109].

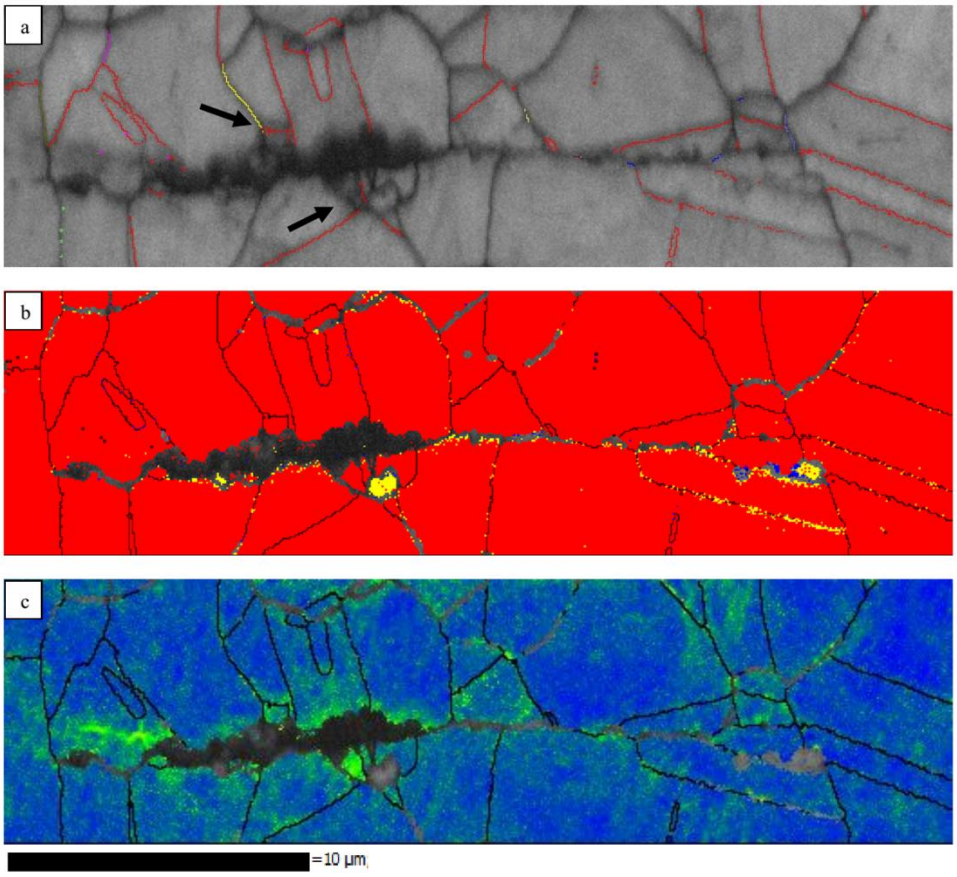

Fig. 7.11. EBSD maps (a) band contrast with CSL, (b) phase map, (c) Kernel misorientation of Incoloy 800H/HT starting (as-received) sample after 1000 hours SCW exposure. Σ3:red, Σ7:blue, Σ9:violet, Σ11:yellow, Σ27:green

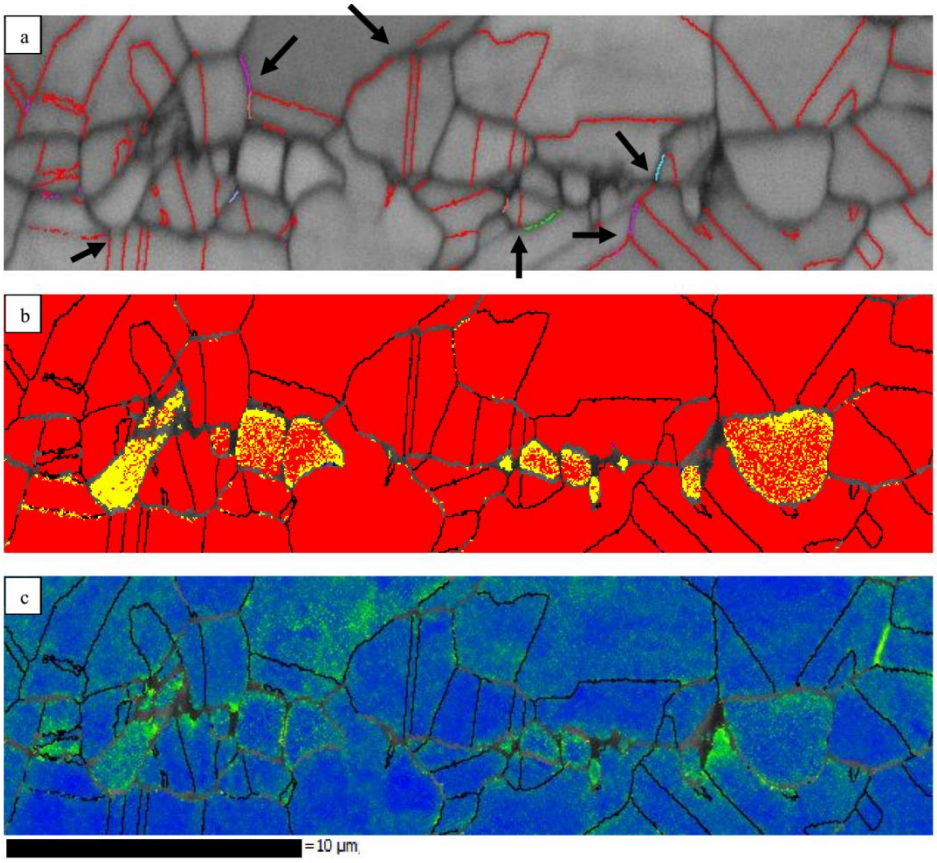

Fig. 7.12. EBSD maps (a) band contrast with CSL, (b) phase map, (c) Kernel misorientation of Incoloy 800H/HT UDR50 sample after 1000 hours SCW exposure. Σ3:red, Σ7:blue, Σ9:violet, Σ11:yellow, Σ27:green

7.6.4. Effect of texture

As we showed previously, UDR and CR samples exhibit different textures [97]. Texture of UDR samples mainly consists of Copper {112}<111> and Goss {110}<001> while it is Brass {110}<112> for the CR samples [97,124]. Brass and Goss share similar plane but Copper has a different plane. In principle, different crystallographic planes have different atomic density. Furthermore, diffusion through atomic planes strongly depends on the atomic plane density i.e. compactness. In FCC crystal structure, {110} planes have higher planar atomic density than {112} planes. Therefore faster diffusion is expected to happen along {112} planes. This is also in agreement with other oxidation studies on the FCC planes [152,153]. Having said that, we expect to observe a higher oxidation in UDR samples possessing Copper texture component. Fig.7.1

confirms that the UDR samples show higher weight change than CR samples, although the differences are not significant.

There are some differences in the existing literatures concerning the oxidation of Incoloy 800 family (800H, 800HT, 800H/HT) in SCW [133,134,137,138]. These differences in morphology, composition and structure of oxides are depending on the SCW test apparatus and conditions (e.g. temperature, static/dynamic, flow rate, dissolved oxygen content), as well as the exact alloy composition.

7.7. Conclusion

In the present study, we investigated the oxidation of thermo-mechanically processed Incoloy 800H/HT in SCW. The results would contribute to oxidation behavior database of various alloys in SCW for application in GEN IV SCWR. The main conclusions of the study are as follows:

- The oxidation resistance in SCW has been improved by the thermo-mechanical processing. Upon this improvement, not only the oxide scale spallation and exfoliation has mitigated, but also the size of external iron oxide has been reduced.

- Altering the GBCD was found to be effective in improving the oxidation resistance of Incoloy 800H/HT in SCW, particularly at the incoherent interfaces of carbides on the oxide scale. These interfaces appear to be susceptible to crack propagation. Increasing the CSL boundaries along with secure triple junctions would suppress the crack propagation and could enhance the oxidation resistance.

- Decreasing the grain size also improved the oxidation resistance of Incoloy 800H/HT in SCW. Smaller grain size provides faster diffusion path for Cr cation and enables them to reach the surface and form the protective Cr_2O_3. Moreover, the smaller grain size would encourage the formation of hematite.

- UDR samples showed higher weight change compared to CR samples. This is associated with the different textures and particularly the presence of Copper texture component in UDR samples.

CHAPTER 8

CONCLUSION AND FUTURE WORK

8.1. CONCLUSION

In this thesis, Zircaloy-4 as the current fuel cladding material, and Incoloy 800H/HT as a candidate for future fuel cladding materials, were studied. The objectives of this study were fulfilled as follows:

The role of surface roughness on the properties of the current fuel cladding was elaborated in detail. Increasing the surface roughness effect resulted in higher weight gain upon oxidation in air and autoclave environments. Analysis of the oxide texture showed that by increasing the oxidation time, the pole figures' intensity was increased. Although there were considerable changes in zirconium substrate texture, no major differences were detected in the oxide texture. The most significant difference detected during the oxide growth stage was the decreasing percentage of tetragonal phase content in the oxide layer.

Considering the results, it was concluded that surface roughness have some effects on the oxidation, hydriding and mechanical properties of Zircaloy-4. Increasing the surface roughness would increase the weight gain due to the surface area effect and/or the amount of tetragonal phase. The surface area effect is more noticeable at the initial oxidation stages.

A novel experimental method, based on the synchrotron radiation for characterizing zirconium alloys in the oxidized and hydrided states was developed. Using these techniques, a qualitative analysis of Zr electronic structure at its oxide, hydride and alloyed states was performed. Various oxidation, hydriding and surface roughness treatments were applied to the pure Zr and Zircaloy-4 model alloy to define their effects and differences on the XPS and XANES spectra. In order to decipher the differences in XANES spectra, DFT simulations using WIEN2k code was done. Comparing the experimental with simulations spectra, it was found that the monoclinic phase of ZrO_2 offers a stronger barrier against hydrogen ingress as compared to the tetragonal phase. Moreover, a perspective insight of using synchrotron-based techniques for characterizing the Zr compounds was offered.

In addition to the current fuel cladding material, Incoloy 800H/HT as a candidate material for future fuel cladding material was studied. Since texture can influence a wide range of material properties including formability, weldability, creep, oxidation and radiation resistance, a comprehensive textural study of deformed - through various rolling strains with two different rolling modes - and then annealed samples of Incoloy 800H/HT was performed. Two different textures were obtained through two rolling modes: unidirectional rolling (UDR) and cross-rolling (CR). The final deformation texture of UDR samples was a typical brass texture while the dominant texture of the cross-rolled samples oscillated between brass and ND rotated brass. Also, it was found that the final recrystallized texture depends on the deformation mode applied before annealing: for UDR samples, a combination of Goss, copper and rotated brass textures was dominant, while the CR samples retained the brass texture.

In pursuit of the texture origin in the differently rolled samples (UDR and CR), the macro and micro texture evolution and kinetics of recrystallization in the highly deformed Incoloy 800H/HT along with two different rolling paths were studied. EBSD investigations show that the presence of (111) // ND grains in UDR samples led to extensive twin formation, which mainly resulted in copper and Goss formation. The results show that oriented nucleation played a significant role in determining the final annealing texture, although clear footprints of oriented growth can be tracked in the formation of Cu and Rex-B components. Besides, it is found that the UDR samples exhibited a faster recrystallization kinetic. The presence of γ-fibre with a higher stored energy was responsible for altering the recrystallization rate upon changing the rolling mode.

The GBCD evolution of the TMP samples, with a view to the feasibility of grain boundary engineering in Incoloy 800H/HT, was also analyzed. It was found that the uunidirectional rolling mode initially led to enhanced Σ3 boundaries up to 50% deformation. However, by increasing the strain the number of Σ3 boundaries slightly declined. Cross-rolled samples possessed a higher fluctuation in the Σ3 boundaries particularly in lower deformation strains (<50%). Furthermore, different rolling paths were resulted to different interactions and numbers of $\Sigma 3^n$ boundaries. Indeed, the mechanism of twinning proliferation was found to be different in UDR and CR samples. For UDR samples, new twin formation was the main mechanism, while twin regeneration and interactions of $\Sigma 3^n$ boundaries were the dominant ones for the CR samples.

Proliferation of $\Sigma 3^n$ boundaries and connectivity disruption of High Angle Grain Boundaries (HAGB) networks were mainly observed in low to medium deformation (<50%) with UDR and medium to high deformation (≥50%) with CR. Hence, the proposed TMP in the aforementioned criteria shows the potential for GBE of Incoloy 800H/HT.

Finally, the oxidation resistance of the thermo-mechanically processed samples in supercritical water was evaluated and the role of various microstructural parameters was investigated. The oxidation resistance in SCW had been improved by the thermo-mechanical processing. Upon this improvement, not only the oxide scale spallation and exfoliation has mitigated, but also the size of external iron oxide has been reduced.

It was found that altering the GBCD is effective in improving the oxidation resistance of Incoloy 800H/HT in SCW, particularly at the incoherent interfaces of carbides on the oxide scale. These interfaces appear to be susceptible to crack propagation. Increasing the coincidence site lattice (CSL) boundaries along with secure triple junctions would supress the crack propagation and could enhance the oxidation resistance.

Furthermore, decreasing the grain size also improved the oxidation resistance of Incoloy 800H/HT in SCW. Smaller grain size provides a faster diffusion path for Cr cation to reach the surface and form the protective Cr_2O_3. Moreover, the smaller grain size would encourage the formation of hematite. Besides, the UDR samples showed higher weight change compared to the CR samples. This is correlated to the different textures and particularly the presence of copper texture component in UDR samples.

8.2. CONTRIBUTIONS TO ORIGINAL KNOWLEDGE

- The role of surface roughness on the properties of the Zircaloy-4 fuel cladding

  The effect of surface roughness on the oxide structure, texture, allotropies, hydriding, oxidation rate and weight gain of Zircaloy-4 fuel cladding tubes was studied. The presented results show that the surface roughness affects the oxidation behavior of Zircaloy-4, particularly at the initial oxidation stages.

- Synchrotron-based techniques for characterizing zirconium oxide and hydride

  A novel experimental method, based on synchrotron radiation, for characterizing zirconium alloys in their oxidized and hydrided states was developed for the first time. Utilizing this method, for the first time, a qualitative analysis of the electronic structure of Zr in its oxide, hydride and alloyed states was performed and a perspective insight regarding using synchrotron-based techniques for characterizing the Zr compounds was offered.

- The deformation and recrystallization textures in differently rolled Incoloy 800H/HT in a wide range of deformation strains

  The deformation and recrystallization textures as well as recrystallization kinetics of Incoloy 800H/HT, heavily deformed via different strain paths, were analyzed and discussed in detail for the first time.
  The origin of texture differences was identified and explained with the aim of orientation imaging microscopy.

- The effect of microstructure and GBCD on the oxidation resistance of Incoloy 800H/HT in supercritical water

  The presence of iron oxide islands and the effect of carbides on the oxidation behavior of Incoloy 800H/HT in supercritical water were elaborated for the first time.
  The effects of grain size, texture and GBCD on the oxidation resistance of Incoloy 800H/HT was discussed for the first time.

8.3. FUTURE WORK

- In Chapter 2, the effect of surface roughness on texture and oxidation of Zircaloy-4 tubes was studied. Since the coolant surrounds these cladding tubes in a reactor, it would be informative to evaluate the thermo-hydraulic effects of surface roughness in reactor environments.

- In Chapter 3, Zr $M_{4,5}$ XANES spectra was measured with synchrotron radiation. Measurement and simulation of Zr $L_{2,3}$ XANES and EXAFS would be useful to develop a complete model for simultaneous zirconium oxidation and hydriding. Furthermore, to elaborate the role of hydride concentration in the model, samples with various hydride contents could be tested.

- In Chapter 5, the recrystallization of a heavily rolled (90%) Incoloy 800H/HT was studied. A future work could consider the same experimental procedure for a medium deformed (50-70%) alloy to investigate the preferred nucleation sites. Moreover, in-situ annealing of a medium deformed sample could reveal remarkable information about the very beginning of the nucleation stage.

- In Chapter 6, a potential of engineering the grain boundaries in Incoloy 800H/HT was shown. It would be of great interest to evaluate the extent to which this microstructural manipulation may affect the mechanical and physical properties (for example stress corrosion cracking or tensile and creep strength) of Incoloy 800H/HT.

- In Chapter 7, it was shown that the carbides play a significant role in the heterogeneous morphology of Incoloy 800H/HT oxide layer. It would be of interest to apply a specific heat treatment to remove the carbides and investigate the oxidation behavior of Incoloy 800H/HT to determine to what extent carbides are effective.

- In Chapter 6 and Chapter 7, the evolution of grain boundary character distribution and oxidation resistance of Incoloy 800H/HT in SCW were studied respectively. It would be of great importance to investigate the effect of irradiation on the stability of grain boundary character distribution, as well as the oxidation behavior of Incoloy 800H/HT in SCW.

References

[1] U.S. DOE Nuclear Energy Research Advisory Committee and the Generation IV International Forum, A Technology Roadmap for Generation IV Nuclear Energy Systems, 2002.

[2] www.world-nuclear.org/info/Current-and-Future-Generation/Nuclear-Power-in-the-World-Today/ (2014).

[3] C.R.F. Azevedo, Eng. Fail. Anal. 18 (2011) 1943.

[4] The OECD Nuclear Energy Agency for the Gen IV International Forum, Technology Roadmap Update for Generation IV Nuclear Energy Systems, 2014.

[5] U.S. DOE Nuclear Energy Research Advisory Committee and the Generation IV International Forum, Gen IV International Forum Annual Report, 2008.

[6] T. Allen, J. Busby, M. Meyer, D. Petti, Mater. Today 13 (2010) 14.

[7] S. Baindur, Bull. Can. Nucl. Soc. 29 (2008) 32.

[8] C. Sun, R. Hui, W. Qu, S. Yick, Corros. Sci. 51 (2009) 2508.

[9] G.S. Was, S. Teysseyre, in:, T.R. Allen, P.J. King, L. Nelson (Eds.), Proc. 12th Int. Conf. Environ. Degrad. Mater. Nucl. Power Syst. – Water React., TMS, 2005.

[10] K. Barbalace, (n.d.).

[11] L. Tan, K. Sridharan, T.R. Allen, J. Nucl. Mater. 348 (2006) 263.

[12] W. Ren, R. Swindeman, in:, Proc. ASME 2010 Press. Vessel. Pip. Div., Bellevue, Washington, 2010.

[13] A.K. Roy, V. Virupaksha, Mater. Sci. Eng. A 452-453 (2007) 665.

[14] Special Metals Corporation, INCOLOY Alloy 800H & 800HT, 2004.

[15] L. Tan, T.R. Allen, J.T. Busby, J. Nucl. Mater. 441 (2013) 661.

[16] G. Gupta, P. Ampornrat, X. Ren, K. Sridharan, T.R. Allen, G.S. Was, J. Nucl. Mater. 361 (2007) 160.

[17] L. Tan, K. Sridharan, T.R. Allen, J. Nucl. Mater. 371 (2007) 171.

[18] T. Watanabe, Res Mech. Int. J. Struct. Mech. Mater. Sci. Volume 11 (1984) 47.

[19] H. Abe, M. Furugen, J. Mater. Process. Technol. 212 (2012) 1687.

[20] M. Furugen, C. Hayashi, J. Mech. Work. Technol. 10 (1984) 273.

[21] O. Montmitonnet, R. Loge, M. Hamery, Y. Chastel, J. Doudoux, J. Aubin, J. Mater. Process. Technol. 126 (2002) 814.

[22] A.. Huntz, B. Lefevre, F. Cassino, Mater. Sci. Eng. A 290 (2000) 190.

[23] D.P. Guillen, T.S. Yoder, Nucl. Eng. Des. 238 (2008) 2480.

[24] P.-Å. Krogstadt, R.A. Antonia, Exp. Fluids 27 (1999) 450.

[25] S. Uran, B. Veal, M. Grimsditch, J. Pearson, A. Berger, Oxid. Met. 54 (2000) 73.

[26] J.L. Evans, J. Mater. Eng. Perform. 19 (2010) 1001.

[27] J. Lin, H. Li, J.A. Szpunar, R. Bordoni, A.M. Olmedo, M. Villegas, A.J.G. Maroto, Mater. Sci. Eng. A 381 (2004) 104.

[28] A. Yilmazbayhan, A.T. Motta, R.J. Comstock, G.P. Sabol, B. Lai, Z. Cai, J. Nucl. Mater. 324 (2004) 6.

[29] W. Qin, C. Nam, H. Li, J. Szpunar, Acta Mater. 55 (2007) 1695.

[30] B. Bhushan, ed., Modern Tribology Handbook, CRC Press, 2001.

[31] J.H. Baek, K.B. Park, Y.H. Jeong, J. Nucl. Mater. 335 (2004) 443.

[32] N. Birks, G. H.Meier, F.S. Pettit, High-Temprature Oxidation of Metals, 2nd ed., Cambridge University Press, 2006.

[33] W.B. Blumenthal, The Chemical Behaviour of Zirconium, D. Van Nostrand Inc., 1985.

[34] E. Tenckhoff, J. ASTM Int. 2 (2005) 1.

[35] J. Favergeon, C.Valot, T. Montesin, G. Bertrand, Mater. Sci. Forum 408-412 (2002) 999.

[36] N. Pétigny, P. Barberis, C. Lemaignan, C. Valot, M. Lallemant, J. Nucl. Mater. 280 (2000) 318.

[37] X. Iltis, F. Lefebvre, C. Lemaignan, J. Nucl. Mater. 224 (1995) 109.

[38] B. Cox, J. Nucl. Mater. 249 (1997) 87.

[39] M.G. Glavicic, J.A. Szpunar, Y.P. Lin, J. Nucl. Mater. 245 245 (1997) 147.

[40] E. Djurado, P. Bouvier, G. Lucazeau, J. Solid State Chem. 149 (2000) 399.

[41] P. Barberis, J. Nucl. Mater. 226 (1995) 34.

[42] A.J.G. Maroto, R. Bordoni, M. Villegas, A.M. Olmedo, M.A. Blesa, A. Iglesias, P. Koenig, J. Nucl. Mater. 229 (1996) 79.

[43] N. A. P. Kiran Kumar, J. A. Szpunar, Z. He, J. Nucl. Mater. 403 (2010) 101.

[44] T.R. Allen, R.J.M. Konings, A.. Motta, Compr. Nucl. Mater. 5 (2012) 49.

[45] J.A. Szpunar, W. Qin, H. Li, N.A.P. Kiran Kumar, J. Nucl. Mater. 427 (2012) 343.

[46] H. Akhiani, J.A. Szpunar, Appl. Surf. Sci. 285 (2013) 832.

[47] H. Akhiani, J. Szpunar, in:, 33rd Annu. Conf. Can. Nucl. Soc., 2012, pp. 1–10.

[48] M. Boots, D. Muir, A. Moewes, J. Synchrotron Radiat. 20 (2013) 272.

[49] A. Roustila, J. Chene, C. Severac, J. Alloy Compd. 357 (2003) 330.

[50] Y.M. Wang, Y.S. Li, P.C. Wong, K.A.R. Mitchel, Appl. Surf. Sci. 72 (1993) 237.

[51] W.F. Stickle, P.E. Sobol, J. Chastain, R.C. King, Handbook of X-Ray Photoelectron Spectroscopy, Physical Instruments Inc., 1995.

[52] P. Blaha, K. Schwarz, G. Madsen, D. Kvasnicka, J. Luitz, WIEN2k, An Augmented Electronic, Plane Wave+Local Orbitals Program for Calculating Crystal Properties, Techn. Universitat Wien, Austria, 2001.

[53] N.A.P. Kiran Kumar, J.A. Szpunar, Mater. Sci. Eng. A 528 (2011) 6366.

[54] V.N. Fokin, Y.U.I. Malov, E.E. Fokina, S.P. Shilkin, Int. J. Hydrogen Energy 21 (1996) 969.

[55] A. Gomez Sanchez, W. Schreiner, G. Duffó, S. Ceré, Appl. Surf. Sci. 257 (2011) 6397.

[56] K. Linga Murty, I. Charit, Prog. Nucl. Energy 48 (2006) 325.

[57] B.W. Veal, D.J. Lam, D.G. Westlake, Phys. Rev. B 19 (1979).

[58] C.-O.A. Olsson, D. Landolt, Corros. Sci. 46 (2004) 213.

[59] B. Luerßen, J. Janek, S. Günther, M. Kiskinova, R. Imbihl, Phys. Chem. Chem. Phys. 4 (2002) 2673.

[60] A. Lyapin, L.P.H. Jeurgens, P.C.J. Graat, E.J. Mittemeijer, J. Appl. Phys. 96 (2004) 7126.

[61] S. Yamanaka, K. Yamada, K. Kurosaki, M. Uno, K. Takeda, H. Anada, T. Matsuda, S. Kobayashi, J. Alloys Compd. 330-332 (2002) 313.

[62] P. Steiner, S. Hufner, N. Martensson, B. Johansson, Solid State Commun. 37 (1981) 73.

[63] A. Yilmazbayhan, A.T. Motta, R.J. Comstock, G.P. Sabol, B. Lai, Z. Cai, J. Nucl. Mater. 324 (2004) 6.

[64] K. Mo, G. Lovicu, H.-M. Tung, X. Chen, Y. Miao, J.B. Hansen, J.F. Stubbins, J. Nucl. Mater. 443 (2013) 366.

[65] H.M. Tawancy, A. Ul-Hamid, A.I. Mohammed, N.M. Abbas, Mater. Des. 28 (2007) 686.

[66] L. Tan, L. Rakotojaona, T.R. Allen, R.K. Nanstad, J.T. Busby, Mater. Sci. Eng. A 528 (2011) 2755.

[67] Special Metals Corporation, The Story of the "INCOLOY Alloy Series" from 800 through 800H, 800HT, 2004.

[68] N.P. Gurao, S. Sethuraman, S. Suwas, Mater. Sci. Eng. A 528 (2011) 7739.

[69] P.P. Bhattacharjee, M. Joshi, V.P. Chaudhary, J.R. Gatti, M. Zaid, Metall. Mater. Trans. A 44 (2013) 2707.

[70] M.Y. Huh, S.Y. Cho, O. Engler, Mater. Sci. Eng. A 315 (2001) 35.

[71] O. Engler, V. Randle, Introduction to Texture Analysis, 2nd ed., CRC Press, 2010.

[72] B. Ravi Kumar, B. Mahato, N.R. Bandyopadhyay, D.K. Bhattacharya, Mater. Sci. Eng. A 394 (2005) 296.

[73] R.D. Doherty, D.A. Hughes, F.J. Humphreys, J.J. Jonas, D.J. Jensen, M.E. Kassner, W.E. King, T.R. McNelley, H.J. McQueen, A.D. Rollett, Mater. Sci. Eng. A 238 (1997) 219.

[74] F.J. Humphreys, J. Mater. Sci. 6 (2001) 3833.

[75] B. Verlinden, J. Driver, I. Samajdar, R.D. Doherty, Thermo-Mechanical Processing of Metallic of Metallic Materials, Elsevier, Pergamon Press, Oxford, 2007.

[76] G. Wassermann;, J. Grewen, Texturen Metallischer Werkstoffe, Springer, Berlin, 1962.

[77] K. Sekine, J. Wang, Mater. Trans. 40 (1999) 1.

[78] T. Leffers, R.K. Ray, Prog. Mater. Sci. 54 (2009) 351.

[79] F.J. Humphreys, M. Hatherly, Recrystallization and Related Annealing Phenomena, Elsevier, Oxford, 2004.

[80] T. Leffers, Textures Microstruct. 22 (1993) 53.

[81] A.A. Saleh, E. V. Pereloma, A.A. Gazder, Mater. Sci. Eng. A 528 (2011) 4537.

[82] N. Rajmohan, J. Szpunar, Acta Mater. 48 (2000) 3327.

[83] K. Sztwiertnia, Mater. Lett. 123 (2014) 41.

[84] K. Sztwiertnia, Int. J. Mater. Res. 99 (2008) 178.

[85] L. Bracke, K. Verbeken, L. Kestens, J. Penning, Acta Mater. 57 (2009) 1512.

[86] U. Schmidt, K. Lucke, Texture Cryst. Solids 3 (1979) 85.

[87] S.G. Chowdhury, S. Das, P.K. De, Acta Mater. 53 (2005) 3951.

[88] K. Lucke, in:, C.M. Brakman, E.J. Mittemeijer (Eds.), ICOTOM 7, Netherlands Society for Materials Science, 1984, p. 195.

[89] R.E. Schramm, R.P. Reed, Metall. Mater. Trans. A 6A (1975).

[90] I.. Dillamore, W.. Roberts, Acta Metall. 12 (1964).

[91] S.G. Chowdhury, S. Datta, B.R. Kumar, P.K. De, R.N. Ghosh, Mater. Sci. Eng. A 443 (2007) 114.

[92] M. Sekine, N. Sakaguchi, M. Endo, H. Kinoshita, S. Watanabe, H. Kokawa, S. Yamashita, Y. Yano, M. Kawai, J. Nucl. Mater. 414 (2011) 232.

[93] S. Wronski, M. Wrobel, A. Baczmanski, K. Wierzbanowski, Mater. Charact. 77 (2013) 116.

[94] Z.R. Zhang, K. Sekine, Mater. Sci. Eng. A 423 (2006) 243.

[95] S. Suwas, N.P. Gurao, in:, M.S.J. Hashmi (Ed.), Compr. Mater. Process., Elsevier, 2014, pp. 81–105.

[96] Y.H. Sha, C. Sun, F. Zhang, D. Patel, X. Chen, S.R. Kalidindi, L. Zuo, Acta Mater. 76 (2014) 106.

[97] H. Akhiani, M. Nezakat, J. Szpunar, Mater. Sci. Eng. A (2014) DOI: 10.1016/j.msea.2014.07.035.

[98] N.P. Gurao, SAE Tech. Pap. (2014).

[99] T. Morikawa, K. Higashida, Mater. Trans. 51 (2010) 620.

[100] J. Park, J. Szpunar, Acta Mater. 51 (2003) 3037.

[101] W.G. Burgers, Nature 160 (1947) 398.

[102] D. Barbier, N. Gey, S. Allain, N. Bozzolo, M. Humbert, Mater. Sci. Eng. A 500 (2009) 196.

[103] J.W. Christian, S. Mahajan, Prog. Mater. Sci. 39 (1995) 1.

[104] E. Aernoudt, P. Van Houtte, T. Leffers, in:, Mater. Sci. Technol. A Comprehensivce Treat., 2005.

[105] G. Ming-xing, W. Ming-pu, S. Kun, C. Ling-fei, L. Ruo-shan, L. Shu-mei, Trans. Nonferrous Met. Soc. China 3 (2008) 333.

[106] U. Schmidt, K. Lucke, Texture Cryst. Solids 3 (1979) 85.

[107] M. Oyarzábal, a. Martínez-de-Guerenu, I. Gutiérrez, Mater. Sci. Eng. A 485 (2008) 200.

[108] D.A. Porter, K.E. Easterling, M.Y. Sherif, Phase Transformations in Metall and Alloys, CRC Press, Boca Raton FL, 2009.

[109] C.B. Thomson, V. Randle, J. Mater. Sci. 32 (1997) 1909.

[110] V. Randle, Mater. Sci. Technol. 26 (2010) 253.

[111] V. Randle, G.S. Rohrer, H.M. Miller, M. Coleman, G.T. Owen, Acta Mater. 56 (2008) 2363.

[112] V. Randle, G. Owen, Acta Mater. 54 (2006) 1777.

[113] A.J. Schwartz, W.E. King, M. Kumar, Scr. Mater. 54 (2006) 963.

[114] T. Watanabe, in:, D.A. Molodov (Ed.), Microstruct. Des. Adv. Eng. Mater., Wiley-VCH, Weinheim, Germany, 2013, p. 403.

[115] V. Randle, Acta Mater. 52 (2004) 4067.

[116] S. Spigarelli, M. Cabibbo, E. Evangelista, G. Palumbo, Mater. Sci. Eng. A 352 (2003) 93.

[117] J.J. Kai, F.R. Chen, T.S. Duh, Mater. Trans. 45 (2004) 40.

[118] L. Tan, K. Sridharan, T.R. Allen, R.K. Nanstad, D.A. McClintock, J. Nucl. Mater. 374 (2008) 270.

[119] E. a. West, G.S. Was, J. Nucl. Mater. 392 (2009) 264.

[120] S. Xia, H. Li, T.G. Liu, B.X. Zhou, J. Nucl. Mater. 416 (2011) 303.

[121] V. Randle, Acta Mater. 47 (1999) 4187.

[122] E.. Lehockey, D. Limoges, G. Palumbo, J. Sklarchuk, K. Tomantschger, a Vincze, J. Power Sources 78 (1999) 79.

[123] E.M. Lehockey, G. Palumbo, P. Lin, Scr. Mater. 39 (1998) 353.

[124] H. Akhiani, M. Nezakat, A. Sonboli, J. Szpunar, Mater. Sci. Eng. A (2014).

[125] M. Caul, J. Fiedler, V. Randle, Scr. Mater. 35 (1996) 831.

[126] D.S. Lee, H.. S. Ryoo, S.K. Hwang, Mater. Sci. Eng. A 354 (2003) 106.

[127] P. Davies, V. Randle, 17 (2001) 615.

[128] D.J. Drabble, C.M. Bishop, M. V. Kral, Metall. Mater. Trans. A 42 (2010) 763.

[129] F. Shi, X. Li, Y. Hu, C. Su, C. Liu, Acta Metall. Sin. 26 (2013) 497.

[130] V. Randle, M. Coleman, Acta Mater. 57 (2009) 3410.

[131] P. Kritzer, J. Supercrit. Fluids 29 (2004) 1.

[132] L. Zhang, Y. Bao, R. Tang, Nucl. Eng. Des. 249 (2012) 180.

[133] M. Fulger, M. Mihalache, D. Ohai, S. Fulger, S.C. Valeca, J. Nucl. Mater. 415 (2011) 147.

[134] L. Tan, T.R. Allen, Y. Yang, Corros. Sci. 53 (2011) 703.

[135] G.S. Was, P. Ampornrat, G. Gupta, S. Teysseyre, E. a. West, T.R. Allen, K. Sridharan, L. Tan, Y. Chen, X. Ren, C. Pister, J. Nucl. Mater. 371 (2007) 176.

[136] L. Tan, X. Ren, K. Sridharan, T.R. Allen, Corros. Sci. 50 (2008) 2040.

[137] M. Fulger, D. Ohai, M. Mihalache, M. Pantiru, V. Malinovschi, J. Nucl. Mater. 385 (2009) 288.

[138] S. Mahboubi, G.A. Button, J. Kish, in:, 19th Pacific Basin Nucl. Conf., Vancouver, 2014.

[139] S. Penttilä, a. Toivonen, J. Li, W. Zheng, R. Novotny, J. Supercrit. Fluids 81 (2013) 157.

[140] M. Nezakat, H. Akhian, S. Penttilä, J. Szpunar, Corros. Sci. (n.d.).

[141] G. Nolze, a. Winkelmann, Cryst. Res. Technol. 49 (2014) 490.

[142] J. Litz, a. Rahmel, M. Schorr, Oxid. Met. 30 (1988) 95.

[143] U. Krupp, H. Christ, 31 (2000) 47.

[144] R.N. Durham, B. Gleeson, D.J. Young, 50 (1998).

[145] C. Ostwald, H.J. Grabke, Corros. Sci. 46 (2004) 1113.

[146] P. Berthod, Oxid. Met. 68 (2007) 77.

[147] W.F. Chu, A. Rahmel, 15 (1980) 331.

[148] G. Neumann, C. Tuijn, Self-Diffusion and Impurity Diffusion in Pure Metals: Handbook of Experimental Data, Elsevier Ltd., 2009.

[149] J. Park, C.J. Altstetter, Metall. Trans. A 18A (1987) 43.

[150] S.J. Rothman, L.J. Nowicki, G.E. Murch, J. Phys. F-Metal Phys. 10 (1980) 383.

[151] H. Akhiani, M. Nezakat, M. Sanayei, J. Szpunar, Mater. Des. (n.d.).

[152] R. Bès, S. Gavarini, N. Millard-Pinard, S. Cardinal, a. Perrat-Mabilon, C. Peaucelle, T. Douillard, J. Nucl. Mater. 427 (2012) 415.

[153] L.P. Bonfrisco, M. Frary, J. Mater. Sci. 45 (2009) 1663.

Appendix

COPYRIGHT PERMISSION

For previously published manuscripts that form a part of a thesis, written permission from the publisher (copyright holder) is required by the College of Graduate Studies and Research (CGSR). All of the manuscripts used in this thesis were published or are under review in the Elsevier's journal. Therefore, this appendix includes the copyright permissions from the Elsevier for each of the papers in this thesis. Also, the below quotation, which is copied from the Elsevier website in October 2014, is applicable for all enclosed manuscripts in the thesis. (https://help.elsevier.com/app/answers/detail/a_id/565/session/L3RpbWUv/p/8045)

"*As an author, you retain rights for a large number of author uses, including use by your employing institute or company. These rights are retained and permitted without the need to obtain specific permission from Elsevier. These include:*

- *The right to make copies of the article for your own personal use, including for your own classroom teaching use.*
- *The right to make copies and distribute copies (including through e-mail) of the article to research colleagues, for the personal use by such colleagues (but not commercially or systematically, e.g. via an e-mail list or list serve).*
- *The right to post a pre-print version of the article on Internet web sites including electronic pre-print servers, and to retain indefinitely such version on such servers or sites (see also our information on electronic preprints for a more detailed discussion on these points.).*
- *The right to post a revised personal version of the text of the final article (to reflect changes made in the peer review process) on the author's personal or institutional web site or server, with a link to the journal home page (on elsevier.com).*
- *The right to present the article at a meeting or conference and to distribute copies of such paper or article to the delegates attending the meeting.*
- *For the author's employer, if the article is a 'work for hire', made within the scope of the author's employment, the right to use all or part of the information in (any version of) the article for other intra-company use (e.g. training).*

- *Patent and trademark rights and rights to any process or procedure described in the article.*
- *The right to include the article in full or in part in a thesis or dissertation (provided that this is not to be published commercially).*
- *The right to use the article or any part there of in a printed compilation of works of the author, such as collected writings or lecture notes (subsequent to publication of the article in the journal).*
- *The right to prepare other derivative works, to extend the article into book-length form, or to otherwise re-use portions or excerpts in other works, with full acknowledgement of its original publication in the journal."*

Copyright Permission for Manuscript #1 (Chapter 2)

ELSEVIER LICENSE
TERMS AND CONDITIONS

Oct 23, 2014

This is a License Agreement between Hamed Akhiani ("You") and Elsevier ("Elsevier") provided by Copyright Clearance Center ("CCC"). The license consists of your order details, the terms and conditions provided by Elsevier, and the payment terms and conditions.

All payments must be made in full to CCC. For payment instructions, please see information listed at the bottom of this form.

Supplier	Elsevier Limited The Boulevard,Langford Lane Kidlington,Oxford,OX5 1GB,UK
Registered Company Number	1982084
Customer name	Hamed Akhiani
Customer address	57 Campus Drive Saskatoon, SK S7N5A9
License number	3494470861421
License date	Oct 22, 2014
Licensed content publisher	Elsevier
Licensed content publication	Applied Surface Science
Licensed content title	Effect of surface roughness on the texture and oxidation behavior of Zircaloy-4 cladding tube
Licensed content author	Hamed Akhiani,Jerzy A. Szpunar
Licensed content date	15 November 2013
Licensed content volume number	285
Licensed content issue number	n/a
Number of pages	8
Start Page	832
End Page	839
Type of Use	reuse in a thesis/dissertation
Intended publisher of new work	other

Portion	full article
Format	both print and electronic
Are you the author of this Elsevier article?	Yes
Will you be translating?	No
Title of your thesis/dissertation	ZIRCALOY-4 AND INCOLOY 800H/HT ALLOYS FOR THE CURRENT AND FUTURE NUCLEAR FUEL CLADDINGS
Expected completion date	Dec 2014
Estimated size (number of pages)	160
Elsevier VAT number	GB 494 6272 12
Permissions price	0.00 USD
VAT/Local Sales Tax	0.00 USD / 0.00 GBP
Total	0.00 USD
Terms and Conditions	

INTRODUCTION

1. The publisher for this copyrighted material is Elsevier. By clicking "accept" in connection with completing this licensing transaction, you agree that the following terms and conditions apply to this transaction (along with the Billing and Payment terms and conditions established by Copyright Clearance Center, Inc. ("CCC"), at the time that you opened your Rightslink account and that are available at any time at http://myaccount.copyright.com).

GENERAL TERMS

2. Elsevier hereby grants you permission to reproduce the aforementioned material subject to the terms and conditions indicated.

3. Acknowledgement: If any part of the material to be used (for example, figures) has appeared in our publication with credit or acknowledgement to another source, permission must also be sought from that source. If such permission is not obtained then that material may not be included in your publication/copies. Suitable acknowledgement to the source must be made, either as a footnote or in a reference list at the end of your publication, as follows:

"Reprinted from Publication title, Vol /edition number, Author(s), Title of article / title of chapter, Pages No., Copyright (Year), with permission from Elsevier [OR APPLICABLE SOCIETY COPYRIGHT OWNER]." Also Lancet special credit - "Reprinted from The Lancet, Vol. number, Author(s), Title of article, Pages No., Copyright (Year), with permission from Elsevier."

4. Reproduction of this material is confined to the purpose and/or media for which

permission is hereby given.

5. Altering/Modifying Material: Not Permitted. However figures and illustrations may be altered/adapted minimally to serve your work. Any other abbreviations, additions, deletions and/or any other alterations shall be made only with prior written authorization of Elsevier Ltd. (Please contact Elsevier at permissions@elsevier.com)

6. If the permission fee for the requested use of our material is waived in this instance, please be advised that your future requests for Elsevier materials may attract a fee.

7. Reservation of Rights: Publisher reserves all rights not specifically granted in the combination of (i) the license details provided by you and accepted in the course of this licensing transaction, (ii) these terms and conditions and (iii) CCC's Billing and Payment terms and conditions.

8. License Contingent Upon Payment: While you may exercise the rights licensed immediately upon issuance of the license at the end of the licensing process for the transaction, provided that you have disclosed complete and accurate details of your proposed use, no license is finally effective unless and until full payment is received from you (either by publisher or by CCC) as provided in CCC's Billing and Payment terms and conditions. If full payment is not received on a timely basis, then any license preliminarily granted shall be deemed automatically revoked and shall be void as if never granted. Further, in the event that you breach any of these terms and conditions or any of CCC's Billing and Payment terms and conditions, the license is automatically revoked and shall be void as if never granted. Use of materials as described in a revoked license, as well as any use of the materials beyond the scope of an unrevoked license, may constitute copyright infringement and publisher reserves the right to take any and all action to protect its copyright in the materials.

9. Warranties: Publisher makes no representations or warranties with respect to the licensed material.

10. Indemnity: You hereby indemnify and agree to hold harmless publisher and CCC, and their respective officers, directors, employees and agents, from and against any and all claims arising out of your use of the licensed material other than as specifically authorized pursuant to this license.

11. No Transfer of License: This license is personal to you and may not be sublicensed, assigned, or transferred by you to any other person without publisher's written permission.

12. No Amendment Except in Writing: This license may not be amended except in a writing signed by both parties (or, in the case of publisher, by CCC on publisher's behalf).

13. Objection to Contrary Terms: Publisher hereby objects to any terms contained in any purchase order, acknowledgment, check endorsement or other writing prepared by you, which terms are inconsistent with these terms and conditions or CCC's Billing and

Payment terms and conditions. These terms and conditions, together with CCC's Billing and Payment terms and conditions (which are incorporated herein), comprise the entire agreement between you and publisher (and CCC) concerning this licensing transaction. In the event of any conflict between your obligations established by these terms and conditions and those established by CCC's Billing and Payment terms and conditions, these terms and conditions shall control.

14. Revocation: Elsevier or Copyright Clearance Center may deny the permissions described in this License at their sole discretion, for any reason or no reason, with a full refund payable to you. Notice of such denial will be made using the contact information provided by you. Failure to receive such notice will not alter or invalidate the denial. In no event will Elsevier or Copyright Clearance Center be responsible or liable for any costs, expenses or damage incurred by you as a result of a denial of your permission request, other than a refund of the amount(s) paid by you to Elsevier and/or Copyright Clearance Center for denied permissions.

LIMITED LICENSE

The following terms and conditions apply only to specific license types:

15. **Translation**: This permission is granted for non-exclusive world **English** rights only unless your license was granted for translation rights. If you licensed translation rights you may only translate this content into the languages you requested. A professional translator must perform all translations and reproduce the content word for word preserving the integrity of the article. If this license is to re-use 1 or 2 figures then permission is granted for non-exclusive world rights in all languages.

16. **Posting licensed content on any Website**: The following terms and conditions apply as follows: Licensing material from an Elsevier journal: All content posted to the web site must maintain the copyright information line on the bottom of each image; A hyper-text must be included to the Homepage of the journal from which you are licensing athttp://www.sciencedirect.com/science/journal/xxxxx or the Elsevier homepage for books athttp://www.elsevier.com; Central Storage: This license does not include permission for a scanned version of the material to be stored in a central repository such as that provided by Heron/XanEdu.

Licensing material from an Elsevier book: A hyper-text link must be included to the Elsevier homepage at http://www.elsevier.com . All content posted to the web site must maintain the copyright information line on the bottom of each image.

Posting licensed content on Electronic reserve: In addition to the above the following clauses are applicable: The web site must be password-protected and made available only to bona fide students registered on a relevant course. This permission is granted for 1 year only. You may obtain a new license for future website posting.

For journal authors: the following clauses are applicable in addition to the above: Permission granted is limited to the author accepted manuscript version* of your paper.

***Accepted Author Manuscript (AAM) Definition:** An accepted author manuscript (AAM) is the author's version of the manuscript of an article that has been accepted for publication and which may include any author-incorporated changes suggested through the processes of submission processing, peer review, and editor-author communications. AAMs do not include other publisher value-added contributions such as copy-editing, formatting, technical enhancements and (if relevant) pagination.

You are not allowed to download and post the published journal article (whether PDF or HTML, proof or final version), nor may you scan the printed edition to create an electronic version. A hyper-text must be included to the Homepage of the journal from which you are licensing athttp://www.sciencedirect.com/science/journal/xxxxx. As part of our normal production process, you will receive an e-mail notice when your article appears on Elsevier's online service ScienceDirect (www.sciencedirect.com). That e-mail will include the article's Digital Object Identifier (DOI). This number provides the electronic link to the published article and should be included in the posting of your personal version. We ask that you wait until you receive this e-mail and have the DOI to do any posting.

Posting to a repository: Authors may post their AAM immediately to their employer's institutional repository for internal use only and may make their manuscript publically available after the journal-specific embargo period has ended.

Please also refer to Elsevier's Article Posting Policy for further information.

18. **For book authors** the following clauses are applicable in addition to the above: Authors are permitted to place a brief summary of their work online only.. You are not allowed to download and post the published electronic version of your chapter, nor may you scan the printed edition to create an electronic version. **Posting to a repository:** Authors are permitted to post a summary of their chapter only in their institution's repository.

20. **Thesis/Dissertation**: If your license is for use in a thesis/dissertation your thesis may be submitted to your institution in either print or electronic form. Should your thesis be published commercially, please reapply for permission. These requirements include permission for the Library and Archives of Canada to supply single copies, on demand, of the complete thesis and include permission for UMI to supply single copies, on demand, of the complete thesis. Should your thesis be published commercially, please reapply for permission.

Elsevier Open Access Terms and Conditions

Elsevier publishes Open Access articles in both its Open Access journals and via its Open

Access articles option in subscription journals.

Authors publishing in an Open Access journal or who choose to make their article Open Access in an Elsevier subscription journal select one of the following Creative Commons user licenses, which define how a reader may reuse their work: Creative Commons Attribution License (CC BY), Creative Commons Attribution – Non Commercial - ShareAlike (CC BY NC SA) and Creative Commons Attribution – Non Commercial – No Derivatives (CC BY NC ND)

Terms & Conditions applicable to all Elsevier Open Access articles:

Any reuse of the article must not represent the author as endorsing the adaptation of the article nor should the article be modified in such a way as to damage the author's honour or reputation.

The author(s) must be appropriately credited.

If any part of the material to be used (for example, figures) has appeared in our publication with credit or acknowledgement to another source it is the responsibility of the user to ensure their reuse complies with the terms and conditions determined by the rights holder.

Additional Terms & Conditions applicable to each Creative Commons user license:

CC BY: You may distribute and copy the article, create extracts, abstracts, and other revised versions, adaptations or derivative works of or from an article (such as a translation), to include in a collective work (such as an anthology), to text or data mine the article, including for commercial purposes without permission from Elsevier

CC BY NC SA: For non-commercial purposes you may distribute and copy the article, create extracts, abstracts and other revised versions, adaptations or derivative works of or from an article (such as a translation), to include in a collective work (such as an anthology), to text and data mine the article and license new adaptations or creations under identical terms without permission from Elsevier

CC BY NC ND: For non-commercial purposes you may distribute and copy the article and include it in a collective work (such as an anthology), provided you do not alter or modify the article, without permission from Elsevier

Any commercial reuse of Open Access articles published with a CC BY NC SA or CC BY NC ND license requires permission from Elsevier and will be subject to a fee.

Commercial reuse includes:

- Promotional purposes (advertising or marketing)

- Commercial exploitation (e.g. a product for sale or loan)
- Systematic distribution (for a fee or free of charge)

Please refer to Elsevier's Open Access Policy for further information.

21. **Other Conditions**:

Questions? customercare@copyright.com or +1-855-239-3415 (toll free in the US) or +1-978-646-2777.

Gratis licenses (referencing $0 in the Total field) are free. Please retain this printable license for your reference. No payment is required.

Copyright Permission for Manuscript #2 (Chapter 3)

ELSEVIER LICENSE
TERMS AND CONDITIONS

Oct 23, 2014

This is a License Agreement between Hamed Akhiani ("You") and Elsevier ("Elsevier") provided by Copyright Clearance Center ("CCC"). The license consists of your order details, the terms and conditions provided by Elsevier, and the payment terms and conditions.

All payments must be made in full to CCC. For payment instructions, please see information listed at the bottom of this form.

Supplier	Elsevier Limited The Boulevard,Langford Lane Kidlington,Oxford,OX5 1GB,UK
Registered Company Number	1982084
Customer name	Hamed Akhiani
Customer address	57 Campus Drive Saskatoon, SK S7N5A9
License number	3494841177120
License date	Oct 23, 2014
Licensed content publisher	Elsevier
Licensed content publication	Journal of Alloys and Compounds
Licensed content title	The electronic structure of zirconium in hydrided and oxidized states
Licensed content author	Hamed Akhiani,Adrian Hunt,Xiaoyu Cui,Alexander Moewes,Jerzy Szpunar
Licensed content date	Available online 19 October 2014
Licensed content volume number	n/a
Licensed content issue number	n/a
Number of pages	1
Start Page	None
End Page	None
Type of Use	reuse in a thesis/dissertation
Intended publisher of new work	other

Portion	full article
Format	both print and electronic
Are you the author of this Elsevier article?	Yes
Will you be translating?	No
Title of your thesis/dissertation	ZIRCALOY-4 AND INCOLOY 800H/HT ALLOYS FOR THE CURRENT AND FUTURE NUCLEAR FUEL CLADDINGS
Expected completion date	Dec 2014
Estimated size (number of pages)	
Elsevier VAT number	GB 494 6272 12
Permissions price	0.00 USD
VAT/Local Sales Tax	0.00 USD / 0.00 GBP
Total	0.00 USD

Terms and Conditions

INTRODUCTION

1. The publisher for this copyrighted material is Elsevier. By clicking "accept" in connection with completing this licensing transaction, you agree that the following terms and conditions apply to this transaction (along with the Billing and Payment terms and conditions established by Copyright Clearance Center, Inc. ("CCC"), at the time that you opened your Rightslink account and that are available at any time at http://myaccount.copyright.com).

GENERAL TERMS

2. Elsevier hereby grants you permission to reproduce the aforementioned material subject to the terms and conditions indicated.

3. Acknowledgement: If any part of the material to be used (for example, figures) has appeared in our publication with credit or acknowledgement to another source, permission must also be sought from that source. If such permission is not obtained then that material may not be included in your publication/copies. Suitable acknowledgement to the source must be made, either as a footnote or in a reference list at the end of your publication, as follows:

"Reprinted from Publication title, Vol /edition number, Author(s), Title of article / title of chapter, Pages No., Copyright (Year), with permission from Elsevier [OR APPLICABLE SOCIETY COPYRIGHT OWNER]." Also Lancet special credit - "Reprinted from The Lancet, Vol. number, Author(s), Title of article, Pages No., Copyright (Year), with permission from Elsevier."

4. Reproduction of this material is confined to the purpose and/or media for which

permission is hereby given.

5. Altering/Modifying Material: Not Permitted. However figures and illustrations may be altered/adapted minimally to serve your work. Any other abbreviations, additions, deletions and/or any other alterations shall be made only with prior written authorization of Elsevier Ltd. (Please contact Elsevier at permissions@elsevier.com)

6. If the permission fee for the requested use of our material is waived in this instance, please be advised that your future requests for Elsevier materials may attract a fee.

7. Reservation of Rights: Publisher reserves all rights not specifically granted in the combination of (i) the license details provided by you and accepted in the course of this licensing transaction, (ii) these terms and conditions and (iii) CCC's Billing and Payment terms and conditions.

8. License Contingent Upon Payment: While you may exercise the rights licensed immediately upon issuance of the license at the end of the licensing process for the transaction, provided that you have disclosed complete and accurate details of your proposed use, no license is finally effective unless and until full payment is received from you (either by publisher or by CCC) as provided in CCC's Billing and Payment terms and conditions. If full payment is not received on a timely basis, then any license preliminarily granted shall be deemed automatically revoked and shall be void as if never granted. Further, in the event that you breach any of these terms and conditions or any of CCC's Billing and Payment terms and conditions, the license is automatically revoked and shall be void as if never granted. Use of materials as described in a revoked license, as well as any use of the materials beyond the scope of an unrevoked license, may constitute copyright infringement and publisher reserves the right to take any and all action to protect its copyright in the materials.

9. Warranties: Publisher makes no representations or warranties with respect to the licensed material.

10. Indemnity: You hereby indemnify and agree to hold harmless publisher and CCC, and their respective officers, directors, employees and agents, from and against any and all claims arising out of your use of the licensed material other than as specifically authorized pursuant to this license.

11. No Transfer of License: This license is personal to you and may not be sublicensed, assigned, or transferred by you to any other person without publisher's written permission.

12. No Amendment Except in Writing: This license may not be amended except in a writing signed by both parties (or, in the case of publisher, by CCC on publisher's behalf).

13. Objection to Contrary Terms: Publisher hereby objects to any terms contained in any purchase order, acknowledgment, check endorsement or other writing prepared by you, which terms are inconsistent with these terms and conditions or CCC's Billing and

Payment terms and conditions. These terms and conditions, together with CCC's Billing and Payment terms and conditions (which are incorporated herein), comprise the entire agreement between you and publisher (and CCC) concerning this licensing transaction. In the event of any conflict between your obligations established by these terms and conditions and those established by CCC's Billing and Payment terms and conditions, these terms and conditions shall control.

14. Revocation: Elsevier or Copyright Clearance Center may deny the permissions described in this License at their sole discretion, for any reason or no reason, with a full refund payable to you. Notice of such denial will be made using the contact information provided by you. Failure to receive such notice will not alter or invalidate the denial. In no event will Elsevier or Copyright Clearance Center be responsible or liable for any costs, expenses or damage incurred by you as a result of a denial of your permission request, other than a refund of the amount(s) paid by you to Elsevier and/or Copyright Clearance Center for denied permissions.

LIMITED LICENSE

The following terms and conditions apply only to specific license types:

15. **Translation**: This permission is granted for non-exclusive world **English** rights only unless your license was granted for translation rights. If you licensed translation rights you may only translate this content into the languages you requested. A professional translator must perform all translations and reproduce the content word for word preserving the integrity of the article. If this license is to re-use 1 or 2 figures then permission is granted for non-exclusive world rights in all languages.

16. **Posting licensed content on any Website**: The following terms and conditions apply as follows: Licensing material from an Elsevier journal: All content posted to the web site must maintain the copyright information line on the bottom of each image; A hyper-text must be included to the Homepage of the journal from which you are licensing athttp://www.sciencedirect.com/science/journal/xxxxx or the Elsevier homepage for books athttp://www.elsevier.com; Central Storage: This license does not include permission for a scanned version of the material to be stored in a central repository such as that provided by Heron/XanEdu.

Licensing material from an Elsevier book: A hyper-text link must be included to the Elsevier homepage at http://www.elsevier.com . All content posted to the web site must maintain the copyright information line on the bottom of each image.

Posting licensed content on Electronic reserve: In addition to the above the following clauses are applicable: The web site must be password-protected and made available only to bona fide students registered on a relevant course. This permission is granted for 1 year only. You may obtain a new license for future website posting.

For journal authors: the following clauses are applicable in addition to the above: Permission granted is limited to the author accepted manuscript version* of your paper.

***Accepted Author Manuscript (AAM) Definition:** An accepted author manuscript (AAM) is the author's version of the manuscript of an article that has been accepted for publication and which may include any author-incorporated changes suggested through the processes of submission processing, peer review, and editor-author communications. AAMs do not include other publisher value-added contributions such as copy-editing, formatting, technical enhancements and (if relevant) pagination.

You are not allowed to download and post the published journal article (whether PDF or HTML, proof or final version), nor may you scan the printed edition to create an electronic version. A hyper-text must be included to the Homepage of the journal from which you are licensing athttp://www.sciencedirect.com/science/journal/xxxxx. As part of our normal production process, you will receive an e-mail notice when your article appears on Elsevier's online service ScienceDirect (www.sciencedirect.com). That e-mail will include the article's Digital Object Identifier (DOI). This number provides the electronic link to the published article and should be included in the posting of your personal version. We ask that you wait until you receive this e-mail and have the DOI to do any posting.

Posting to a repository: Authors may post their AAM immediately to their employer's institutional repository for internal use only and may make their manuscript publically available after the journal-specific embargo period has ended.

Please also refer to Elsevier's Article Posting Policy for further information.

18. **For book authors** the following clauses are applicable in addition to the above: Authors are permitted to place a brief summary of their work online only.. You are not allowed to download and post the published electronic version of your chapter, nor may you scan the printed edition to create an electronic version. **Posting to a repository:** Authors are permitted to post a summary of their chapter only in their institution's repository.

20. **Thesis/Dissertation**: If your license is for use in a thesis/dissertation your thesis may be submitted to your institution in either print or electronic form. Should your thesis be published commercially, please reapply for permission. These requirements include permission for the Library and Archives of Canada to supply single copies, on demand, of the complete thesis and include permission for UMI to supply single copies, on demand, of the complete thesis. Should your thesis be published commercially, please reapply for permission.

Elsevier Open Access Terms and Conditions

Elsevier publishes Open Access articles in both its Open Access journals and via its Open Access articles option in subscription journals.

Authors publishing in an Open Access journal or who choose to make their article Open Access in an Elsevier subscription journal select one of the following Creative Commons user licenses, which define how a reader may reuse their work: Creative Commons Attribution License (CC BY), Creative Commons Attribution – Non Commercial - ShareAlike (CC BY NC SA) and Creative Commons Attribution – Non Commercial – No Derivatives (CC BY NC ND)

Terms & Conditions applicable to all Elsevier Open Access articles:

Any reuse of the article must not represent the author as endorsing the adaptation of the article nor should the article be modified in such a way as to damage the author's honour or reputation.

The author(s) must be appropriately credited.

If any part of the material to be used (for example, figures) has appeared in our publication with credit or acknowledgement to another source it is the responsibility of the user to ensure their reuse complies with the terms and conditions determined by the rights holder.

Additional Terms & Conditions applicable to each Creative Commons user license:

CC BY: You may distribute and copy the article, create extracts, abstracts, and other revised versions, adaptations or derivative works of or from an article (such as a translation), to include in a collective work (such as an anthology), to text or data mine the article, including for commercial purposes without permission from Elsevier

CC BY NC SA: For non-commercial purposes you may distribute and copy the article, create extracts, abstracts and other revised versions, adaptations or derivative works of or from an article (such as a translation), to include in a collective work (such as an anthology), to text and data mine the article and license new adaptations or creations under identical terms without permission from Elsevier

CC BY NC ND: For non-commercial purposes you may distribute and copy the article and include it in a collective work (such as an anthology), provided you do not alter or modify the article, without permission from Elsevier

Any commercial reuse of Open Access articles published with a CC BY NC SA or CC BY NC ND license requires permission from Elsevier and will be subject to a fee.

Commercial reuse includes:

- Promotional purposes (advertising or marketing)
- Commercial exploitation (e.g. a product for sale or loan)

- Systematic distribution (for a fee or free of charge)

Please refer to Elsevier's Open Access Policy for further information.

21. **Other Conditions**:

Questions? customercare@copyright.com or +1-855-239-3415 (toll free in the US) or +1-978-646-2777.

Gratis licenses (referencing $0 in the Total field) are free. Please retain this printable license for your reference. No payment is required.

Copyright Permission for Manuscript #3 (Chapter 4)

ELSEVIER LICENSE
TERMS AND CONDITIONS

Oct 22, 2014

This is a License Agreement between Hamed Akhiani ("You") and Elsevier ("Elsevier") provided by Copyright Clearance Center ("CCC"). The license consists of your order details, the terms and conditions provided by Elsevier, and the payment terms and conditions.

All payments must be made in full to CCC. For payment instructions, please see information listed at the bottom of this form.

Supplier	Elsevier Limited The Boulevard,Langford Lane Kidlington,Oxford,OX5 1GB,UK
Registered Company Number	1982084
Customer name	Hamed Akhiani
Customer address	57 Campus Drive Saskatoon, SK S7N5A9
License number	3494470786826
License date	Oct 22, 2014
Licensed content publisher	Elsevier
Licensed content publication	Materials Science and Engineering: A
Licensed content title	Evolution of deformation and annealing textures in Incoloy 800H/HT via different rolling paths and strains
Licensed content author	Hamed Akhiani,Majid Nezakat,Jerzy A. Szpunar
Licensed content date	22 September 2014
Licensed content volume number	614
Licensed content issue number	n/a
Number of pages	14
Start Page	250
End Page	263
Type of Use	reuse in a thesis/dissertation
Intended publisher of new work	other

Portion	full article
Format	both print and electronic
Are you the author of this Elsevier article?	Yes
Will you be translating?	No
Title of your thesis/dissertation	ZIRCALOY-4 AND INCOLOY 800H/HT ALLOYS FOR THE CURRENT AND FUTURE NUCLEAR FUEL CLADDINGS
Expected completion date	Dec 2014
Estimated size (number of pages)	160
Elsevier VAT number	GB 494 6272 12
Permissions price	0.00 USD
VAT/Local Sales Tax	0.00 USD / 0.00 GBP
Total	0.00 USD

Terms and Conditions

INTRODUCTION

1. The publisher for this copyrighted material is Elsevier. By clicking "accept" in connection with completing this licensing transaction, you agree that the following terms and conditions apply to this transaction (along with the Billing and Payment terms and conditions established by Copyright Clearance Center, Inc. ("CCC"), at the time that you opened your Rightslink account and that are available at any time at http://myaccount.copyright.com).

GENERAL TERMS

2. Elsevier hereby grants you permission to reproduce the aforementioned material subject to the terms and conditions indicated.

3. Acknowledgement: If any part of the material to be used (for example, figures) has appeared in our publication with credit or acknowledgement to another source, permission must also be sought from that source. If such permission is not obtained then that material may not be included in your publication/copies. Suitable acknowledgement to the source must be made, either as a footnote or in a reference list at the end of your publication, as follows:

"Reprinted from Publication title, Vol /edition number, Author(s), Title of article / title of chapter, Pages No., Copyright (Year), with permission from Elsevier [OR APPLICABLE SOCIETY COPYRIGHT OWNER]." Also Lancet special credit - "Reprinted from The Lancet, Vol. number, Author(s), Title of article, Pages No., Copyright (Year), with permission from Elsevier."

4. Reproduction of this material is confined to the purpose and/or media for which

permission is hereby given.

5. Altering/Modifying Material: Not Permitted. However figures and illustrations may be altered/adapted minimally to serve your work. Any other abbreviations, additions, deletions and/or any other alterations shall be made only with prior written authorization of Elsevier Ltd. (Please contact Elsevier at permissions@elsevier.com)

6. If the permission fee for the requested use of our material is waived in this instance, please be advised that your future requests for Elsevier materials may attract a fee.

7. Reservation of Rights: Publisher reserves all rights not specifically granted in the combination of (i) the license details provided by you and accepted in the course of this licensing transaction, (ii) these terms and conditions and (iii) CCC's Billing and Payment terms and conditions.

8. License Contingent Upon Payment: While you may exercise the rights licensed immediately upon issuance of the license at the end of the licensing process for the transaction, provided that you have disclosed complete and accurate details of your proposed use, no license is finally effective unless and until full payment is received from you (either by publisher or by CCC) as provided in CCC's Billing and Payment terms and conditions. If full payment is not received on a timely basis, then any license preliminarily granted shall be deemed automatically revoked and shall be void as if never granted. Further, in the event that you breach any of these terms and conditions or any of CCC's Billing and Payment terms and conditions, the license is automatically revoked and shall be void as if never granted. Use of materials as described in a revoked license, as well as any use of the materials beyond the scope of an unrevoked license, may constitute copyright infringement and publisher reserves the right to take any and all action to protect its copyright in the materials.

9. Warranties: Publisher makes no representations or warranties with respect to the licensed material.

10. Indemnity: You hereby indemnify and agree to hold harmless publisher and CCC, and their respective officers, directors, employees and agents, from and against any and all claims arising out of your use of the licensed material other than as specifically authorized pursuant to this license.

11. No Transfer of License: This license is personal to you and may not be sublicensed, assigned, or transferred by you to any other person without publisher's written permission.

12. No Amendment Except in Writing: This license may not be amended except in a writing signed by both parties (or, in the case of publisher, by CCC on publisher's behalf).

13. Objection to Contrary Terms: Publisher hereby objects to any terms contained in any purchase order, acknowledgment, check endorsement or other writing prepared by you, which terms are inconsistent with these terms and conditions or CCC's Billing and

Payment terms and conditions. These terms and conditions, together with CCC's Billing and Payment terms and conditions (which are incorporated herein), comprise the entire agreement between you and publisher (and CCC) concerning this licensing transaction. In the event of any conflict between your obligations established by these terms and conditions and those established by CCC's Billing and Payment terms and conditions, these terms and conditions shall control.

14. Revocation: Elsevier or Copyright Clearance Center may deny the permissions described in this License at their sole discretion, for any reason or no reason, with a full refund payable to you. Notice of such denial will be made using the contact information provided by you. Failure to receive such notice will not alter or invalidate the denial. In no event will Elsevier or Copyright Clearance Center be responsible or liable for any costs, expenses or damage incurred by you as a result of a denial of your permission request, other than a refund of the amount(s) paid by you to Elsevier and/or Copyright Clearance Center for denied permissions.

LIMITED LICENSE

The following terms and conditions apply only to specific license types:

15. **Translation**: This permission is granted for non-exclusive world **English** rights only unless your license was granted for translation rights. If you licensed translation rights you may only translate this content into the languages you requested. A professional translator must perform all translations and reproduce the content word for word preserving the integrity of the article. If this license is to re-use 1 or 2 figures then permission is granted for non-exclusive world rights in all languages.

16. **Posting licensed content on any Website**: The following terms and conditions apply as follows: Licensing material from an Elsevier journal: All content posted to the web site must maintain the copyright information line on the bottom of each image; A hyper-text must be included to the Homepage of the journal from which you are licensing athttp://www.sciencedirect.com/science/journal/xxxxx or the Elsevier homepage for books athttp://www.elsevier.com; Central Storage: This license does not include permission for a scanned version of the material to be stored in a central repository such as that provided by Heron/XanEdu.

Licensing material from an Elsevier book: A hyper-text link must be included to the Elsevier homepage at http://www.elsevier.com . All content posted to the web site must maintain the copyright information line on the bottom of each image.

Posting licensed content on Electronic reserve: In addition to the above the following clauses are applicable: The web site must be password-protected and made available only to bona fide students registered on a relevant course. This permission is granted for 1 year only. You may obtain a new license for future website posting.

For journal authors: the following clauses are applicable in addition to the above: Permission granted is limited to the author accepted manuscript version* of your paper.

***Accepted Author Manuscript (AAM) Definition:** An accepted author manuscript (AAM) is the author's version of the manuscript of an article that has been accepted for publication and which may include any author-incorporated changes suggested through the processes of submission processing, peer review, and editor-author communications. AAMs do not include other publisher value-added contributions such as copy-editing, formatting, technical enhancements and (if relevant) pagination.

You are not allowed to download and post the published journal article (whether PDF or HTML, proof or final version), nor may you scan the printed edition to create an electronic version. A hyper-text must be included to the Homepage of the journal from which you are licensing athttp://www.sciencedirect.com/science/journal/xxxxx. As part of our normal production process, you will receive an e-mail notice when your article appears on Elsevier's online service ScienceDirect (www.sciencedirect.com). That e-mail will include the article's Digital Object Identifier (DOI). This number provides the electronic link to the published article and should be included in the posting of your personal version. We ask that you wait until you receive this e-mail and have the DOI to do any posting.

Posting to a repository: Authors may post their AAM immediately to their employer's institutional repository for internal use only and may make their manuscript publically available after the journal-specific embargo period has ended.

Please also refer to Elsevier's Article Posting Policy for further information.

18. **For book authors** the following clauses are applicable in addition to the above: Authors are permitted to place a brief summary of their work online only.. You are not allowed to download and post the published electronic version of your chapter, nor may you scan the printed edition to create an electronic version. **Posting to a repository:** Authors are permitted to post a summary of their chapter only in their institution's repository.

20. **Thesis/Dissertation**: If your license is for use in a thesis/dissertation your thesis may be submitted to your institution in either print or electronic form. Should your thesis be published commercially, please reapply for permission. These requirements include permission for the Library and Archives of Canada to supply single copies, on demand, of the complete thesis and include permission for UMI to supply single copies, on demand, of the complete thesis. Should your thesis be published commercially, please reapply for permission.

Elsevier Open Access Terms and Conditions

Elsevier publishes Open Access articles in both its Open Access journals and via its Open Access articles option in subscription journals.

Authors publishing in an Open Access journal or who choose to make their article Open Access in an Elsevier subscription journal select one of the following Creative Commons user licenses, which define how a reader may reuse their work: Creative Commons Attribution License (CC BY), Creative Commons Attribution – Non Commercial - ShareAlike (CC BY NC SA) and Creative Commons Attribution – Non Commercial – No Derivatives (CC BY NC ND)

Terms & Conditions applicable to all Elsevier Open Access articles:

Any reuse of the article must not represent the author as endorsing the adaptation of the article nor should the article be modified in such a way as to damage the author's honour or reputation.

The author(s) must be appropriately credited.

If any part of the material to be used (for example, figures) has appeared in our publication with credit or acknowledgement to another source it is the responsibility of the user to ensure their reuse complies with the terms and conditions determined by the rights holder.

Additional Terms & Conditions applicable to each Creative Commons user license:

CC BY: You may distribute and copy the article, create extracts, abstracts, and other revised versions, adaptations or derivative works of or from an article (such as a translation), to include in a collective work (such as an anthology), to text or data mine the article, including for commercial purposes without permission from Elsevier

CC BY NC SA: For non-commercial purposes you may distribute and copy the article, create extracts, abstracts and other revised versions, adaptations or derivative works of or from an article (such as a translation), to include in a collective work (such as an anthology), to text and data mine the article and license new adaptations or creations under identical terms without permission from Elsevier

CC BY NC ND: For non-commercial purposes you may distribute and copy the article and include it in a collective work (such as an anthology), provided you do not alter or modify the article, without permission from Elsevier

Any commercial reuse of Open Access articles published with a CC BY NC SA or CC BY NC ND license requires permission from Elsevier and will be subject to a fee.

Commercial reuse includes:

- Promotional purposes (advertising or marketing)
- Commercial exploitation (e.g. a product for sale or loan)

- Systematic distribution (for a fee or free of charge)

Please refer to Elsevier's Open Access Policy for further information.

21. **Other Conditions**:

Questions? customercare@copyright.com or +1-855-239-3415 (toll free in the US) or +1-978-646-2777.

Gratis licenses (referencing $0 in the Total field) are free. Please retain this printable license for your reference. No payment is required.

Copyright Permission for Manuscript #4 (Chapter 5)

ELSEVIER LICENSE
TERMS AND CONDITIONS

Oct 22, 2014

This is a License Agreement between Hamed Akhiani ("You") and Elsevier ("Elsevier") provided by Copyright Clearance Center ("CCC"). The license consists of your order details, the terms and conditions provided by Elsevier, and the payment terms and conditions.

All payments must be made in full to CCC. For payment instructions, please see information listed at the bottom of this form.

Supplier	Elsevier Limited The Boulevard,Langford Lane Kidlington,Oxford,OX5 1GB,UK
Registered Company Number	1982084
Customer name	Hamed Akhiani
Customer address	57 Campus Drive Saskatoon, SK S7N5A9
License number	3494470007261
License date	Oct 22, 2014
Licensed content publisher	Elsevier
Licensed content publication	Materials Science and Engineering: A
Licensed content title	The origin of annealing texture in a cold-rolled Incoloy 800H/HT after different strain paths
Licensed content author	Hamed Akhiani,Majid Nezakat,Ali Sonboli,Jerzy Szpunar
Licensed content date	1 December 2014
Licensed content volume number	619
Licensed content issue number	n/a
Number of pages	11
Start Page	334
End Page	344
Type of Use	reuse in a thesis/dissertation
Portion	full article

Format	both print and electronic
Are you the author of this Elsevier article?	Yes
Will you be translating?	No
Title of your thesis/dissertation	ZIRCALOY-4 AND INCOLOY 800H/HT ALLOYS FOR THE CURRENT AND FUTURE NUCLEAR FUEL CLADDINGS
Expected completion date	Dec 2014
Estimated size (number of pages)	160
Elsevier VAT number	GB 494 6272 12
Permissions price	0.00 USD
VAT/Local Sales Tax	0.00 USD / 0.00 GBP
Total	0.00 USD

Terms and Conditions

INTRODUCTION

1. The publisher for this copyrighted material is Elsevier. By clicking "accept" in connection with completing this licensing transaction, you agree that the following terms and conditions apply to this transaction (along with the Billing and Payment terms and conditions established by Copyright Clearance Center, Inc. ("CCC"), at the time that you opened your Rightslink account and that are available at any time at http://myaccount.copyright.com).

GENERAL TERMS

2. Elsevier hereby grants you permission to reproduce the aforementioned material subject to the terms and conditions indicated.

3. Acknowledgement: If any part of the material to be used (for example, figures) has appeared in our publication with credit or acknowledgement to another source, permission must also be sought from that source. If such permission is not obtained then that material may not be included in your publication/copies. Suitable acknowledgement to the source must be made, either as a footnote or in a reference list at the end of your publication, as follows:

"Reprinted from Publication title, Vol /edition number, Author(s), Title of article / title of chapter, Pages No., Copyright (Year), with permission from Elsevier [OR APPLICABLE SOCIETY COPYRIGHT OWNER]." Also Lancet special credit - "Reprinted from The Lancet, Vol. number, Author(s), Title of article, Pages No., Copyright (Year), with permission from Elsevier."

4. Reproduction of this material is confined to the purpose and/or media for which permission is hereby given.

5. Altering/Modifying Material: Not Permitted. However figures and illustrations may be altered/adapted minimally to serve your work. Any other abbreviations, additions, deletions and/or any other alterations shall be made only with prior written authorization of Elsevier Ltd. (Please contact Elsevier at permissions@elsevier.com)

6. If the permission fee for the requested use of our material is waived in this instance, please be advised that your future requests for Elsevier materials may attract a fee.

7. Reservation of Rights: Publisher reserves all rights not specifically granted in the combination of (i) the license details provided by you and accepted in the course of this licensing transaction, (ii) these terms and conditions and (iii) CCC's Billing and Payment terms and conditions.

8. License Contingent Upon Payment: While you may exercise the rights licensed immediately upon issuance of the license at the end of the licensing process for the transaction, provided that you have disclosed complete and accurate details of your proposed use, no license is finally effective unless and until full payment is received from you (either by publisher or by CCC) as provided in CCC's Billing and Payment terms and conditions. If full payment is not received on a timely basis, then any license preliminarily granted shall be deemed automatically revoked and shall be void as if never granted. Further, in the event that you breach any of these terms and conditions or any of CCC's Billing and Payment terms and conditions, the license is automatically revoked and shall be void as if never granted. Use of materials as described in a revoked license, as well as any use of the materials beyond the scope of an unrevoked license, may constitute copyright infringement and publisher reserves the right to take any and all action to protect its copyright in the materials.

9. Warranties: Publisher makes no representations or warranties with respect to the licensed material.

10. Indemnity: You hereby indemnify and agree to hold harmless publisher and CCC, and their respective officers, directors, employees and agents, from and against any and all claims arising out of your use of the licensed material other than as specifically authorized pursuant to this license.

11. No Transfer of License: This license is personal to you and may not be sublicensed, assigned, or transferred by you to any other person without publisher's written permission.

12. No Amendment Except in Writing: This license may not be amended except in a writing signed by both parties (or, in the case of publisher, by CCC on publisher's behalf).

13. Objection to Contrary Terms: Publisher hereby objects to any terms contained in any purchase order, acknowledgment, check endorsement or other writing prepared by you, which terms are inconsistent with these terms and conditions or CCC's Billing and Payment terms and conditions. These terms and conditions, together with CCC's Billing and Payment terms and conditions (which are incorporated herein), comprise the entire

agreement between you and publisher (and CCC) concerning this licensing transaction. In the event of any conflict between your obligations established by these terms and conditions and those established by CCC's Billing and Payment terms and conditions, these terms and conditions shall control.

14. Revocation: Elsevier or Copyright Clearance Center may deny the permissions described in this License at their sole discretion, for any reason or no reason, with a full refund payable to you. Notice of such denial will be made using the contact information provided by you. Failure to receive such notice will not alter or invalidate the denial. In no event will Elsevier or Copyright Clearance Center be responsible or liable for any costs, expenses or damage incurred by you as a result of a denial of your permission request, other than a refund of the amount(s) paid by you to Elsevier and/or Copyright Clearance Center for denied permissions.

LIMITED LICENSE

The following terms and conditions apply only to specific license types:

15. **Translation**: This permission is granted for non-exclusive world **English** rights only unless your license was granted for translation rights. If you licensed translation rights you may only translate this content into the languages you requested. A professional translator must perform all translations and reproduce the content word for word preserving the integrity of the article. If this license is to re-use 1 or 2 figures then permission is granted for non-exclusive world rights in all languages.

16. **Posting licensed content on any Website**: The following terms and conditions apply as follows: Licensing material from an Elsevier journal: All content posted to the web site must maintain the copyright information line on the bottom of each image; A hyper-text must be included to the Homepage of the journal from which you are licensing athttp://www.sciencedirect.com/science/journal/xxxxx or the Elsevier homepage for books athttp://www.elsevier.com; Central Storage: This license does not include permission for a scanned version of the material to be stored in a central repository such as that provided by Heron/XanEdu.

Licensing material from an Elsevier book: A hyper-text link must be included to the Elsevier homepage at http://www.elsevier.com . All content posted to the web site must maintain the copyright information line on the bottom of each image.

Posting licensed content on Electronic reserve: In addition to the above the following clauses are applicable: The web site must be password-protected and made available only to bona fide students registered on a relevant course. This permission is granted for 1 year only. You may obtain a new license for future website posting.

For journal authors: the following clauses are applicable in addition to the above:

Permission granted is limited to the author accepted manuscript version* of your paper.

***Accepted Author Manuscript (AAM) Definition:** An accepted author manuscript (AAM) is the author's version of the manuscript of an article that has been accepted for publication and which may include any author-incorporated changes suggested through the processes of submission processing, peer review, and editor-author communications. AAMs do not include other publisher value-added contributions such as copy-editing, formatting, technical enhancements and (if relevant) pagination.

You are not allowed to download and post the published journal article (whether PDF or HTML, proof or final version), nor may you scan the printed edition to create an electronic version. A hyper-text must be included to the Homepage of the journal from which you are licensing athttp://www.sciencedirect.com/science/journal/xxxxx. As part of our normal production process, you will receive an e-mail notice when your article appears on Elsevier's online service ScienceDirect (www.sciencedirect.com). That e-mail will include the article's Digital Object Identifier (DOI). This number provides the electronic link to the published article and should be included in the posting of your personal version. We ask that you wait until you receive this e-mail and have the DOI to do any posting.

Posting to a repository: Authors may post their AAM immediately to their employer's institutional repository for internal use only and may make their manuscript publically available after the journal-specific embargo period has ended.

Please also refer to Elsevier's Article Posting Policy for further information.

18. **For book authors** the following clauses are applicable in addition to the above: Authors are permitted to place a brief summary of their work online only.. You are not allowed to download and post the published electronic version of your chapter, nor may you scan the printed edition to create an electronic version. **Posting to a repository:** Authors are permitted to post a summary of their chapter only in their institution's repository.

20. **Thesis/Dissertation**: If your license is for use in a thesis/dissertation your thesis may be submitted to your institution in either print or electronic form. Should your thesis be published commercially, please reapply for permission. These requirements include permission for the Library and Archives of Canada to supply single copies, on demand, of the complete thesis and include permission for UMI to supply single copies, on demand, of the complete thesis. Should your thesis be published commercially, please reapply for permission.

Elsevier Open Access Terms and Conditions

Elsevier publishes Open Access articles in both its Open Access journals and via its Open Access articles option in subscription journals.

Authors publishing in an Open Access journal or who choose to make their article Open

Access in an Elsevier subscription journal select one of the following Creative Commons user licenses, which define how a reader may reuse their work: Creative Commons Attribution License (CC BY), Creative Commons Attribution – Non Commercial - ShareAlike (CC BY NC SA) and Creative Commons Attribution – Non Commercial – No Derivatives (CC BY NC ND)

Terms & Conditions applicable to all Elsevier Open Access articles:

Any reuse of the article must not represent the author as endorsing the adaptation of the article nor should the article be modified in such a way as to damage the author's honour or reputation.

The author(s) must be appropriately credited.

If any part of the material to be used (for example, figures) has appeared in our publication with credit or acknowledgement to another source it is the responsibility of the user to ensure their reuse complies with the terms and conditions determined by the rights holder.

Additional Terms & Conditions applicable to each Creative Commons user license:

CC BY: You may distribute and copy the article, create extracts, abstracts, and other revised versions, adaptations or derivative works of or from an article (such as a translation), to include in a collective work (such as an anthology), to text or data mine the article, including for commercial purposes without permission from Elsevier

CC BY NC SA: For non-commercial purposes you may distribute and copy the article, create extracts, abstracts and other revised versions, adaptations or derivative works of or from an article (such as a translation), to include in a collective work (such as an anthology), to text and data mine the article and license new adaptations or creations under identical terms without permission from Elsevier

CC BY NC ND: For non-commercial purposes you may distribute and copy the article and include it in a collective work (such as an anthology), provided you do not alter or modify the article, without permission from Elsevier

Any commercial reuse of Open Access articles published with a CC BY NC SA or CC BY NC ND license requires permission from Elsevier and will be subject to a fee.

Commercial reuse includes:

- Promotional purposes (advertising or marketing)
- Commercial exploitation (e.g. a product for sale or loan)
- Systematic distribution (for a fee or free of charge)

Please refer to Elsevier's Open Access Policy for further information.

21. **Other Conditions**:

v1.6